STUDIES OF LASER-PLASMA X-RAY AND ION SOURCES FROM SOLID AND LOW- DENSITY FOAM TARGETS

By

Channprit Kaur

Enrolment No. PHYS01201504009

Bhabha Atomic Research Centre, Mumbai, India

A thesis submitted to the

Board of Studies in Physical Sciences

In partial fulfilment of requirements

for the Degree of

DOCTOR OF PHILOSOPHY (PHYSICS)

of

HOMI BHABHA NATIONAL INSTITUTE

April 2019

Homi Bhabha National Institute

Recommendation of the Viva Voce Committee

As members of the Viva Voce Committee, we certify that we have read the dissertation prepared by Miss Channprit Kaur entitled "Studies of Laser-Plasma X-Ray and Ion sources from solid and low density foam targets" and recommend that it may be accepted as fulfilling the thesis requirement for the award of Degree of Doctor of Philosophy.

Chairman: Dr. B. K. Nayak	BKNayak	Date: 08/04/2019
Guide/Convenor: Dr. M. N. Deo		Date: 08/04/2019
External Examiner: Prof. V. K. Tripathi	V.K. Tripathi	Date: 08/04/2019
Member: Prof. M. Krishnamurthy		Date: 08/04/2019
Member: Dr. Vas dev		Date: 08/04/2019
Member: Dr. A. Arya		Date: 08/04/2019
Technology Advisor : Dr. S. Chaurasia	SChaurasia	Date: 08/04/2019

Final approval and acceptance of this thesis is contingent upon the candidate's submission of the final copies of the thesis to HBNI.

I/We hereby certify that I/we have read this thesis prepared under my/our direction and recommend that it may be accepted as fulfilling the thesis requirement.

Date: 08/04/2019

Dr. M. N. Deo

Place: Mumbai

Guide/Convener

STATEMENT BY AUTHOR

This dissertation has been submitted in partial fulfilment of requirements for an advanced degree at Homi Bhabha National Institute (HBNI) and is deposited in the Library to be made available to borrowers under rules of the HBNI.

Brief quotations from this dissertation are allowable without special permission, provided that accurate acknowledgement of source is made. Requests for permission for extended quotation from or reproduction of this manuscript in whole or in part may be granted by the Competent Authority of HBNI when in his or her judgment the proposed use of the material is in the interests of scholarship. In all other instances, however, permission must be obtained from the author.

Channprit Kaur

DECLARATION

I, hereby declare that the investigation presented in the thesis has been carried out by me. The work is original and has not been submitted earlier as a whole or in part for a degree / diploma at this or any other Institution/University.

Channprit Kaur

List of Publications

In Refereed Journal:

Related to Thesis

1. In situ measurement of ions parameters of laser produced ion source using high resolution Thomson Parabola Spectrometer.

   S. Chaurasia, **Channprit Kaur**, V. Rastogi, A.K. Poswal, D.S. Munda, R.K. Bhatia and V. Nataraju

   Journal of Instrumentation **11,** 1 (2016).

2. K-shell X-ray Spectroscopy of Laser produced Aluminum Plasma.

   Channprit Kaur, S. Chaurasia, A.K. Poswal, D.S. Munda, A. Rossall, M.N. Deo, S. M. Sharma.

   J. Quant. Spectro. and Radiative Transfer **187**, 20 (2017).

3. *Enhancement of keV X-rays from low-density cellulose triacetate (TAC) foam targets*.

   S. Chaurasia, **Channprit Kaur**, N. G. Borisenko, J. Pasley, A. Orekhov, M. N. Deo

   Physics of Plasma **24 (7)**, 073110 (2017).

4. *Interaction of high power laser with polymeric low-density foam targets.*

   Channprit Kaur, S. Chaurasia, N. G. Borisenko, A. Orekhov, P. Leshma, A. A. Gromove, A. Akunets, M. N. Deo

   Quantum Electronics **47 (6)**, 495-502 (2017).

5. *X-ray and ion emission studies from sub-nanosecond laser irradiated SiO_2 foam targets.*

   Channprit Kaur, S. Chaurasia, A. A. Pisal, A. K. Rossal, D. S. Munda, A. V. Rao, M. N. Deo, S. M. Sharma.

   ***Laser Part. Beams*,** **35 (3)**, 505-512 (2017).

6. L-shell spectroscopy of Neon and fluorine like copper ions of laser produced plasma.

   Channprit Kaur, S. Chaurasia, Narendra Singh, Sunny Aggrawal, ArunGoyal, Man Mohan, M.N. Deo.

   Physics of Plasma 26, 023301 (2019).

7. Ions dynamics of plasma produced by sub-nanosecond laser irradiated on low density $(CD_2)_n$ foam.

   Channprit Kaur, S. Chaurasia, A. I. Gromov, Nataliya G Borisenko, A. A. Akunet.

   Manuscript Submitted.

8. Demonstration of Gold foam plasma as a bright X-ray source and slow ion emitters

   Channprit Kaur, S. Chaurasia, N. G. Borisenko, A. Rossall, A. Orekhov, P. Leshma, A. A. Gromove, A. Akunets.

   Manuscript submitted.

9. Interaction of low density foam targets with ultra-short laser pulse.

   Channprit Kaur *et al.*

   Manuscript under preparation

Other than Thesis

10. Comparative studies of Laser induced plasma in TEOS and MTMS based aerogels and solid quartz.

    A. Venkateswara Rao, **Channprit Kaur**, A. A. Pisal, S. Chaurasia, M. N. Deo, and S. M. Sharma.

    MRS Advances 2, no.**57,** 3531-3536(2017).

11. Metal nano-particles modernized layers and those with polymers for laser thermonuclear targets.

    Akimova, I. V., A. A. Akunets, N. G. Borisenko, S. Chaurasia, A. I. Gromov, **Channprit Kaur**, D. S. Munda et al.

    Conference Series, IOP Publishing, **vol. 907**, no. 1, p. 012018 (2017).

Conference/ Symposium Attended:

- Attended BRNS School – ‘Computational methodologies across length scales’ from 28 August to 9 September, 2017 at BARC, Mumbai.
- Attended ICTS workshop - ‘Laser Plasma Accelerator’ from 06 March 2017 to 17 March 2017 at International Centre for Theoretical Sciences (ICTS-TIFR), Bangalore.
- Attended JOINT ICTP-IAEA school 2017- ‘Atomic Processes in plasma’ from 27 February to 3 March 2017 at Miramare, Trieste, Italy.
- Attended SERB school 2014- ‘High Intensity Laser Plasma Interaction’ from May 5-23 at IIT Delhi, Delhi.
- **Oral Presentation:** “L-shell spectroscopy of Neon and fluorine like copper ions from laser produced plasma” at ECLIM-2018 held in Crete, Greece during October 22-26, 2018.
- **Oral talk** in Science Academies Lecture Workshop On “Lasers and their Applications”, January 20-21, 2018, Indian Women Scientists’ Association (IWSA), Navi Mumbai, India
- **Poster Presentation:** “X-ray and ion emission studies from low density gold targets” at EPS-2018 held in Prague, Czech Republic, during July 2-6, 2018.

- **Poster Presentation:** "Ions dynamics of plasma produced by sub-nanosecond laser irradiated on low density $(CD_2)_n$ foam" at 26th DAE-BRNS National Laser Symposium held at BARC, Mumbai, India during December 20-23, 2017.
- **Poster Presentation:** "X-ray and ion emission studies from subnanosecond laser irradiated SiO_2 foam targets" at 34th European Conference on Laser Interaction with Matter (ECLIM) held at Moscow, Russia during September 18-23, 2016.
- **Poster Presentation:** "X-ray and ion emission studies of SiO_2 foam imposed to intense laser system" at COMPEC- 2016 held in BARC, Mumbai, India during April 13-16, 2016.
- **Poster Presentation: "**K-shell X-ray spectroscopy of laser produced Aluminum plasma" at International conference NLS-2015 held in RRCAT, Indore, India during December 2-5, 2015.
- **Poster Presentation:** "X-ray emission studies of laser produced SiO_2 foams plasma" at ICPMCSC-2015 conference in Ratnam college, Mumbai, India.
- **Poster Presentation:** "Optimization of X-ray and ion emission from laser produced Aluminum plasma" at International conference CDAMOP-2015 held in Delhi University, Delhi, India during March 11-14, 2015.

Channprit Kaur

Dedicated

To

My Loving Parents…

ACKNOWLEDGEMENTS

First, I would like to pay my sincerest gratitude to my supervisor, Dr. M. N. Deo for his continuous support during the tenure of my PhD. I am highly grateful to Dr. S. Chaurasia for his guidance, cooperation, encouragement and constant support during my whole Ph.D. His enthusiasm for science, hard work and mission for providing high-quality work, has made a deep impression on me. I would also like to thank my doctoral committee members Dr. S. M. Sharma, Dr. N. K.Sahoo, Dr. Krishnamurthy, Dr. Vas Dev and Dr. B. K. Nayak for their valuable suggestions. My special thanks to Dr. Ashok Arya for his motivation and discussions. I am grateful to Mr. Ashwini Poswal for helping me in Python and useful discussions. Thanks to my group members who are always ready to help; Sh. C. G. Murali, Leshma, Vinay Rastogi and Usha Rao, D. S. Munda and Ritesh Sable. Special thanks to D. S. Munda and Ritesh Sable for the strong support during the experiments. I must thank the administrative staff for the support during tenure of my PhD. I sincerely thank Dr. John Pasley for simulations, corrections and valuable suggestions. I am grateful to Dr. Nataliya and her research group for providing various foam targets which are the center of this thesis. Many thanks to Dr. Andrew Rossall for performing hydrodynamic simulations. Thanks to Prof A. V Rao and Dr. Abhijit Pisal for providing silica aerogel targets. Many thanks to G. Ravinder Kumar and all TIFR team members for their valuable support for successful running of experiments performed in TIFR. I thank Krishna Bhangre and all the workshop members whom I could disturb anytime for help during my research.

I consider life outside PhD equally important. Thanks to IWSA for providing home away from my home. I really enjoyed my stay there. I am lucky to have special friends Nidhi, Anil, Usha, Ashok and Abhishek for making life easier during hard times. Thanks to Sarita, Sukhdeep and Raman for creating the cheerful environment. Many thanks to Madhu, Swati, Meera, Indresh, Dipayan, Purushottam, Pulkit, Dyaneshwar, Harish, Priyanka, Naini, Saheli, Swapan and Swayam….the list is never ending.

I am very grateful to my loving parents and my elder brother, Gagandeep Singh who always believe in me and support my decisions. Their unconditional love and blessings are the keys to make me move forward. Special thanks to my nephews Arshveer and Eknoor for making my life beautiful. Finally, my dearest friend, Baltej Singh, deserve a major share for his constant support and encouragement. The planning of the work, broad discussions and quality time spend together means a lot to me.

Channprit Kaur

CONTENTS

	Page No.
Synopsis	xvii
List of Figures	xxix
List of Tables	xxxiv
Aberrations	xxxv

Chapter 1- Introduction

1.1 Introduction 1
1.2 Plasma: fourth state of matter 1
1.3 Physical properties of plasma 3
1.3.1 Quasi-neutrality 3
1.3.2 Plasma frequency 4
1.3.3 Ionization in plasma 5
1.3.4 Conditions for existence of plasma 5
1.4 Atoms in strong fields 5
1.5 Electrons in electromagnetic fields 7
1.6 Laser plasma interaction (LPI) 8
1.6.1 Inverse Bremsstrahlung (IB) absorption 12
1.6.2 Resonance Absorption 14
1.6.3 Parametric decay instabilities 15
1.7 Laser plasma as an X-ray source 17
1.7.1 Mechanism of X-ray production 18
1.7.2 Characteristics of LPP X-ray source 20
1.7.3 Spectroscopy of LPP X-rays 22
1.8 Equilibrium models in plasma 27
1.8.1 Complete thermal equilibrium (CTE) 27
1.8.2 Local thermal equilibrium (LTE) 28
1.8.3 Corona equilibrium (CE) 28
1.8.4 Collisional radiative equilibrium (CRE) 29
1.9 Laser produced plasma as an ion source 30
1.10 Foams 31
1.10.1 Types of foams 32
1.10.2 Laser interaction with foam targets 33
1.10.3 Applications of foam targets 35
1.11 Summary 36
1.12 Motivation and objective of present thesis 36

Chapter 2- Experimental Tools and Techniques

2.1 Introduction ... 39
2.2 Laser systems ... 40
2.2.1 Nd: Glass 500 ps/30 J laser system ... 40
2.2.2 100 TW Ti: Sapphire Laser system ... 42
2.3 Vacuum chamber ... 42
2.4 X-ray diagnostics ... 43
2.4.1 Inversion layer Si photodiodes (XUV-100) ... 44
2.4.2 X-ray crystal spectrometer and alignment ... 45
2.4.3 X-ray streak camera ... 48
2.4.4 NaI detector ... 51
2.5 Ion diagnostics ... 52
2.5.1 Faraday Cup (Ion collector) ... 52
2.5.2 Thomson Parabola Spectrometer (TPS) ... 54
2.6 Shadowgraphy set up ... 68
2.7 Summary ... 69

Chapter 3- K- and L-shell Spectroscopic Studies of Laser-Plasma X-rays

3.1 Introduction ... 71
3.2 K-shell spectroscopy of Al and Si plasma ... 72
3.2.1 Description of the experiment ... 73
3.2.2 Calibration of the crystal spectrometer ... 74
3.2.3 Code for image processing ... 76
3.2.4 Scaling of resonance lines intensity with respect to laser intensity ... 77
3.2.5 Measurement of plasma parameters ... 79
3.2.5.1 Temperature estimation ... 79
3.2.5.2 Density estimation ... 83
3.2.5.3 Determination of temperature and density using FLYCHK ... 86
3.2.6 Conversion efficiency of laser to X-ray ... 88
3.2.7 Angular distribution of resonance lines ... 88
3.3 K-shell spectra of Si plasma ... 90
3.4 L-shell spectroscopy of Cu plasma ... 92
3.4.1 Determination of plasma parameters ... 98
3.4.2 Effect of laser intensity on the abundance of charge states in the plasma ... 104
3.5 Summary ... 109

Chapter 4 -X-ray and Ion Emission Studies from Plastic Foams

4.1 Introduction 111
4.2 Experiments Techniques and Targets 113
4.3 Laser Transmission through TAC Foams 115
4.4 Study of keV X-ray emission from TAC foams 116
4.5 Ion spectroscopy of TAC foam 117
4.5.1 Effect of density on convoluted charge states of ion in TAC 120
4.5.2 Effect of density on different charge states of ions in TAC 121
4.6 Studies on TAC with Constant Areal Density 121
4.6.1 X-ray Conversion Efficiency 122
4.7 Studies on TAC irradiated with ultrashort laser pulse 128
4.8 Summary 130

Chapter 5- X-ray and Ion Emission Studies from Silica Aerogel and Deuterated Foams

5.1 Introduction 133
5.2 Studies from silica aerogel 134
5.2.1 Description of the experiment 134
5.2.2 Method of Preparation of SiO_2 Foam Targets 135
5.2.3 Effect of target densities on soft and hard X-ray yields 136
5.2.4 Effect of target densities on distribution of ions 138
5.2.5 Simulation results to verify the volume effect 139
5.2.6 Comparison of the K-shell spectra 141
5.3 Studies from Deuterated $(CD_2)_n$ Foams 142
5.3.1 Distribution of flux deuterium ions 143
5.3.2 Distribution of peak velocity of deuterium ions 145
5.3.3 Velocity mapping 147
5.3.4 Thomson Parabola data analysis 149
5.3.5 Comparison of X-ray flux 151
5.4 Summary 152

Chapter 6-Studies from Gold Foams

6.1 Introduction 155
6.2 Experimental procedure 157
6.3 Target Preparation 158
6.4 X-rays emission studies from gold foam.. 159
6.5 Comparison of photo peak 171
6.6 Comparison of radiation from pinhole camera used in TPS 172
6.7 Optical shadowgraphy of solid gold and 0.1 g/cc gold foam targets 172
6.8 Comparison of ions signal of gold foam with solid one 173
6.9 Summary 180

Chapter 7-Summary and Future Research Plans

7.1 Summary 181
7.2 Future Research Plans 186
References

SYNOPSIS

Soon after the discovery of laser in 1960 [1], the field of laser matter interaction gain popularity. With passage of time, a gain in the intensity of laser is obtained via chirped pulse amplification, which was introduced by recent Nobel prize 2018 winner Strickland & Mourou [2] in 1985, and other compression technologies. The maximum laser intensity reached to ultra-relativistic regime ($\approx 10^{23}$ W/cm^2) in today's world [3]. The interaction of the intense laser with the surface of target results into the formation of plasma with a very high density ($10^{19} - 10^{23}$/cm^3) and temperature (10 eV- 10 keV). This enables us to virtually reach the temperature of about the sun core (10 million Kelvin) by rapidly heating the material with the intense lasers ($\geq 10^{12}$ W/cm^2). The interaction of laser with plasma extends the field of light matter interaction by introducing several non-linear phenomena which are beyond the Einstein's photo electric effect. The study of the properties of matter under high temperature and high-density conditions is important in basic sciences as well as in advanced scientific technologies. The laser produced plasma (LPP) is demonstrated as a bright source of X-rays and ions. The LPP X-ray source has been proven to be a most promising alternative to conventional (X-ray tubes) as well as synchrotron X-ray sources. The compactness, easily accessibility and short pulse length of these X-ray sources has significantly facilitated the scientific research fields such as radiobiology, X-ray microscopy, astrophysical and fusion applications, measurement of opacity of materials, X-ray driven shock studies for Equation-of-State (EOS) of materials at extreme conditions and so on [4-7]. In the same way, laser ion sources (LIS) offer an essential impact on various technological areas like cancer therapy, proton radiography, ion-driven fast ignition, very large scale integrated circuit fabrication, laser mass spectroscopy, material modification, ion implantation and others [8-10]. The detailed characteristics of these X-ray and ion sources are needed in order to use them in various applications. Furthermore, the laser-plasma interaction is responsible for the concept of inertial confinement fusion (ICF) in early 1970 [4].The stars, as a huge source of energy, have inspired the scientists to generate energy from controlled nuclear fusion. The ICF scheme involves irradiating hydrogen isotopes with powerful laser beam to compress and heat them to the point of fusion. However, the irradiation of the fuel target has limitations, arising from the inhomogeneities present in laser-matter interaction, which leads to both parametric and hydrodynamic instabilities resulting in target pre-heating and inefficient compression. This problem should be removed in order the access a new source of energy. Among other, most prominent solution of the problem lies in smart target design. In order to reduce instabilities, the idea of coating the pellets with low density foams came into picture. This is because the absorption of laser light in the low-density foam targets is different than in solids. The smoothening of laser pulse and shock amplification is observed from foam targets. Moreover, the demand for high flux X-rays in practical applications and in indirect drive ICF has triggered extensive research for the enhancement of the X-ray yield of laser-produced plasmas (LPP). For a large X-ray yield, absorption of the laser energy inside the target should be high. However, the conversion efficiency of laser energy to X-ray from the solid targets is low due to the large reflection of the laser light near the critical density surface of solid targets. For the enhancement of X-ray yield, various factors like laser characteristics (power density, pulse duration, and wavelength) and target properties have been optimized. For example, to enhance the X-ray yield, the use of a pre-pulse, defocusing the laser to increase the plasma volume, structured targets, gas targets, and low-density targets have been made [12-14]. The use of low-density targets has been proven as a prominent candidate for the enhancement of X-ray emission. The studies of X-ray and ions from foam targets become essential for understanding of peculiar nature of the laser interaction with foam targets as well as from the ICF point of view. The burning core of ICF plasma produces bright X-ray source which is useful in the diagnosis of core conditions essential for comparison with simulations and understanding fusion yields. These X-rays are used as backlighter for the surrounding shell of hot dense matter whose properties are important in understanding of the efficacy of the ICF and global morphology [5]. The absorption and fluorescence spectra of mid-Z impurities or dopants in the warm dense shell facilitates to reveal the optical depth, temperature, and density of the shell. The studies of X-ray and ions should be carried out simultaneously for better understanding of the laser plasma interaction processes.

Considering the above facts, the main focus of the present thesis is the characterization of X-ray and ion emission studies using various types of targets irradiated with nano, pico and femto second laser pulses. These studies cover various aspects of laser plasma interaction. All the experimental studies are performed using 30J /500 ps Nd: Glass laser, 2 J/8 ns Nd: Glass laser available at Laser Shock Laboratory, BARC and 1 J/25fs Ti: Sapphire laser, TIFR, Mumbai. The simulations using atomic and hydrodynamic codes are also carried out. The research work primarily focuses on to study the conversion efficiency of laser to X-rays as a function of target density, spectroscopic studies for determination of plasma parameters, evolution of ions and the energy distribution of ions for metallic solids and foam targets (low to high Z). The laser pulse is long resulting in a long length scale of the plasma. The advantage of using long scale length plasma lies in availability of sufficient space and time for the laser to interact with the plasma. In the long pulse laser case, plasma is produced by leading part of pulse and most of the absorption of remaining laser pulse in plasma occur via inverse Bremsstrahlung process in which the electrons generated in initial ionization mechanisms (by multiphoton ionization and cascade ionization process) oscillate in laser electric field in the presence of ions and transfer their energies to ions through collision. Most of the experiments in the thesis are performed at laser intensity up to $5x10^{14}$ W/cm^2; collisional absorption is the dominant absorption mechanism. To collect data with wide range of various aspects in a single shot, various plasma diagnostics have been developed in our lab. The soft as well as hard X-ray emission is monitored with system of Si photodiodes with adequate filtering in order to choose different spectral ranges. X-ray streak camera provides the temporal evolution of X-rays and spectral analysis is done using crystal spectrometer and grating spectrometer. Measurement of temporal evolution of plasma inside the target and in the vacuum at different delays with respect to incident laser is possible with shadowgraphy set up. Emission of integrated ions along various angles from the target normal is investigated using Faradays ions collector employing Time-of-Flight (TOF) technique. The evolution of different charge states of ions is recorded with Thomson parabola Ion Spectrometer (TPS).

The thesis consists of seven chapters. The **chapter 1** is intended to provide concise overview of plasma with its properties and the interaction of long and ultrashort pulses with matter through various absorption processes. The mechanism of production of LPP X-ray sources, its characteristics and applications are discussed. As the thesis involves spectroscopic studies; an introduction to equilibrium models and atomic processes in plasma is given. Laser plasma as an ion source and mechanism of ion acceleration is also described. A brief introduction of inertial confinement fusion scheme is provided. Lastly, the foams, their type and interaction with laser are discussed. In the end of the chapter, the motivation and objective of the present research work is described.

Chapter 2 offers a brief overview of the experimental facility such as Nd: Glass laser system, Ti: Sapphire laser system. The in-house developed X-ray and ion diagnostics such as X-ray photodiodes, crystal spectrometer and ion collectors are discussed. The detail of X-ray streak camera including its installation and alignment is also provided. The high resolution and high dispersion Thomson parabola spectrometer (TPS) comprising of Time-of-Flight diagnostics has been developed for the characterization of ions with energy in the range from 1 keV to 1MeV/nucleon and incorporated in the Laser plasma experimental chamber [6]. The development of Thomson parabola ion spectrometer, its data analysis software is discussed in detail. The simulations performed by SIMION 7.0 software before developing TPS for determination of electric and magnetic field values and ion trajectories is discussed. The ion spectrometer is optimized with graphite target. The analysis of carbon ions of charge states C^{1+} to C^{6+} in the energy range from 3 keV to 300 keV is discussed which involves the verification by Time-of-Flight measurement and SIMION software. The analysis of the experimental recorded images is performed in Python software. The details of data analysis software using Python to measure *in situ* ion's parameters is provided. The angular distribution of convoluted and individual charge states of carbon ions is discussed.

In **chapter 3**, the determination of properties of plasma using spectroscopy techniques are discussed. A detail characterization of plasma temperature and density is performed using analytic models and atomic codes. The properties of plasma are strongly dependent on the bulk (or average) parameters. The main plasma parameters are the degree of ionization, the plasma temperature, the density. The emission spectroscopy of plasma is an efficient tool and well-established field to diagnose temperature and density of plasma. The excited states in which X-ray transitions take place can belong to K-, L- or M- shell. The experiments are performed on 10 mm thick Al slab, quartz glass and SiO_2 foam. The experimental detail is provided including laser parameter, X-ray crystal spectrometer (resolution 25 mÅ) consisting of Thallium Acid Phthalate (TAP) crystal and X-ray CCD camera. The K-shell spectrum of Al and Si plasma originated from highly charged He- and H-like ions. The variation of intensity of resonance lines is calculated as a function of laser intensity and found to follow a power law $I_x = (I_L)^\alpha$, where, I_x is the X-ray flux of different K-shell resonance lines of He-like Al, I_L is intensity of laser and αis a scaling exponent. The scaling component α has been calculated for all resonance lines and found to be 2.2, 2.2, 2.3 for He_β, He_γ and He_δ respectively. The plasma temperature is estimated by line ratio method. For this, pair of the Ly_α (*1s-np*) with He-like satellite (*nln'l'-1sn'l'*) lines and He_β resonance line with Li-like (*$1s2l3l'$-$1s^2 2l$*) are used. For density estimation, stark broadening of Ly_β is chosen. The contribution of Doppler and instrumental broadening is subtracted. The temperature and densities calculated by analytical models are 260 eV-420 eV and 1.6-2.8×10^{20} cm^{-3} respectively which is in good agreement with the results obtained by FLYCHK (T_e=160 eV, T_h=1 keV, f=0.008 and $n_e=5\times10^{20}$ cm^{-3}) in which two temperature model (thermal and supra thermal electrons) is used for temperature and density estimation. The angular distribution of X-ray intensities has been found to be anisotropic varying according to power law $\cos(\theta)^n$, θ is the angle from the target normal (laser direction). The effect of opacity is observed on He-like resonance lines (*$1s^2$-1snp*) and found to more pronounced lines with low n i.e. He_β (*$1s^2$-1s3p*) in comparison to higher n. The angular distribution of different charge states of Al ions has observed using Thomson Parabola Spectrometer. The higher charged ions Al XI, Al XII and Al XIII are more directional towards target normal. With increasing angle from target normal, the flux of lower charge states of Al will increase [7]. The quantitative measurement of laser to X-ray energy conversion efficiency is also performed. The estimation of temperature using line ratio method for Al and Si plasma shows higher temperature value for H-like line in comparison to He-like lines. This is signature of emission of lines from different regions of plasma since the observed spectrum is integrated along the line of sight as well as in time.

In other type of experiment, for confirming plasma temperature, L-shell X-ray spectroscopy of Copper plasma is performed. Although the L-shell ionization of high Z atoms can be achieved easily yet complex structured spectroscopic models are required to solve these spectra. The L-shell ions are observed in many astrophysical phenomenons and also in laboratory. The spectrum involves the Ne-, F- and O- like Rydberg resonance lines along with some of the inner shell satellite lines of Copper plasma, in the wavelength range of 7.9-9.5Å. The spectrum is obtained experimentally using a TAP crystal spectrometer. The observed lines result from the transitions among 2p-nd, 2p-ns and 2s-nd (n= 4 to 6) levels. Transition wavelengths, transition probabilities and oscillator strengths of these lines are calculated using the Multi-Configuration Dirac-Fock (MCDF) method. In this computation, the contribution of relativistic corrections such as two-body Breit corrections and QED corrections due to vacuum polarization and self-energy has also been considered. FLYCHK simulations are used to analyze the distribution of the various charge states of the Copper ions and to find the temperature and density of plasma. Moreover, the effect of self-absorption of the plasma (opacity), as well as of supra thermal electrons on charge state distribution of ions, are also studied. The synthetic spectrum provides a best-match with the experimental spectrum at a laser intensity of 1.3×10^{14} W/cm^2 for T_c=150eV, T_h=1000 eV, f=0.008 and density 4.5×10^{20} cm^{-3}. The temperature and density ranges calculated using a radiative hydrodynamic code is in agreement with the experimentally determined values. The effect of change in laser intensity on the L-shell spectrum of Cu is studied which indicates the switching between lower (Cu XX) and higher charge states (Cu XXI, Cu XXII) at higher laser intensities.

In **Chapter 4,** X-ray and ion emission studies from low-density cellulose triacetate polymer is discussed. The laser to X-ray conversion efficiency (few keVs) is found to decrease with increasing target material density. The efficiency is reduced by two times for

TAC with density 10 mg cm^{-3} in comparison to 2 mg cm^{-3} TAC. The duration and amplitude of laser pulses transmitted through the target decreases with increasing column target density (the product of target material density and its thickness). On the other hand, the flux of ions as well as their energies is found to increase with increasing target material density. The peak of the ion energy spectrum is shifted towards higher energies with increasing laser radiation intensity. The effect of TAC density on individual charge states of Carbon and Oxygen is observed using TPS signal. The energy and flux of individual charge states is high for higher density TAC (10 mg cm^{-3}) [8]. Further verification is done by keeping the areal density constant at 0.2 mg/cm^2 by varying the target thickness in inverse proportion to the density. Mass-matched cellulose triacetate foam targets with densities of 2 mg/cc, 4 mg/cc, 7 mg/cc, and 20 mg/cc were used. The X-ray yield in the spectral range (5–8 keV) and (4.5–16 keV) was found to be enhanced by approximately 2.3 times in foam targets with the density of 2 mg/cc (under-dense) compared with foam targets with the density of 20 mg/cc (over-dense) [9].

The ultrashort X-rays are a great choice for time resolved applications. The physics of laser matter interaction changes by reducing the pulse of laser. Keeping this in view, the TAC foam targets are irradiated by 30 fs/ 1J Ti: Sapphire laser system. Different ranges of X-rays are observed by silicon photodiodes and hard X-rays are observed by NaI detector. The TAC foam with densities 2, 4, 5, 7, 10 and 15 mg/cc are used for this purpose. The hard X-rays are observed by NaI detector. The both soft and hard X-ray flux is found to increase by many folds with decreasing the density of the TAC foam.

Chapter 5, provides the detailed study of X-ray and ion emission from silica aerogel and deuterated foam targets. The objective of the conducted experiments is to investigate the scenario of laser absorption in foam targets, laser-to-X-ray energy conversion, spectra of ions emitted from the plasma, as well as volume heating of the target material. Different low-density targets such as silica aerogel (SiO_2) and deuterated foam (CD_2) are used for this purpose. The soft X-ray (0.9–1.56 keV) and hard X-ray (3.4–16 keV) emission from low-density SiO_2 aerogel foam targets (pure silica aerogel with density 50 and 70 mg/cc, (25% CH_3 + 75% SiO_2) with densities 60 and 40 mg/cc) is compared with solid quartz. An enhancement of 2.5 times in soft X-ray emission and a decrease of 1.8 times in hard X-ray emission for 50 mg/cc SiO_2 aerogel foam is observed compared with the solid quartz. From the ion collector's data, the ion flux from the solid quartz is found to be more directional in comparison to SiO_2 aerogel foam. This behavior was attributed to the volume effect, which has been further verified by shadowgraph profiles of the plasma plume at two different time scales (2 and 8 ns after laser irradiation) during the plasma evolution and 2D hydrodynamic simulations [10].

Experimental investigation of ion dynamics from deuterated foam plasma (CD_2 foam) is performed by comparing the effect of target density on the evaluation of ions. The $(CD_2)_n$ foam with densities 275 and 440mg/cc have been used. The peak ion velocity and ion flux are presented as a function of the laser intensity and target densities. Both the parameters are found to be maximum in the direction of target normal for both densities and are related by power law (I_L), with laser intensity (I_L). However, the scaling factor is more in case of 440 mg/cc in comparison to 275 mg/cc indicating a high velocity and more flux of ions in high dense CD_2. For the detailed studies of ions dynamics, a velocity mapping of ion collector's signal is done in Python which indicate the presence of more energetic ions in case of 440 mg/cc in comparison to 275 mg/cc CD_2 at the same laser energy. The ion spectrometry of $(CD_2)_n$ foam plasma was also done using high resolution Thomson parabola spectrometer aligned at 45° from target normal. It reveals that the effect of density of target on ion energy is more pronounced towards target normal instead of 45°. The deuterated foams are also radiated by ultrashort pulses

In **Chapter 6,** laser interaction with gold foam targets are studied. The laser to X-ray conversion efficiency (CE) can be increased by many folds by using high Z (Z>20) targets. This happens because ions with several bound electrons dominate in the resulting plasma which gives rise to complex (many electrons) line emission processes. Due to these characteristics, L- and M-band of high Z materials are used for X-ray back-lighter in absorption spectroscopy experiments. Further, the use of foam targets for increasing X-ray flux is attracting great attentions in fusion research. In this chapter, enhancement in X-ray emission and reduction of kinetic energy of ions from low density foam plasma is demonstrated by performing experiment and its validation with hydrodynamic simulation. The plasma is produced by irradiation of solid gold and gold foam targets (densities 0.2 g/cc, 0.13 g/cc and 0.1 g/cc) at intensities in the range of 4×10^{13}-1×10^{14} W/cm^2. Time resolved X-ray emission is measured by X-ray streak camera with 10 ps resolution. The X-ray flux measured by streak camera from low density gold foam shows a 13% enhancement in comparison to solid gold in the spectral range > 0.8 keV and above. Decrease in velocity of ions is observed in low density gold foam. In solid gold, thermal ions peak velocity is 31×10^4 m/s and spread in narrow energy width, however, in case of 0.1 g/cc, peak velocity reduces to 6×10^4 m/s towards target normal and emitted in broad energy range. Shadowgraph results also provide evidence of narrower expansion of plasma from solid gold. However, total ion flux from low density gold foam is comparable to ion flux of solid gold indicating the process of volumetric absorption.

Chapter 7 summarizes the outcomes of the work done, its usefulness and contribution to the current field of laser plasma research along with possible future directions. The interest of the present thesis work mainly lies in X-ray and ion emission studies from laser generated plasma. The work performed in this thesis helps to develop basic understanding of laser interaction with low density foams. The Laser produced X-ray as well as ion sources are optimized to be used in various applications. The detail study of LPP X-ray emission is performed which involves the free-free, free-bound and bound-bound emission. The bound-bound transitions are utilized to diagnose the laser produced plasma which is important in Inertial Confinement Fusion and astrophysical phenomenon. The plasma temperature and density are investigated by utilizing line spectrum from highly charged ions (H-like, He-like and Li-like) of low-Z elements. Further investigation of plasma parameters is performed using L-shell emission spectrum from mid-Z elements. The angular distribution of X-ray emission, ion flux of integrated charge states, ion velocities as well as individual charge states of ions are calculated. Furthermore, the experiments performed on low density foam targets proved them to be a higher yield X-ray source. All the low Z foam as well as high Z foams including polymeric foams, silica aerogel, deuterated and gold foams are irradiated with subnanonescond and ultrashort laser pulses. Higher flux of soft X-rays is observed in case of low density foams in comparison to their corresponding solids or high-density targets. In case of ultrashort laser pulse, large increment in hard X-rays as well as soft X-rays in case of low density TAC foams is observed in comparison to higher density TAC. In all the studies, the more isotropic nature of ions from the low-density targets is sign of volumetric absorption of laser light and less density gradients towards target normal. The presence of lower energy ions in low-density foam targets shows the less energy loss in hydrodynamic motion. The presence of less energetic ions in case of low density foams are also verified by results of Thomson Parabola Spectrometer. The shadows of the produced plasma clearly show the large volume of plasma inside the foam target and large size of expanding plasma plume. The calculations performed by hydrodynamic simulations indicate the effect of target density on temperature and density profile of plasma. This demonstration of low density foam targets as bright X-ray sources is important for using these targets in applications such as indirect drive ICF, X-ray backlighters and radiography experiments.

References

[1] T. H. Maiman, "Stimulated optical radiation in Ruby," *Nature*, vol. 187, no. 4736, pp. 493–494, 1960.

[2] D. Strickland and G. Mourou, "Compression of amplified chirped optical pulses," *Opt. Commun.*, vol. 56, no. 3, pp. 219–221, 1985.

[3] C. Danson, D. Hillier, N. Hopps, and D. Neely, "Petawatt class lasers worldwide," *High Power Laser Sci. Eng.*, vol. 3, 2015.

[4] R. S. Craxton *et al.*, "Direct-drive inertial confinement fusion: A review," *Phys. Plasmas*, vol. 22, no. 11, 2015.

[5] S. B. Hansen, E. C. Harding, P. F. Knapp, M. R. Gomez, T. Nagayama, and J. E. Bailey, "Fluorescence and absorption spectroscopy for warm dense matter studies and ICF plasma diagnostics," *Phys. Plasmas*, vol. 25, no. 5, p. 56301, 2018.

[6] S. Chaurasia *et al.*, "In situ measurement of ions parameters of laser produced ion source using high resolution Thomson Parabola Spectrometer," *J. Instrum.*, vol. 11, no. 8, 2016.

[7] C. Kaur *et al.*, "K-shell X-ray spectroscopy of laser produced aluminum plasma," *J. Quant. Spectrosc. Radiat. Transf.*, vol. 187, pp. 20–29, 2017.

[8] C. Kaur *et al.*, "Interaction of high-power laser radiation with low-density polymer aerogels," *Quantum Electron.*, vol. 47, no. 6, pp. 495–502, 2017.

[9] S. Chaurasia, C. Kaur, N. G. Borisenko, J. Pasley, A. Orekhov, and M. N. Deo, "Enhancement of keV X-rays from low-density cellulose triacetate (TAC) foam targets," *Phys. Plasmas*, vol. 24, no. 7, 2017.

[10] C. Kaur *et al.*, "X-ray and ion emission studies from subnanosecond laser-irradiated SiO2aerogel foam targets," *Laser Part. Beams*, vol. 35, no. 3, pp. 505–512, 2017.

LIST OF FIGURES

Figure 1.1 *Solid to plasma phase transition with increasing temperature.*

Figure 1.2 *Multi photon ionization and tunneling ionization*

Figure 1.3 *Difference in density scale length for long and ultrashort pulse.*

Figure 1.4 *(a) Schematic of laser matter interaction (b) temperature and density profile with different regions.*

Figure 2.1 *Schematic of laser chain with experimental chamber.*

Figure 2.2 *Picture of Laser chain and vacuum chamber with diagnostics*.

Figure 2.3 *(a) Photo of Silicon photodiodes covered with different filters (b) schematic of photodiode.*

Figure 2.4: *Schematic of the crystal spectrometer. The crystal is at 45° with respect to the target normal. The laser axis coincides with the target normal.*

Figure 2.5 *(a) Photograph of X-ray streak camera (b) schematic of streak camera.*

Figure 2.6 *Radiograph of the (c) the SS mesh and fruit fly with magnification (a) ×0.3 (b) ×1.5.*

Figure 2.7 *Schematic of NaI detector*

Figure 2.8 *Schematic of Ion collector*

Figure 2.9 *(a) Screen shot of the simulation in SIMION showing the flight paths of ions through magnet and ESA (b) cross section of a plane perpendicular to the ion accelerator direction along xx' showing the profiles of carbon ions.*

Figure 2.11 *(a) Schematic of TPS (b) Design of TPS (c) Ion collector signal and (d) Image of carbon plasma obtained by experiment and overlapped parabolas of Carbon (dotted) provided by SIMION software.*

Figure 2.12 *(a)Variation of magnetic field at the center of axis i.e. in the path of ion beam with changing the distance between two magnets. (b) Three-dimensional magnetic field mapping in the plane of the pin-hole and axis of ion source.*

Figure 2.13 *3D view of ion spectrum enable to measure the qualitatively the flux of ion of particular energy.*

Figure 2.14 *(a) Image showing matched parabolas generated by python (red ones) with experimental data and online calculation of different parameters of carbon plasma (b) Graph showing energy verses flux for all charge states of Carbon.*

Figure 3.1 *(a-d) K-shell X-ray line emission spectrum form Al plasma showing the different wavelength windows available by changing the distance between the plasma and the TAP crystal.*

Figure 3.2 *Processed intensity plot of the $He_β$ line from Al plasma with 8 bit BMP(—), Promise (-----), and the Python (…) software developed by our group.*

Figure 3.3 *Figure showing variation of intensity of $He_β$, $He_γ$, and $He_δ$ spectral lines as a function of laser intensity.*

Figure 3.4 (a) *Plot of difference between ratio of resonance lines obtained experimentally and lines generated by FLYCHK $He_β$/ $He_γ$ (solid line)*γ*, $He_β$ /$He_δ$ (dash-dotted line), $He_β$/ $He_ε$ (dotted line)* (b) *Experimental spectrum obtained for Aluminum plasma (solid line) and spectrum generated from the FLYCHK code (dotted lines) for T_c= 160 eV, T_h=1000 eV, f=0.008, and density = $5×10^{20}$ cm^{-3}.*

Figure 3.5 (a-d) *Variation of intensity of K-shell resonance lines $He_β$, $He_γ$, $He_δ$ and $He_ε$ with respect to angle from target normal, (e-h) images of charge states of Al ions detected by a Thomson parabola ion spectrometer as a function of angle between the target normal and the Thomson parabola ion spectrometer.*

Figure 3.6 *Energy level scheme of H-, He- and Li-like Silicon ions.*

Figure 3.7 *Experimental spectrum matched with FLYCHK for (a) He-like Silicon at T_c = 180 eV (b) for H-like lines at T_c = 380 eV keeping T_h = 1000 eV, f = 0.009 and n_e = 7 $×10^{20}$ cm^{-3}.*

Figure 3.8 *Schematic of the experimental setup.*

Figure 3.9 *(a) The experimental spectrum with theoretical predicted lines intensity in the spectral range 7.8 Å-9.4 Å recorded for Ne-, F- and O-like ions of Copper. The relative transition rates are drawn. (b) The labeled experiment spectrum at a laser intensity of 1.3 $×10^{14}$ W/cm^2.*

Figure 3.10 *(a) Energy level diagram of resonance lines from Ne-like Cu and their Na-like satellites. (b) Na-like satellite corresponding to Ne-like resonance line.*

Figure 3.11 *Dependence of the ratio of 4C to 4D lines and Na-like satellite to 4D line on (a) plasma temperature and (b) electron density as calculated by FLYCHK.*

Figure 3.12 *The experimental spectrum (at $1.3×10^{14}$ W/cm^2 laser intensity) overlaid with a synthetic spectrum at a plasma temperature 170 eV and a density $6.5×10^{20}$ cm^{-3}.*

Figure 3.13 *Best match of experimental spectrum with synthetic spectrum at T_c=150 eV, T_h=1000 eV, f=0.008 and density = $4.5×10^{20}$ cm^{-3}.*

Figure 3.14 *(a) Experimental spectra at various laser intensities (b & c) zoom of part (a) to show a comparison of the populations of Ne-like, F-like and O-like ions at different laser intensities.*

Figure 3.15 *Spatial Temperature profile of plasma generated by* HYADES *after irradiation of 1×10^{14} W/cm^2 laser intensity at time delays of (a) 0.1 ns (b) .7 ns with respect to laser.*

Figure 3.15 *Distribution of charge states of copper for different temperatures at an electron density of 5×10^{20} cm^{-3} as obtained from FLYCHK simulations (a) excluding the effects of opacity, and (b) including the effects of opacity. Distribution of Cu XXII (O-like), Cu-XXI (F-like), Cu-XX (Ne-like) ions at the same electron density as obtained from FLYCHK simulations (c) excluding the effects of opacity, and (d) including the effects of opacity. The distribution of charge states of Cu at 1×10^{21} cm^{-3} is obtained from FLYCHK simulations (e) excluding the effects of opacity (f) including the effects of opacity.*

Figure 4.1 *Schematic of experimental set up.*

Figure 4.2 *TAC targets with a density of 4 mg/cm^3 (a) Hermetic Millipore box with four targets on metallised mounts prepared for transportation to the laser setup and a microphotograph of a TAC plastic aerogel sample (blue) inside a ring holder. (b) SEM record of 2 mg/cc and 4 mg/cc TAC foam.*

Figure 4.4 *(a) Scaling of hard X-rays using photodiode covered with 20 µm thick Al filter (4 -16 keV) and 5 µm thick Ni filter (5-8keV) for 4mg/cc TAC. Effect of foam density on hard X-ray emission in the spectral range (b) (5 keV-8 keV) and (c) (4.5-16 keV) for 6.18 J laser energy.*

Figure 4.5 *(a) Scaling of four ion collectors signals placed at different angles with laser intensity for 4 mg/cc dense TAC target. (b) & (c) Comparison of ions amplitude for four densities of TAC at 22.5° and 67.5° from target normal respectively at 4.9J laser energy.*

Figure 4.6 *Calculated (curves) and experimental (points) angular distributions of the ion flux P (a) and the ion velocities u (b) for CTA targets of different density for a laser energy of ~4.9 J.*

Figure 4.7 *Images obtained with the Thomson mass spectrometer for TAC targets with a density of 2 (a), 3 (b), 4 (c), and 10 mg cm^{-3} (d) for a laser energy of ~4.9 J superimposed with the calculated curves for oxygen (yellow curves) and carbon (red curves) ions.*

Figure 4.9 *Effect of foam density on soft X-ray emission in the spectral range (5keV-8keV) for a constant areal density 0.2mg/cm^2.*

Figure 4.10 *Effect of foam density on soft X-ray emission in the spectral range (4.5 -16keV) for a constant areal density 0.2 mg/cm^2.*

Figure 4.11 *Shadowgraph of 2 mg/cc foam target at a delay of (a) t = 0 ns, (b) t = 4.8 ns, (c) t = 8.3 ns relative to the arrival of the laserpulse, and for the 20 mg/cc foam targets at delays of (d) t = 0 ns, (e) t = 4.8 ns, and (f) t = 8 ns.*

Figure 4.12 *Schematic of Experimental set up.*

Figure 4.13 *(a) Soft X-ray flux recorded by photo-diodes in different energy ranges (b) Hard X-ray flux recorded by NaI detector.*

Figure 5.1 *Schematic of various X-ray and ions diagnostics used in the experiment.*

Figure 5.2 *Images of (a) Silica aerogel foams, (b) SEM images of silica aerogel.*

Figure 5.3 *Comparison of (a) Soft X-ray fluxand (b) hard X-ray flux from solid quartz with SiO_2 foam of various densities such as 50mg/cc, 25% CH_3 + 75% SiO_2foam of 60 mg/cc and 40 mg/cc densities.*

Figure 5.4 *Shadowgraph of solid quartz (a) at t = 0 ns (b) at t = 2 ns (c) at t = 8 ns after laser pulse on the targets, and for foam targets at (d) t = 0 ns (e) at t = 2 ns (f) at t = 8 ns after laser pulse on the targets. The dotted circle in each image is showing the region of plasma.*

Figure 5.5 *Angular distribution of the thermal ion flux from the 50 mg/cc SiO_2 foam and quartz for two laser shots of approximately same energy.*

Figure 5.6 *(a-b) Contour plots for solid quartz and SiO_2 foam for electron density. (c-d) for electron temperature after a delay of t = 1 ns with respect to the start of the laser pulse on the target.*

Figure 5.7 *Experimental spectrum matched with FLYCHK for He-like lines of the Silicon in the (a) quartz at T_c = 180 eV, T_h = 1000 eV, f = 0.009 and $n_e = 7 \times 10^{20}$ cm^{-3} (b) SiO_2 foam at T_c = 190 eV, T_h = 800 eV, f = 0.01 and $n_e = 4 \times 10^{20}$ cm^{-3}.*

Figure 5.8 *(a) Typical signal of ion collector placed at 22.5° from target normal at 3 J laser energy (target: 0.275 gm/cc CD_2 foam).*

Figure 5.9 *Peak amplitude of ions with respect to laser intensity for (a) 275 mg/cc (b) 440 mg/cc CD_2 target (c) comparison of integrated flux for all both densities at 22.5°.*

Figure 5.10 *(a) Peak velocity at all angles corresponding to 275 mg/cc CD_2, (b) peak velocity at all angles corresponding to 440 mg/cc CD_2 (c) comparison of peak velocity for 440 and 275 mg/cc CD_2 foam at 22.5° (d) comparison of peak velocity for 440 and 275 mg/cc CD_2 foam at 45° and 52°.*

Figure 5.11 *Angular distribution of ions of various velocities for (a), (b), (c) 275 mg/cc CD_2 foam and (d), (e), (f) for 440 mg/cc CD_2 foam at different energies of incident laser.*

Figure 5.12 *(a) Data recorded by Thomson Parabola Spectrometer (TPS) (b) Analysis of the same data for extraction of ions energy and ion flux. Energy Vs flux for (c) 275 mg/cc and (d) 440 mg/cc CD_2 foam at different intensities of laser (e-f) effect of target density on energy and flux of ions at two laser energies.*

Figure 5.13 *(a)X-ray streak for 275 mg/cc CD_2 at various laser energies (b) X-ray streak for 440 mg/cc CD_2 at various laser energies (c) X-ray flux for all densities of CD_2 with varying laser energy. (d) X-ray pulse width in ns for all densities of CD_2 foam.*

Figure 6.1 *Schematic of experimental setup*

Figure 6.2 (a) *Metal nanoparticle layer cut, scale 100 micrometers (b) SEM picture of an Au ultra-dispersive layer obtained by an improved technique aimed at the production of more fine powder. The size of particles ~ 30nm. Scale 1 μm.*

Figure 6.3 *Time resolved X-ray signal recorded by X-ray streak camera at laser intensity* $\approx 1 \times 10^{14}$ *W/cm*^{2} *for (a) solid gold, 19.3 g/cc (b) 0.2 g/cc gold foam target (c) plot of X-ray signal at different intensities of laser (d) scaling of X-ray pulse width and integrated flux of X-rays with different laser intensities.*

Figure 6.4 *(a) Comparison of X-ray streak signal for solid gold with three densities of gold foam (0.1, 0.13, and 0.2 g/cc) (b) zoom part of figure (a) showing reduction in X-ray flux from solid gold.*

Figure 6.5 *Variation of (a) conversion efficiency for the 0.2 g/cc gold foam with different intensities of laser (b) conversion efficiency for different densities of gold target.*

Figure 6.6 *(a) Hydrodynamic profiles obtained in the calculation of the interaction of laser radiation* $q = 10^{14}$ *W / cm*^{2} *with plane targets made of gold at the moment t = 1 ns. Thick lines refer to the targets with initial density of* $\rho_0 = 19.32$ *g / cm*^{3}*, thin ones - with* $\rho_0 = 0.2$ *g / cm*^{3}*; density - solid lines (1), (3); temperature - dashed lines (2), (4); plasma emissivity - dotted lines (5), (6) (b) The maximum plasma emissivity is located at a distance R1 and R2 from the plasma surface (0). Through the pinhole (P) these areas are projected at a distance of X1 and X2 from the axis 00 on the image.*

Figure 6.7 *The X-ray yield as a function of time for a low-density target* ($\rho_0 = 0.2$ *g / cm*^{3}) *at different intensities of laser.*

Figure 6.8 *The X-ray yield as a function of time for a target heated by a laser intensity* 10^{14} *W / cm*^{2}*: solid line – target has initial density 19.32 g/cm*^{3}*; dotted line - initial density 0. 2 g/cm*^{3}*.*

Figure 6.9 *(a) Scaling of photo peak amplitude from signal of ion collector with laser intensity (b) angular distribution of photo peak for solid gold and gold foam (0.1 g/cc).*

Figure 6.10 *Comparison of plasma size for (a) solid gold (b) 0.1 g/cc gold foam (c) plot for comparison of 0.1 g/cc foam and solid gold target.*

Figure 6.11 *Shadowgraphy results showing expansion of gold plasma (a) before arrival of laser pulse (b) after 2 ns of laser pulse arrival (c) after 8.2 ns of laser pulse arrival and (d-f) are showing expansion plasma for 0.1 g/cc gold foam targets just before arrival of laser pulse, at 2 ns and at 8.2 ns after arrival of laser pulse respectively.*

Figure 6.12 *(a) Ion collector signal (placed at 22.5* ^{O} *from target normal) comprises of time of flight and ion amplitude at different laser intensities for 0.2 g/cc gold foam. (b)*

Scaling of ion peak velocity for ion collectors placed at three angles (22.5º, 45º and 52º from target normal) for 0.2 g/cc gold foam target.

Figure 6.13 *(a) comparison of ion flux for different target densities at angle 22.5° from target normal. (b) zoomed portion of the circled area near to photo peak.*

Figure 6.14 *Angular distribution of peak velocities of thermal ions for 0.1 g/cc gold foam with that of solid gold. Angular distribution of slow ions for 0.1 g/cc gold foam is also drawn.*

Figure 6.15 *Results of Thomson parabola spectrometer for (a) solid gold (b) 0.2 g/cc gold foam (c) 0.1 g/cc gold foam (d) plot of proton flux with respect to proton energies for solid gold and gold foam targets with densities 0.2 and 0.1 g/cc*

LIST OF TABLES

Table 3.1 *Transitions and Wavelengths of H-like and He-like spectral lines with satellites along with their branching ratio and calculated plasma temperature. Since the resolution of our crystal spectrometer is up to two decimal places, an average wavelength is presented for transitions having a difference in wavelength in the third or higher decimal place.*

List of abbreviations

LPI	*Laser plasma interaction*
LPP	*Laser produced plasma*
CE	*Conversion Efficiency*
ICF	*Inertial Confinement Fusion*
LTE	*Local Thermal Equilibrium*
CRE	*Corona Radiative Equilibrium*
IB	*Inversion Bremmtrahlung*
TPS	*Thomson Parabola Spectrometer*
IC	*Ion collector*
FC	*Faraday Cup*
TAP	*Thallium Acid Pthalate*
NaI	*Sodium Iodide Detector*
ns	*nanosecond*
ps	*picosecond*
fs	*femtosecond*
H-like	*Hydrogen like*
He-like	*Helium like*
Li-like	*Lithium like*
Ne-like	*Neon like*
O-like	*Oxygen like*
F-like	*Flourine like*
TAC	*Cellulose Triacetate*
SiO_2	*Silica aerogel*

Chapter 1

Introduction

1.1 Introduction

This chapter is intended to provide concise overview of plasma and its properties, laser plasma interaction, their applications as an X-ray and ion source and interaction of laser with low density foam targets. In the first two sections (1.2 & 1.3), basics of plasma and its properties is given. The behavior of atoms in intense fields is described followed by the detail of the laser plasma interaction (section 1.4). This section also provides the difference between long pulse and ultrashort laser interaction with plasma. In the next sections, the laser plasma as an X-ray source, mechanism of X-ray production, characteristics of laser plasma X-rays and their applications in various fields is given. The details of the bound-bound transitions including atomic processes in plasma, equilibrium models are also included. Lastly, the foam targets, their types, interaction of laser light with foam targets and their applications are discussed.

1.2 Plasma: fourth state of matter

The word *plasma* has Greek origin and means that *something molded*. It was first used by Tonks and Langmuir, in 1929 [1], to describe the oscillation of electrons during discharge. Plasma occupies fourth position in the hierarchy of states of matter divided according to their characteristics kinetic energy and constituent bonds holding their atoms together. The first three fundamental states of matter are *solid, liquid and gas*. Going from one state to other means that increasing the thermal energy (temperature) of atoms or molecules to overcome their binding potential energy. The amount of energy required for phase transition is called 'latent heat'. But the transition of gas to plasma is not a phase transition because it occurs with gradually increasing temperature. A very high temperature is required for reaching the plasma state. For example, ionizing a hydrogen atom, a minimum energy of the order of 13.6 eV (1eV=11,600 K) is required to overcome binding energy of electron with nucleus. So, the formation of plasma takes place at huge temperature of the order of millions of Kelvin. Due to this reason, plasma mostly does not exist on the Earth's surface under normal conditions but can be artificially generated from neutral gas, for example, the conducting gas in a fluorescent tube or in a neon sign is in plasma state. The statement often used is that perhaps 99 % of the universe is in plasma state; keeping in view of the fact that stellar interior and atmosphere, gaseous nebulae are plasma. The plasma can be defined as follow [2]

> 'Plasma is a quasi-neutral gas of charged and neutral particles exhibiting collective behavior'

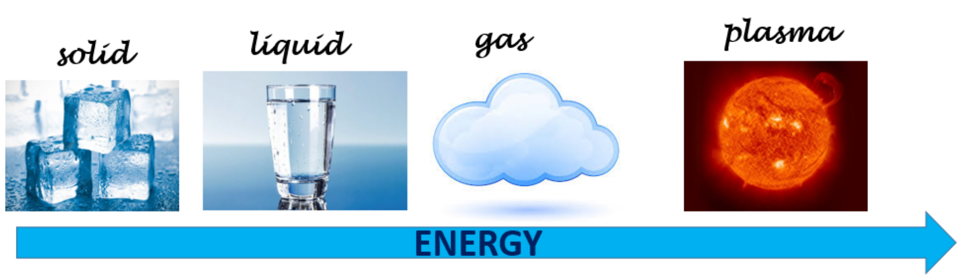

Figure 1.1 *Solid to plasma phase transition with increasing temperature*

1.3 Physical properties of plasma

1.3.1 Quasi-neutrality

Plasma consists of electrons, ions and neutral particles. There are long range coulomb forces in the plasma; each particle interacts simultaneously with a considerable number of other charged particles under the influence of long range electromagnetic fields present in the plasma. Under the influence of these fields, electrons move rapidly than ions due to their lighter mass. Without external disturbance, plasma is macroscopically neutral because of cancellation of microscopically space charge fields in the interior of plasma. In the absence of external forces, the departure from macroscopic neutrality over larger distances is not possible as the charged particles are able to cancel the excess space charge present due to large coulomb forces. But the large coulomb forces in comparison to thermal particle kinetic energy results in disturbance of macroscopic neutrality. Therefore, a plasma temperature of several millions of degrees Kelvin would be required to balance the electric potential energy with the average thermal particle energy. Departures from macroscopic electrical neutrality can naturally occur only over distances in which a balance is obtained between the thermal particle energy, which tends to disturb the electrical neutrality, and the electrostatic potential energy resulting from any charge separation, which tends to restore the electrical neutrality. This distance is of the order of a characteristic length parameter of the plasma, called the Debye length [3]. The relation between Debye length (λ_D) with plasma temperature (T_e) and plasma density (n_e) is given by

$$\lambda_D = \sqrt{\frac{\varepsilon_o k T_e}{n_e e^2}} \tag{1.1}$$

where, ε_o is the permittivity of free space, k is Boltzmann's constant, e is electronic charge. Debye length denoted a distance over which fluctuating electric potential may appear and condition of macroscopically neutrality is not satisfied. The value of Debye length is very small (generally few μm to mm) except interstellar where this distance can be few meters.

1.3.2 Plasma frequency

When a plasma is disturbed from equilibrium position, the electrons, being more mobile than the heavier ions, are accelerated to maintain quasi neutrality, but due to their inertia they move back and forth around the equilibrium position and results in collective oscillations around heavy mass ions. These collective motions are characterized by natural frequency of oscillation known as plasma frequency. The plasma frequency can be written as

$$\omega_p = \sqrt{\frac{n_e e^2}{m_e \varepsilon_o}} \tag{1.2}$$

Thermal motion of electrons in the plasma causes these oscillations to propagate and plasma oscillation will convert into plasma waves. The dispersion relation will be

$$\omega^2 = \omega_p^2 + \frac{3}{2} k^2 v_{th}^2 \tag{1.3}$$

v_{th} $(\frac{2kT}{m})$ is thermal velocity of electrons. Despite heavy mass of ions, ion wave known as ion acoustic waves are also present in plasma. The dispersion relation of ion acoustic waves is

$$\frac{\omega}{k} = (\frac{KT_e + \gamma_i KT_i}{M})^{1/2} \cong v_s,\ v_s \text{ is sound velocity/acoustic velocity} \tag{1.4}$$

1.3.3 Ionization in plasma

Under thermodynamic equilibrium, the degree of ionization in the plasma is related to the temperature. The amount of ionization for plasma in local thermal equilibrium is given by Saha's equation

$$\frac{n_i}{n_n} \cong 2.4 \times 10^{15} \frac{T^{3/2}}{n_i} e^{-U_i/KT} \tag{1.5}$$

where, n_i and n_n are the number density of ionized atoms and of neutral atoms, T is the temperature in K, K is Boltzmann constant, U_i is ionization energy of the atoms.

1.3.4 Conditions for existence of plasma

The three main conditions for any ionized gas to be in plasma state are

1. The dimensions of the entire plasma should be much larger than Debye length.
2. The number of particles within a Debye sphere is very large (N>>1).
3. The electron neutral frequency should be less than plasma frequency.

To produce plasma, energy must be supplied to neutral particles. These energy supplies can be in the form of thermal energy, energetic ion beam, large dc voltages or intense electromagnetic field. The discovery of laser light facilitates the availability of very intense electromagnetic field which when focus generates plasma in very small fraction of a second. This laser produced plasma is the basis of discussion for this thesis. Before understanding the physics of laser plasma interaction, there are two important topics need to be discuss:

1.4 Atoms in strong fields

When laser light incident on a solid surface, the electric field associated with this electromagnetic wave is obviously larger than the binding forces holding the atoms together.

For almost a century it was believed that atom can be ionized when incident light has equal or higher energy than the ionization energy of atoms, known as photoionization. If this is the case than today, we would not be able to ionize atom with laser pulse because energy of one IR photon (1.2398 eV) is not sufficient to ionize a single atom. Fortunately, this problem has resolved thirty years before the invention of lasers (1960), when Goeppert-Mayer (1931) [4] submitted her thesis on two photon absorptions. She supports a different pathway of ionization of atoms under extreme fields known as multiphoton ionization which was observed experimentally by Voronov and Delone (1965) [5] and Agostini (1968) [6]. In multiphoton ionization, when energy of single photon is not sufficient to ionize atom ($h\nu \ll I_p$), but intensity is high enough that electron absorb n photons of moderate energy, the electron eject from the atom leaving the atom in ionized state ($nh\nu \gg I_p$). This process of multiphoton absorption is highly non-linear and can be explained by perturbation theory. The N-photon ionization rate of the atom varies as $\sigma_N I^N$ where σ_N is the generalized cross section of the process and I is laser intensity in W/cm^2. The n photon cross section σ_N decreases with n, but rate depends on the intensity of light. The intensity should be high enough so that it can compensate low cross section and makes ionization feasible. Typically, the multiphoton ionization dominates for the intensity range 10^{13}-10^{14} W/cm^2. In this thesis, most of the experiments and studies are carried out in this intensity range.

At intensities (>10^{14} W/cm^2), the electric field is so intense to distort the coulomb potential barrier of atom. The electrons can tunnel through this barrier and atom is ionized known as tunnel ionization as shown in Figure 1.2 [7]. At further high intensities (>10^{15} W/cm^2), the suppression of barrier is so large that it becomes lower than binding energy of electron in atom. So, the electron no longer feels the coulomb barrier of atom and promote to continuum leaving the atom in ionized state. This process is known as above the barrier ionization [8]. The determination of dominance of ionization process is provided by Keldysh [9] and is given by ratio of the laser frequency to tunneling frequency

$$\gamma = \frac{\omega}{\omega_{tun}} = \sqrt{\frac{I_P}{2U_p}} \tag{1.6}$$

where U_p is pondermotive energy of the electrons associated with quiver motion of electrons I_P is ionization potential and ω_{tun} is tunneling frequency. The Keldysh parameter decreases with increasing laser intensity. For γ>1, multiphoton ionization dominates.

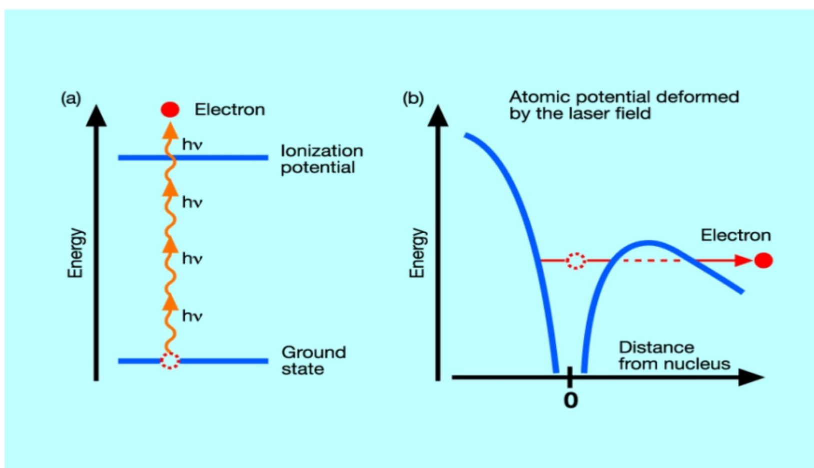

Figure 1.2 *Multi photon ionization and tunneling ionization*

1.5 Electrons in electromagnetic fields

As laser light consists of transverse electric and magnetic field that are perpendicular to each other and perpendicular to the direction of propagation. Due to oscillatory nature of the field, the electron also starts oscillating in the presence of field with same frequency of light field. This is known as quiver motion of electrons in non-relativistic regime. For a linearly polarized light, electron oscillations are linear to the direction of laser light. However, at very high intensities (in relativistic regime), magnetic field also starts affecting the motion. The quiver energy of the electron in the non-relativistic regime is given by

$$E_{osc} = \frac{e^2E^2}{4m\omega^2} \tag{1.7}$$

Apart from oscillatory motion of the electron in the uniform laser field, there is another nonlinear force known as pondermotive force affecting the motion of free electrons. This is attributed to gradient in the field. The Gaussian shape of the laser pulse results in inhomogeneity of field or intensity in both space and time. Instead of facing a sinusoidal field over their orbits, electrons now face a varying field. The pondermotive force pushes the electrons away from high field regions [10]

$$F_p = -\frac{e^2}{4m\omega^2}\vec{\nabla}\overrightarrow{E^2}(x) = -\vec{\nabla}U_p \tag{1.8}$$

The field of laser light is oscillating with angular frequency ω, U_p is the pondermotive energy and is the cycled averaged quiver energy of the electron in the complete cycle of oscillating laser electric field.

1.6 Laser plasma interaction (LPI)

The process of laser plasma interaction depends upon laser parameters (pulse width, wavelength, intensity) and target properties (optical properties, density, atomic number, structure etc.). In the very first step, the laser interacts with the cold material and deposits its energy. The laser gets absorbed up to the skin depth of the material. The materials get heated, evaporated and ionized. However, the interaction process of long pulse and ultra-short laser pulse with matter is quite different [11].

In the case of **long pulse** plasma interaction [12] on the basis of the spatial Gaussian profile for intensity of laser light, the production of plasma can be divided into different stages according to different value of intensity. The plasma production is initiated during the rising part of laser pulse and rest of the laser pulse interacts with this expanding plasma. For sufficiently low intensity of laser in the rising edge, $I \leq 10^7$ W/cm^2, the incident laser pulse heats the target surface without melting or vaporizing it. The incident laser light gets absorbed up to skin depth of the target surface. Further the absorbed energy is carried into the interior of the target by thermal conduction. For intensity range 10^6-10^9 W/cm^2, the laser light melts and evaporate the surface of solid. As the intensity is increases further, ionization of the atoms takes place. The ablation threshold for all material is generally is less than 10^{10} W/cm^2. Above this intensity, the ionization begins. The seed ionization is initiated through multiphoton ionization, tunneling and over the barrier mechanism. After the initial ionization, there is a subsequent growth in ionization accomplished by avalanche process. There is generation of free electrons which start oscillate under the electric field of laser, collide with the surrounding atoms and ionize them further. Because of this sudden ionization, the density of electrons increases at a very high rate. This leads to formation of the plasma on the front surface of the target. This plasma plume expands in vacuum with high velocity and create low density corona with a monotonically decreasing density profile. Once the plasma corona is created, the laser light is not able to penetrate further and reflect back. Some part of remaining laser interacts with this plasma plume by various absorption mechanisms. The propagation of laser light inside the plasma follows the dispersion relation

$$\omega_L^2 = \omega_p^2 + k_L^2 c^2 \tag{1.9}$$

where ω_L and ω_p are the laser frequency and plasma frequency respectively. K_L is the wave number of laser light; c is the speed of light in vacuum. The group velocity can be calculated from Eq. 1.9 as

$$v_g = c\left(1 - \frac{\omega_p^2}{\omega_L^2}\right) \tag{1.10}$$

The group velocity decreases with the increase in electron density and finally becomes zero when plasma frequency becomes equal to laser frequency. The density at which this happens is known as critical density. The region with density greater than critical density is over dense and region with density less than critical density is under dense. The index of refraction is imaginary at this point. The laser can penetrate up to critical density region, the expression for critical density n_c is given by

$$n_c = \frac{\omega_o^2 m_e \varepsilon_o}{e^2} = \frac{1.12\times10^{21}}{\lambda^2} \tag{1.11}$$

where λ is laser's wavelength in micron. Most of the absorption of laser light occurs at or near the critical density surface. Laser will further absorb or reflect depending upon its incidence angle and polarization. The main absorption mechanisms for the long pulse laser are Inverse Bremmstrahlung (IB), resonance absorption and parametric decay instabilities. This interaction of long pulse laser with plasma can be divided into three regions: 1.) Corona region 2.) Electron conduction region and 3.) Compressed region.

In the corona region, the laser energy is deposited to electrons and then further energy beyond critical surface is transported via electron and photons thermal flux. Figure 1.4(b) shows the temperature and density profile for all the above regions. The temperature is maximum at the absorption front and then there is a steep temperature gradient towards ablation front. Therefore, most of the emission occurs between the ablation and absorption front. There is also a 'diffusive radiation conduction' process due to generation of soft X-rays originated in the region of densities greater than critical density. This radiation ablation front move ahead of the electron ablation front towards shock region and preheat the target material.

In case of **ultra-short (≈fs)** laser, [13], melting of the surface is with no time for thermal conduction as electron to lattice (via phonons) heat transfer occurs is in ps scale. The atoms feel a very high electric field of laser pulse. The detachment of electrons from the lattice is so fast and electron gets accelerated to very high energy. The cause of ionization is mainly via tunneling and over the barrier mechanism. The pulse terminates before any material leave the surface and there is no laser plasma interaction. The difference in interaction mechanism for long and ultra-short pulse is present even after the switching off the laser pulse. There is significant density scale length in case of interaction of ns pulse because of large interaction time in contrast to steep density gradient in ultrashort pulse laser. The expression for scale length is roughly given by $L = C_s\tau$, where $C_s = \frac{2}{\gamma-1}(\frac{ZKT_e}{M_i})^{1/2}$ is ion speed (≈ 10^7 cm/s) and τ is pulse width of laser. In case of ultrashort interaction, collisional absorption mechanism is less dominating and collisional-less absorption including resonance absorption, vacuum heating, and anomalous skin-layer heating plays dominant role. These ultrashort pulses give rise to production of very high energetic electrons and relatively cold background plasma. These energetic electrons via collision with ions gives rise to very high energy photons (up to MeV) in continuum spectrum while background plasma for keV-sub-keV line or continuum emission.

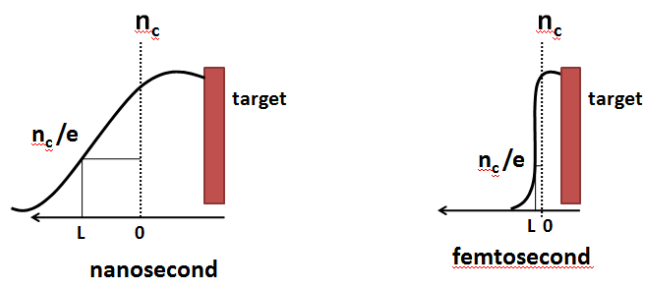

Figure 1.3 *Difference in density scalelength for long and ultrashort pulse.*

The various absorption process involved in laser plasma interaction are discussed below

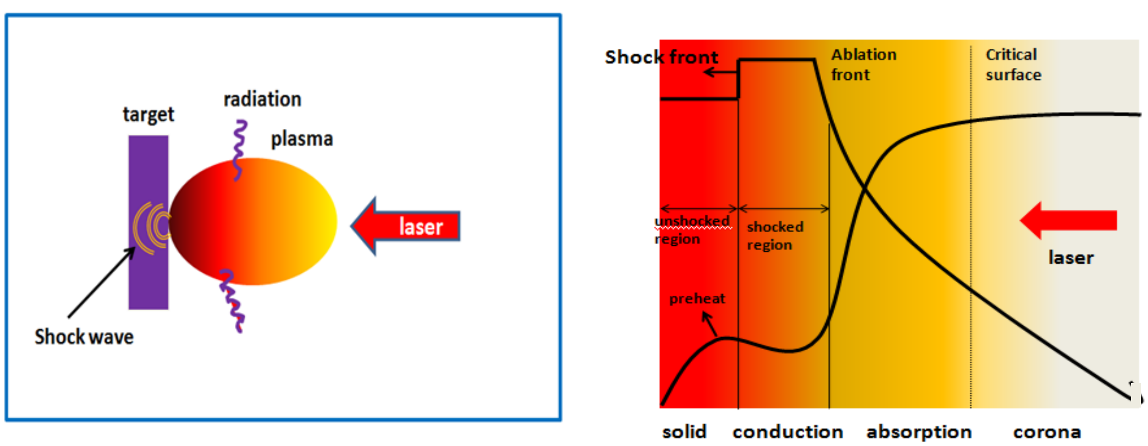

Figure 1.4 *(a) schematic of laser matter interaction (b) temperature and density profile with different regions.*

1.6.1 Inverse Bremsstrahlung (IB) absorption

When laser light incident on the target, it can be refracted, reflected or absorb by the target material. One of the simplest deposition mechanisms is Inverse Bremsstrahlung Absorption. It is the classical process of absorption of laser light in plasma. In IB, the electrons oscillate in the field of laser and then transfer their energy to ions through coulomb collision.

The presence of a scattering field (of ions) is necessary for the absorption of laser light by electrons. In other words, the incident laser electric field drives electron currents and this energy is converted into heat energy leads to 'Joule heating' of plasma. In this way, the incident light energy is deposited in the form of increased thermal energy (temperature). Since this process depends upon the collision between electron and ions, so the absorption coefficient would scale as the electron-ion collision frequency. The frequency of the collision for Maxwellian distribution is given by [14], [15]

$$\vartheta_{ei} = 3\times10^{-6}\frac{n_e Z_{eff}}{T_e^{3/2}} ln\,\Lambda\, s^{-1} \tag{1.12}$$

where n_e and T_e are the plasma density and temperature in units of cm^{-3} and eV respectively. The quantity $Z_{eff} = {\langle Z^2\rangle}/{\langle Z\rangle}$where, Z is the charge state of ion and <> showing the average over all species present, Λ= ${9N_D}/{\langle Z\rangle}$ is coulomb logarithm in which N_D is number of particles in Debye's sphere. The v_{ei} scales with plasma temperature as $T_e^{-3/2}$, so with the increase in plasma temperature, the collisional absorption become less effective. The Newton's equation after the inclusion of electron-ion collision term modifies as

$$m\frac{\partial v}{\partial t} = -eE - m\vartheta_{ei}v \tag{1.13}$$

The dielectric constant takes the following form [16]

$$\varepsilon = 1 - \frac{\omega_p^2}{\omega^2\left(1+i\frac{\vartheta_{ei}}{\omega}\right)} \tag{1.14}$$

This introduces an imaginary term in dispersion relation, which provides the coefficient for Inverse Bremmstrahlung absorption of laser with frequency ω is approximately

$$k_{IB} = \frac{\vartheta_{ei}}{c}\frac{\omega_p^2}{\omega^2}\frac{1}{\sqrt{1-\frac{\omega_p^2}{\omega^2}}} \tag{1.15}$$

With dimension of inverse length, here c is speed of light, ω_p is plasma frequency, or natural frequency of electrons in the plasma. In this way, electrons gain energy from laser and after several oscillation periods they will collide with solid target and ionize them in cascading fashion which results in formation of plasma in contrast to higher intensities cases where potential energy of electron exceeds the ionization energy of atom and laser will ionize the atom directly. This will lead to formation of low density corona from which expand in vacuum with very high velocity.

At higher laser intensities (>10^{14} W/cm^2), electrons acquire higher quiver velocity ($\vartheta_q = \frac{eE_0}{m\omega}$) and consequently a reduction in absorption processes. Quiver energy of electrons exceeds the thermal energy as the electrons gain energy from the laser at a higher rate in comparison to the rate at which they share the energy with each other. Due to this, there is lack of low energy electrons or thermal electrons. The cross section of IB is inversely proportional to the velocity of electrons, hence reduction in low energy electrons leads to reduction in IB.

1.6.2 Resonance Absorption

It is a collisionless absorption process unlike IB. Resonance absorption occurs when laser light has an electric field component along the density gradient ∇n [17]. Specifically, when p-polarized light (electric field is parallel to plane of incidence) is incident at an oblique angle on the density gradient of plasma, an evanescent wave is excited by the reflected wave in over dense region. This evanescent wave has frequency equal to the laser frequency and carries both longitudinal and tangential components. The component of E parallel to density gradient drives electron plasma waves (Langmuir wave). The electric field is high at the critical surface and will resonantly excite the plasma waves. In this way, the energy is transferred from light to waves and then to plasma through wave breaking, collisional damping, or Landau damping (collisionless). The same phenomenon is not possible by using s-polarized light. One more condition for resonance absorption is that angle of incidence θ should be small enough so that critical density surface can be nearly approachable. Due to density gradient, refraction of laser light occurs and maximum distance of penetration or the plasma density at the turning point is given by

$$n_t = n_c \cos^2 \theta \tag{1.16}$$

If angle of incidence θ is large than there is more difference in the two densities. An electric field in the direction of density gradient should be great as possible but simultaneously θ should be less. Maintaining this condition will result in increment in absorption by resonant process. In resonance absorption, very energetic electrons known as hot electrons are produced.

1.6.3 Parametric decay instabilities

At higher laser intensities, laser coupling with plasma takes place through resonance absorption and excitation of various plasma modes. Outward propagation of excited plasma modes leads to loss in energy while damping of modes inside the plasma results in absorption. In parametric decay instabilities, the interaction of laser light with plasma modes (electron plasma wave and ion acoustic wave) takes place. The growth rate of these collective modes depends upon the plasma density scale length. Growth of these modes increases in case of long pulse laser due to the presence of large density scale length. Depending on the modes of decay of incident laser pulse, these instabilities can be classified as follow

1.6.3.1 Two Plasmon decay

As the name implies the electromagnetic wave decays into two electron plasma waves i.e. $\omega_{em} = \omega_{ep1} + \omega_{ep2}$. Therefore, $\omega_L = \omega_p[1 + {3k_{ep1}^2 v_{th}^2}/{\omega_p^2}]^{1/2} + \omega_p[1 + {3k_{ep2}^2 v_{th}^2}/{\omega_p^2}]^{1/2} \geq 2\omega_p$. This implies $\omega_p \leq {\omega_L}/{2}$ i.e. $n_e \leq {n_c}/{4}$, the two plasmon decay takes place up to critical density layer.

1.6.3.2 Parametric decay

In this decay, the incident electromagnetic wave decays into electron plasma and ion acoustic wave i.e. $\omega_{em} = \omega_{ep} + \omega_{ia}$.Therefore, $\omega_L = \omega_p[1 + {3k_{ep}^2 v_{th}^2}/{\omega_p^2}]^{1/2} + K_{ia}C_s \geq \omega_p$ .The relation $\omega_p \leq \omega_L$, implies that $(n_e \leq n_c)$, the parametric instability takes place up to critical density layer.

1.6.3.3 Stimulated Raman scattering

In this process, the incident electromagnetic wave excite electron plasma wave and rest of the energy is scattered as electromagnetic wave i.e. $\omega_{em} = \omega_{em}\,(scattered) + \omega_{ep}$. Therefore, $\omega_p[1 + {3k_s^2 c^2}/{\omega_p^2}]^{1/2} + \omega_p[1 + {3k_{ep2}^2 v_{th}^2}/{\omega_p^2}]^{1/2} \geq 2\omega_p$. This implies, $\omega_p \leq {\omega_L}/{2}$ i.e. $n_e \leq {n_c}/{4}$. This process also takes place up to critical surface. This process consists of one forward Raman scattering and one backward scattering wave.

1.6.3.4 Stimulated Brillouin scattering

In this process, the incident electromagnetic wave excite ion acoustic wave and rest of the energy is scattered as electromagnetic wave i.e. $\omega_{em} = \omega_{em}\,(scattered) + \omega_{ia}$. Therefore, $\omega_p[1 + {3k_s^2c^2}/{\omega_p^2}]^{1/2} + K_{ia}C_s \geq 2\omega_p$. This implies, $\omega_p \leq \omega_L$ i.e. $n_e \leq n_c$. This process also takes place up to critical surface.

Beside these above-mentioned absorption processes, other processes such as vacuum heating, $j\times B$ heating also occurs in case of high intense lasers.

1.7 Laser plasma as an X-ray source

The interaction of pulsed high-power laser with matter result in production of plasma with high temperature (10 eV- 10keV) and density ($10^{19} - 10^{23}/cm^3$). Laser produced plasma can be considered as Black body with emission extended to X-rays and gamma-rays. These plasmas have high brightness in X-ray region. The laser produced X-ray sources have proved a better alternative to conventional X-ray sources [18]–[20]. Their small size comparable to laser focal spot (10-100 μm), small duration (10^{-13} s-10^{-9} s), high brightness (10^{17} W/cm^2), increases their excellence to use them in various applications. The properties of these X-ray sources depend on varying laser parameters such as laser pulse duration, wavelength, intensity etc. This is due to the change in interaction mechanism of laser with plasma. In fact, properties of X-ray depend upon the dominant absorption mechanism. The peak of X-ray emissivity is in the plasma region which combines both high temperature and density typically just beyond the critical density surface where electron conduction ensures efficient energy transport.

1.7.1 Mechanism of X-ray production

The main mechanism of radiation emission is via free-free, free-bound and bound-bound. The three processes are defined below [21]–[23]

1.7.1.1 Free-free

This is also known as Bremmstrahlung emission. In this mechanism, the free electrons while passing through Coulomb fields of ions radiate electromagnetic radiation. To calculate the total power radiated by this process in plasma, consider an electron having velocity ν interact with ion. The impact parameter of this interaction is b. The interaction time (τ) and dominant frequency in the radiated electromagnetic spectrum are 2b/ν and ν/4πb respectively. The total energy radiated by accelerated electron in the form of electromagnetic radiation is given by Larmor formula

$$\Delta E = \frac{2}{3}\frac{e^2 a^2 \tau}{c^3} \approx \frac{4}{3}\frac{Z^2 e^6}{m^2 c^3 b^3 v} \tag{1.17}$$

Consider the number of electron ion collision per unit time with ion density n_i with impact parameter lies in the range b and $b+db$ is $2\pi n_i v b db$. The total power radiated per electron can be calculated from above equation by integrating in the limits b_{min} (De-broglie wavelength) to b_{max} (Debye length). Considering the Maxwellian distribution of velocities of electrons, the total Bremmstrahlung power radiated per unit volume is

$$W_B = 1.6\times10^{-27} Z\, n^2 T_e\, (eV)^{\frac{1}{2}}\, erg\ \ sec^{-1} cm^{-3} \tag{1.18}$$

To obtain spectral distribution of Bremmstrahlung emission, the integration is to be done in frequency limits ($\vartheta_{min}\ to\ \vartheta_{max}$) instead of b and using $\vartheta_{min} = v/4\pi\lambda_D$ and $\vartheta_{max} = mv^2/2h$, the electrons distribution is Maxwellian, the final expression of spectral intensity comes out to be

$$W_B^{\lambda} \cong 2.10^{-27}\, Z\, n_e^2 T_e^{-1/2} \lambda^{-2} \exp\left(-\frac{hc}{\lambda k_B T_e}\right) \;\; erg\, sec^{-1} cm^{-4} \tag{1.19}$$

The maximum emission occurs at a wavelength, λ_{max}(Å), of 6200/T_e (eV). This peak emission in case of blackbody occurs at 2500/T_e (eV). Moreover, the blackbody emission is proportional to T^4 (Stefan's law) whereas Bremmstrahlung emission varies as $T^{1/2}$.

1.7.1.2 Free-bound

In this process, the free electron recombines in the bound state of an ion (charge Z+1) results in emission of photon leaving the ion in Z charge state. This also produced continuum electromagnetic spectrum. When a free electron is captured by a (Z+1) fold ionized atom, leading to a transition to a bound state of a Z-fold ionized atom, a photon is emitted with an energy

$$h\vartheta = \frac{1}{2}\, mv^2 + E_Z^n \tag{1.20}$$

the first term on right hand side represents the initial kinetic energy of the electron and the energy of the final atomic state, Z is the ion charge and *n* is the principle atomic number. The electron can take energy value in continuum so the radiation emitted is continuous in nature. But the contribution to each transition to the continuum is accompanied by satisfaction of the condition $h\vartheta \geq E_Z^n$ (recombination edge), due to this there are jumps in the continues spectrum of recombination. The spectral intensity of the recombination continuum can be expressed in terms of Bremmstrahlung as

$$W_r^{v} \cong W_B^{v}.\, 2\,.\, 10^{-32} \frac{Z^3 n_e^2}{T_e^{3/2}} \sum_{n=1}^{\infty} \frac{1}{n^3} \exp\left(\frac{Z^2 E_H}{n^2 K_B T_e} - \frac{hc}{k_B T_e}\right) \;\; erg\, sec^{-1} cm^{-3} Hz^{-1} \tag{1.21}$$

1.7.1.3 Bound- Bound

This emission takes place from transition between discrete levels of ionized atoms. The transitions from excited to lower states in ionized atoms give rise to atomic lines. These transitions are caused by bound electrons. These lines are characteristic of atoms generating them and provide information about the physical condition of plasma. Strong contribution comes from the transition from ground states (resonance lines). However, transition from the excited state is very helpful in the determination of plasma temperature because these transitions escape from the plasma without substantial re-absorption. Power emitted per unit volume as line radiation from plasma is given by

$$P_{bb} = 3.5 \times 10^{-25} \, (kT_e)^{-1/2} n_e \sum n_{i+1} \exp\left(-E_i/_{kT_e}\right) W/_{cm^3} \qquad (1.22)$$

The bound-bound transitions are very useful in determining wealth of information about plasma. The detail of these transitions is provided in chapter 3.

1.7.2 Characteristics of LPP X-ray source

Rise time of X-ray emission is the time needed to heat the plasma, while the plasma cooling sets the fall time of X-ray emission. The transverse size of the source is given by the focal spot dimension (f) or by the hydrodynamic expansion at the sound velocity in the medium $d_h=c_s\tau$ where τ is laser pulse duration. Since the transverse size is given by the hydrodynamic expansion, if the focal spot dimensions are smaller than the contribution of the hydrodynamic expansion the X-ray source shows a shape with longitudinal and transversal dimension depending on heat transport and matter ablation mechanisms. Otherwise, plasma develops a shape with the diameter of the order of the focal spot size and length roughly equal to $c_s\tau$. For what concerns the angular distribution we see that this one shows a cylindrical symmetry, whose axis is orthogonal to the target surface, regardless of the angle of incidence of the laser beam. The angular distribution is found to fit the function $I\lambda(\theta) = I\lambda cos^n(\theta)$ where θ is the angle of emission and n is a parameter depends on experimental condition.

1.7.2.1 Dependence of conversion efficiency on target properties

The conversion efficiency (CE) is dependent on the atomic number (Z) of the target. For very low Z targets for example plastics, bare ions exist in plasma. The bound-bound emission is absent here. The major contribution in X-ray emission comes from Bremsstrahlung emission.

For medium Z targets (Z<20), higher charge states come into existence and plasma consists of H-like through Be-like ions. Even the single emission lines of bound-bound spectrum carry significant fraction of total X-ray emission energy between 0.5-10 keV. These medium Z elements are very useful for the spectroscopic studies due to high brightness of spectral line in this case

When high Z (Z>20) is used, ions with several bound electrons dominates in plasma. The X-ray emission spectrum is difficult to analyze due to the presence of complex many electron line emission. The high density of these lines makes it difficult to resolve the quasi continuum band of these lines.

In short, the very low Z and high Z targets produce continuum/ Quasi-continuum X-rays. The conversion efficiency of X-rays increases with Z. This is the reason to use high Z materials as backlighter sources in absorption spectroscopy experiments.

1.7.2.2 Dependence of X-ray conversion efficiency on laser parameters

Laser wavelength: CE increases with decreasing wavelength. The penetration of shorter wavelength laser is more which gives rise to higher collisional absorption providing a high yield of X-rays.

Laser intensity: The laser intensity on targets affects the plasma temperature. The plasma temperature decides the ionization balance and hence emission of X-rays from different ions species takes place.

Laser pulse length: When we move from nanosecond to picosecond regions, the conversion efficiency decreases. In nanosecond pulse case, laser energy is absorbed completely in long scale length plasma via collisional processes. This in turn increases the X-ray flux. But in case of picosecond pulse, there is decrease in plasma density scale length and collisional absorption becomes less effective.

1.7.2.3 Dependence of X-ray conversion efficiency on laser focusing condition

The X-ray yield also dependent on the focusing conditions of laser on the surface of the target. If the laser is disturbed from best focus, the plasma volume increases giving rise to higher X-ray flux. The maximum of the CE is found with the target displaced slightly away with respect to the position of the beam waist, in the direction of the propagation of laser. This is highly dependent on the focal length of the focusing lens. As you move away from the best focus, hard X-ray yield reduces and soft X-ray flux increase due to volume effect.

1.7.3 Spectroscopy of LPP X-rays

It is not possible to directly measure the temperature of plasma by using a thermometer as we can do it case of a gas. In case of plasma, many techniques serve this purpose for example using Langmuir probe, one can measure temperature and density of laboratory plasma. But it can affect the properties of plasma which is to be measured and has limitations. Fortunately, by studying the X-ray emission spectrum from laser produced plasma, we can measure the temperature and density of plasma. The rate of collision in plasma is influenced by the distribution of electrons in bound states which depends upon plasma temperature and density. The interpretation of spectrum requires knowledge of charge state distribution as well as population of excited levels. The rate equations should be solved in which population and depopulation of levels by various processes like ionization, recombination (3 body), collisional excitation and deexcitation, radiative decay, absorption etc. The dominance of collisional and radiative processes depends upon the type of equilibrium in which plasma exists. The various atomic processes such as collisional and radiative processes [24] as well as equilibrium models are described in next sections.

1.7.3.1 Collisional processes

The collisions among charge particles and photons are responsible for the existence of various atomic processes in the laser produced plasma. The collision takes place between free electrons, between ions and ions and in between ion and electrons. Collisions plays important role in the determination of free electron and ion velocity distribution and the population of electrons among the various states. A collision is said to be occur when two particles transfer energy during collision. It can be divided into two types- elastic and inelastic. In elastic collision, the total kinetic energy is conserved. But in inelastic collision, the energy absorbed by ions results in the excitation of bound electrons. In case of elastic collisions, after a number of collisions the free ions and electrons comes in thermal equilibrium and follows Maxwell velocity distribution which provides the plasma temperature. However, the thermodynamic equilibrium among particles of same mass (electron-electron, ion-ion) reached rapidly. The thermal equilibrium depends upon the timescale over which these changes occurs and if timescale is very rapid than it is not possible to show the plasma with a particular velocity distribution. Generally, laser produced plasma shows non-Maxwellian velocity distribution due to the presence of hot electrons in the plasma. In inelastic collision unlike elastic, the kinetic energy is not conserved. Different collisional ionization and recombination processes occurring in plasma are described below

a. Collisional ionization

An atom is said to be ionized when an electron ejected from it. For the ejection of electrons from atomic orbitals enough energy is to be supplied to overcome the coulomb barrier of electron (ionization potential) due to nucleus. This energy can be supplied by photons or electrons or by collision. In case of collisional ionization, electron is ejected by energetic electron. In electron impact ionization, incident electron has kinetic energy in excess of ionization energy of electron. Hence, electron impact ionization in plasma will dominate when electron temperature is several times the ionization potential of gas being ionized. The atoms having one or more electrons ejected are called multiply ionized. These multiple stripped ions can be formed in two different ways- first is removal of many electrons in single collision process and second is removal of electron in single event and then repetition of these ionizing events. The step wise ionization process dominates over first one. The ionization by fast ions can also take place but this required a very high energy of ions due to their heavy mass in comparison to electrons and generally not dominates in laser plasma. The rate of photoionization is less than the rate of collisional ionization because of lower interaction cross section between photon and ions.

b. Autoionization

This process takes place in doubly excited atoms, when an electron is de excited from a doubly excited level, instead of the emission of photon, the extra energy is supplied to an electron (already in excited state) and this electron ejected out from the ion.

$$A^{**} \rightarrow A^{+} + e^{-} \tag{1.23}$$

The autoionization is not a dominant process due to less probability of doubly excited atoms.

c. Radiative recombination

In electron-ion recombination, the free electron recombines in the bound state of atom. The excess energy is transferred in the form of photons, internal vibrational or rotational modes or kinetic energy of the contributing particles. It is a two-body recombination in which an electron combines with an ion and excess energy is released in the form of photon.

$$A^{+} + e^{-} \rightarrow A + h\nu \tag{1.24}$$

The energy of the emitted photon is equal to the sum of kinetic energy of the incident electron and the ionization energy of the shell in which the electron is captured. The spectrum produced in this process is continuous in nature due to continuity in energy of incident electron.

d. Three body recombination

It is the inverse of collisional ionization. In this process, excess energy in recombination is supplied to a third body (T)

$$A^{+} + e + T \rightarrow A^{*} + T \tag{1.25}$$

e. Dielectronic recombination

In this process, the electron recombines in a bound state of an ion and simultaneously an electron from another bound shell is excited to higher energy level. The ion thus in doubly excited state. This doubly excited ion has two channels of decay- autoionization and radiative decay. In radiative decay, the transition to lower state takes place in the presence of spectator electrons. The lines observed in this transition are called satellite lines. It is like resonance lines in the presence of an extra electron. These satellite lines are very useful in the determination of plasma temperature and density.

1.7.3.2 Radiative processes

The photons with wide range of energies are produced by free-bound transitions. The bound-bound transitions emit photon with discrete energy. These photons get absorbed in plasma and give rise to so many excitation and recombination processes.

a. Photo ionization

When the energy of the incident photon exceeds the ionization energy of the electron, the electrons is ejected out leaving the atom in ionized state. This energy is sufficient to overcome the coulomb barrier of electron due to nucleus. The process can be described below

$$A + h\nu \rightarrow A^{+} + e^{-} \tag{1.26}$$

where A is atom to be ionized, $h\nu$ is the energy of photon and e^- is ejected electron.

b. Spontaneous emission

Spontaneous emission is the process in which transitions from a higher energy level of atom to a lower energy state result in emission of a photon. Spontaneous emission is ultimately responsible for most of the light we see all around us.

b. Stimulated emission

Stimulated emission is the process by which an incoming photon of a specific frequency can interact with an excited atomic electron, causing it to drop to a lower energy level. The liberated energy transfers to the electromagnetic field, creating a new photon with a phase, frequency, polarization and direction of travel that are all identical to the photons of the incident wave.

c. Stimulated radiative recombination

The rates of stimulated emission, stimulated radiative recombination, photo excitation and photo ionization depend on the energy of photons. However, the spontaneous emission and radiative recombination are independent processes.

1.8 Equilibrium models in plasma

As mentioned earlier, the knowledge of population distribution of atomic levels is essential to reveal the various plasma parameters such as internal energy, opacity, equation of state. The distribution of population among various energy levels depends upon the plasma temperature and density. The various plasma models opted for the plasma diagnostic are described below [25].

1.8.1 Complete thermal equilibrium (CTE)

In this model, plasma is in detailed balance means the rate of direct processes is equal to the inverse processes.

- each direct process is balanced by the inverse
    - excitation ↔ de-excitation
    - ionization ↔ 3-body recombination
    - photoionization ↔ photorecombination
    - autoionization ↔ dielectronic capture
    - radiative decay (spontaneous+stimulated) ↔ photoexcitation

At temperature T, the population of atomic levels is determined by the Boltzmann distribution and Saha ionization distribution. Here electron, ion and radiation temperature are same. Therefore, the Planck's law is used to define the radiation distribution, electron level population is defined by Boltzmann law and ionization distribution is by Saha's equilibrium, free electron is by Maxwellian distribution.

1.8.2 Local thermal equilibrium (LTE)

Due to decoupling of photons from plasma, laser produced plasma will be never found in complete thermal equilibrium. The existence of local thermal equilibrium defines by the characterisitics collision time between electron and ions. If this is shorter than the other processes than plasma is in LTE. If this condition is verified, then plasma is characterizing by a unique temperature. One can determine plasma temperature by Boltzmann plot method. This is a simple procedure and not requires any complicated calculations. Only energies and statistical weights are sufficient for temperature determination. The validity of LTE is given by Mc Whirter criterion [26] which is written as

$$n_e \geq 1.6\times 10^{12} T^{1/2} (\Delta E)^3 \qquad (1.27)$$

1.8.3 Corona equilibrium (CE)

This type of equilibrium occurs at very low density of plasma generally present in the astrophysical situations and in the corona of the sun. In this equilibrium, the collisions are responsible for excitation but de-excitations are purely radiative due to low density. Hence, collisional ionization and excitations are balanced by radiative recombination and spontaneous decays. The population in the excited states is determined by taking the balance between collisional excitation from and radiative decay to the ground level. The population in the ground levels is determined by the balance between collisional ionization rates, radiative and dielectronic recombination rates. The free electrons in coronal model are assumed to follow Maxwellian velocity distribution. The use of coronal model is denied when collisional processes are also significant in de populating the levels compared to radiative processes.

1.8.4 Collisional radiative equilibrium (CRE)

The deviation from LTE occurs when the radiative processes are not negligible, plasma is non-Maxwellian, or due to some unbalanced processes. It is the most general approach to plasma kinetics. In this model, detailed atomic model is required. It includes the rate of all collisional and radiative processes to find the population of atoms. One should choose important atomic processes and level of accuracy according to the particular problem to be solved. In this thesis, atomic calculations are made by using the code FLYCHK [27] based on CR modeling. It approaches to LTE in case of high density and to coronal model in case of low density.

The photons emitted in the plasma propagates through plasma before getting reabsorbed in other regions or escaping through the plasma. If the plasma has a substantial physical extent or if plasma has absorption coefficient at frequency of the emitted radiation, then the plasma is considered to be optical thick. In this case the equation of radiative transfer need to include radiative rate coefficients. The radiative transport equation need population distribution which is calculated by rate equations. In CR model, CR equations and radiative transfer equations need to be solved self-consistently.

1.9 Laser produced plasma as an ion source

Being an excellent source of X-rays, the LPP is an excellent source of energetic ions as well. The radiation processes in plasma are closely related to the motion of ions and electrons as well as the processes involved for energy transport. The ions in plasma is of different charge states and have a range energy keV to MeV. The plasma produced by laser has more density near the surface of target known as Knudsen layer. Within this layer, higher ionization states are generated by collision of ions with each other and thermodynamic expansion of plasma starts and this expanding plasma consists of large number of transient species such as ions, electrons, neutral particles and emits intense radiation from visible to X-rays. In the high-density zone, plasma density is too high and rate of recombination is reasonable. The charge states leaving this zone by thermal expansion and charge separation mechanism is said to be frozen [28]. When plasma expands adiabatically, the recombination rate is enhanced due to plasma cooling. A critical recombination zone is formed, length of which is measured by critical distance [29] given by

$$L_{cr} \approx T_e^{13/12} v^{14/16} \tau_l^{13/6} / n_{cr}^{8/18} d^{8/6} \qquad (1.28)$$

where, T_e, υ, τ_l,n_{cr} and $d$electron temperature, ion velocity, laser pulse duration, critical density and focus spot size respectively.

The acceleration of ions from the plasma can be described by various phenomenon (contaminants on target surface, hot electrons, charge separation) but the most dominating mechanism is the charge separation. The electrons being the lightest species acquire very high thermal velocity while interacting with laser pulse and escape from plasma. The charge separation between ions and electrons results in an electrostatic field which accelerates the ions to very high velocities and hence higher energies. In case of **long pulse** laser, these ions contribute as thermal ions as they are produced by thermal electrons. There are fast ions also which are attributed to the hot electrons present in plasma. But their flux is small in case of long pulse laser. In case of **ultrashort** lasers, the credit of charge separation goes to hot electrons which are abundant in this case and hence ions get energy up to 10’s of MeV. The energy of the ions depends upon the laser and target parameters. As discussed earlier, the plasma plume formed by laser light expands in vacuum due to presence of pressure gradient. This pressure gradient is closely related to the laser spatial profile. The preferential direction of plasma emission is along the target normal. The final distribution of kinetic energies of ions in vacuum follows a shifted Maxwell-Boltzmann-Coulomb distribution [30].The shift is due to the acceleration produced by charge separation.

At higher laser intensities (>10^{16} W/cm^2), the strong pondermotive force gives rise to plasma wake field acceleration and target normal sheath acceleration mechanism generating electron beam with energy up to GeV range. These table top laser accelerator is a hot topic of research in today’s age.

1.10 Foams

Porous material consists of randomly distributed solid fibers or membranes of very small sizes of the order of few microns to few hundred microns and the size of the pores also lie in this range. These low-density foam targets are randomized 3D network of solid fibers. The size and separation of the fibers depends upon the density of foam targets. The density lies between few mg/cc to few hundred mg/cc. There are many types of foam available for studies of laser plasma interaction. The difference in these is due to size of fibers and pores.

1.10.1 Types of foams

1.10.1.1 Low Z and high Z foams

Depending upon the size of pores, the foams can be divided into two categories- large pore foams and small pore foams [31], [32]. The large pore foams consists of porous plastics ($[CH]_n$, $[CH_2]_n$), porous Beryllium and agar-agar ($C_{12}H_{18}O_9$) with pore sizes 30-100 μm and solid fibers with thickness ranging from 0.1-1 μm. The small pore foams accompany cellulose triacetate ($C_{12}H_{16}O_8$) and trimethylolpropanetriacrylate ($C_{15}H_{20}O_6$) with pore sizes 1-10 μm and solid fibers with thickness ranging from 0.01-0.1 μm. The high Z foams are useful for high density compression and high temperature heating of plasma. They are used in hohlraum design in indirect derive ICF. The examples include SnO_2, TaO_2 and Gold foams etc.

1.10.1.2 Silica aerogel

An aerogel is an open-celled mesoporous (pores ranging from 2-50 nm in diameter) solid that is composed of a network of interconnected nano-structures and that exhibits a porosity (non-solid volume) of no less than 50%. Silica gels are composed of two components- a solid, nanoporous silica-based framework which gives the gel its rigidity and solid foam. Another component is liquid. Silica gels are produced by sol-gel process, in which nanoparticles suspended in a liquid solution (a sol) are invoked to interconnect and foam a continuous, porous, nanostructures network of particles across the volume of the liquid medium (gel) [33]–[35].

Further details of the targets are given in the relevant chapters where details of experimental studies of these targets are discussed. The peculiar behavior of foam targets while interacting with laser increase their interest in this field. These targets play a major role in inertial confinement fusion in the suppression of hydrodynamics instabilities during the compression of capsules, shock pressure amplification and homogenization of X-rays.

1.10.2 Laser interaction with foam targets

The interaction of laser pulse with foam targets is different in comparison to interaction with solid targets. The random distribution of density leads to behavior in case of foam targets. The interaction of laser with foam targets can be explained by following steps

The process of homogenization

Due to the random distribution of the solid fibers in foam targets, the laser interacts with stochastically distributed density. When laser hits the solid fibers, it gets reflected in random directions due to random orientation of solids. The laser light reaches the regions which are not possible if laser hits directly to homogeneous targets. The solid components of foam are heated and spread in the nearby cavities. Because of this internal evaporation, the depth of the region of interaction of laser beam with porous material will change from the initial geometric opacity length which would governed by solid components and their distribution in materials. This will attain some final value which depends on the dynamics of internal evaporation of the material and resultant plasma. The disintegration of solid components in the surrounding cavity by internal evaporation continues until the material become fully homogeneous. The homogeneous medium has density equal to the average density of material [36]–[38].

This process ends after a time $t_{fast} \sim \frac{\delta_0}{V_i}$ where δ_0 is the pore size and V_i is the velocity of expansion equals to speed of ions. This leads to the size of denser regions greater than b_o but density is less than solid density. After this, the collision of plasma fluxes coming from different directions takes place which leads to dissipation of shock wave. This is slow process and result in total homogenization of the plasma. The duration is approximately equals to laser pulse duration.

$$t_{slow} \sim \frac{(\delta_o - b_1)^2}{\lambda_i V_i} \tag{1.29}$$

b_1 is the current thickness of the dense matter regions and λ_i is the length of ion-ion collision. The foam can be divided into two categories on the basis of relation of their density with critical density - supercritical and subcritical. In the initial stage of interaction of laser with foam targets, laser can penetrate up to an initial transparency length given by

$$L_o \cong C \left(\frac{\rho_s}{\rho_a}\right)^{1/5} \delta_o \tag{1.30}$$

where, δ_o is the pore size, the constant C equals to $\pi^2/2$ for hair-like and $\pi/2$ for film- like structure material. In the starting of interaction, the laser faces the two types of regions, one with density greater than critical one (solid fibers) and one with density lower than critical one (pores). The laser beam deeply penetrates the structured material as it would in case of targets with homogeneous densities. But after the homogenization of the targets, the penetration depth of laser changes according to subcritical and super critical foam targets. In the case of supercritical foam, after full homogenization i.e. after filling of the pores by the expansion of heated solid fibers, situation is same as if laser has to interact with homogeneous material having same average density. The laser will interact with the hydro dynamically expand plasma and can penetrate up to critical density only. The inner regions get heated by thermal conduction or shock wave.

But in the case of subcritical foam targets, after the full homogenization the density of the foam is still less than the critical density and laser light can penetrate further into the foam which are in cold state, here the homogenization process starts again. The time needed for full homogenization in case of sub critical foam targets is longer than the time to reach critical density. However, situation is different in case of super critical foam targets.

1.10.3 Applications of foam targets

As discussed in previous section, the property of high efficiency of absorption of laser pulse in foam targets makes them special in field of LPI [39], [40]. Another application includes

1 Increase of the ablation pressure

2 High velocity in absorbed energy transfer

3 Smoothening action of radiation inhomogeneity

The foam layer smoothens the irradiance inhomogeneities further preventing any instabilities to grow. Foam layer is used in the formation of outer layer of spherical shell of Inertial Confinement Fusion (ICF) targets. This would reduce the requirement of number of laser beams to avoid the Rayleigh Taylor instabilities which will otherwise degrade the ignition process. Also, because of higher ablation pressure, the further compression and heating of the thermonuclear fuel takes place in comparison to bare ablator layer. Unlike in the solid target where laser can penetrate up to critical surface only, in the case of foam even with super critical density the laser has the chance to penetrate deeply into the target which will result in higher ablation pressure.

1.11 Summary

As the thesis is based on experimental studies on X-ray and ion emission from laser produced plasma. The basics of laser plasma are discussed in this chapter. Starting with a brief introduction about plasma with its properties, the laser plasma interaction is discussed with different processes of laser absorption. The production mechanism of X-rays and ions, their characteristics is given. The knowledge of the different atomic processes in plasma and equilibrium models is essential for doing spectroscopic studies. In the end, foam targets, types, application and their laser-foam interaction is discussed.

1.12 Motivation and objective of present thesis

The role of above discussed laser-plasma X-rays sources in ICF is most important. In indirect drive ICF scheme, X-rays are not only used for diagnostic purpose but also contribute to reach the ignition conditions [41]. In this process, the fusion capsules are kept in hohlraum made up of high Z materials. The fusion capsules are not directly heated by the hohlraum but by the X-rays produced from heating up of hohlraum after irradiation with laser. This results in homogeneous heating of capsules. The burning core of an Inertial Confinement Fusion (ICF) plasma produces bright X-ray source which is useful in the diagnosis of core conditions essential for comparison to simulations and understanding fusion yields. These X-rays also backlight the surrounding shell of warm, dense matter, whose properties are critical to understanding the efficacy of the inertial confinement and global morphology [42], [43]. Analysis of the absorption and fluorescence spectra of mid-Z impurities or dopants in the warm dense shell facilitate in revealing the optical depth, temperature, and density of the shell [44]. In addition, structural dynamics of crystalline materials can be accomplished by time resolved ultrafast X-ray diffraction and absorption techniques with resolution of the order of sub-picosecond and sub-Angstrom. These table top X-ray sources facilitated the absorption spectroscopy of chemical and biological processes occurring in non-crystalline phases in laboratory setting in contrast to large synchrotron sources. The generation of synchrotron-like X-ray radiation via Betatron radiation from laser wakefield accelerators gives rise to X-ray free electron laser. They are used for radiography of dynamic shock in high energy density experiments. Synchrotron light sources produce monochromatic or broadband pulses of duration tens to 100 picoseconds with peak brightness of order 10^{23} photons/s/mm^2/mrad^2/0.1%BW. XFELs produce monochromatic pulses with a duration of few 10's femtoseconds with a brightness of 10^{30}-10^{34} photons/s/mm^2/mrad^2/0.1%BW [45]. The table top laser accelerators scaled down the size of huge accelerators. This laser produced plasma based heavy ion source has become one of the most useful front end in the heavy ion accelerators for example in Large Hydron Collider (LHC) at CERN and has applications in various fields such as cancer therapy [46], proton radiography [47], ion-driven fast ignition [48], laser mass spectroscopy, material modification , ion implantation.

The purpose of this thesis is the optimization of these lasers driven X-ray and ion sources which is essential for using them in variety of applications. The diagnosis of plasma properties such as plasma temperature, density and ionization distribution of highly charged states using K- and L-shell X-ray spectrum from mid and high-Z metals. The distribution of kinetic energy of ablated species affects the deposited film quality, substrate property and particle beam unity in applications such as thin film deposition, ion implantation and ion accelerators. The knowledge of angular distribution of velocities and flux of different charge states of ions is essential for the study of dynamic expansion of plasma plume from the target surface. The ions can be treated as finger prints of the expanding plasma plume in vacuum. The observation of ion along with X-rays helps in providing clear understanding of the laser plasma interaction. The other main objective of the thesis is to study laser interaction with low density foam targets. The applications and importance of these low-density foam targets is already described in above sections. The objective includes the comparison of X-ray yields, ion yields for different density of the foam and with solids, distribution of ions energies and flux in different directions from plasma corona as a function of density. To achieve these objectives, different X-ray and ion diagnostics are used for example flat crystal spectrometer to observe spectral lines, X-ray streak camera to see X-ray time profile, ion collectors at different angles for capturing hydrodynamic motions of ions, Thomson parabola spectrometer to study energy and flux distribution of individual charge states, shadowgraphy to observe plasma expansion dynamics as well as volumetric absorption.

Chapter 2

Experimental Tools and Techniques

2.1 Introduction

As discussed earlier, the studies of laser plasma interaction play a key role in several applications. The laser plasma interaction (LPI) can be explored by experimental, simulation or analytic approach. The later methods help for interpretation of the experimental data in order to understand the physical phenomenon in LPI. So, the three branches should run hand in hand in order to reach on proper conclusions. The laser produced plasma consists of electrons, ions and neutral particles. The interaction of these particles with the laser pulse and with each other makes laser plasma a very rich source of information from geophysics to astrophysical information. This information can be obtained experimentally using three main components, i.e., Laser, target and diagnostics. The plasma is created by irradiating the laser on target surface. The information of the ongoing processes in the plasma can be extracted with the help of very fast detectors because the ongoing processes are very fast and short lived. Simultaneous recording of the different processes facilitates in understanding the collective nature of these processes. The studies of ions and X-rays are not independent of each other. The simultaneous investigation of both is required for better understanding of the scenario of laser plasma interaction. Very fast X-ray and ion diagnostics are used for carrying out the work presented in the thesis. This chapter dedicated to provide the details about laser systems and the advanced diagnostics for accomplishment of X-ray and ion emission studies. The further detail of the experimental setup is provided along with the results at the appropriate places in the following chapters.

2.2 Laser systems

The first chapter explains the need of a high-power laser to produce highly dense and hot plasma. This results in the development of multigiggawatt to petawatt laser systems. The biggest laser systems in the world involve NIF, USA; NOVA, LLNL; GEKKO, Japan; VULCAAN, Rutherford, UK and L3-HAPLS, ELI beamlines, Europe. Apart from these MJ laser systems, several KJ laser systems are available across the world.

2.2.1 Nd: Glass 500 ps/30 J laser system

Most of the present studies are carried out using Nd: Glass laser system having 30 J/ 500 ps with focused intensity in the range 10^{13}-10^{15} W/cm^2. The laser system consists of commercial laser oscillator [Model SL 312 TE] with a preamplifier capable of delivering 100 mJ energy per pulse. The master oscillator involves a flash lamp pumped Nd: YAG rod which generates an output pulse of 4-5 mJ/3ns with single longitudinal mode selection. The TEM_{00} mode is selected by an inter-cavity aperture and a Pockel's cell is used for Q switching the laser pulse. The Q-switched pulse is then passed through compression system. The compression system consists of two lenses, a quarter wave plate, SBS-cell with CCl_4 liquid and a polarizer. The duration of the pulse is reduced to 300-800 ps duration which further depends upon the focusing geometry of the lens. The pulse is then propagated through a pre-amplifier and double pass amplifier. The final pulse repetition rate is 10 Hz with a peak to background contrast of 10^5:1. The oscillator is made to work in single shot mode and is synchronized with five in-house developed amplifiers using a fast-synchronized circuit. The amplifier unit consists of two 19×300 mm glass rods pumped by six xenon filled flash lamps, two 38×300 mm and one

50×300 mm glass rods pumped with twelve flash lamps and one 75mm×300 mm amplifier pumped by 18 flash lamps. The glass rods are designed in such a way that the diameter keeps on increasing to maintain the laser light intensity below the damage threshold limit of Nd: Glass rods and optics used. The spatial filters are used to remove non-uniformity and laser beam magnification. Two Faraday isolators are used to protect any back reflection from plasma which can damage the optics and the laser oscillator. The diameter of the beam is 75 mm after the amplifiers chain which is then focused to 100 μm at the surface of the target using f/5 lens. The schematic of the laser system is shown in Figure 2.1. For more detail of the laser system; readers are referred to [49].

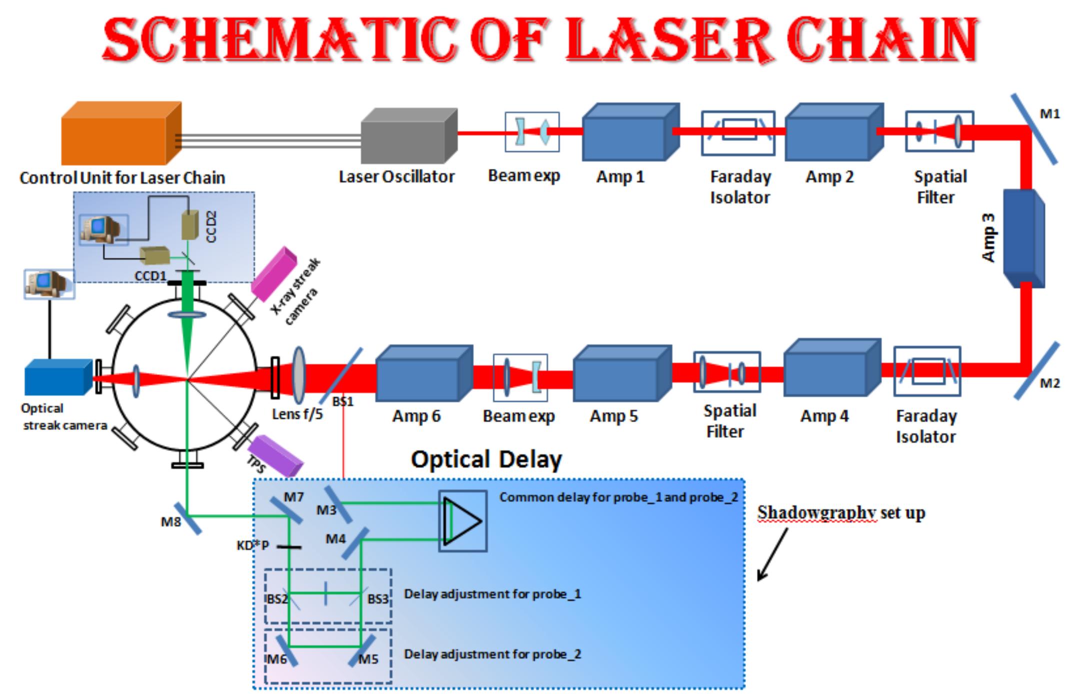

Figure 2.1 *Schematic of laser chain with experimental chamber.*

2.2.2 100 TW Ti: Sapphire Laser system

The 100 TW/800 nm/25 fs laser system is available at TIFR, Mumbai [50].The laser system is Chirped Pulsed Amplification (CPA) based Ti: Sapphire with peak power of 100 TW at 10 Hz repetition rate. The laser system is commercially bought from the Amplitude Technologies$_{TM}$. The main components are the femtosecond oscillator, a booster, a REGEN, 10 Hz multipass amplifiers and a compressor. The laser beam was focussed by off-axis parabolic mirror (OPA) to a spot size of 20 μm and peak intensity of 10^{19} W/cm^2. The output from the oscillator is amplified to microjoule level by the booster which uses a compact multipass amplifier. The saturable absorber cleans the pulse by removing the ASE background before seeding to the stretcher. This system also has acousto-optic programmable gain control filters, which prevent gain narrowing and bandwidth reduction. A stretched pulse with energy 1 mJ at 10 Hz is produced by the first amplification stage, the REGEN. The two Pockel cells are used for this purpose; one allows the stretched seed into the REGEN, other dumps out the pulse to the amplifiers. The first multipass amplifier (pre-amplifier) is pumped by 2 J Nd: YAG laser at 532 nm, whereas, the second multipass amplifier (main amplifier) is pumped by 8 J laser. Due to heavy pumping, the Ti: Sapphire crystal in the amplifier is cooled cryogenically to avoid any non-linearity due to thermal loading.

2.3 Vacuum chamber

The vacuum chamber for Nd: Glass laser is cylindrical in shape and semi spherical from the top with length and diameter of 800 and 600 mm, respectively. The target is placed at the center of the chamber. The target is put on a motorized stage with a control pad outside the chamber so that fresh position would be available for every shot. The target area is shown in

Figure 2.2. There are total 41 ports in the chamber and all are usable. Thus, the chamber has the highest degree of accessibility for different diagnostics. The chamber is evacuated up to a vacuum of 10^{-6} mbar.

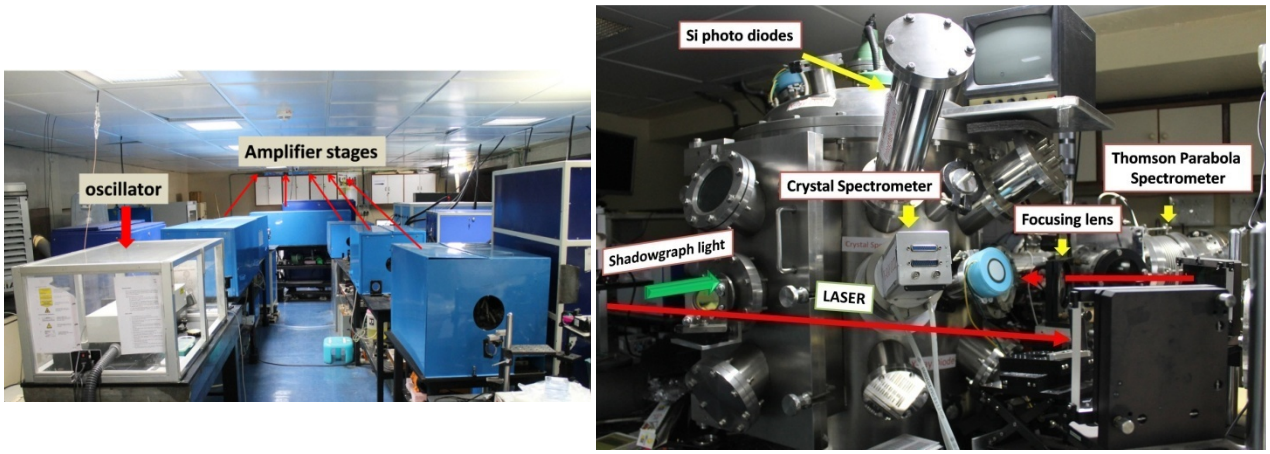

Figure 2.2 *Picture of Laser chain and vacuum chamber with diagnostics*.

2.4 X-ray diagnostics

As soon as the plasma becomes fully ionized, broad bremmstrahlung and line emission starts because of the electron-ion interactions in the hot dense plasma and transitions in atomic orbital of higher charged ions, respectively. The spatial, spectral and temporal resolution of the emitted radiation can be performed with the help of different diagnostics. The soft X-rays in the range of few hundred eV and hard X-rays are very important for biological imaging and in improving contrast and spatial resolution. The soft and hard X-ray emission can be recorded using photo diodes. The time resolved studies are important for measuring the X-ray pulse width and dynamic information of time varying hydrodynamics and radiative processes in plasma. Streak cameras can perform the time resolution of these fast processes. For recording the bound-bound transitions, spectral resolution of the signal is required; crystal or gratings are the suitable candidates for this. The details of all the diagnostics used are provided below

2.4.1 Inversion layer Si photodiodes (XUV-100)

This unique class of silicon photo diodes provides a wide range of sensitivity from 6 eV to 17,600 eV. One electron hole pair is created per 3.63 eV of incident energy corresponding to extremely high conversion efficiency of E_{ph}/3.63 eV. The design includes single channel as well as four channel arrays of detector to cover wide range of X-rays. The four-channel detector is mounted on S.S. flange of diameter 135 mm connected with the BNC feed-through which are then connected to the output unit. The detector is inversion type with an effective area of 100 mm^2 and is unbiased. A pre-amplifier is attached for better signal. For avoiding impedance mismatch, a buffer is connected at the output circuitry. The reverse bias is applied to reduce the capacitance (C_F) and to increase signal to noise ratio. The output efficiency (V_{out}) is proportional to the incident radiation power as

$$V_{out} = Q/_{C_F} \tag{2.1}$$

where, Q denotes the charge created by one photon.

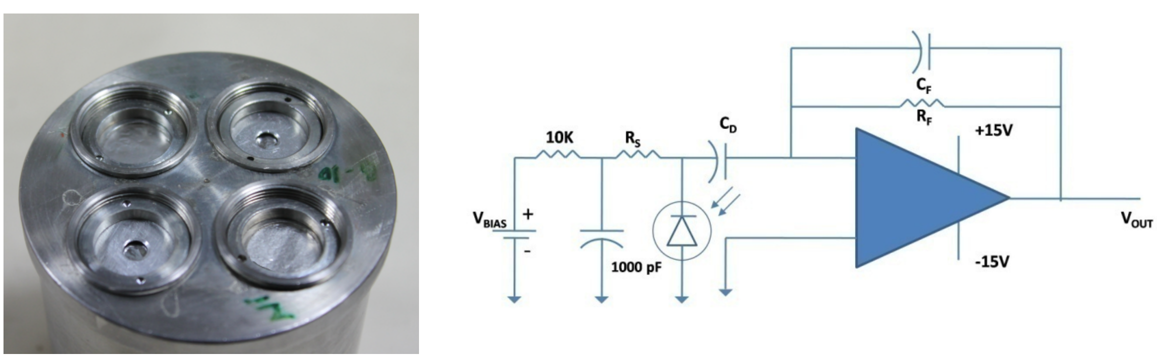

Figure 2.3 *(a) Photo of Silicon photodiodes covered with different filters (b) schematic of photodiode.*

All the components are enclosed in a metal box to achieve EMI resistance and to avoid electromagnetic noise. The biasing is supplied through DC power supply. The detector operates in integration mode and its sensitivity can be changed by changing the capacitance in the circuit as it can be seen from Eq. (2.1).

2.4.2 X-ray crystal spectrometer and alignment

The laser-plasma is a rich source of line emission due to the presence of highly charged ions. The line emission can originate from K-, L- and M-shell of these ions. The crystal spectrometers are widely used for the line emission studies. In spite of small wavelength range (4-12 Å), they are the first choice of experimentalist due to very high resolution. The crystal spectrometer was coupled with CCD cameras in conjunction with micro channel plates (MCP). This geometry requires a very high vacuum ($\leq 10^{-5}$ mbar) environment. We used a planar crystal spectrometer for the measurement of line spectrum. It is the simplest form all spectrographs for the dispersion of soft X-rays produced from laser-plasma. It uses a flat crystal of Thallium Acid Phthalate (TAP) for the Bragg reflection. The Bragg angle depends upon the position of crystal and plasma source. The polychromatic X-rays from LPP subtend different angle on the crystal at different points which are reflected by crystal in accordance with Bragg condition i.e. $2d\sin\theta=n\lambda$. The reflected X-rays are recorded by X-ray detectors such as X-ray CCD camera, Image intensifier or X-ray streak camera. When the X-ray source is a point source and collimated, the X-ray spectrum can be recorded by moving crystal up and down using motorized translation stage. However, in laser produced plasma, the plasma expands spherically which subtends a range of angles at different positions on the crystals. The wavelengths satisfying Bragg's condition results in a spectrally dispersed spectrum on detector plane (X-ray CCD). If θ_1 and θ_2 are angles subtended by X-rays at either ends of the crystal, then according to Bragg's law we will get minimum and maximum wavelengths given by

$$\lambda_1 = 2dsin\theta_1 \tag{2.2}$$

$$\lambda_2 = 2dsin\theta_2 \tag{2.3}$$

These wavelengths can be written as follow in terms of geometric parameters

$$\lambda_1 = 2d(2h + x_0)/[(2h + x_0)^2 + L^2]^{1/2} \tag{2.4}$$

$$\lambda_2 = 2d(2h - x_0)/[(2h - x_0)^2 + L^2]^{1/2} \tag{2.5}$$

where $2x_0$ is the difference between wavelenghts, *h* is vertical height of plasma source with respect to crystal, *L/2* is the horizontal distance between plasma source and centre of crystal (*L* is the distance between source and detector) as shown in Figure 2.4. The spectral resolution of crystal spectrometer can be written as

$$\Delta\lambda = \frac{2d}{[1+(2h/L)^2]^{1/2}}[\delta\theta + \delta x/L[1 + ({}^{2h}/_{L})^2] \tag{2.6}$$

where, $\Delta\lambda$ is the wavelength interval covered by ideally monochromatic X-rays from the plasma source. The first term in square bracket is the crystal dependent term (rocking curve) which is 0.45 mrad for TAP crystal at 8Å and second term depends on source and detector's characteristics.

The spectrum resolution of crystal depends on the source size, distance between source and detector and the rocking angle of the crystal. Therefore, for a fixed focal spot diameter (fixed source size) if we increase distance between source and detector, resolution of the spectrometer will increase linearly with distance however, at the same time X-ray flux reduces according to $1/L^2$. Optimization of the X-ray flux and distance between source and detector is necessary. The spectral range covered for a particular position of crystal will be reduced. In our experiment, we modified our experimental chamber and adjusted the distance between the source and detector to obtain a higher resolution for the study of a strong X-ray flux from LPP. For flexibility in covered spectrum range, we have mounted our target on motorized Z-stage. Spectral range can be varied by changing the vertical distance between plasma source and crystal, though spectral range covered for a single setting is less than 1Å. The (001) plane of the TAP crystal is used with size 50 x 10 mm^2, thickness of 2 mm, 2d spacing of 25.75 Å. The crystal housing is placed at 45º to the target normal. The crystal was kept at a distance of 17.5 cm from the target. The source to detector distance is 35.0 cm. The detector unit was mounted on a flange having a taper angle of 15^o and was connected to the port of vacuum chamber. The recording unit comprises of either P-11 phosphor screen followed by image intensifier tube and then CCD camera with KF 50 flange or X-ray CCD camera.

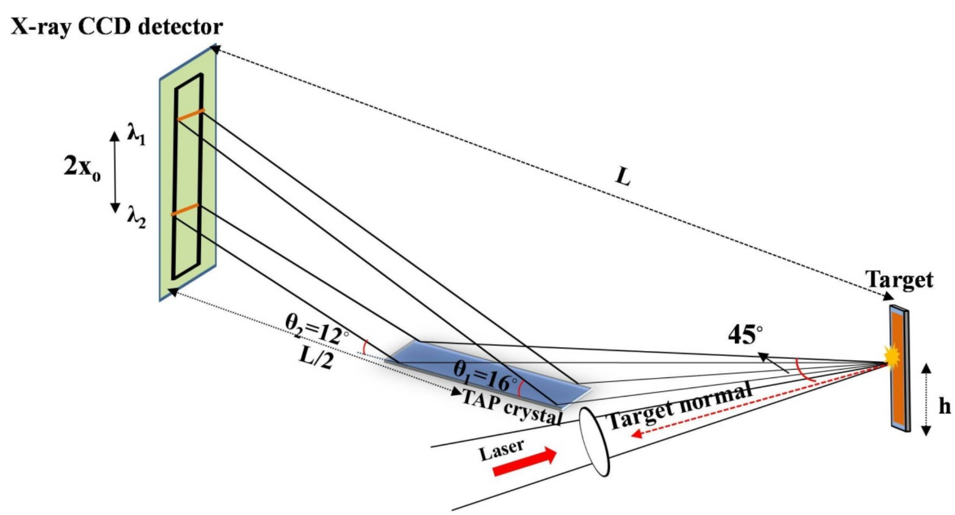

Figure 2.4: *Schematic of the crystal spectrometer. The crystal is at 45° with respect to the target normal. The laser axis coincides with the target normal.*

2.4.3 X-ray streak camera

The interaction of laser with plasma and the processes involved therein are very fast. The change in plasma properties takes place in less than picoseconds duration. There is a huge temperature and density gradient with respect to space as well as with time while interacting with sub ns laser. Thus, the X-ray emission is not independent of time. To get a better understanding of ultrafast processes in LPP and to perform time resolved imaging of phenomenon, the time resolved studies are very useful. The streak cameras provide the information of intensity, spacing and timing of the observed phenomenon. The photons of different energies hit the photo-cathode which converts them into electrons. These electrons enter a ramp voltage circuit. The electrons which arrive early will feel a less deflection than the electrons which arrive later due rising voltage with times in ramp circuit. In this way, the signal is resolved with respect to time. These electrons pass through micro channel plate, get multiplied and finally hit phosphor screen at the output side of the MCP where these electrons will again convert into photons and captured by CCD camera. The photo and block diagram of the streak camera is shown in Figure 2.5. The camera can record and measure spatial-temporal parameters of ongoing fast-running processes in the field of soft X-ray radiation in a single-frame mode as well as in streak mode of sweeping. The image formed at the camera output is recorded with the help of a CCD readout unit and is stored into a personal computer.

The CCD readout unit has two modes for image recording, namely continuous and waiting according to STAT and DYN modes of X-ray camera operation. A photosensitive working area of changeable slit Au and CsI photo cathodes is a narrow strip with a 0.1 mm width and a length somewhat greater than 15 mm that in one case is deposited on a very thin substrate from nitrocellulose (parylene) and in the other case is deposited on a substrate from beryllium foil of a 15 μm thickness. Both substrates are transparent for soft X-rays.

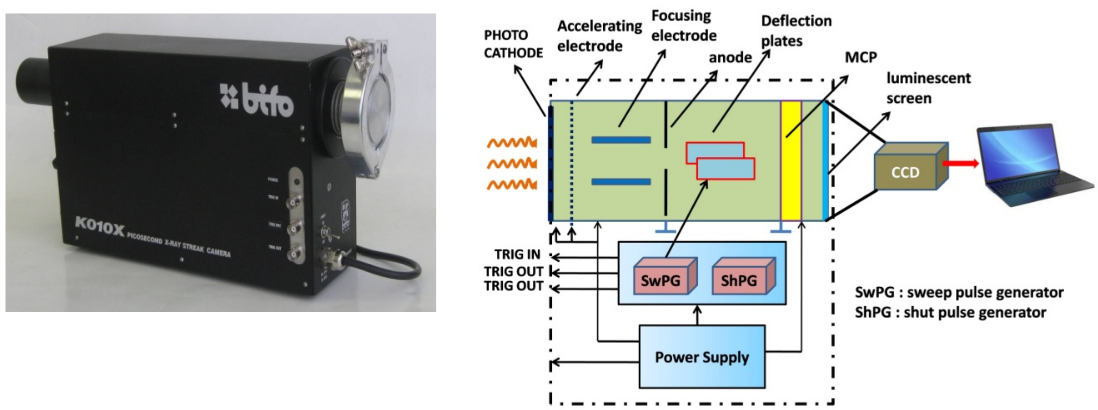

Figure 2.5 *(a) Photograph of X-ray streak camera (b) schematic of streak camera*

2.4.3.1 Calibration of X-ray streak camera

The calibration and description of sweep speed of the X-ray streak camera are very important to accurately record the transient phenomenon. The delay between the arrival of laser pulse and triggering of camera should be adjusted. The sweep coefficients are selected according to the life time of the phenomenon which is going to be recorded and any non-linearity in sweep should be removed. The lifetime of the phenomenon is a consequence of pulse duration of the X-ray emitted of laser plasma. The pulse duration is roughly equal to the laser pulse duration, but in case of the long scale length plasma, the plasma would not die even after switching off the laser pulse due to the interactions taking place in plasma corona region. In the output of the streak camera, the horizontal axis provides the time axis (in ps) and vertical axis provides the spatial resolution. The flux of X-ray is determined by the z-axis i.e. from the pixel values. The X-ray streak camera is placed at an angle of 22.5º from the target normal. A B-10 filter is placed in front of the camera to allow X-rays of energy >0.8 keV. During calibration of the camera, the gain and delay is adjusted for every sweep. All the calibrations are performed at the oscillator energy of the laser (150 mJ). The camera needs to be trigger prior to the event to record the complete information during laser plasma interaction. First the delay between the laser pulse and triggering of streak camera is adjusted with the help of delay generator. Keeping the camera in the streak mode with microsecond sweep stage, the tuning of delay is performed by changing DL so that the X-ray streak is appeared on the screen. The delay is adjusted for every sweep coefficient. The sweep of 3 ns/cm is found to be sufficient in our case. These calibrations are performed at the oscillator energy, the intensity of laser and hence X-rays flux is low. So, the adjustment of the gain has set while performing actual experiments at higher intensities of the laser. For getting the temporal information from the streak image, the pixels should be converted into time according to sweep stage. The pixel to time conversion factor has provided by the manufactures. This factor has also calibrated to reduce any non-linearity. For this, the laser is divided into two pulses. The optical delay is provided between these pulses which are calculated by MHz oscilloscope. These pulses are recorded by X-ray streak camera and the delay is calculated between the peak of the streak appeared on the screen. The final correction is made for every reading.

The streak camera is optimized in framing mode by taking the radiograph of SS mesh of known diameter and spacing between the wires as shown in Figure 2.6(a). The spatial resolution of the camera is ~50 μm and the temporal resolution can be by adjusting high voltage time width and delay between event and the trigger time of the streak time. The magnification of the framing camera depends on the ratio of the distance between detector to object and source to object. Figure 2.6(b) and 2.6(c) are showing the X-ray imaging of fruit fly at two different magnification. The fly is kept between the layers of B-10 filter before the photo cathode.

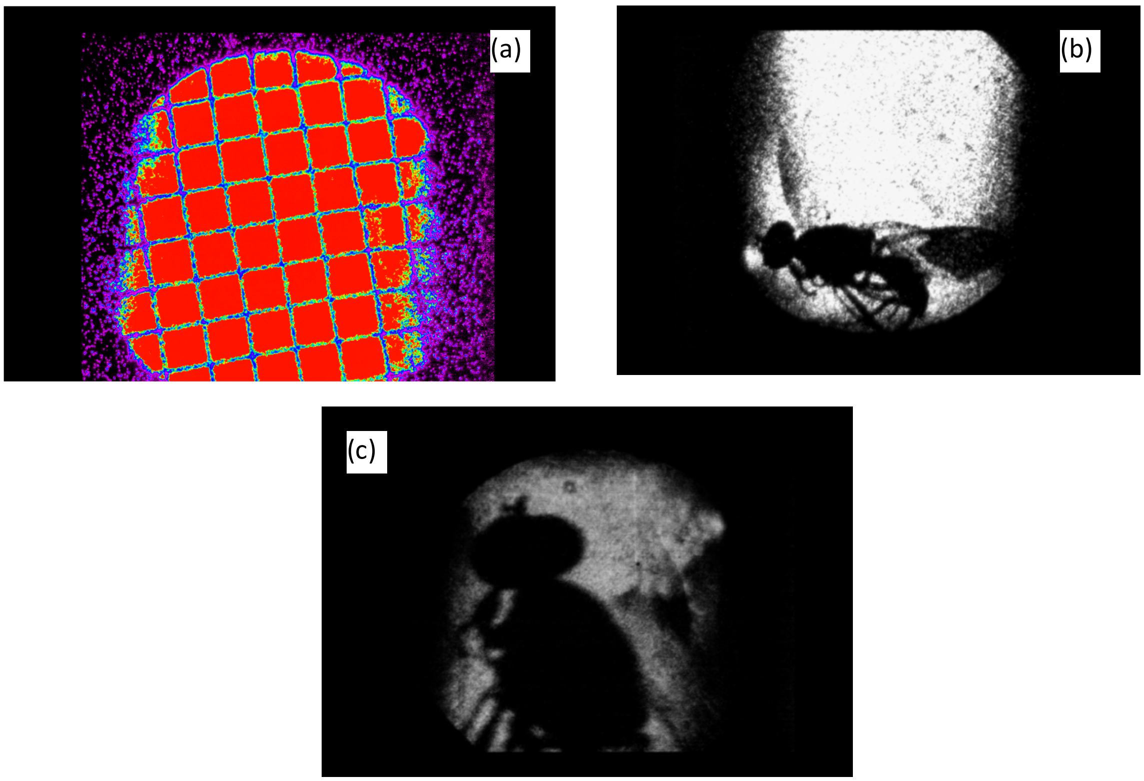

Figure 2.6 *Radiograph of the (a) the SS mesh and fruit fly with magnification (b) ×0.3 (c) ×1.5*

2.4.4 NaI detector

For the measurement of hard X-rays, NaI detector is used. The detector consisting of NaI crystal with photo multiplier tube is placed outside the vacuum chamber and covered with lead shield to avoid the pile-up. When the high-energy photon is incident on the detector, the electrons knock out to provide the output signal. Pile up is caused when more than one photon is incident on the detector surface but it records it as one photon with higher energy.

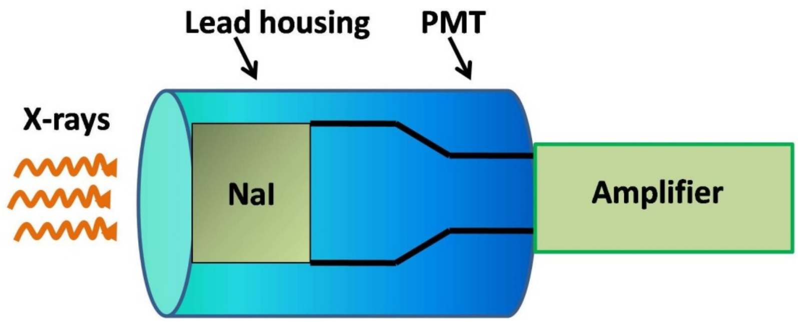

Figure 2.7 *Schematic of NaI detector*

To avoid this, a 5 mm diameter aperture is situated prior to NaI crystal which helps in receiving less than one photon per laser shot. The count rate is reduced to 0.1 counts/ per pulse. The detector is biased with 750 V dc power supply. The output signal of the NaI is fed to the amplifier. The schematic of the NaI detector head is shown in Figure 2.7.

2.5 Ion diagnostics

Ion emission studies including evolution of ions in vacuum from target surface, energy distribution of ions, average and maximum charge states, abundance of ions species play a key role in better understanding of processes involved in laser plasma interaction. For the present thesis work, two main ion diagnostics are used, i.e., Faraday collectors and Thomson Parabola Spectrometer. The details of these diagnostics are presented below

2.5.1 Faraday Cup (Ion collector)

The Faraday cup consists of a conducting metallic disc, which accepts anion beam. The ions are converted into a proportional voltage. The schematic of ion collector is shown in Figure

2.8. Our ion collector is the simplest and most common type of probe with a plane collector and a grid for ion and electron separation. The separation is done by means of a static field that exists between the grounded grid and the biased (negative) collector, which will solve the problem of the contribution of secondary electron emission. The large area Faraday cup can be placed far away from the target to give better resolution. The grid also separates primary electrons from the ions to be measured. The transparency(ε) of the grid is 60 %. The ion collector signal can be written as

$$I_{coll}(t) = \frac{U_c(t)}{\left\{\varepsilon R_{load}\left[1+\frac{\overline{\gamma}(t)}{\bar{z}(t)}\right]\right\}} = \frac{ed[N(t)\bar{z}(t)]}{\bar{z}(t)} \tag{2.7}$$

where $U_c(t)$ is the voltage amplitude of the collector signal on oscilloscope, $N(t)$ is the number of ions reaching the charge collector and R_{load} is the load resistance, ε is transparency of entrance grid. $\bar{\gamma} = \frac{\sum_i \gamma_i n_{i,j}}{\sum_j n_{i,j}}$ and $\bar{z} = \frac{\sum_i z_i n_{i,j}}{\sum_j n_{i,j}}$ are the average secondary ion electron emission coefficient in the entrance grid for a given moment.

The time distribution of ion charge Q can be written as

$$\frac{dQ}{dt} = \frac{ed[N(t)\bar{z}(t)]}{dt} \rightarrow I_{coll}(t) = \frac{U_c(t)}{\left\{\varepsilon R_{load}\left[1+\frac{\overline{\gamma}(t)}{\bar{z}(t)}\right]\right\}} \tag{2.8}$$

The factor $\left[1+\frac{\overline{\gamma}(t)}{\bar{z}(t)}\right]$ = 1.5 for v =7 ×10^6 cm/sec),

= 1.0 for v>1×10^7 cm/sec,

and = 0.5 for intermediate velocity,

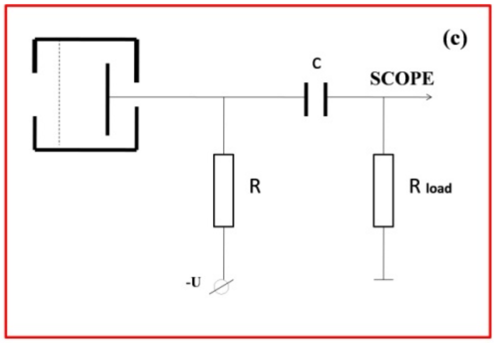

Figure 2.8 *Schematic of Ion collector*

2.5.2 Thomson Parabola Spectrometer (TPS)

The ion collectors with Time-of-Flight (TOF) will provide information about the energy of the integrated charge states of ions according to arrival time of ions. From laser produced plasmas, we have ions of various charge states having a broad range of energy. Charge resolved measurements can be possible if energy spread of the ions is smaller than the extraction fields. The most powerful alternative tool is Thomson Parabola Spectrometer to separate the charge particles according to their mass, charge and momentum.

2.5.2.1 Working principle of Thomson Parabola

Single field (either electric or magnetic field) would not be able to provide the charge state distribution with corresponding energy values. The Thomson Parabola is named after J. J. Thomson [51] and is comprises of parallel electric and magnetic fields on a plane perpendicular to the direction of ion beam. The Lorentz force $\vec{F} = q(\vec{E} + \vec{v} \times B)$ deflected the ions in direction parallel to the electric field (E) and perpendicular to the magnetic field (B), where, v is the velocity of ions, q = Ze is the ion charge, Z is ions charge state & e is the electric charge. The deflection caused by both field results into the formation of separate parabola corresponding to each charge state. The ions of single charge state get distributed along the length of the parabola according to their energy.

2.5.2.2 Simulations for design of Thomson Parabola using SIMION 7.0 software

The ion source from laser produced plasma expands in 2π direction with the maximum emission towards the target normal. The Thomson Parabola Spectrometers requires a collimated and very small size ion source for high resolution. For this purpose, a 2 mm aperture of ring type ion collector is used with a pinhole of diameter 150 μm just 2 mm before TPS. The simulations were carried out using SIMION 7.0 software for optimization of experimental parameters. It uses finite difference method to calculate the field values at grid points generated around the electrodes.

(a)

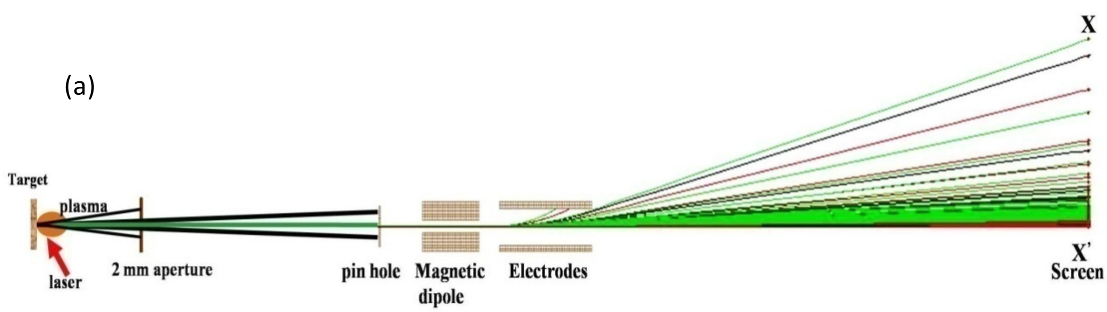

(b)

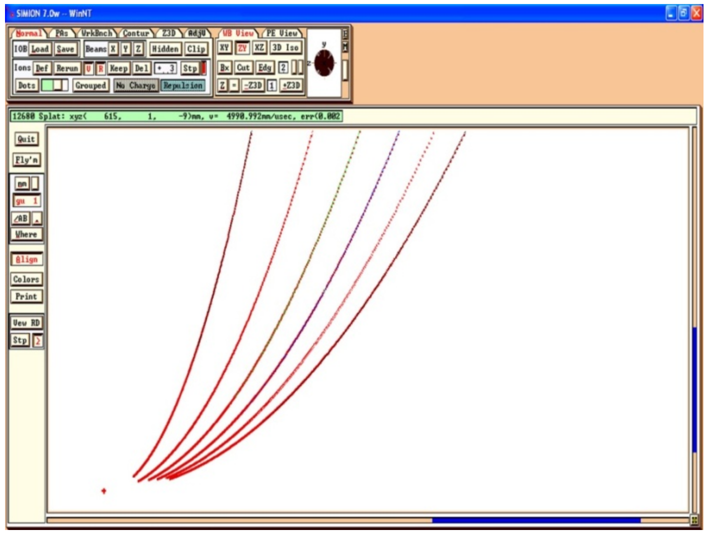

Figure 2.9 *(a) Screen shot of the simulation in SIMION showing the flight paths of ions through magnet and ESA (b) cross section of a plane perpendicular to the ion accelerator direction along xx' showing the profiles of carbon ions.*

First of all, the potential arrays for magnetic and electric field are created. For magnetic field, dipoles of size 50 mm (*l*) × 50 mm (*w*) × 10 mm (*h*) with a pole gap of 6 mm were chosen and for electric field, two rectangular electrodes with dimensions as 80 mm (*l*) × 50 mm (*w*) were used and placed parallel to each other with a gap of around 16 mm. These two arrays are placed on a single optical bench. The directions of the magnetic field and electric field are vertically up and down respectively. These are separated by a distance of 15 mm from each other. In order to select a beam with less divergence, an electrode plate with pinhole (0.15 mm diameter) is placed at 2mm before magnetic dipole.

For each charge state, a different group of ions is created with energy in the range of 3 KeV to 1 MeV. Then these ions were allowed to pass through magnetic and electric field sequentially as shown in the Figure 2.9(a). The trajectories of ions under the effect of electric and magnetic fields were recorded on a screen XX' placed at a distance of 600 mm from pinhole position. The cross-sectional view at the XX' plane gives the parabolic images of the ions for a given charge state is shown in Figure 2.9(b). The final values of magnetic and electric fields are 300 Gauss Tesla and 14000 V/m for carbon ions of charge states C^{1+} to C^{6+} according to the detector size and ion's energy range.

2.5.2.3 Design and development of Thomson Parabola Spectrometer with ion collector spectrometer

An ion spectrometer, composed of a time-of-flight spectrometer (TOFS) and Thomson Parabola Spectrometer (TPS), has been developed [52] to measure energy spectra and the analysis of species by laser-driven ions as shown in Figure 2.11(a) (schematic) and (b) (3D view). Time-of-Flight (TOF) is a tool to measure complete energy spectrum of the ions in a single shot but with poor resolution and unable to separate charge states. TPS have high resolution and capable to resolve all the charge state but having a limitation on measuring the energy spectrum, the constrained being enforced by the detector size. To get the optimum results, the coupling of TOF spectrometer and TPS is useful. We have simultaneously run these two spectrometers (i.e., TPS & TOFS) for the comparison of independent measured data and for taking advantage from each spectrometer. Real-time and shot-to-shot characterizations have been possible with the TOFS, and species of ions can be analyzed with the TPS. The two spectrometers show very good agreement as can be seen from Figure 2.11(c-d). For this purpose, ring type ion collector with 2 mm aperture is placed at the center of the entrance of TPS assembly. When the ion beam passed through this ion collector, the central part of the beam will pass through the aperture and proceed towards TPS and outer part is collected by ion collector. This collector acts as the beam intensity controller and is also used for collimation (ion beam shaping) of the ion beam entering in TPS assembly. Here, the ring ion collector functions as a Faraday cup, with the difference that, it is not completely destructive. The housing of TPS is installed at 45º angle from the target normal. The output assembly consists of MCP and CCD camera connected to PC. The detector is optimized to reduce noise. The deflection of the non-relativistic charge particles under the individual magnetic and electric field is tested which can be written in the form of equation as

$$x(detector) = \alpha \frac{ZeB}{(mE_k)^{1/2}} \text{ and } y(detector) = \beta \frac{ZeV}{E_k} \quad (2.9)$$

The more details can be found in [53]. Eq. 2.9 shows that for a fixed magnetic or electric field, ions of higher charge state and lower kinetic energy will see higher deflection and vice-versa. All ions receive a deflection in a single straight line (as shown in Figure 2.10) in the individual fields which makes the separation impossible. The separation is possible if we use magnetic and electric field simultaneously. The origin has shifted at one end in order to cover a large spectral range on our detector screen. Combining the magnetic and electric fields together results the parabola for each charge state on the detector as shown in Figure 2.10(d) and the equation of parabola can be written as

$$y(detector) = \left[\left(\frac{\beta}{\alpha^2}\right)\left(\frac{m}{Z}\right)\frac{1}{e}\frac{V}{B^2}\right] x^2(detector) \quad (2.10)$$

From the equation, it is inferred that, the ions of identical mass/charge (m/Z) ratios are arranged on the same parabola, for the fixed values of V and B. The points of intersection of parabolas with the line x/y = constant, that is the line passing the origin of the coordinates, correspond to ions of fixed velocity and be written as $v = \sqrt{2}\left({}^{\beta}/_{\alpha}\right)\left({}^{V}/_{B}\right)\left({}^{x}/_{y}\right)$. This velocity is independent of the (m/Z) ratio called as iso-velocity line (shown in Figure 2.11(d), blackline). From Eq. 2.9, we can drive momentum per unit charge and kinetic energy per unit charge can be written as

$$p/_{Z_i} = \sqrt{2\alpha e}\, B/_{x} \qquad \& \; {E_k}/_{Z_i} = \beta e\, V/_{y} \tag{2.11}$$

Here, p/Z_i is inversely proportional to magnetic deflection (x) and independent of the electric deflection. Any vertical line x = constant (red line in Figure 2.11(d)) corresponds to a constant momentum per unit charge and E_k/Z_i depend only on the electric field deflection. Any ions on the vertical line y=constant (yellow color line in Figure 2.11(d)) have a constant energy per charge.

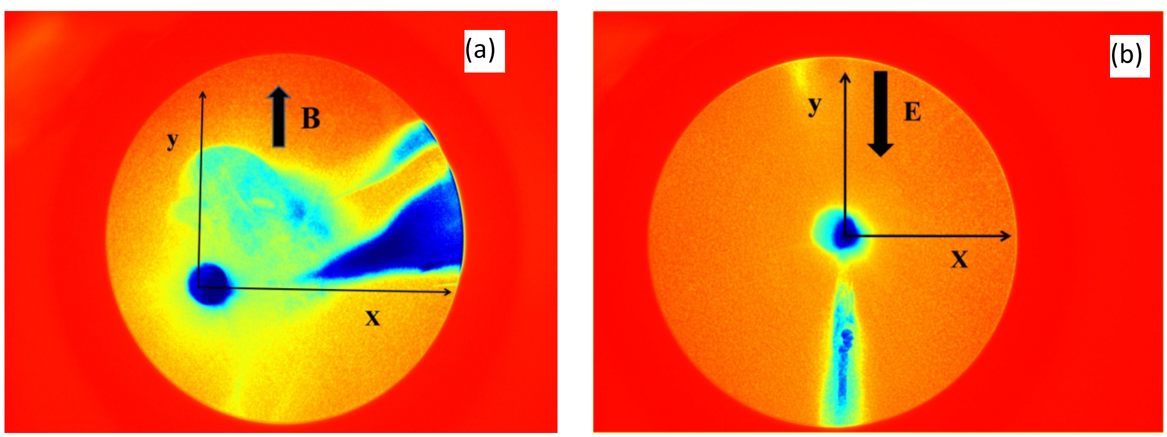

Figure 2.10 *The experimentally observed images showing deflection of charge particle in the (a) Magnetic field (b) Electric field.*

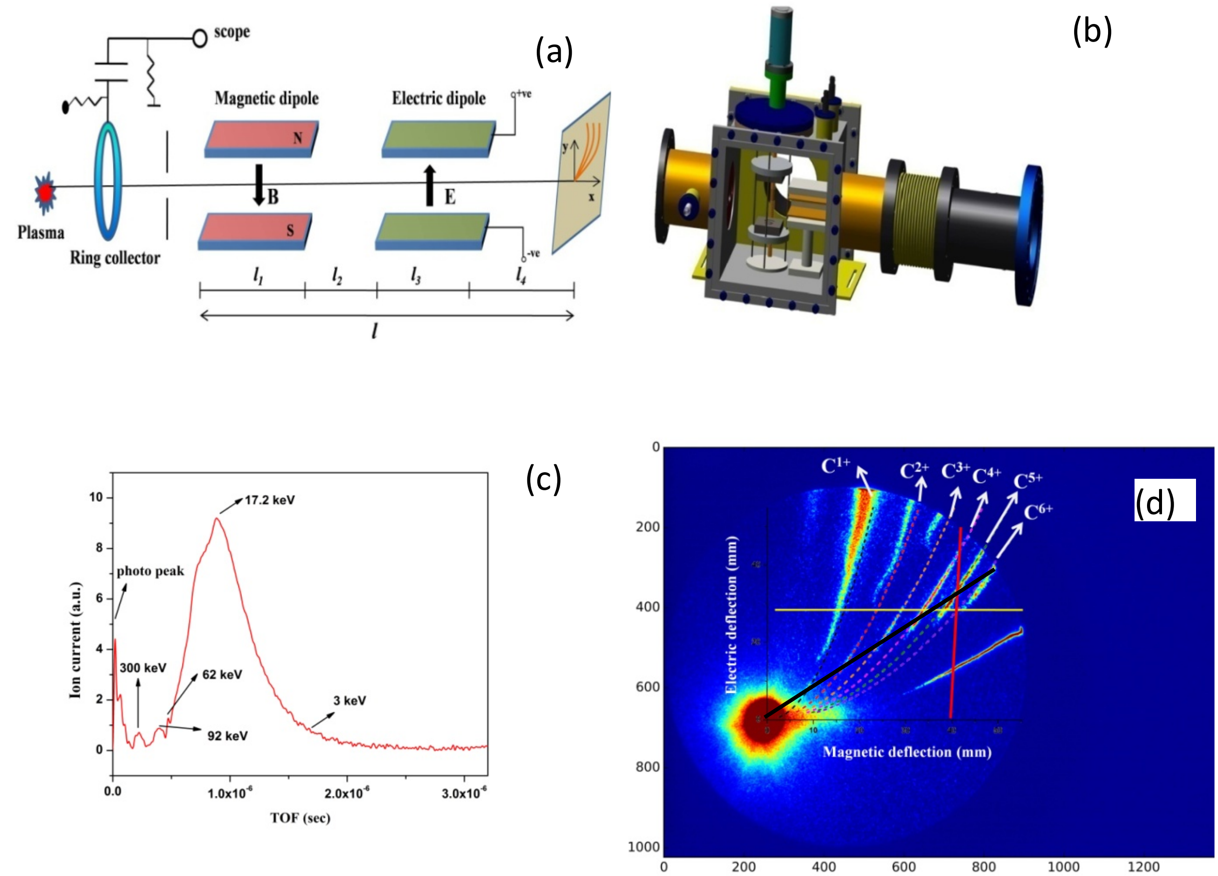

Figure 2.11 *(a) Schematic of TPS (b) Design of TPS (c) Ion collector signal and (d) Image of carbon plasma obtained by experiment and overlapped parabolas of Carbon (dotted) provided by SIMION software.*

For optimization of the TPS, the experiment was performed on 30 J Nd: Glass laser system. The graphite targets were mounted on the four axes motorized translational stage in the vacuum chamber evacuated to 3.8×10^{-6} mbar pressure. The laser was focused on the graphite to a diameter of 100 μm such that, laser intensity was about 5×10^{13} -7×10^{14} W/cm^2. The target was rotated by 45º with respect to the laser beam so that maximum ion flux will reach the ion spectrometer. To cover large spectral range of ion's energy (a few 100 eV to MeV), a variable magnetic and electric field is required as can be seen from Eq. 2.11. In earlier TPS, it was done by putting solenoid based magnetic field in a housing designed for TPS. To get high value of magnetic field, big power supplies which can deliver kilo-ampere current to generate kilo Gauss magnetic field and large number of winding are required which make magnetic shoes very bulky.

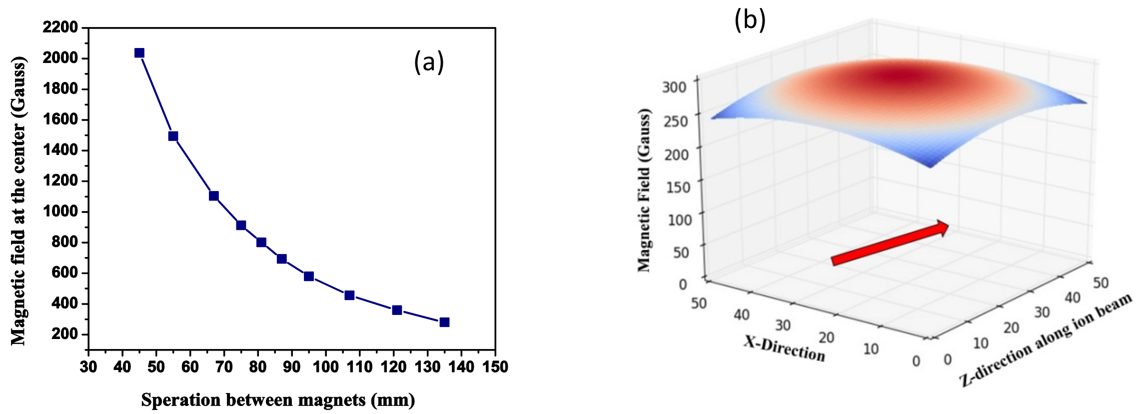

Figure 2.12 *(a)Variation of magnetic field at the center of axis i.e. in the path of ion beam with changing the distance between two magnets. (b) Three-dimensional magnetic field mapping in the plane of the pin-hole and axis of ion source.*

Two permanent magnets were mounted inside the housing through heavy duty linear magnetic feed-through attached with micrometer screw. The magnetic field value can be altered by varying the distance between the magnets with micrometer screw with maintenance the axis of symmetry. The magnetic field can be varied from 150 Gauss to 2 kGauss at the center of magnetic poles (which is also the axis of ion beam) measured by Hall probe (DTM-151 Digital Teslameter) as shown in Figure 2.12(a). The three-dimensional mapping of magnetic field inside TPS at a plane parallel to magnet surface and coinciding with the axis of the ion beam is performed. The recorded data was interpolated for whole area between two magnets using our software and plotted as shown in Figure 2.12(b).

The change in electric field is easy as it is connected with two feed-through and power supply was kept outside. Two copper electrodes were connected with –ve and +ve polarity of electric field. The voltage difference between two electrodes can be varied from 0 V to 10 kV. We coupled detection system using a very flexible bellow compatible to 10^{-7} mbar with the TPS housing. This enables us to cover large energy spectra range by shifting the origin at one corner of the MCP from the center.

A 75 mm diameter two-stage MCP detector, with phosphor screen in Chevron configuration from the photonics company with an amplification of about 10^6-10^7 is placed at a distance of l_4=380 mm from the end of the electrodes. The phosphor screen of the micro-channel Plate (MCP) was captured by f/5 lens on the optical CCD camera (Pixelfly) and captured in the PC using frame grabber card. The parabola recorded for the graphite plasmas at the laser intensity of 2×10^{14} W/cm^2 is shown in Figure 2.11(d). The magnetic field and electric field are kept at 310 Gauss and 13950 V/m respectively. The experimental observation was in fairly good agreement with the theoretical simulation done by the SIMION 7.0 code for the same magnetic and electric field. Deviation in C^{1+} charge state might be due to stray electric and magnetic field effect. The more deviation in the lower energy and lower charge states is due to spending more time in the field (due to long time of flight). Protons of energy from 15 keV to 45 keV are also present due to impurity on the targets. The energy spectrum of ions is also recorded with the ion collector as shown in Figure 2.11(c).

The 3D plot of experimental data enables us to measure the charge states, energy and flux of ions at particular energy of particular charge state. The brightness of the parabola traces on the MCP is proportional to the flux (number density) of the ions. The 3D plot of the carbon ion spectrum on MCP at laser intensity 2×10^{14} W/cm^2 is shown in the Figure 2.13. In case of calibrated MCP with the help of ion accelerators, the quantitative values of flux for each charge state at any energy can be measured.

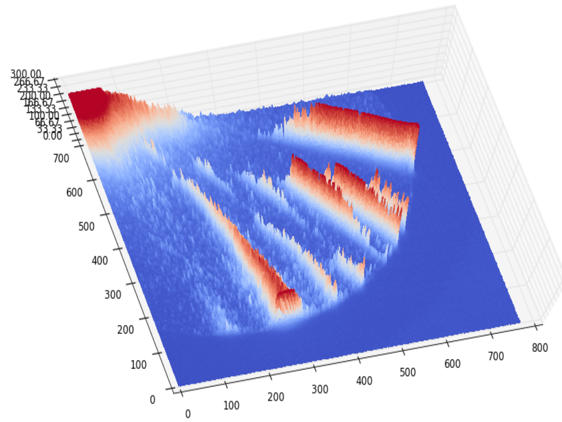

Figure 2.13 *3D view of ion spectrum enable to measure the qualitatively the flux of ion of particular energy.*

2.5.2.4 Development of software for analysis of the TPS data

A program is written in such a manner that it recalls BMP images recorded by CCD detector and read intensity values of pixels from the region of interest from the image. These values are stored in 2-D array. The image is converted to mm unit from pixel as our calculations from Eq. 2.10 are in mm. These equations are used in the program for plotting overlapped parabolas for all charge states. Initially, the magnetic field is measured using hall probe but this magnetic field value does not give the precise parameters for parabola due to backlash of the micrometer and theoretically generated parabola significantly deviated for lower charge states. So, to get the more accurate values of magnetic field, a correction is incorporated for lower charge state parabola to fit them with experimental parabola. This value of magnetic field is used to theoretically generate different parabola for other higher charge states. This correction was not possible in the SIMION code. Then parabolas were drawn by providing correct value of E and B in Eq. (2.10) and agree to the experimental data as shown in Figure 2.14. Such a correction is not possible in SIMION code as it considers ideal cases of parameters.

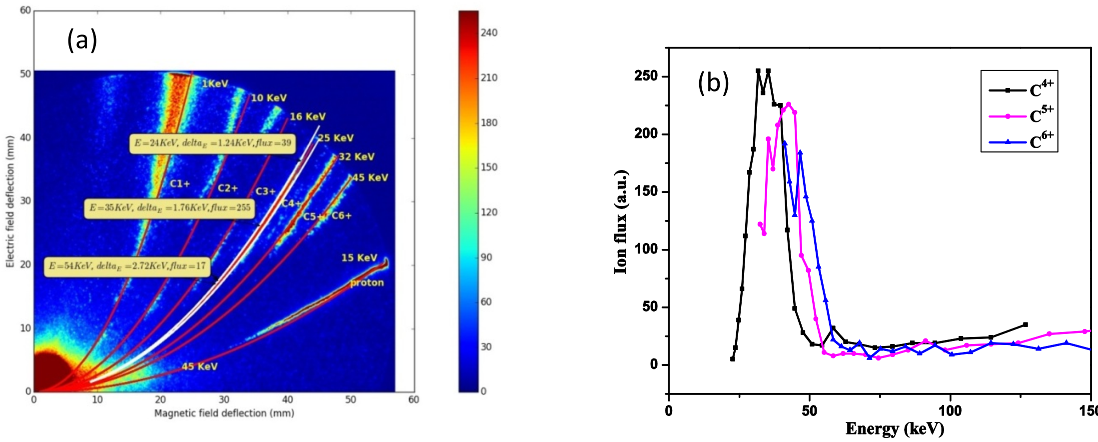

Figure 2.14 *(a) Image showing matched parabolas generated by python (red ones) with experimental data and online calculation of different parameters of carbon plasma (b) Graph showing energy verses flux for all charge states of Carbon.*

Online measurement of energy and flux of ions: Second program is written for online measurement of the energy and flux at different positions of each charge state. For a specific charge state, the unique energy value is unique on parabola. This program calculates energy at each point of fitted parabola for a single charge state at a time and read the corresponding flux from recorded image and these values are stored in an array of energy verses flux in a file. The procedure is performed for all charge states of carbon. An overlapped graph is plotted of fitted parabola and measured intensities. This graph is made interactive so that it can show the energy and flux at any point of any charge state by just moving the cursor on the graph as shown in Figure 2.14(a). Also, it facilitates us to provide the complete energy range on the detector and the flux at each point for a particular charge state as shown in Figure 2.14(b). Using this software, we can measure in situ the ion energy spectrum and flux at each energy value for individual charge state as shown in Figure 2.14(b).

Online calculation of resolution: The problem of mass and energy resolution for TP is much more complicated. Each point on an ion energy distribution processes from the same laser shot is having different energy and mass resolution. The energy resolution can be deduced by differentiating second part of Eq. 2.11 as

$$\frac{dE}{E} = \left|\frac{d\beta}{\beta}\right| + \left|\frac{dV}{V}\right| + \left|\frac{dy}{y}\right| \tag{2.12}$$

First term is constant $\frac{d\beta}{\beta} = 0$, measured potential variation is not more than 1-2% so

$$\frac{dV}{V} = 0 \tag{2.13}$$

$$\frac{dE}{E} = \left|\frac{dy}{y}\right| \tag{2.14}$$

So, from the above equation it is clear that energy resolution of the TPS is energy dependent. Higher the energy higher will be the resolution. Also, higher the charge state for particular energy, higher will be the resolution. The lower resolution for low energy ion can be explained as follows. The energy of the ions $E= 1/2\ mv^2$ implies $v \propto \sqrt{E}$, so for lower energy the ion velocity will be lower i.e. the ions will spend more time in the TOF path. Since the bunch of ions has tendency to spread in the direction perpendicular to the direction of acceleration due to thermal expansion and coulomb repulsion between ions (space charge effect), so by the time it reaches the TPS, spread is enough to reduce the resolution as can be seen in Figure 2.13. For lower charge states, e.g., C^{1+} ions, the spread in lower energy part is very large. Since, $\frac{E}{Z} \propto \frac{1}{y}$, so, for constant E/Z, y is constant. Now E/Z= 6E/6Z= constant. This means at fixed y value, the C^{1+} state will have to spend more time than C^{6+}, as energy is 6 times less and hence resolution will be poor for C^{1+} charge state. In the MCP, the deflection in y direction can be from 0-70 mm. The width of parabola (Δy) varies from few hundreds of μm to few mm. The parabola width is influenced by quantity and charge states of ions, the time of flight (ion energy) from pinhole to MCP, geometry of the measurement (i.e. pin hole diameter and number of aperture). The energy resolution of the Thomson parabola is 0.026 for C^{4+} charge state @31 keV. Similarly, mass resolution can be calculated by first part of the Eq. 2.11, i.e., $x(l) = \alpha \frac{ZeB}{(mE_k)^{\frac{1}{2}}}$

So, maximum possible error in mass estimation can be expressed as

$$\frac{dm}{m} = \left|\frac{d\alpha}{\alpha}\right| + \left|\frac{dB}{B}\right| + \left|\frac{dE}{E}\right| + \left|\frac{dx}{x}\right| \tag{2.15}$$

the first two term in the right-hand side are not changeable and is of dB/B~2-3% in the area of interest for a single shot so the mass resolution can be written as

$$\frac{dm}{m} = \left|\frac{dE}{E}\right| + \left|\frac{dx}{x}\right| \tag{2.16}$$

dx/ x is similar to *dy/y*, with position on the parabola. The deflection *x* on MCP is 0-70 mm. The mass resolution is calculated at every point of the parabola of all charge states along *x* direction for example the mass resolution is 0.026@ 35 keV for C^{4+} ions of carbon plasma.

2.5.2.5 Angular distribution of Carbon ions

The angular dependency for ions for all charge states of carbon plasma detected by TOFS by rotating the target at various angles with respect to laser beam as shown in Figure 2.15(a). To confirm this, we have also measured angular distribution of ions by keeping target at fix position and placing four ion collectors at different angles with respect to target normal. This result is also following the same trend as in case of TOFS measurement. Angular dependency of individual charges states is measured from the TPS images for the same laser shots which were taken for TOFS measurement as shown in Figure 2.15(b). From the Figure 2.15(b) higher charge states ions are more collimated towards target normal. The lower charge state shows higher divergence which is similar to thermal ion flux measured by ion collectors. Figure 2.15(a) shows the energy of ions Vs ions flux for charge state C^{4+}. It is clear from the figure that, for individual charge state, the energy spectrum is much broader at the target normal having higher energy part. The higher energy part of spectrum reduces (narrower spectrum) by increasing the angle of TPS from target normal. From the Figure 2.15(a), it is also clear that the total ions flux also reduces as we move away from target normal. Hansen et al (1997) [54] has done the experiments on Ag target for state of charge experiments and reported that the charge component of the plasma plume is more strongly ejected towards target normal. More detailed studied has been done in [55] using retarding potential ion spectrometer. They reported that the direction of the emission cone relative to target normal is dependent on the charge states. It decreases gradually with the charge state. We also get similar behavior in our experiment for the energy close to thermal energy of ions measured by IC. But for other energies e.g. @ 40keV, the trend is different as shown in Figure 2.16(b-c). Here angular distribution of ion flux for charge state C^{5+} is broader than C^{4+} charge state. Even same behavior is observed for total number of ions (i.e. area under the curve) where ion flux for C^{5+} ion is slowly decreases than C^{4+} ion for one set of energy range (20-50 keV) as shown in Figure 2.16(c).

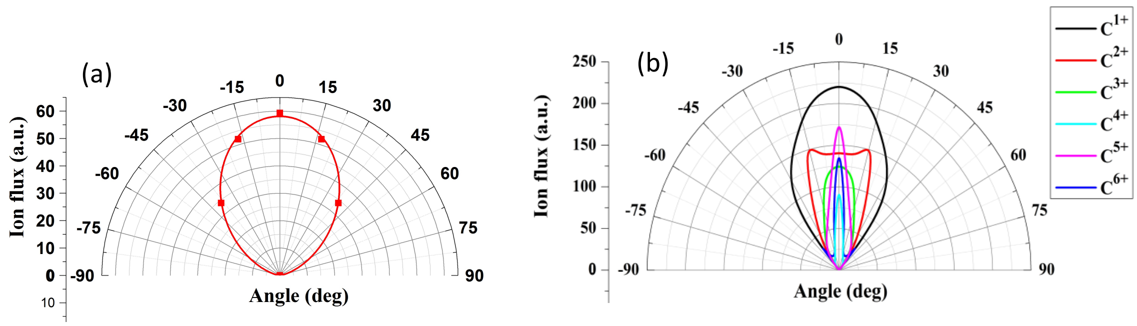

Figure 2.15 *Angular distribution of ion flux of all charge states of carbon obtained by (a) ion collector signal (b) TPS data*

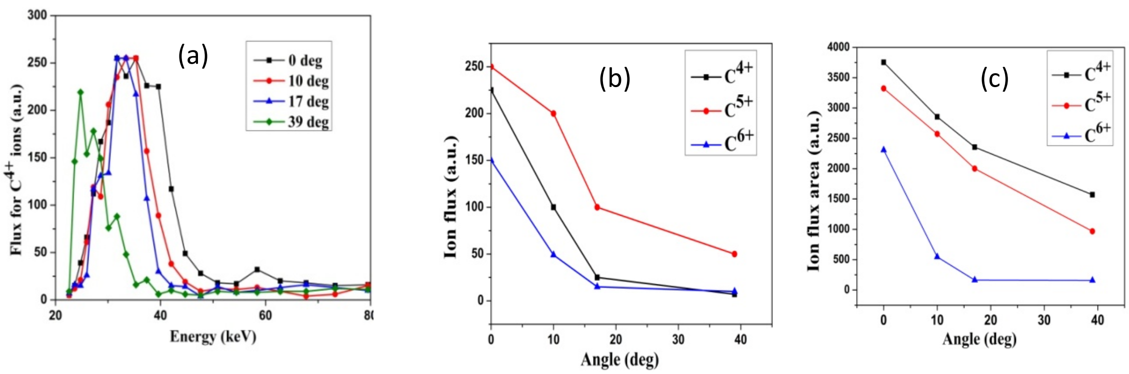

Figure 2.16 *(a) Distribution of ion flux for various energies at different angles between target normal and TPS for fourth state of Carbon (C^{4+}) (b) Ion flux for various charge states verses angle between target normal and TPS at a fixed ion energy of 40 keV. (c) area under the curve for different charge states of carbon with respect to angle.*

2.6 Shadowgraphy set up

To capture the plasma dynamics, two frames optical transverse shadowgraphy is used. The shadowgraphy set up is shown in Figure 2.1 (blue shade). The shadowgraphy light used was second harmonics of main laser beam (532 nm @ 300 ps pulse width). The spatial and temporal resolution of 12 μm and 300 ps was aligned to measure the plasma evolution. Different optical delays are provided to the s and p polarized light to probe the target surface and plasma evolution at different time with respect to laser irradiation. The probe light will investigate the side view of the target. Half part of the probe light will pass cover inside view of the target and half will capture expanding plasma plume. The light after probing the target is split into s and p polarized and captured by the fast CCD cameras. More details of the setup are provided in [56].

2.7 Summary

This chapter provides overview of the laser systems, X-ray and ion diagnostics used. The X-ray diagnostics involves Silicon photo-diodes, X-ray streak camera and crystal spectrometer, NaI detector. The calibration of X-ray streak camera and crystal spectrometer is discussed. The main ion diagnostics are Faraday collector and Thomson Parabola Spectrometer. The high resolution/high dispersion ion spectrometer comprising of a ring type ion collector and Thomson parabola with varying magnetic field using permanent magnetic and electric fields has been developed. This enables to get complete energy spectrum with low resolution in single shot and a particular energy range of interest with very high resolution. The electric and magnetic fields can be changed from a few volts to several kV and a few Gauss (100 Gauss) to 2 kGauss respectively. This enables to measure the ion energy spectrum from 1 keV to 1 MeV/ nucleon. The spectrometer is optimized by using laser produced carbon plasma. The carbon ions of charge states C^{1+} to C^{6+} are measured in the energy range from 3 keV to 300 keV which is also verified by time-of-flight measurement. Protons of energy ranging from 15 keV to 45 keV are also registered on the MCP. A commercially available software SIMION 7.0 is used for the designing of TPS. The simulation results are closely matching with the experiment results. The SIMION code deals with the ideal conditions and hence cannot correct the fairly large deviation for the lower charge states. Also, the SIMION code cannot provide the resolution information and in situ measurements of ions parameters such as ion energy, momentum, energy and mass resolution at each point. To overcome this difficulty, we designed and developed a software using python code for the in-situ measurements of the ions parameters and its resolution at each point. Results from our own code are better than the SIMION software. The energy resolution of this spectrometer is $\Delta E/E \sim 0.026$@ 31 keV and mass resolution is $\Delta m/m \sim 0.026$ @ 35 keV for charge state C^{4+} of carbon plasma. In the future, we are planning to calibrate our MCP with the known ion source such as Pelletron available at our institute which will enable us to get quantitative information of ion flux. Also, in the software we will include the non- linear part of electric and magnetic fields and the fringe effect to get better results.

Chapter 3

K- and L-shell Spectroscopic Studies of Laser-Plasma X-ray

3.1 Introduction

Emission spectroscopy is a commonly utilized technique employed to diagnose the temperature and density of a plasma. The strongest emission may lie anywhere from IR to the X-ray wavelengths depending upon the temperature and other properties of the plasma. Spectroscopic studies involve recording the spectrally resolved electromagnetic radiation and then analyzing this data to determine the plasma parameters. Spectroscopy can be applied to astrophysical sources, as well as laboratory plasmas such as plasma torches, magnetically confined plasmas (tokomaks), and laser-produced plasmas, and other phenomena. In Inertial Confinement Fusion (ICF), dopants may be added to the fuel shell in order to produce X-ray emission that can inform the determination of temperature and density in the imploding plasma [57]. The X-ray emission from laser produced plasma comprises a combination of free-free, free-bound and bound-bound emission. The atomic physics of laser-produced plasma and the various equilibrium states that may be present in such plasma are discussed in chapter-1. The spectrum of bound-bound transitions is dependent upon the electronic populations in various atomic orbitals of ions with various charge states. It also depends upon the atomic processes taking place in the plasma. These processes are mediated by the plasma temperature and density which are in turn dependent upon the details of the laser-target interaction. In the present experiments, a sub-nanosecond pulse interacts with a solid target to generate an emission spectrum. The rapid heating results in both violent expansions into the vacuum and the production of high ion-charge states in the hot plasma. The emission spectrum consists of spectral lines from a range of different charge states. In the present experiment, we have used Aluminum (Al), Silicon (Si) and Copper (Cu) as targets for performing spectroscopic studies. The detailed results and analysis are presented in following sections.

3.2 K-shell spectroscopy of Al and Si plasma

The transitions which result in bound-bound X-ray emission, and the resultant X-ray radiation, are classified principally according to the final state in the electronic transition involved, and specifically whether the electron ends up in the K-, L-, M-, N-, or O- shell. The K-, L-, and M- spectra consists of lines originated from the transitions to (1s-, 2s-), (2p-, 3p-) and 3d- levels respectively. K-shell spectra can easily be achieved with a moderately intense laser (~10^{13} W/cm^2) for low Z targets. However, the requirement of extreme energy and density for ionization make achieving such emission more challenging in the case of high Z targets. An extensive study of K- shell spectra from plasmas has been carried out in the past, in part due to the ease with which it can be analyzed [58]–[63]. The relative simplicity of calculations related to these transitions make them a rich source of information about the plasma. On the other hand, although the L -shell ionization of high Z atoms can be achieved easily, complex structured spectroscopic models are required to analyze these spectra.

Here, a detailed study of K-shell X-ray emission spectra generated by a 30 J, 500 ps Nd: Glass laser, focused to an intensity of 10^{13}-2×10^{14} W/cm^2 is performed. The K-shell spectra including resonance lines from He-like and H-like ions along with their satellites is particularly interesting because it is a rich source of information about the plasma.

3.2.1 Description of the experiment

The experiment is carried out using an Nd: Glass laser which provides an output energy of 30 J per pulse with pulse duration of 500 ps. The laser is incident on a 10 mm thick Al slab and focused to a spot size of 120 μm using an f/5 lens, yielding a peak intensity of 2×10^{14} W/cm^2. The experimental chamber is evacuated to a pressure 4×10^{-5} mbar. An X-ray crystal spectrometer using a Thallium Acid Phthalate (TAP) crystal placed at 45° with respect to the laser axis (target normal) is used for the line emission studies in the spectral range of 5.5-7.5 Å enabling the measurement of He-β, γ, δ, ε and H-like lines. These resonance lines are due to Al XII, Al XIII and Al XIV ions. Two stacked aluminized polycarbonate foils (Alexander Vacuum Research, Inc., trade name: B-10) having a 1/e cut-off of 0.9 keV are used to prevent the scattered visible light from entering the spectrometer. The TAP crystal spectrally resolves X-ray emission from the laser-produced plasma. These Bragg-reflected X-rays are detected by an X-ray CCD camera (Model VISION 4M, from Rigaku innovative) giving a wavelength resolution of 25 mÅ. To obtain a wide range of X-ray energies, the crystal is mounted on a motorized Z-stage which can move up and down by 15 mm. By changing the height of the crystal with respect to the source we are able to cover a spectral range of 5.5-7.5 Å. A schematic of the crystal spectrometer along with the experimental setup is shown in Figure 2.4 (chapter-2). The X-ray spectra are analysed using a code written in Python. To facilitate the angular distribution studies, the target is mounted on the motorized X-Y-Z-Θ stages. The angular distribution of K-shell resonance lines with associated satellites and Al XII, Al XIII and Al XIV ions are studied by mounting an X-ray crystal spectrometer and a Thomson parabola spectrometer (TPS) are mounted at 45° in front side with respect to target normal. Two ion collectors are installed at an angle of 22.5° and 45° with respect to target normal to measure the ion temperature and plasma expansion velocity.

3.2.2 Calibration of the crystal spectrometer

The spectral resolution of a crystal depends on the source size, the distance between the source and the detector and the rocking angle of the crystal. Therefore, for a fixed focal spot diameter (i.e., a fixed source size) that if we increase distance between source and detector, the resolution of the spectrometer will increase linearly with distance. However, at the same time X-ray flux reduces according to $1/L^2$. Optimization is therefore necessary between the resolution, spectral window, and the signal to noise ratio. In the experiment described here, the experimental chamber is modified such that the distance between the source and the detector can be increased to obtain a higher resolution for the study of the K-shell emission from an Al plasma. To enable the spectral window being observed to be varied, the target is mounted on a motorized Z-stage. The spectral window accessible as a consequence lies between 5.5 Å and 7.5 Å. However, the spectral range covered when the crystal is in a particular position is less than 1 Å as shown in Figure 3.1(a-d). In the present experiment, a TAP (thallium acid phthalate) crystal with (001) plane of size 50×10 mm^2 , and with a thickness of 2 mm is used. This crystal has a 2d spacing of 25.75 Å. The crystal was kept at a distance of 175 cm from the target. The source to detector distance is 350 cm. The detector unit is mounted on a flange having a taper angle of 15°, connected to a vacuum chamber port.

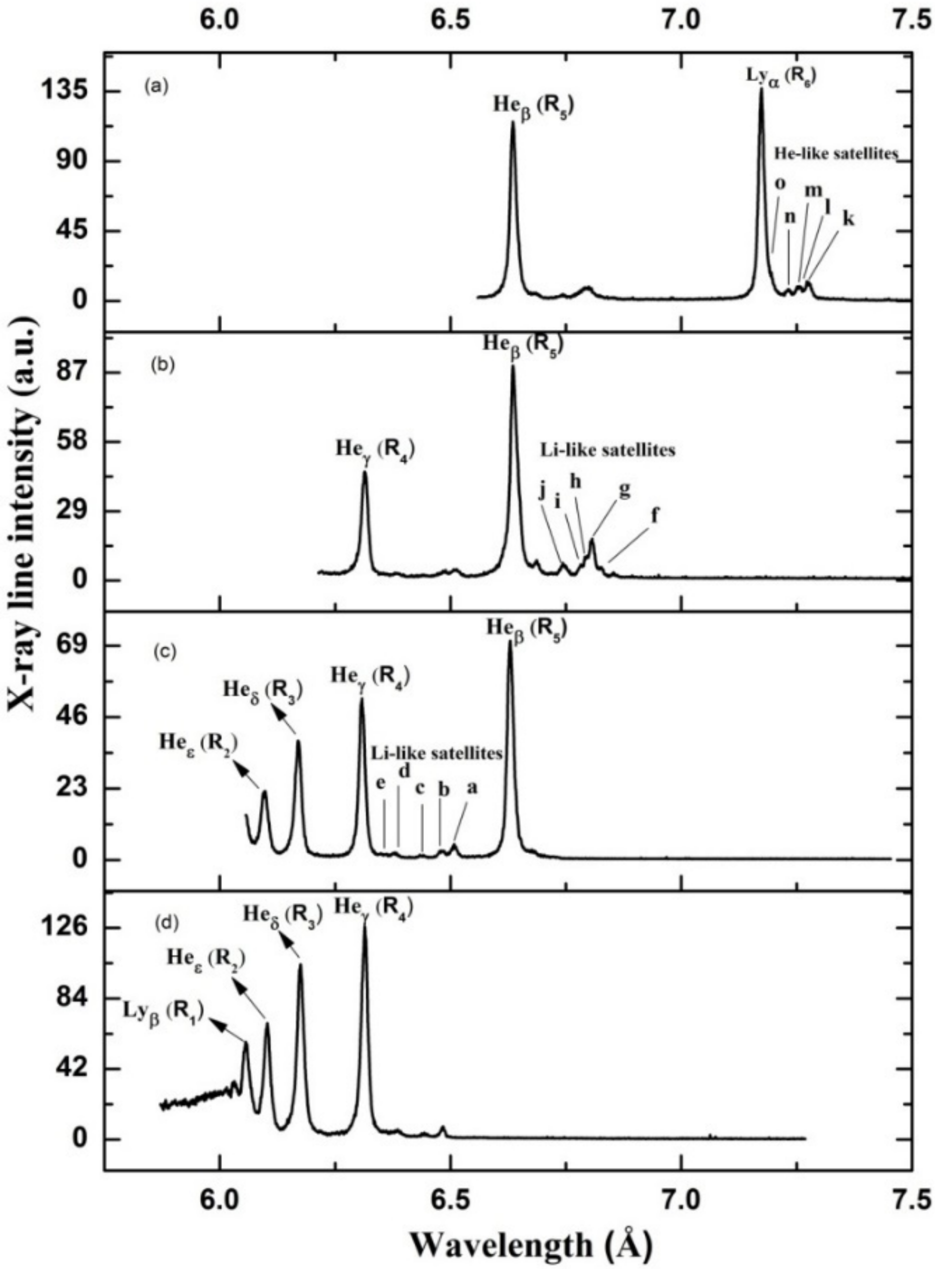

Figure 3.1 *(a-d) K-shell X-ray line emission spectrum form Al plasma showing the different wavelength windows available by changing the distance between the plasma and the TAP crystal.*

3.2.3 Code for image processing

In this experiment, a soft X-ray scientific digital CCD camera from Rigaku (Model X-VISION – 4M) is employed for the detection of X-ray lines. The CCD image sensor is a back illuminated sensor with 2048×2048 pixels. The pixel size is 13.5 μm×13.5 μm and the image area is 27.6 mm×27.6 mm. The CCD uses a 16-bit read-out unit with read-out speed of 25 kpixels/s so it takes ~168 s to read all of the pixels. The readings are initially stored in detector's on-board memory and after finishing read-out the data is transferred to the PC.

The camera is provided with proprietary software, which collects data and saves it as a raw image without compression loss or alternatively as a BMP image of 8-bit resolution with some compression. Analyzing the images provided by this software, presented several difficulties. Firstly, the software can export the image in BMP format with 8-bit integer values but not in ASCII format, so information is lost. Since the BMP images have lower resolution, it is always preferable to use the raw file to analyze data. Secondly, the proprietary software has the option of full binning but using this option tends to result in read-out saturation due to a large collection of charge from a whole column of pixels and limited read-out range. Additionally, only 2/3rd of the CCD is illuminated, and binning an un-illuminated region can contribute to a false signal. To overcome these shortcomings, we have developed software written in Python to handle the raw data files. Firstly, this code imports the raw data file with full 16-bit resolution without any compression loss. Two-dimensional image data on camera chip is recorded and each column of pixels corresponds to same energy, so several pixels with same energy are added to reduce the noise in recorded spectra. In this manner, the noise is reduced by a factor of √n, where n is the number of rows on the image (In our case n = 100) added to get spectrum. Figure 3.2 shows a comparison between the spectrum produced from the freely available image processing software PROMISE [64] and that produced by our code. From the figure it is clear that the data processed by proprietary software is showing saturation whereas that produced by our code is not.

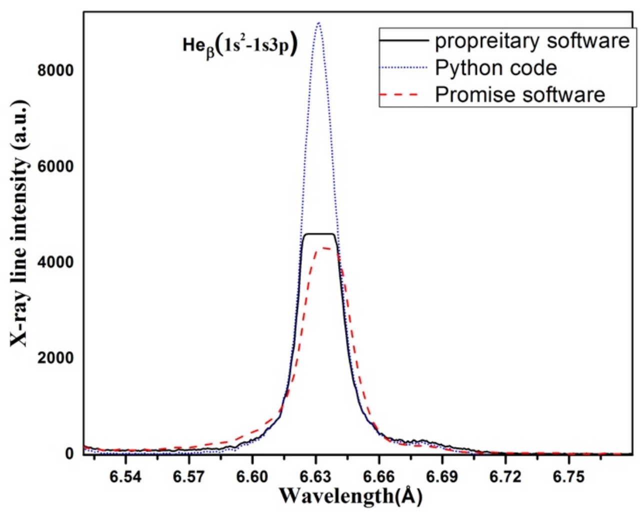

Figure 3.2 *Processed intensity plot of the He$_\beta$ line from Al plasma with 8 bit BMP(—), Promise (-----), and the Python (…) software developed by our group.*

3.2.4 Scaling of resonance lines intensity with respect to laser intensity

The study of X-ray conversion efficiency as a function of different parameters such as laser energy and variation of focal spot size plays a key role in the optimization of a laser-produced plasma X-ray source. Laser intensity can be varied by two methods: one is changing the laser energy whilst keeping laser spot size constant and the laser pulse duration fixed and the other method is by defocusing the laser on target whilst keeping a constant laser energy and pulse duration [64]. In the latter case, the laser intensity increases as we move towards best focus position due to a reduction in the beam diameter. In reference [9], it is shown that changing the laser energy is a more efficient method to increase the conversion of laser energy into X-rays. In our case, we have studied the K-shell X-ray line emission yield from Al plasma as a function of laser intensity keeping the laser pulse duration and laser focal spot size fixed at 500 ps and 120 μm respectively. The He_β, He_γ and He_δ intensities as a function of laser intensity are shown in Figure 3.3. These scale as $I_x = (I_L)^\alpha$, where I_x is the X-ray flux of different K-shell resonance lines of He-like Al, I_L is the intensity of the laser and α is a scaling exponent. The scaling component α has been calculated for all resonance lines and found to be 2.2, 2.2, and 2.3 for He_β, He_γ, and He_δ respectively, which is in the same range as reported elsewhere [65]. The increase in the resonance line yield can be inferred from the fact that as the laser intensity increases, the temperature and thus thermal emission rapidly increase resulting in an enhancement in ionic line intensities. Due to a relatively long pulse, 500 ps in our case, the interaction time of the laser with the plasma is long, which gives rise to a stronger scaling as compared to that observed with ultra-short pulses [65].

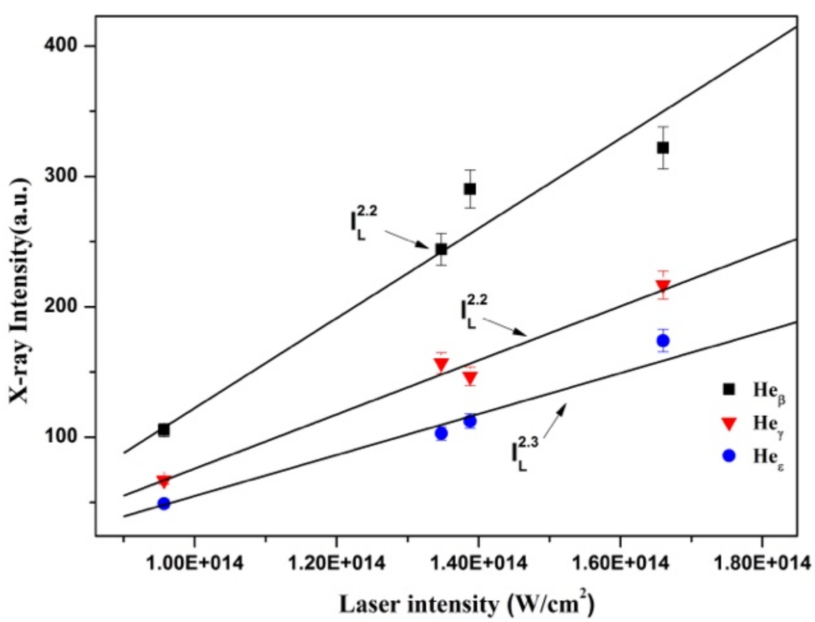

Figure 3.3 *Figure showing variation of intensity of He_β, He_γ, and He_δ spectral lines as a function of laser intensity.*

3.2.5 Measurement of plasma parameters

The intensity of various resonance lines (Ly_α, Ly_β, He_β, He_γ, etc.) and associated satellites and the plasma parameters calculated using various models and simulations are discussed below.

3.2.5.1 Temperature estimation

The ratio of a satellite line to its parent resonance line is a good diagnostic for the estimation of plasma temperature. Satellites are formed from doubly excited levels in He-like and Li-like ions. Transitions from these doubly excited levels appear on the long wavelength side of the resonance lines of H-like and He-like ions. These are resonance transitions in the presence of an additional electron in the excited state known as a spectator electron. There will be a number of satellites depending upon the excited state of this spectator electron, but the most intense and distinguishable satellite will arise from transitions having a spectator electron in the n = 2 excited state. For higher values of n, these satellites become inseparable from the parent resonance line. In the case of H-like ions, the main transition i.e. 1s-np will take place in the presence of a spectator electron in the n'l' state i.e. nln'l'-1sn'l' (transition from He-like ions). In case of He-like ions, there are two channels of radiative decay of doubly excited states from the $1s2l3l'$ state, one is the $1s^22l$ (satellite to He_β resonance line) and the other is $1s^23l$ (satellite to He_α resonance line). In the past, plasma parameters have been largely estimated using the He_α line and its satellites. In the present study, the plasma temperature is estimated using the He_β and Ly_α lines and their corresponding satellites using the model described in [12], which is more appropriate as the opacity effect is less for transitions with higher n values.

The intensities of Li-like satellites are proportional to rate coefficients for dielectronic recombination and the fractional abundance of He-like ions. The ratio of intensities of a Li-like satellite to a He-like resonance line is independent of the fractional abundance of the He-like ions but strongly depends upon temperature as resonance lines are produced by electron impact excitation. The intensity of the satellite line is given by [66], [67]

$$I_{sat} = N_{He} N_e C_{diel} \frac{A_{rad}}{A_{auto} + A_{rad}} \tag{3.1}$$

where, N_{He} and N_e are the densities of the He-like ion ground state and electrons respectively. C_{diel} is the dielectronic capture rate coefficient. The value $\frac{A_{rad}}{A_{auto} + A_{rad}}$ is the branching ratio for the decay of a satellite level by radiation (A_{rad}) against the auto-ionization rate (A_{auto}). The ratio of dielectronic capture rate to auto-ionization rate is given by the principle of detailed balancing

$$\frac{C_{diel}}{A_{auto}} = \frac{h^3}{2\left(2\pi mkT\right)^{3/2}} \frac{g_s}{g_1} \exp\left({-E_{sat}}/{kT}\right) \tag{3.2}$$

where g_s and g_1 are the statistical weights of the satellite level and the He-like ion ground state respectively, E_{sat} is the energy difference between these, T is electron temperature, *h*, *m* and *k* are Plank's constant, the mass of an electron and the Boltzmann constant respectively. Therefore, the satellite intensity is given by,

$$I_{sat} = N_{He} N_e \frac{4\pi^{3/2} a_0^3}{T^{3/2}} \frac{g_s}{g_1} \frac{A_{rad} A_{auto}}{A_{auto} + A_{rad}} \exp\left({-E_{sat}}/{kT}\right). \tag{3.3}$$

The intensity of the He-like ion resonance line is given as

$$I_{res} = N_{He} N_e \left(C_{coll} + D_{diel}\right) \tag{3.4}$$

where C_{coll} is the collisional excitation rate coefficient and D_{diel} is the additional contribution of dielectronic recombination. After substituting in all of the parameters, the intensity of the resonance line is given as

$$I_{res} = N_{He} N_e 8 \left(\frac{\pi}{3}\right)^{1/2} \frac{h a_0}{m} \frac{f}{E_{res} T^{1/2}} P \exp\left(-E_{res}/T\right)\left(1+\alpha\right) \tag{3.5}$$

where α ~D/C, f is the oscillator strength for excitation of the resonance line, and P is the gaunt factor.

Therefore, the relative intensity of a satellite to its resonance line is given as

$$\frac{I_{sat}}{I_{res}} = \frac{\sqrt{3} m \pi a_0^2}{2h} \frac{1}{fP} \frac{E_{res}}{kT} \frac{g_s}{g_1} \frac{A_{rad} A_{auto}}{A_{auto} + \sum A_{rad}} \exp\left[\frac{E_{res} - E_{sat}}{kT}\right] \frac{1}{1+\alpha} \tag{3.6}$$

Here α is a correction factor which gives the contribution of unresolved satellites, after omitting the term (1+α) and taking $f \sim 0.55$ and $P \sim 0.2$ with T in eV, Equation (3.6) can be expressed as

$$\frac{I_{sat}}{I_{res}} = 953.7 \times 10^{-19} \frac{E_{res}}{T} \frac{g_s}{g_1} \frac{A_{rad} A_{auto}}{A_{auto} + \sum A_{rad}} \exp\left[\frac{E_{res} - E_{sat}}{kT}\right] \tag{3.7}$$

where E_{res} and E_{sat} are energies of the resonance line and the satellite line above the ground state of a He-like ion. The ratio of the intensities of satellite lines and their resonance line were compared with data provided in reference [13]. Calculated temperatures for various satellites and resonance lines are given in the last column of the Table 3.1. From Table 3.1, it can be seen that the plasma temperature estimated from H-like ion emission is more than the temperature estimated from the He-like ion emission. The reason for this is the spatial position of the occurrence of the formation of H-like and He-like ions. H-like ions are formed near the critical density where laser energy deposition is maximised. However, He-like ions are from the extended portion of the plasmas where the plasma temperature is lower. The temperature estimated from H-like ion emission is more reliable than that estimated from He-like ion emission because the doubly excited level of Li-like ions can be populated in two ways (i) by dielectronic recombination and (ii) by the direct excitation from the inner shell of a Li-like ion. In this case equation 14 may underestimate the electron temperature.

Table 3.1 *Transitions and Wavelengths of H-like and He-like spectral lines with satellites along with their branching ratio and calculated plasma temperature using equation (14). Since the resolution of our crystal spectrometer is up to two decimal places, an average wavelength is presented for transitions having a difference in wavelength in the third or higher decimal place.*

Key	**Wavelength λ(Å)**	**Transition**	**Branching Ratio** $g_s \frac{A_{rad} A_{auto}}{A_{auto} + \sum A_{rad}}$ **(x10^{13})**	$\mathbf{I_{sat}/I_{res}}$	**Temperature (eV)**
R_1(Ly_β)	6.05	1s-3p			
R_2 (He_ε)	6.10	$1s^2$-1s6p			
R_3(He_δ)	6.17	$1s^2$-1s5p			
R_4(He_γ)	6.31	$1s^{2\,1}S$-1s4p ^1P			
a	6.51	$1s^22p\ ^2P$-1s2p4p ^2D			
b,c,d,e	6.48,6.44, 6.38, 6.36	$1s^23l$-1s4p3l			
R_5(He_β)	6.63	$1s^2\ ^1S_0$-1s3p $^1P_1$		1	
f	6.83	$1s^22p\ ^2P$ -1s2p(^3P)3p ^2P	0.016	0.059	267

g	6.81	$1s^2 2p\ ^2P$ -$1s2p(^3P)3p\ ^2D$	0.09	0.19	279
h i	6.74	$1s^2 2p\ ^2P$ -$1s2p(^3P)3p\ ^2S_{1/2}$	0.25	0.11	370
$R_6(Ly_\alpha)$	7.17	$1s^2 2p\ ^2P$ -$1s2p(^3P)3p\ ^2D$			
k	7.27	$1s\ ^2S_{1/2}$-$2p\ ^2P_{3/2}$	15.22	0.091	419
l	7.26	$1s2p\ ^1P_1$-$2p^2\ ^1D_2$			
m	7.25	$1s2p\ ^3P$-$2p^{2\,3}P$			
n	7.23	$1s2s\ ^3S_1$-$2s2p\ ^3P$			
o	7.19	$1s2s\ ^1S_0$-$2s2p\ ^1P_1$ $1s2p\ ^1P_1$-$2p^{2\,1}S_0$ $1s3p\ ^{1,3}P$-$2p3p\ ^{1,3}P\ ^{1,3}D$ $1s3s\ ^{1,3}S$-$2p3s\ ^{1,3}P$			

3.2.5.2 Density estimation

The broadening of ionic lines, especially Lyman and Balmer lines (which originate for Al XIII from the 1s-np state) are appropriate for the determination of density. Many factors contribute to the broadening of ionic lines such as quasi-static broadening by ions, contribution of electron impact, the Doppler effect, and Debye screening. The contribution of electron impact is negligible in laser produced plasma. The main broadening factors are Doppler broadening and ion impact i.e. Debye screening. We have used the Ly_β resonance line (1s – 3p), where n = 3. The effect of opacity on this line intensity is less than for Ly_α due to higher n value transitions, which have a lower oscillator strength. Another reason for choosing the Ly_β line is that the determination of density from Stark broadening is only possible with a shorter distance from the target. Resonance lines of H- like ions are emitting from the area closer to the target. For greater distances, the error in the subtraction of the Doppler broadening resulted in a considerable error in the determination of the electron density. The Ly_β line is Lorentzian in shape [68] and in high density plasma (> 10^{19} /cm^3), Stark broadening is the dominant mechanism, though there will also be broadening due to the Doppler Effect. Doppler broadening is due to the thermal motion of ions which results in a shift of emission lines up or down, depending on whether the ion is moving toward or away from the observer. The magnitude of the shift is proportional to the velocity along the line of sight resulting in a characteristic broadening of spectral lines.

For measurement of Doppler broadening, we have used our ion collector signal and Thomson parabola spectrum for Al XII and Al XIII ions. The thermal ion temperature from the ion collector is measured for the same laser shot as is used for the X-ray spectroscopy. The peaks given by the ion collector are of Maxwellian from which we can obtain the thermal energy and hence the ion temperature. The Doppler broadening can be calculated as

$$\Delta\lambda = \frac{2\lambda}{c}\sqrt{\frac{2kT_i \ln 2}{m}} \tag{3.8}$$

In terms of energy scale, the above formula gets converted into

$$f_G^{doppler} = h\Delta\nu = \frac{2h\nu}{c}\sqrt{\frac{2kT_i \ln 2}{m}} \tag{3.9}$$

where kT_i is ion temperature which is 6 keV in our case from the ion collector data, m is the atomic mass of Al, λ is wavelength of Ly_β and c is the velocity of light. Doppler broadening is found to be 2.41 eV. There is a contribution of instrumental broadening due to the dispersive element in the spectrometer, which is known as instrumental width. In our case the instrumental broadening is 3 eV, which is usually Gaussian in nature. Since instrumental and Doppler broadening is represented by a Gaussian function, to calculate the cumulative effect on the spectrum, a convolution was taken using following formula [69]

$$f_G^{total} = \sqrt{\left(f_G^{inst}\right)^2 + \left(f_G^{doppler}\right)^2} \tag{3.10}$$

Using this formula, the total width of the Gaussian part is given by 3.8 eV. The profile of our Ly_β resonance line is Voigt which consists of a Gaussian profile (resulting from net effect of Doppler and instrumental broadening) and a Lorentzian profile due to Stark broadening. For extracting only Stark broadening we have used the following formula for the width of a Voigt profile [70]

$$f_v = 0.5346 f_{stark} + \sqrt{0.2166 f_{stark}^2 + f_G^2} \tag{3.11}$$

where f_v, f_{stark} and f_G is the FWHM of the Voigt profile, Lorentzian and Doppler respectively. By using the above formula, the width of Lorentzian profile f_L i.e. Stark broadening comes out to be 3.5 eV.Taking the Debye screening effect into consideration, the Holtzmark formula for line width is modified as [71]

$$f_{stark} \approx 0.76 \left(\frac{N_e}{10^{20}}\right)^{0.6} T_e^{0.21} \tag{3.12}$$

where f_{stark} is Stark broadening, N_e is electron density and T_e is temperature of electrons. In this formula, for measuring electron density, we need to know the temperature of the electrons. Using different values of temperature from Table 3.1, the density is found to be in the range of 1.6×10^{20} cm^{-3}-2.8×10^{20} cm^{-3}. The estimation of density from the Stark broadening is more accurate compared to using the ratio of Intercombination (IC) to its resonance line (I_{IC}/I_R) [71].

The method using the ratio of I_{IC}/I_R gives a value of density close to the target that is one order of magnitude less than that calculated by Stark broadening, which is not correct. The density estimation using Stark broadening does not require the knowledge of the ionization state in contrast to the method based on I_{IC}/I_R.

We have calculated the density by using the formula [32] given below

$$f_{stark} = \left(13Z_p h/2\pi Z_n m\right)\left(n_i^2 - n_f^2\right)\left(N_p\right)^{2/3} \qquad (3.13)$$

where Z_p is charge of emitting ion, Z_n is the nuclear charge, N_p is density of perturbers, n_i and n_f are the quantum numbers of initial and final state respectively and m is the mass of an electron. The density of ions is calculated as $2.27\times10^{19}/cm^3$ resulting in a density of electrons of $2.95\times10^{20}/cm^3$. This is in reasonable agreement with value calculated by previous method.

3.2.5.3 Determination of temperature and density using FLYCHK

For the estimation of the temperature and density of the plasma, simulations have been performed using the FLYCHK code [27] which generates a synthetic X-ray emission spectrum for comparison with the experimental data. To find a best fit to the experimental spectrum, a parameter scan has been performed using a range of temperatures from 50-500eV and densities from 10^{12} to10^{21} cm^{-3}. The simulated spectra were instrument broadened with our estimated resolution (3 eV) using a post processor. To get a rough idea of plasma temperature, the intensity ratios of He_β to different resonance lines (obtained by FLYCHK) are calculated for temperatures from 50 to 500 eV. These ratios are then compared with the intensity ratios for the same lines of our experimental spectrum. So, for the plasma temperature in our experiment, this difference should be minimum. The difference between the experimental ratios and ratios produced by FLYCHK are plotted with respect to different temperatures as shown in Figure

3.4(a). From the figure, differences between the line ratios are minimum around a temperature of ~ 160eV.

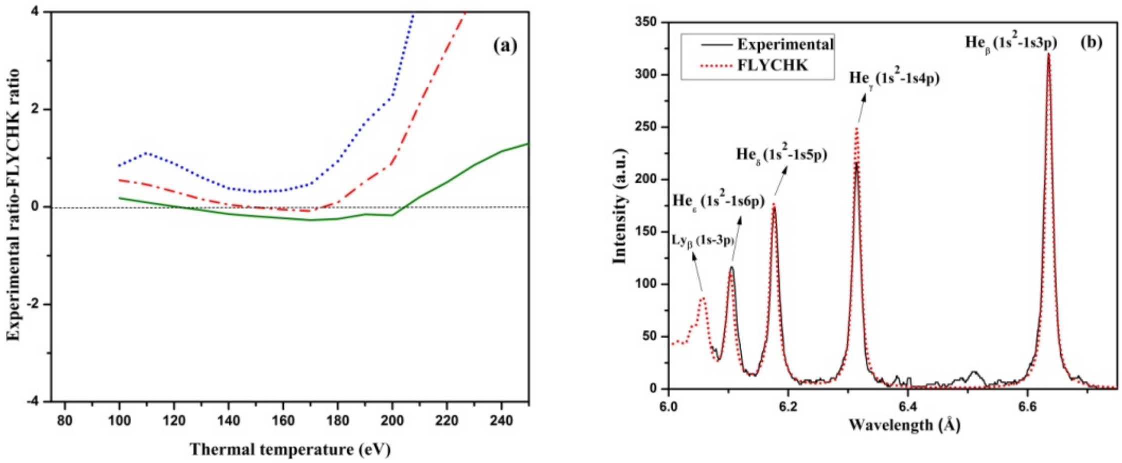

Figure 3.4 (a) *Plot of difference between ratio of resonance lines obtained experimentally and lines generated by FLYCHK He_β/ He_γ (solid line), He_β /He_δ (dash-dotted line), He_β/ He_ε (dotted line)* (b) *Experimental spectrum obtained for Aluminum plasma (solid line) and spectrum generated from the FLYCHK code (dotted lines) for T_c= 160 eV, T_h=1000 eV, f=0.008, and density = 5×10^{20} cm^{-3}.*

This code has used a two temperature (temperature of hot and cold electrons) model. Fine tuning of the synthetic spectra with experimental spectra has been done by changing the cold electron temperature to around 160 eV, the hot electron temperature scans from 0.5-1.5 keV and ratio of hot to cold electron temperature electrons from 0.005-0.1, which yields a best match between the experimental and stimulated spectra at T_c=160 eV, T_h=1000 eV, f=0.008, and density= 5×10^{20} cm^{-3}.

3.2.6 Conversion efficiency of laser to X-ray

The X-ray conversion efficiency is the fraction of absorbed laser energy that is converted into X-ray flux. The laser energy absorbed by the target goes into various degrees of freedom such as ionization energy, thermal energy, ion internal excitation energy etc. Conversion of the laser light into X-rays depends on many parameters such as the atomic numbers of the target, the wavelength of the incident laser, the intensity of laser, and the focal position. We have measured the yield of Ly_{α}, He_{β}, He_{γ}, He_{δ}, He_{ε} and Ly_{β} resonance lines which is found to be 0.54, 0.51, 0.41, 0.35, 0.29 and 0.13 μJ/sr respectively for an incident laser energy 8.4 J.

3.2.7 Angular distribution of resonance lines

Generally, X-ray emission from laser produced plasmas is assumed to be isotropic (at least at the intensities considered here). However, several authors have reported an angular distribution of the bremsstrahlung X-ray flux at some wavelengths [72]. In the majority of the measurements, the X-ray intensity is found to be some power law of cosθ, where θ is the angle between the detector and target normal. The spectral range in these measurements is very broad, since they are based upon differentially filtered X-ray diode measurements. To use laser produced plasma based X-ray sources for some applications in spectroscopy, materials studies and radiography, an approximately monochromatic source is required. For this purpose line emission, especially resonance lines, seem to have more potential than broadband bremsstrahlung emission. It is important to know the angular distribution, i.e., intensity of resonance lines as a function of emission direction with respect to target normal. Plasma non-uniformity, opacity and eclipsing of hot plasma by the target at low take off angles can all lead to such anisotropic emissive behaviour.

Here, the X-ray emission of various radiative transition lines at different angles with respect to the target normal. A large deviation from isotropic emission for the He- like resonance lines is observed. The angular distribution of lines emitted from the K-shell have been studied whilst keeping the laser energy fixed at 10 J. The angle between the crystal spectrometer and laser axis on target was changed by rotating the target with the help of a θ-stage. Each shot was taken on an undisturbed region of the target by moving it on a Y-Z stage. We have chosen s-polarized ($\vec{E}.\nabla\vec{n}_e = 0$) light for this study, so that resonance absorption will not contribute in enhancement of X-ray yield as it would in the case of p- polarized light. Further, by changing the target with respect to laser axis the circular beam will become elliptical with increase of one (horizontal) axis. By increasing the angle, ellipticity will increase and hence the area of focal spot will increase, which leads to a decrease in the laser intensity. For example, for a 45° rotation the focal spot area will increase by $\sqrt{2}$ times and the intensity will go down by $\sqrt{2}$ times. So the value of laser intensity is corrected accordingly to avoid any change in irradiation because of angles.

The angular distribution of the He_β, He_γ, He_δ and He_ε resonance lines are shown in Figure 3.5(a-d). From the figure, it is clear that the He_β line ($1s^2$-1s3p) has a higher level of anisotropy than lines with n=6 ($1s^2$-1s6p) which are less affected by plasma opacity. Lines corresponding to transitions from higher values of n are more appropriate for the calculation of plasma parameters. This justifies our decision to choose He_β and Ly_β for plasma parameter calculations.The TPS records ions from an Al plasma at various angle with respect to target normal at the same laser energy as used for the X-ray measurements are shown in Figure 3.5(e-g). It is clear from the figures that the flux of Al XII, Al XIII, Al XIV ions is decreasing when target normal is away from TPS. The results from the TPS support our measurement of angular dependency of X-ray intensities from various resonance lines.

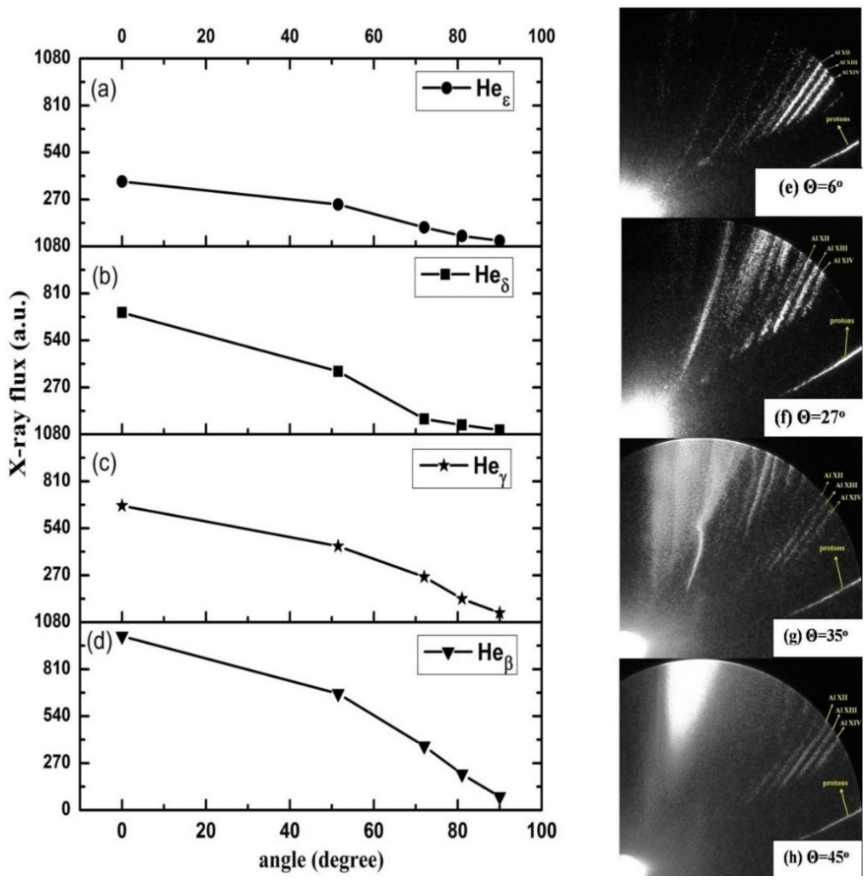

Figure 3.5 (a-d) *Variation of intensity of K-shell resonance lines He$_\beta$, He$_\gamma$, He$_\delta$ and He$_\varepsilon$ with respect to angle from target normal, (e-h) images of charge states of Al ions detected by a Thomson parabola ion spectrometer as a function of angle between the target normal and the Thomson parabola ion spectrometer.*

3.3 K-shell spectra of Si plasma

The resonance line of Si plasma in He-like and H-like ion stage along with their Li-like satellite and He-like satellite lines respectively are observed. The spectrum includes He-α line

($1s^2$-1s2p), the intercombination line ($1s^2\ ^1S_0$-1s2p $^3P_1$) with Li-like satellite ($1s^22p$-$1s2p^2$) of He-α line and Ly-α (1s-2p) with He-like satellite (1s2p-$2p^2$). The energy level scheme is shown in Figure 3.6.

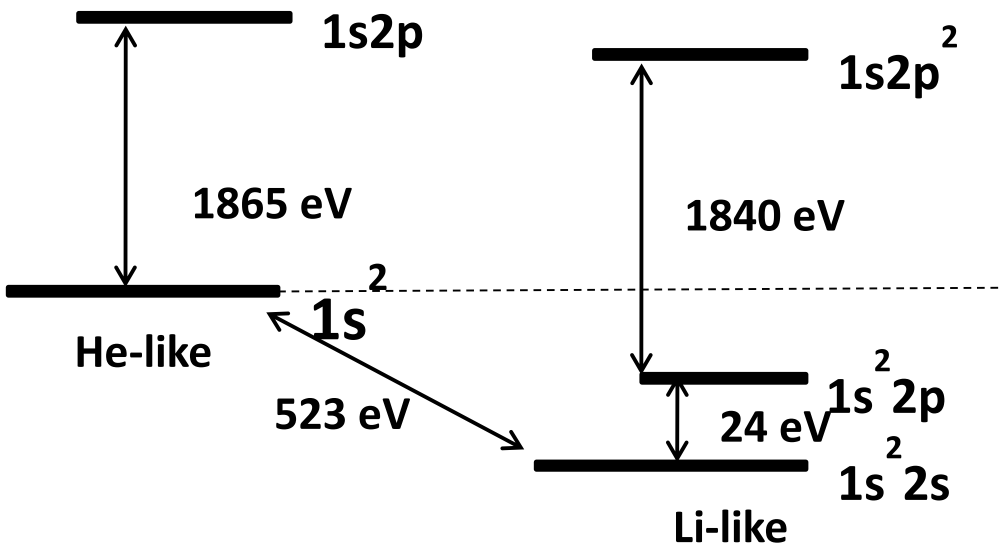

Figure 3.6 *Energy level scheme of H-, He- and Li-like Silicon ions.*

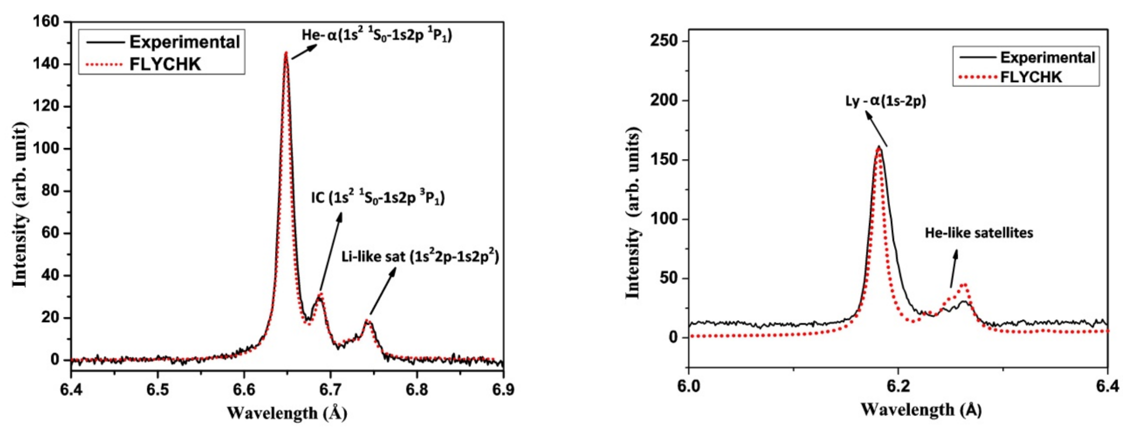

Figure 3.7 *Experimental spectrum matched with FLYCHK for (a) He-like Silicon at T_c = 180 eV (b) for H-like lines at T_c = 380 eV keeping T_h = 1000 eV, f = 0.009 and $n_e = 7 \times 10^{20}\ cm^{-3}$.*

The plasma temperature and density are estimated by taking the ratio of the dielectronic satellite of He-α line, i.e., Li-like satellite (i.e $1s^2 2p$-$1s2p^2$) to its parent resonance line, i.e., He-α line($1s^2$-$1s2p$) and intercombination line ($1s^2\ ^1S_0$-$1s2p\ ^3P_1$) to He-α ($1s^2\ ^1S_0$-$1s2p\ ^1P_1$) and ratio of He-like satellite ($1s2p$-$2p^2$, $1s2s\ ^3S_1$-$2s2p\ ^3P_{0,1,2}$$1s2p\ ^1P_1$-$2p^2\ ^1D_2$) to Ly-α (1s-2p) respectively. For temperature estimation, calculations are carried for both pairs using Eq. (3.7) and using FLYCHK as shown in Figure 3.7. For solving Eq. (3.7), the atomic parameters for lines are calculated using FAC algorithm. From both the cases (calculations and FLYCHK), the temperature corresponding to He-like resonance is 180 eV while for H-like resonance line, it is 380 eV. The same result are obtained for Al plasma.

3.4 L-shell spectroscopy of Cu plasma

L-shell ions are observed in many astrophysical phenomenon and in the laboratory. In astrophysics, the radiation produced by highly charged ions is a key observable from the standpoint of diagnosing the physical properties of non-terrestrial sources. L-shell spectroscopy provides a means to study the average ionization of plasma because the spectrum depends upon the abundance of ions from each charge state which is itself a function of the plasma temperature and density. Mid-Z tracers are used in Inertial Confinement Fusion (ICF) experiments [73] as well as in the production of efficient sources of X-rays [74], in tokomak diagnostics [75], and in astrophysics [76]–[80].In addition, recent astronomical research [81] shows the presence of Cu ions in dwarf stars.

In the recent past, various efforts have been made to investigate L-shell emission from mid-Z elements, such as the line identification of L-Shell copper ions [82]–[89]. However L-shell spectroscopy is still not fully understood and there are relatively few publications detailing the evaluation of plasma parameters based upon L-shell spectra. The identification of L-shell spectra and their use in revealing information about the plasma source is necessary for astrophysical, spectroscopic and laboratory based plasma investigations. The experiment described here is carried out using an Nd: Glass laser with an output energy of 15 J per pulse with a pulse duration of 500 ps. The laser is focused onto a Cu slab to a focal spot diameter of 100 μm using an f/5 lens, yielding intensities up to 4×10^{14} W/cm^2. The experimental chamber is evacuated to a pressure of 4×10^{-5} mbar. An X-ray crystal spectrometer, based upon a Thallium Acid Phthalate (TAP) crystal placed at 45^o with respect to the laser axis, is used for the line-emission studies in the spectral range 7.9-9.5 Å. Two stacked aluminized polycarbonate foils (Alexander Vacuum Research, Inc., trade name: B-10) having 1/e cutoff of 0.9 keV were used to prevent the scattered visible light from entering the spectrometer. The TAP crystal spectrally resolves X-ray emission from the laser produced plasma. The reflected X-rays are detected by an X-ray CCD camera (Model VISION 4M, from Rigaku innovative) which has a spectral resolution of 25 mÅ. A schematic of the crystal spectrometer along with the experimental setup is shown in Figure 3.8 with the sample image of a recorded X-ray spectrum.

The experimental spectrum consists of transitions corresponding to Oxygen (O-) (Cu XXII), Fluorine (F-) (Cu-XXI), Neon (Ne-) (Cu-XX) ions. The formation of these multiply charged ions takes place via collision of free electrons with atoms. The highest charge state of Cu in the present experiment is O-like with an ionization potential of 1.9 keV followed by F-like (1.8 keV) and Ne-like (1.69 keV).

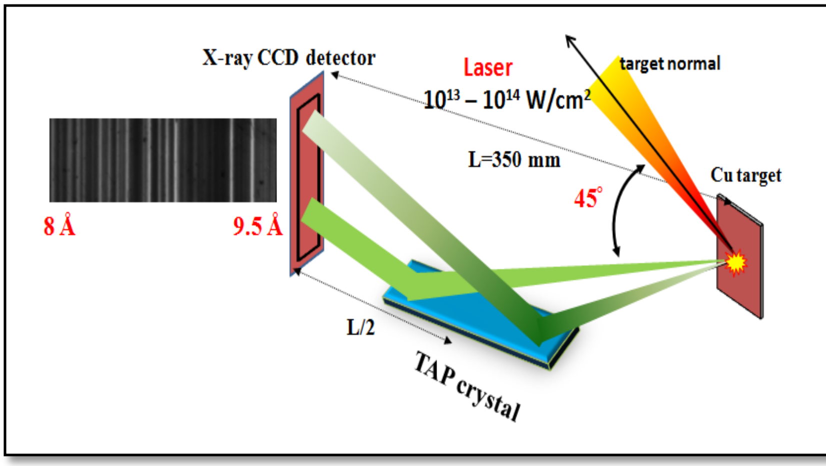

Figure 3.8 *Schematic of the experimental setup.*

The Ne-like ions are easy to produce due to the low energy requirement and the closed-shell ground-configuration in these ions. The shell configuration of Ne-like ions is $1s^2 2s^k 2p^l$ (k=1,2; l=1 to 6). There are in total seven Rydberg series of dipole transitions from $2s^2 2p^6$-$2s^2 2p^5 nl'$ and $2s^2 2p^6$-$2s2p^6 nl'$. A standard notation for Ne-like lines is followed as provided in literature [84] nA: 2s-$np_{3/2}$, nB: 2s-$np_{1/2}$, nC: $2p_{1/2}$-$nd_{3/2}$, nD: $2p_{3/2}$-$nd_{5/2}$, nE: $2p_{3/2}$-$nd_{3/2}$, nF: $2p_{1/2}$-ns, nG: $2p_{3/2}$- ns. The procedure followed for identification of lines and calibration of wavelength is discussed below.

First the identification of the wavelength of the spectral lines is done by ray-tracing, considering the location of the crystal and detector in addition to the dispersion curve of the crystal. Then the dispersion curve of the crystal is coupled with the two most intense lines of the Ne-like (2P-4d) 4C and Ne-like (2p-4d) 2D emission, which results in a spectrum with an error of 25 mÅ. Further identification is done using calculations performed with the General Purpose Relativistic Atomic Structure Package (GRASP) code of Grant *et al.*[83], which employs the MCDF method. The configuration interaction has been included for O-like, F-like and Ne-like Cu. Similar calculations have also been performed using the fully relativistic flexible atomic code (FAC). Transition wavelength, oscillator strength, transition probabilities, and line strength are reported for electric dipole (E1), electric quadrupole (E2), magnetic dipole (M1) and magnetic quadrupole (M2) transitions from the ground level. First, for validation of our code, we match our generated data for some well-studied materials such as Aluminum and Silicon for which extensive K-shell spectra and data are available in the literature. Then we use the same model for our calculation of the spectral lines of Ne-, F-, O- and Na-like ions. Here, we found some new transitions both in measured spectra and calculation, which are not reported earlier and may be useful for plasma parameter estimation.

We compared our calculated results with the available data in the literature. The calculated results are found to be in close agreement with previous results. Furthermore, we predict some new atomic data which may be important for plasma diagnostics.

For Ne-like Cu, In our MCDF calculations, we have included 51 configurations, $2s^22p^6$, $2s^22p^53l$ (l = 0–2), $2s2p^6\ 3l$(l = 0–2), $2s2p^6\ 4l$ (l = 0–3), $2s^22p^54l$ (l = 0–3), $2s^22p^55l$ (l = 0–3), $2s2p^65l$ (l = 0–3), $2s^22p^56l$(l = 0–3), $2s2p^6\ 6l$ (l = 0–3), $2s^22p^57l$ (l = 0–3), $2s2p^67l$ (l = 0–3), $2s^22p^43s^2$, $2s^22p^43p^2$, $2s^22p^43d^2$, $2s2p^53s^2$, $2s2p^53p^2$, $2s2p^53d^2$, $2s^22p^43s3p$, $2s^22p^43p3d$, $2s^22p^43s3d$, $2s2p^53s3p$, $2s2p^53p3d$ and $2s2p^53s3d$ which give rise to 1016 fine structural levels. We mainly focus on one electron excitation by taking 39 configurations of a single excitation. The contributions of two or more electron excitations on energy levels and radiative rates is negligible.

For F-like Cu, in our MCDF calculations, we have included 27 configurations, $2s^22p^5$, $2s2p^6$,$2s^22p^43l$ $(l = 0–2)$, $2s2p^53l$ $(l = 0–2)$, $2p^6\ 3l(l = 0–2)$, $2s^22p^4\ 4l$ $(l = 0–3)$, $2s2p^54l$ $(l = 0–3)$, $2s^22p^45l$ $(l = 0–3)$, $2s2p^55l$ $(l = 0–3)$ which give rise to 492 fine structural levels

For O-like Cu, in our MCDF calculations, we have included 54 configurations, $2s^22p^4$, $2s2p^5$,$2p^6$,$2s^22p^33l$ $(l = 0–2)$, $2s2p^4\ 3l(l = 0–2)$, $2p^5\ 3l(l = 0–2)$, $2s^22p^3\ 4l$ $(l = 0–3)$, $2s2p^44l$ $(l = 0–3)$, $2p^54l(l = 0–3)$, $2s^22p^35l$ $(l = 0–4)$, $2s2p^45l$ $(l = 0–4)$, $2p^5\ 5l(l = 0–4)$,$2s^22p^36l$ $(l = 0–4)$, $2s2p^46l$ $(l = 0–4)$, $2p^5\ 6l(l = 0–4)$which give rise to 1434 fine structural levels. In our calculations, we have also included the contribution of relativistic corrections such as two-body Breit corrections and QED corrections due to vacuum polarization and self-energy.

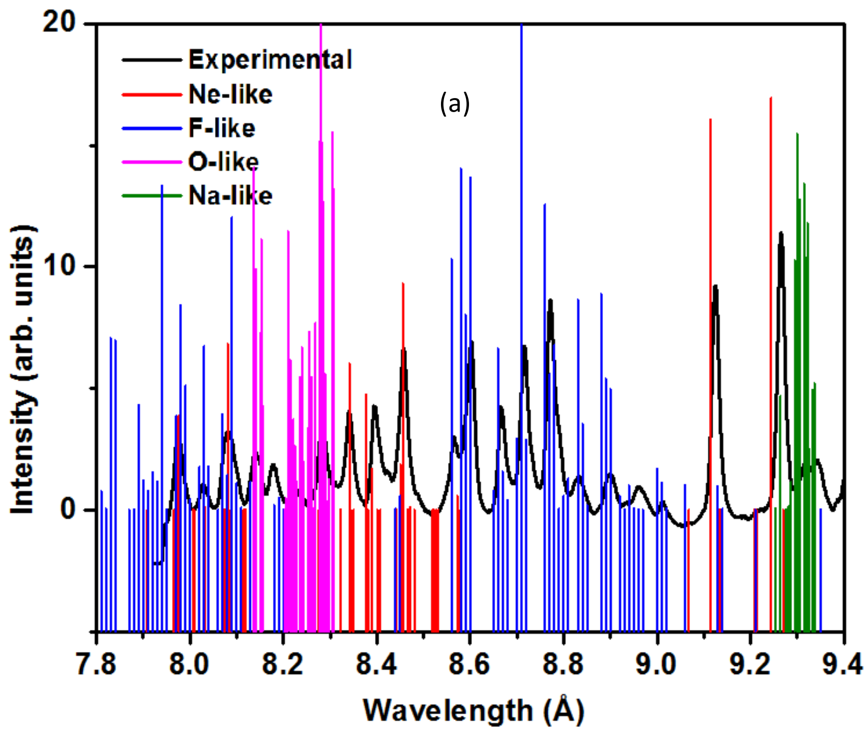

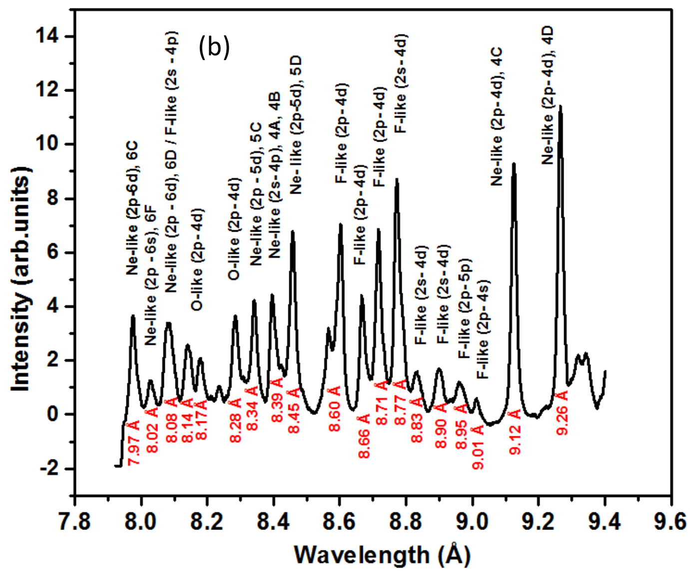

Figure 3.9 *(a) The experimental spectrum with theoretical predicted lines intensity in the spectral range 7.8 Å-9.4 Å recorded for Ne-, F- and O-like ions of Copper. The relative transition rates are drawn. (b) The labeled experiment spectrum at a laser intensity of 1.3 $\times 10^{14}$ W/cm^2.*

For Na-like Cu, in our MCDF calculations, we have included 39 configurations, $2s^2 2p^6 3l$ $(l = 0–2)$, $2s^2 2p^6\, 4l$ $(l = 0–3)$, $2s^2 2p^6 5l$ $(l = 0–4)$, $2s^2 2p^6 6l$ $(l = 0–4)$, $2s^2 2p^6 7l$ $(l = 0–4)$, $2s^2 2p^6 8l$ $(l = 0–4)$,$2s^2 2p^5 3l4l'$ $(l = 0–2,\, l' = 0–3)$ which give rise to 619 fine structural levels. In our calculations, we have also included the contribution of relativistic corrections such as two-body Breit corrections and QED corrections due to vacuum polarization and self-energy.

The transition wavelength, transition rates, and oscillator strengths are calculated. The wavelength and relative transition rates are obtained for different charge states, without considering the ion charge-state populations, and these are shown in Figure 3.9(a) overlaid with the experimentally measured spectrum. All the identified lines are labeled in Figure 3.9(b) and the details of the calculated lines (wavelength, transition rates and oscillator strength) are provided in the appendix. Most of the transition lines in the wavelength range under consideration belong to the 2p-nd transition giving rise to nC and nD pairs and the transitions from the 2p-ns and 2s-nd (n= 4 to 6) levels. The high energy spectral lines are associated with the transition to a $2p_{1/2}$ vacancy in the L-shell and the lower energy spectra result from transitions to fill the $2p_{3/2}$ vacancy.

3.4.1 Determination of plasma parameters

The highly charged ions present in these plasmas are produced via various ionization processes such as photo-ionization, collisional-ionization and auto-ionization. The main recombination processes include radiative recombination, three body recombination and dielectronic recombination. The dominance of collisional or radiative processes decides whether the plasma is in complete thermal equilibrium (CTE), local thermal equilibrium (LTE) or collisional radiative (CRE) equilibrium [82]. This in turn depends upon the temperature and density ranges present in the plasma. The knowledge of the equilibrium state facilitates the interpretation of spectroscopic data to uncover the charge state distribution and populations of the excited states. CTE is not possible in lab environments due to the escape of radiation from the plasma. LTE occurs when the collision time between electrons and ions is short relative to that for other processes taking place in plasma. If LTE is present, then the temperature can be determined easily by the Boltzmann plot method [90]. The collisional radiative equilibrium is non-LTE in the sense that for this to occur, collisions and radiation both must play dominant roles. The solution of this equilibrium lies in solving the rate equations taking care of rates of all collisional and radiative excitation and de-excitation processes.

The validity of applying the LTE equilibrium approximation can be checked by applying the McWhirter's criterion [26] given by

$$n_e \geq 1.6\times10^{12}T^{1/2}(\Delta E)^3 \tag{3.14}$$

where n_e is the electron density, T is plasma temperature, and ΔE is largest electronic transition. In our case, for plasma temperatures greater than 50 eV, the minimum density should be greater than 10^{22} cm^{-3}, for the plasma to be in LTE. The required value is greater than our critical density value. Therefore, we can say that our plasma in not in LTE. We therefore used the CRE based code FLYCHK [27] for the determination of the plasma temperature and density; the detailed procedure is provided below. In FLYCHK opacity effects are included by solving the radiative transport equations.

In the spectrum shown in Figure 3.9 at a laser intensity of 1.3×10^{14} W/cm^2, the identified lines belong to Ne-, F- and O-like copper ions. The intensity of Ne-like lines is higher than that of the F-like lines which indicates that the Ne- like ions are the dominant species. The experimentally observed spectral lines consist of 2p-4d, 2p-5d and 2p-6d transitions. These lines exist in pairs corresponding to resonance lines (nC) with transition $2s^22p^5nd_{3/2}\,^1P_1$-$2s^22p^6\,^1S_0$ and intercombination (IC) (nD) for $2s^22p^5nd_{1/2}\,^3D_1$-$2s^22p^6\,^1S_0$ (n=4 to 6 in our case). The ratio nC/nD is a strong function of the ion abundance which is a function of both the plasma temperature and density [91]. Our experimentally observed spectrum is time integrated but it should be borne in mind that the plasma has strong temperature and density gradients which are a function of time. The Ne-like spectra of Cu dominates for a range of temperatures and densities.

To get a more accurate temperature and density for the most strongly radiating portion of the plasma generated at 1.4×10^{14} W/cm^2, we compare the 4C and 4D lines and the ratio of the 4D to the Na-like IS satellite with the synthetic spectra generated by the FLYCHK code.

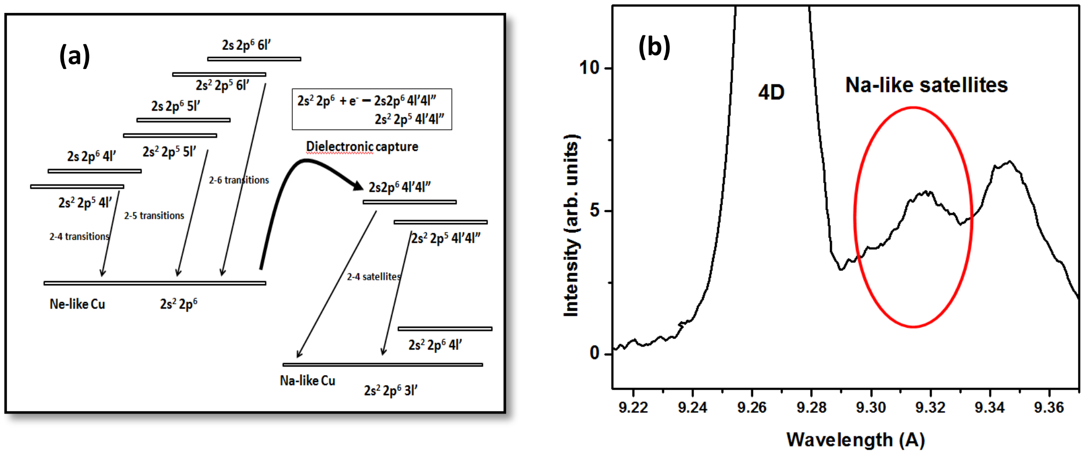

Figure 3.10 *(a) Energy level diagram of resonance lines from Ne-like Cu and their Na-like satellites. (b) Na-like satellite corresponding to Ne-like resonance line.*

The Na-like satellite lines originating from doubly excited Ne-like ions are observed and these have been reported by a few authors [92]–[94] with very high precision. The energy level scheme for Ne-like and Na-like Cu is shown in Figure 3.10(a). The 4D resonance line consists of a Na-like satellite line whose identification is provided in reference 41 with an accuracy on the order of .001 Å. In reference [41], 4C and 4D lines along with several Na-like satellite transitions are given. Due to the comparatively low resolution of our crystal spectrometer, we are not able to distinguish all inner shell satellite lines. In Figure 3.10(b), the experimentally observed satellite transitions are plotted. These consists of transitions from 3s-$4d_{3/2}$, $4p_{3/2}$, $3p_{3/2}$-$4d_{5/2,3/2}$,$4d_{3/2}$-$3s_{1/2}$, $3p_{1/2}$, $3d_{3/2,5/2}$. This satellite emission is also shown by FLYCHK. To match this experimental spectrum, we have run simulations over a wide range of temperatures and densities. Temperature is varied from 100 eV to 400 eV and the density is varied from 1×10^{20} cm^{-3} to 1×10^{21} cm^{-3}.

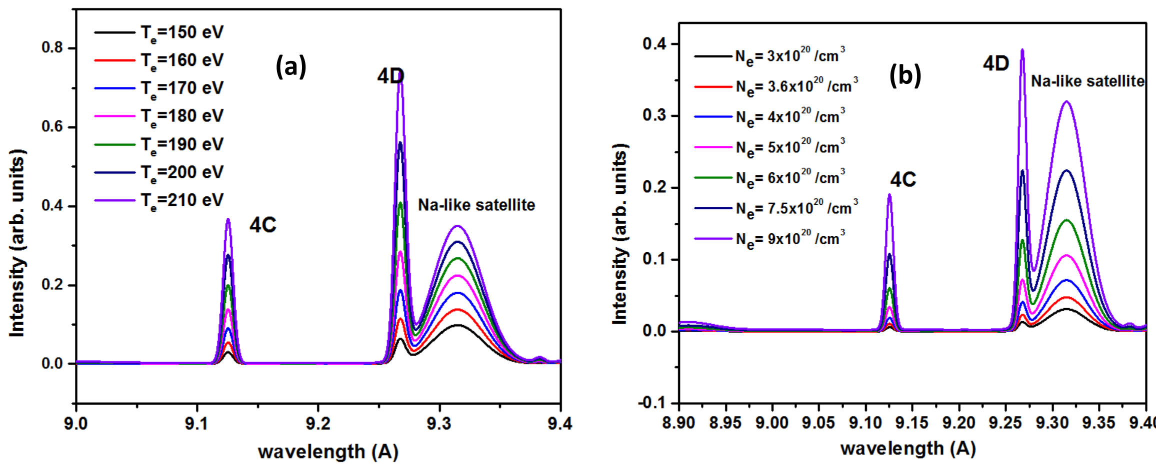

Figure 3.11 *Dependence of the ratio of 4C to 4D lines and Na-like satellite to 4D line on (a) plasma temperature and (b) electron density as calculated by FLYCHK.*

The effect of varying the temperature and density on the ratios (4C/4D and Na-like satellite/4D) is observed by comparing spectra from FLYCHK whilst keeping one parameter (either temperature or density) fixed. The synthetic spectrum is plotted for a temperature range of 150-210 eV (Figure 3.11(a)) and for a density range of 3×10^{20}- 5×10^{20} /cm^3 (Figure 3.11(b)). Figure 3.12 (dotted line) shows the best match regarding the ratio 4C/4D and Na-like satellite / Ne-like resonance at a plasma temperature of 170 eV and a density of 6.5×10^{20} cm^{-3}. Fournier et. Al [88] in their work have shown the effect of varying the escape factor and the fraction of suprathermal electrons on the spectral lines. We included the effect of opacity in our simulation as the level population gets altered with the effects of collisions and photon re-absorption in the plasma. The intensity of a line is a function of the relative abundance of ions and their radiative transition rates and can be written as

$$I_{j,i} = n_j A_{j,i} \tag{3.15}$$

which is a function of both the density of ions and the radiative transition rates. In the presence of plasma self-absorption radiative decay rates are modified $A^{eff} = \varepsilon A_{j,i}$ with ε being the opacity. In our experiment the plasma is considered to be spherical with a diameter of 100 μm. This influences the distribution of charge states of Cu as shown in Figure 3.15(c). Also, the contribution of hot electrons needs to be taken into account.

So, to accurately determine the ratio of resonance lines which are sensitive to plasma temperature and density, the influence of plasma opacity and the fraction of suprathermal electrons (f) have to be taken into account. This also shifts the ionization balance slightly higher. The effect of opacity in the plasma is already introduced in the simulation. The self-absorption results in a reduction of the intensities of the nD lines in comparison to the nC lines. The intensity of our 6C line is more than the 6D resonance line. This indicates a higher opacity in our experimentally produced plasma. But, again, it should be borne in mind that this is a time and space integrated spectrum coming out from different regions of the plasma.

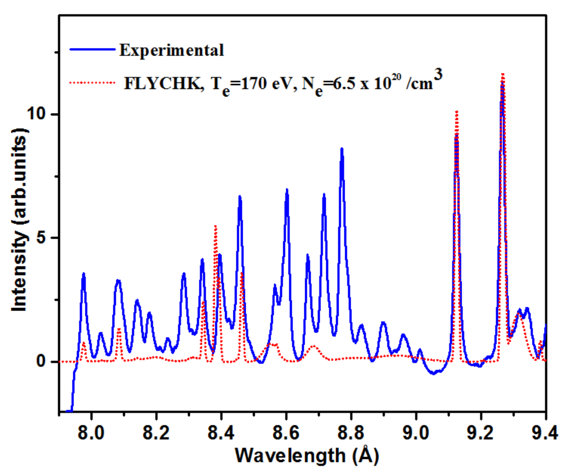

Figure 3.12 *The experimental spectrum (at 1.3×10^{14} W/cm^2 laser intensity) overlaid with a synthetic spectrum at a plasma temperature 170 eV and a density 6.5×10^{20} cm^{-3}.*

The effect of the suprathermal electron temperature and fraction on the spectra is considered as follows. Matching between the synthetic and experimental spectra is performed by keeping the thermal electron temperature at around 170 eV, while the suprathermal electron population temperature is varied from 0.5-1.5 keV and the fraction of energy in the suprathermal electron population is also varied from 0.005-0.1. An increase in the suprathermal electron temperature results in an alteration of the satellite to resonance intensity ratio and an increase in the fraction of suprathermal electrons raises the abundance of F-like ions and hence corresponding intensity ratios. The increase in f-value also results in a lowering of the intensity of the Na-like satellite line. The F-like lines are not distinguishable in FLYCHK because it follows the super-configuration approach, causing these lines to merge together. After several trials using different combinations of T_c, T_h and f the best match between the experimental and stimulated spectra is found to occur at T_c=150 eV, T_h=1000 eV, f=0.008 and density = 4.5×10^{20} cm^{-3}, as shown in Figure 3.13.

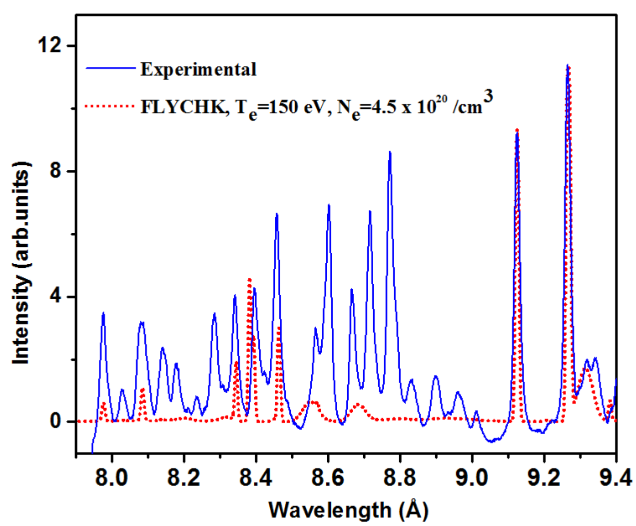

Figure 3.13 *Best match of experimental spectrum with synthetic spectrum at T_c=150 eV, T_h=1000 eV, f=0.008 and density = 4.5×10^{20} cm^{-3}.*

3.4.2 Effect of laser intensity on the abundance of charge states in the plasma

Here, the laser intensity is changed to see its effect upon the abundance of ions of different charge states. These spectra, taken at different laser intensities are plotted in Figure 3.14(a). The intensity of all of the lines increases with an increase in the intensity of the laser. However, the extent of the change of the intensity of the lines from different charge states differs. This is due to the direct dependence of the ion charge state populations on the plasma temperature and density. In Figure 3.14(b-c), the zoomed part of the highlighted region is drawn. Four pairs of charge states (labeled as I, II, III and IV) are compared at varying laser intensities. The first two pairs indicate the increase in O-like Cu ions in comparison to Ne-like and F-like ions and pairs of lines in sections III and IV show comparison of F-like with Ne-like ions.

When the laser intensity is low (1.3×10^{14} W/cm^2), the intensities of Ne-like ion related emission are enhanced in comparison to F-like and O-like emission indicating the abundance of Cu XX ions in comparison to Cu XXI and Cu XXII ions in the plasma. When the laser intensity increases, the intensity ratio of Ne- like ions to F-like ions (shown in circle III and IV) decreases and the intensity of the F-like line at 8.27Å exceeds the intensity of the Ne Like line at 9.12 Å at a laser intensity of 2.4×10^{14} W/cm^2, whilst it is lower at a laser intensity of 1.3×10^{14} W/cm^2. These observations indicate that with increased laser intensity, the population of F-like ions relative to Ne-like ions increases. At the same time, it can also be seen that, on further increase of laser intensity, O-like ions become increasingly prominent until O-like emission dominates at 4.0×10^{14} W/cm^2.

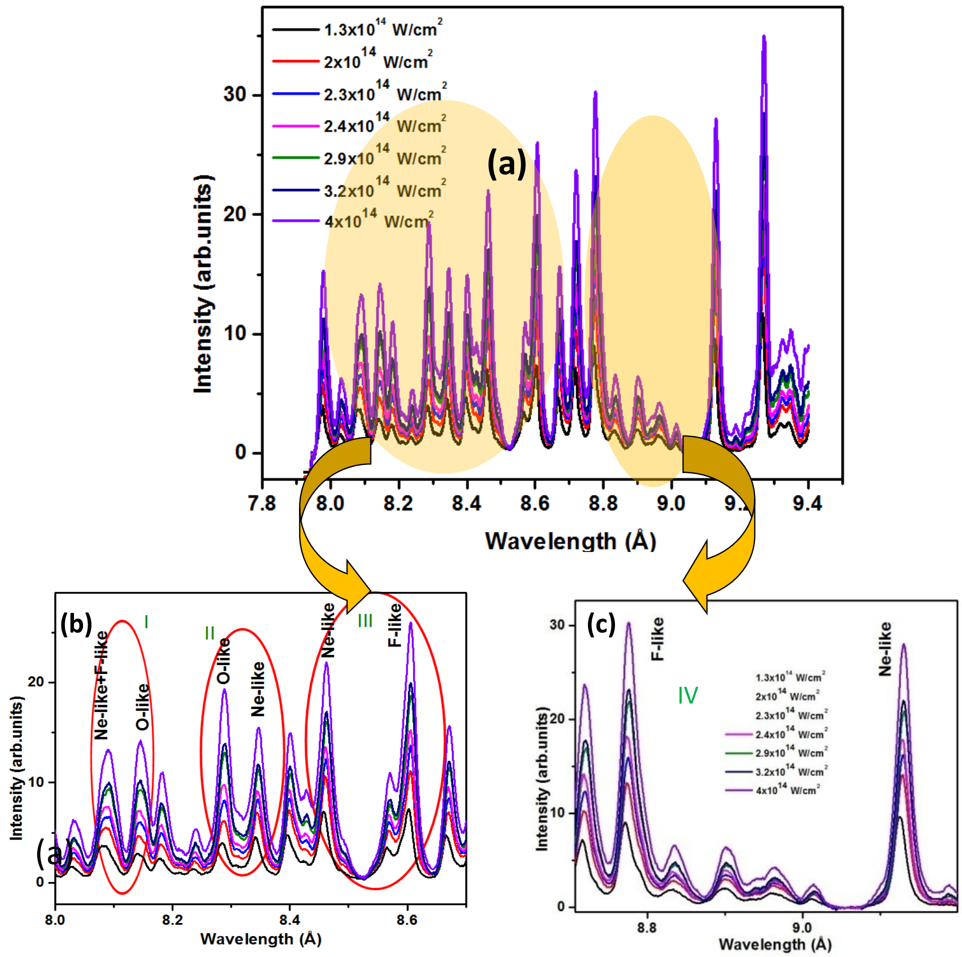

Figure 3.14 *(a) Experimental spectra at various laser intensities (b & c) zoom of part (a) to show a comparison of the populations of Ne-like, F-like and O-like ions at different laser intensities.*

This indicates that the population of Cu XXII ions is more than the population of F-like and Ne-like ions at this intensity. The difference in intensity from O-like ions as compared to Ne-like ions is large in the circled zone II as compared to zone I. This may be due to the fact that in the circled zone I, the Ne-like line is accompanied by a F-like line and by increasing the laser intensity, the population of both F-like and O-like ions increases which results in the intensity of both lines being increased. At 3.2×10^{14} W/cm^2, O-like emission starts to dominate Ne-like and F-like emission. To validate our measurements, we performed FLYCHK simulations to evaluate the charge state distribution and abundance of the charge state of Cu ions at different plasma temperatures and densities with and without the effect of opacity. In the first case, we fixed the plasma density to 5×10^{20} cm^{-3} keeping the opacity off and changing the plasma temperature. The charge state distribution and relative population of the main contributing ions (Ne, F and O-like Cu ions) at different temperature are shown in Figures 3.15(a-b). Without opacity, it is observed that the population of Ne-like ions starts dominating at temperatures greater than 150 eV and this continues up to 400 eV. This contradicts our experimental observations where an increase in the laser intensity (plasma temperature) results in the dominance of emission from higher charge states.

When the effect of opacity is included, the abundance of F-like ions rises abruptly and their relative population becomes more than the Ne-like Cu above 200 eV as shown in Figure 3.15(c-d). Above 210 eV, the population of O-like lines starts dominating and becomes equal to Ne-like at 280 eV. As the temperature is increased even further O-like ion emission dominates F-like ion emission above 350 eV. We have measured plasma temperature and density at a laser intensity of 1.3×10^{14} W/cm^2. For the measurement of temperature and density, we have used only Ne-like lines. FLYCHK does not show the transitions corresponding to F-like and O-like ions which could otherwise be used for further investigation of plasma temperature and density. The presence of O-like lines for the laser intensity 1.3×10^{14} W/cm^2, as shown in Figure 3.15(b-c) indicates the plasma temperature is 250 eV (where O-like ions start to become apparent). As already mentioned our integrated spectrum comes from plasma that has large temperature and density gradients.

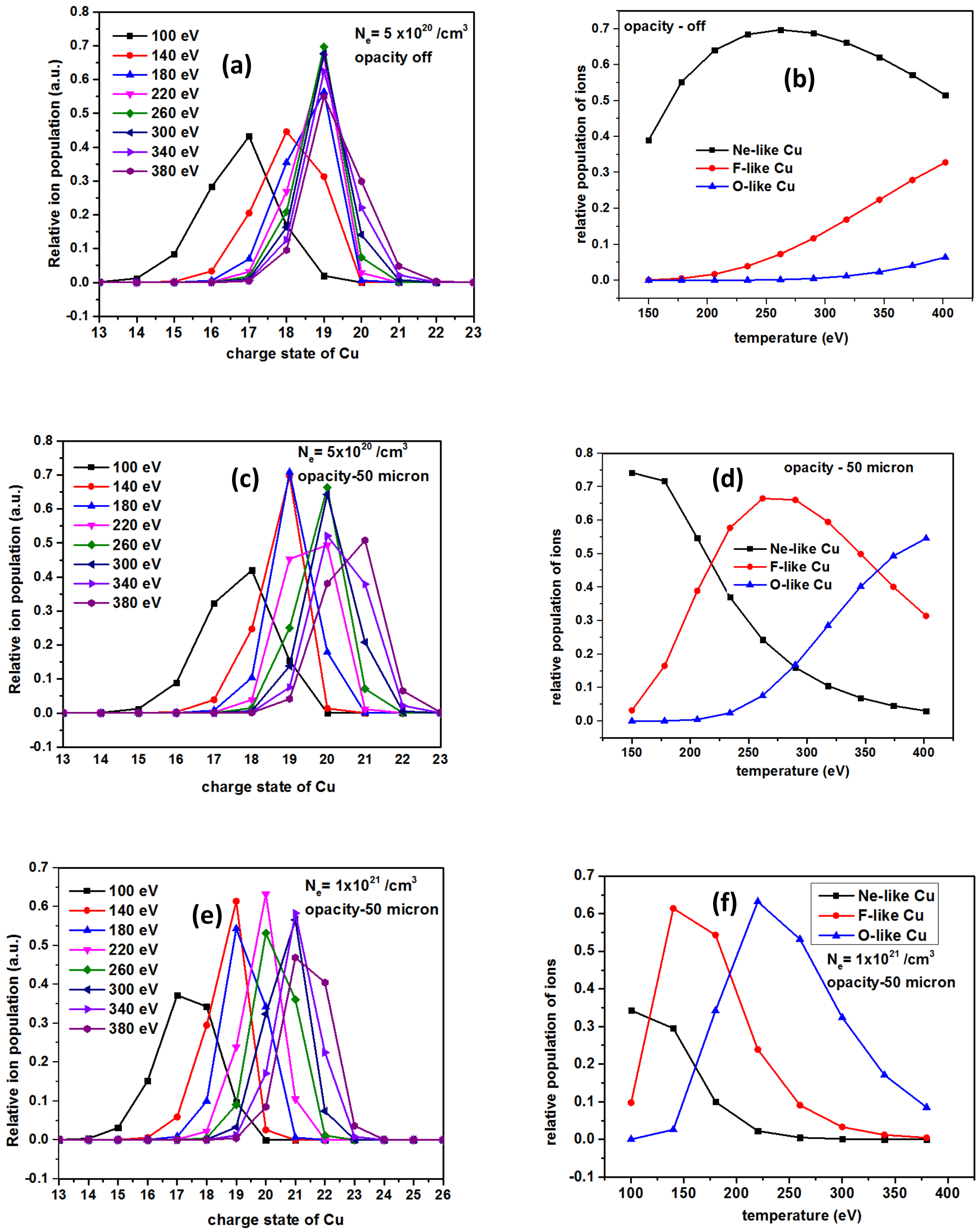

Figure 3.15 *Distribution of charge states of copper for different temperatures at an electron density of 5×10^{20} cm^{-3} as obtained from FLYCHK simulations (a) excluding the effects of opacity, and (b) including the effects of opacity. Distribution of Cu XXII (O-like), Cu-XXI (F-like), Cu-XX (Ne-like) ions at the same electron density as obtained from FLYCHK simulations (c) excluding the effects of opacity, and (d) including the effects of opacity. The distribution of charge states of Cu at 1×10^{21} cm^{-3} is obtained from FLYCHK simulations (e) excluding the effects of opacity (f) including the effects of opacity.*

So, X-ray emission is taking place from hotter regions as well as from colder regions. So, at a laser intensity of 1.3×10^{14} W/cm^2, our plasma temperature is in the range of 150 to 250 eV. When the laser intensity increases, the plasma temperature increases and with it the populations of higher charge states. Dominance of O-like ion emission over Ne-like and F-like ion emission at a laser intensity of 4×10^{14} W/cm^2 indicates that the plasma temperature is on the order of 350 eV, as can be judged from Figure 3.14(d). So, for the laser intensity 1.3×10^{14} W/cm^2- 4×10^{14} W/cm^2, we can say that the plasma temperature ranges from 150 to 350 eV in the region responsible for the bulk of the emission.

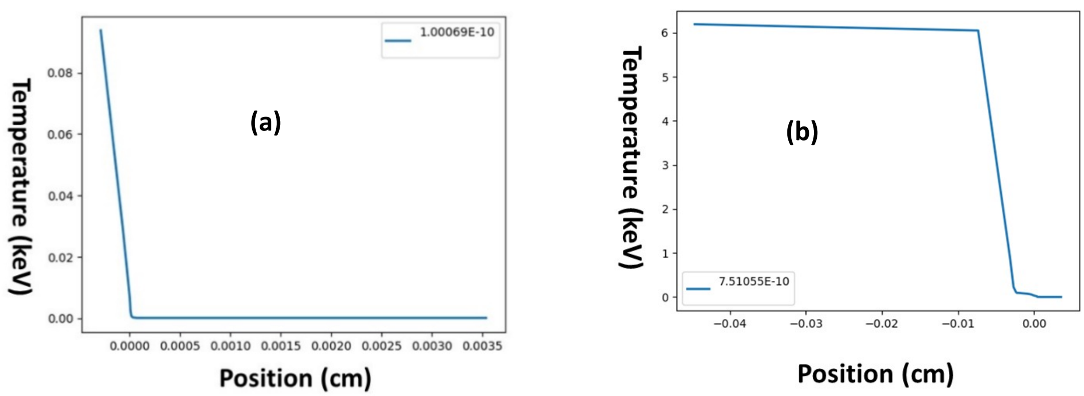

Figure 3.15 *Spatial Temperature profile of plasma generated by* HYADES *after irradiation of 1×10^{14} W/cm^2 laser intensity at time delays of (a) 0.1 ns (b) .7 ns with respect to laser.*

To better understand our results, simulations were performed using the 1-D Lagrangian radiation hydrodynamics simulation code HYADES [95]. These simulations used tabulated SESAME equation of state and a multi-group diffusion approximation for radiation transport based on an average atom LTE ionization model. Electron transport was handled by a flux-limited diffusion approximation. The HYADES results show that there is a region of the plasma that corresponds to the combination of temperature and density conditions that have been estimated above. These simulations further highlight the extremely broad range of plasma density and temperature conditions present, showing temperatures ranging from keV in the low-density corona to below 1 eV in the dense target, with electron densities ranging from below 10^{19} in the corona[1] to above 10^{24} in the shock wave that is propagating into the solid target. Summing over these many different conditions, with appropriate weighting for optical depths, would be required to more accurately reproduce the experimental spectra.

3.5 Summary

In this chapter, spectroscopic studies are described involving X-rays produced by a 30J/500ps Nd: glass laser in the intensity range of 1×10^{13} - 4×10^{14} W/cm^2 interacting with solid targets. Long pulse lasers are effective in producing line emission spectra originating from highly charged ions in contrast to the ultrashort pulse where inner shell characteristics lines (K_α) are produced due to hot electrons. In the case of Al plasma, the experimental spectrum contains He-β, γ, δ, ε and H-like lines. The intensity of lines is found to vary with laser intensity according to a power law $E \propto I^\alpha$ with α=2.2, 2.3, and 2.4 for He_β, Heγ, and He_δ respectively. Plasma parameters have been derived by analyzing the K-shell emission spectra. The plasma temperature is calculated via the ratio of Li-like satellites to the He_β line and the He-like satellite to the Ly_α line. The temperature and densities calculated by analytical models are 260- 420 eV and $1.6\text{-}2.8\times10^{20}$ cm^{-3} respectively which is in good agreement with the results obtained by FLYCHK (T_e=160eV, T_h=1 keV, f=0.008 and n_e=5x10^{20} cm^{-3}). The angular distribution of the resonance lines along with ionization dynamics is studied. The opacity effects are more pronounced for lines with transition from low n lines e.g. He_β ($1s^2$-1s3p)

[1]Note that since this is a 1-D code the densities will be significantly over-estimated in the extremities of the corona.

whereas opacity effects reduce for higher values of transition states n i.e. He_γ, He_δ and He_ε. The L-spectra consists of Ne, F and O- like Rydberg resonance lines along with some of the inner-shell satellite-lines of Copper plasma, in the wavelength range of 7.9 - 9.5Å. The identification of spectral lines and atomic calculations were performed using a Multi-configuration Dirac-Fock (MCDF) method. Lines generated using this simulation are in good agreement with the data available and our experimental results. The average temperature and density of the most strongly radiating portion of the plasma is 150 - 350 eV and 4.5×10^{20} cm^{-3} for laser intensities in the range 1.3×10^{14}- 4×10^{14} W/cm^2. Both the simulations performed using the FLYCHK code and the hydrodynamic simulations are in good agreement with our experimental results. The effect of change in laser intensity on the L-shell spectrum of Cu is studied which indicates the switching between lower (Cu XX) and higher charge states (Cu XXI, Cu XXII) at higher laser intensities.

Chapter 4

X-ray and Ion Emission Studies from Plastic Foams

4.1 Introduction

The increase in the X-ray yield from laser produced plasma is a topic of interest from several decades due to its vast applications in basic research as well as in fusion research. The laser to X-ray conversion efficiency in solid density targets can be very low due to the reflection of most of the laser light from the critical density surface. Many schemes have been implemented to increase the conversion of laser to X-rays so that LPP X-rays sources can be utilized in several other applications such as point projection absorption spectroscopy [96], [97], X-ray radiography [98], X-ray microscopy [99], time resolved diffraction of materials under extreme conditions and opacity measurement [100]. The fraction of laser energy absorbed in the target plasma can be increased in different ways. It is possible to use a laser pre-pulse to produce a plasma corona prior to the arrival of the main pulse, so that the latter would interact with this low density pre-plasma as a result path of absorption in the rarefied subcritical-density expanding plasma would therefore become longer [101]. Another way involves use of mixed-composition targets with different ion charge states Z to improve the conversion efficiency by increasing the Roseland mean opacity coefficient in the mixture of ion charge states [102]. Also, there are various studies on X-ray yield enhancement by slightly displacing the target relative to the best-focus position, which is termed the plasma volume effect [103]. In recent years, to achieve a higher X-ray yield, many experiments and theoretical simulations have been carried out on gas targets [104] and with structured targets [105], for instance, targets covered with nanoparticles or nanowires [106]. With a view to a longer absorption length and volume absorption, aerogel foam structure in the form of a three-dimensional spatial network [107] have been an impressive targets. Low density foam targets of different materials, which may be referred to as stochastically volume-structured targets, are capable of providing absorption of up to 90% of the energy of laser radiation incident on the target. Low Z targets with low-density three-dimensional networks make up a preferred class of materials, which offer certain advantages like the smoothing of the laser radiation profile [108], shock amplitude enhancement [109], and reducing the spatial shock profile non-uniformities and ultimately suppression of R-T instability. Foams with a density gradient have been employed for obtaining an inclined density profile for isentropic compression [110] and as a CH ablator in direct inertial confinement fusion [111]. Many authors have noted that foam targets provide a several times higher absorption than conventional solid targets resulting better X-ray emitter than solid targets [112]. Considerable research interest has been drawn in the interaction of high-power laser radiation with foam targets of a broad density range: from 1 mg/cm^3 to hundreds of mg/cm^3, i.e., from subcritical densities to supercritical ones [113]. The field is highly contributed by the study the interaction of high power pulsed laser with various types of foam targets such as agar-agar [114], plastic foam [115], carbon [116], aerogel foam [117], TAC [118]–[124], gold foam [125]–[128]. Foam targets are also used in the modelling of astrophysical effects in laboratory conditions [129]. For instance, these materials were employed in the modelling of the interaction of circumstellar matter with an exploding stellar shell as well as of the formation of supernovae remnants [130], [131]. Numerous attempts have been made to explain the enhanced X-ray radiation yield properties of foams. For instance, in the numerical simulations of a gold foam [132], it was found that the target heating was determined by the supersonic ionisation wave, unlike the heating of a continuous target. There are many experimental and theoretical data describing the emission of X-ray radiation from low-density foams. However, experimental investigation on detailed analysis of the characteristics of the ions emitted by such targets is very less. This chapter is dedicated to precisely studying the X-ray emission along with the spectroscopic measurement of the ion flux from low-density Cellulose Triacetate (TAC) foams [133], [134].

4.2 Experiments techniques and targets

In the present experiments, the output pulse energy utilized up to 10 J with peak intensity of 2.5×10^{14} W/cm^2 at the target surface. The experimental setup is schematically shown in Figure 4.1. To observe the plasma evolution (the emitted ions), four Faraday ion collectors were positioned at different (22.5°, 45°, 63°, and 67.5°) with respect to the target normal. To observe the charge state distribution with energy, Thomson Parabola Spectrometer (TPS) is used. The details of ion collector and TPS are provided in Chapter 2. The hard X-ray radiation flux was recorded by silicon photodiodes covered with different filters for studying different ranges of the X-ray spectrum: a 20-μm thick Al foil for extracting a range of 4-16 keV or 5-μm thick Ni foil with a 5-8.3 keV transmission band. To measure the spatial and temporal shapes of the laser pulse transmitted through the low-density polymer target, a beam splitter was placed in the path of the transmitted beam. In this case, one part of the beam was directed to a fast photodiode and the other part to a beam profile meter. An Alphalas photodiode with a rise time of 40 ps was connected to an Agilent Technologies oscilloscope with a transmission band of 2.5 GHz.

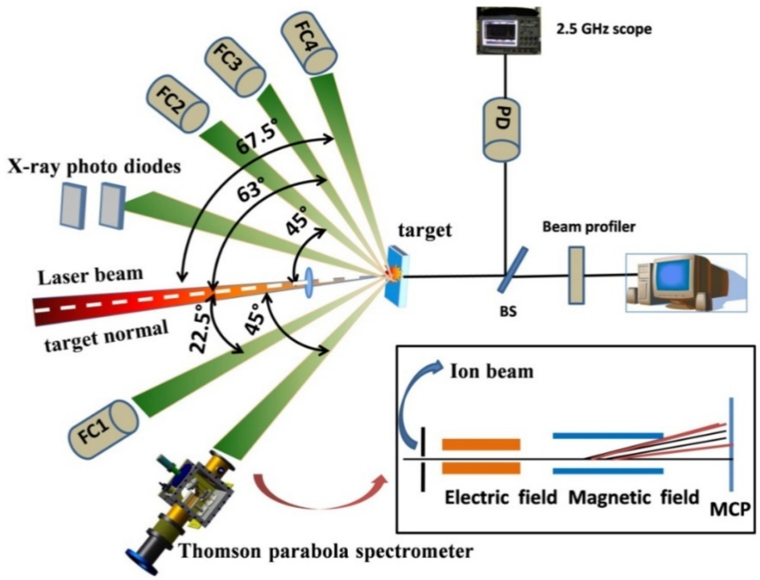

Figure 4.1 *Schematic of experimental set up*

The visually transparent, plane-parallel samples of cellulose triacetate (TAC) $C_{12}H_{16}O_8$ have a highly regular structure in the form of a three-dimensional network polymer (Figure 4.2). The average length, diameter and density of the fibres are 30-50 µm, < 1 µm and 0.1-0.2 g/cc respectively. All samples exhibited a high repeatability and had an invariable aerogel structure, which was laborious in fabrication and measurement [135]. The absence of closed pores and the stable repetitive structure of three-dimensional spatial network of these low-density targets permit to investigate the properties of the plasma after irradiation by using different diagnostics on the same setup at any time for a long period of time. Laboratory techniques of synthesising such targets were considered, for instance, in ref [136]. The mechanical properties of the foams are much different from the properties of silica aerogels. Figure 4.2(b) showing the SEM records of the 2 mg/cc and 4 mg/cc dense TAC foam.

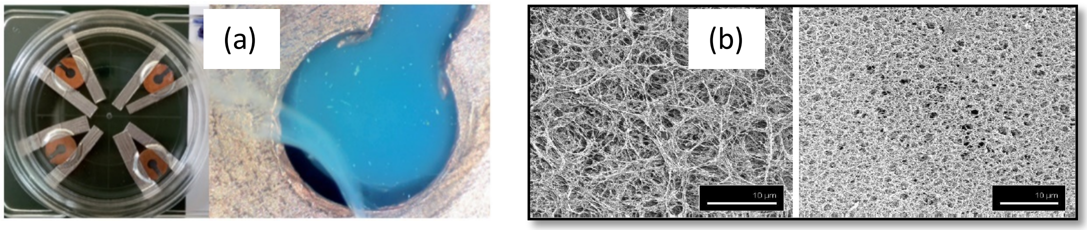

Figure 4.2 *TAC targets with a density of 4 mg/cm^3 (a) Hermetic Millipore box with four targets on metallised mounts prepared for transportation to the laser setup and a microphotograph of a TAC plastic aerogel sample (blue) inside a ring holder. (b) SEM record of 2 mg/cc and 4 mg/cc TAC foam*.

4.3 Laser transmission through TAC foams

The change in the laser temporal profile after passing through low density foam targets are shown in Figure 4.3. In order to remove the contribution of plasma self-emission, we have introduced a band pass filter with 10 nm bandwidth at 1064 nm before the photodiode. It is observed that for higher areal mass density (ρ.x) the pulse duration (FWHM) narrowed down to 360 ps from its original value of 680 ps when passed through the areal mass density of around 600-900 mg/cm^2; it gets further reduced to 176 ps in case of areal mass density of 2000 mg/cm^2 (2 mg/cc, 1000 µm). From the Figure 4.3, it is clear that the laser transmission depends mainly on the areal mass product of ρ.x [where ρ is density in mg/cc and x is target thickness] not on the density of the target. No change in the leading edge of the laser pulse is noticed for different densities of targets. However, the trailing edge of the pulse is getting narrowed down (absorption). This is attributed due to the fast rise time of the laser pulse of our laser system. The rise time of the laser pulse is shorter than the time at which the whole target reaches the critical density and reduces the transparency of the laser pulse.

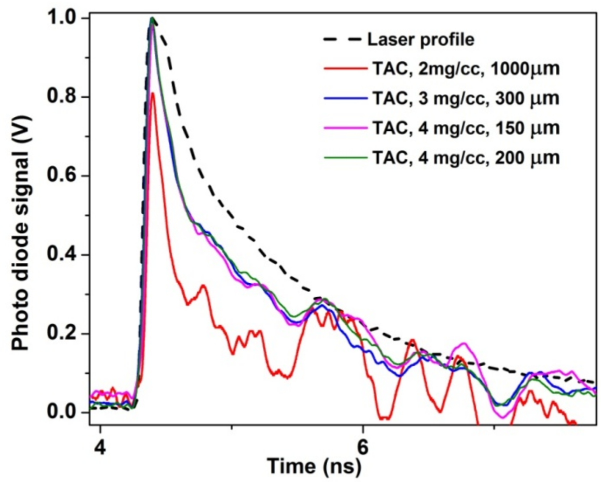

Figure 4.3 *Temporal profile of laser pulse after transmission from low density TAC targets having different areal mass densities.*

4.4 Study of keV X-ray emission from TAC foams

The study of X-ray emission in the spectral ranges namely (4.5-16) keV and (5-8.3) keV from the front surface of the foam targets were studied by keeping the target density fixed and variation in laser intensity (energy) and in other case, laser intensity (energy) was kept fix at 6.18 J and target densities were varied. From Figure 4.4(a), it is observed that the X-ray scales with laser intensity as $I_x = (I_L)^{\alpha}$, where I_x and I_L are the X-ray and laser fluxes respectively and α is the scaling factor and its values for the X-ray flux in the spectral range (4.5-16) keV and (5 -8) keV are 2.3 and 1.8 respectively. Figure 4.4(b-c) show the hard X-ray yield variation with target density (2 mg/cc, 3 mg/cc, 4mg/cc and 10 mg/cc) in the same spectral range, i.e., (4.5-16) keV and (5-8) keV respectively. The X-ray yield increased by a factor of 1.4 to 1.5 times in the under-dense 2 mg/cc foam target compared to over-dense 10 mg/cc in both cases.

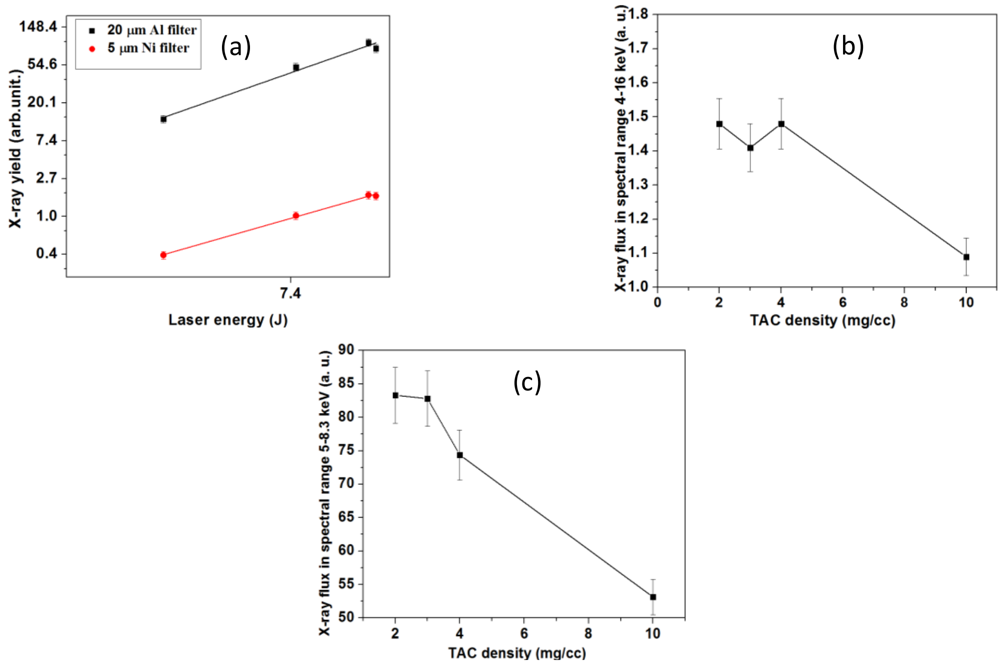

Figure 4.4 *(a) Scaling of hard X-rays using photodiode covered with 20 µm thick Al filter (4 -16 keV) and 5 µm thick Ni filter (5-8keV) for 4mg/cc TAC. Effect of foam density on hard X-ray emission in the spectral range (b) (5 keV-8 keV) and (c) (4.5-16 keV) for 6.18 J laser energy.*

4.5 Ion spectroscopy of TAC foam

4.5.1 Effect of density on convoluted charge states of ion in TAC

The ion emission from the targets of different densities is studied with the help of ion collectors and a high-resolution Thomson Parabola Spectrometer. It is observed that for the same density of the target, the ion flux increases with the laser intensity. Figure 4.5(a) shows the scaling of ion flux recorded by four ion collectors with intensity of laser for TAC target of 4 mg/cc density. The scaling factors for the ion flux recorded at 22.5°, 45°, 63° and 67.5° are 0.5, 1.04, 1.3 and 0.8 respectively. The peak ion flux and peak thermal velocities of the ions increases with the increase in TAC density from 2 mg/cc to 10 mg/cc as shown in Figure 4.5(b-c). It is evident from the ion collector signal placed at 22.5° from the target normal that for lower density target, the TOF profile is broader and is getting narrowed down with increase the density of the target. Similarly, for the IC signal at 67.5°, there are two well resolved peaks present for low density foam targets and separation between the peaks decreases with increase in target density as shown in Figure 4.5(c). Also, amplitude of the second peak is decreasing with increase of density. For 10 mg/cc dense target, both the peaks merged to form a single peak. This can be explained by the fact that the maximum flux and ion velocity are towards the target normal and as we go away from the normal, the flux as well as velocity decreases and hence the time-of-flight resolution increases. This means in both the cases there are two groups of ions but it is difficult to resolve in 22.5° IC case, however, it is resolved in case of 67.5° IC case. But for the case of 10 mg /cc target, single peak is observed. Here, initially it was assumed that these two peaks may be due to different charge states of carbon and oxygen but single peak for 10 mg/cc is contradicting our assumption. After looking the TOF spectrum for 2 mg/ cc for both the ICs (broader width for 22.5° and two almost equal peaks for 67.5°) and single peak in 10 mg/cc for even 67.5° IC, we come to the conclusion that in case of low density foam targets, the laser light is penetrating deep inside the targets and ions are emitted from this reason which is slowed down after passing through the plasma and reaching slightly later to the IC. Similarly, for 3 mg/ cc and 4 mg/cc, there are second peak with reduced amplitude. This reduction in peak is due to lesser laser light penetration in the target and lesser ion coming out form the depth of the target. For 10 mg/cc target, the density is much above the critical density and hence the laser interacts near critical surface resulting single peak.

The angular distribution of ion flux and velocity from various densities of TAC target irradiated at fixed laser energy (4.9 J) are shown in Figure 4.6 (a-b). The angular distribution for the ions flux from different densities show that it is maximum towards the target normal and follow the relation $P(\theta)=P_o\cos^n\theta$, where P_o is the ion flux at the target normal. The values of n for 2, 3, 4, and 10 mg/cc targets are 4.1, 3.7, 3.3 and 3.0 respectively.

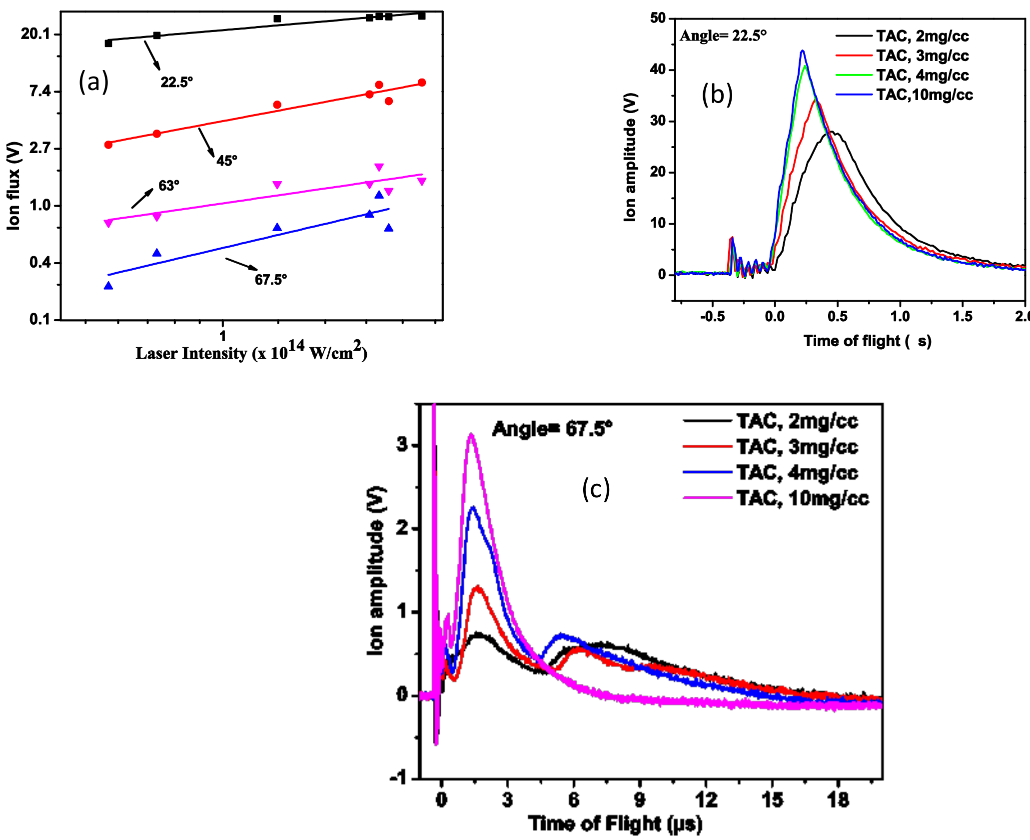

Figure 4.5 *(a) Scaling of four ions collector signals placed at different angles with laser intensity for 4 mg/cc dense TAC target. (b) & (c) Comparison of ions amplitude for four densities of TAC at 22.5° and 67.5° from target normal respectively at 4.9J laser energy.*

The angular distribution of the ion's velocities is plotted in the Figure 4.6(b) which shows that the ion velocities are more isotropic in case of under dense target, though the ion flux is smaller than over-dense targets. This result also verifies the explanation given for the strong explosion resulting in supersonic heat wave travelling in all the direction after the laser light absorption in the geometrical transparency length.

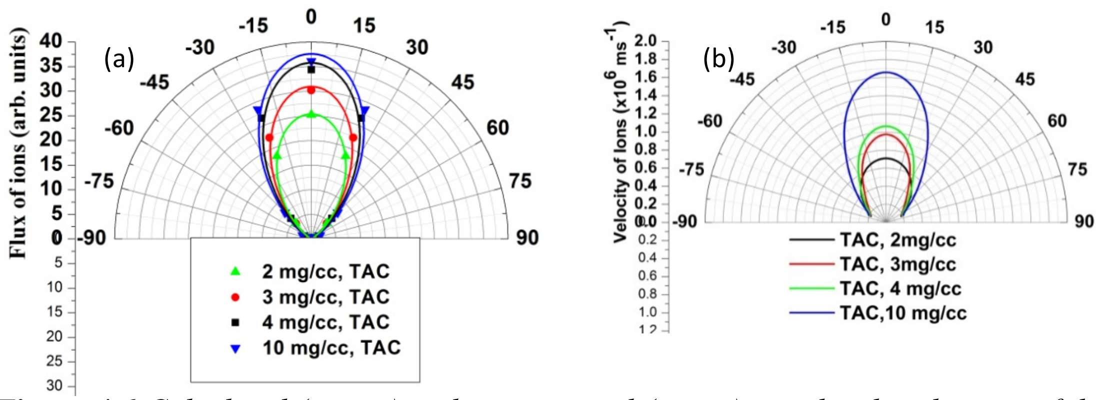

Figure 4.6 *Calculated (curves) and experimental (points) angular distributions of the ion flux P (a) and the ion velocities u (b) for CTA targets of different density for a laser energy of ~4.9 J.*

4.5.2 Effect of density on different charge states of ions in TAC

The Thomson Parabola Spectrometer (TPS) is used to measure energy spectrum of ions of carbon and oxygen. Figure 4.7(a-d) is showing the TPS records for 2mg/cc, 3 mg/cc, 4mg/cc and 10 mg/cc dense TAC target respectively. The TPS data is analysed by plotting synthetic parabolas over experimental images and results are plotted in Figure 4.8(a-d) according to charge states and laser energy. From the Figure 4.8(a-b), it is clear that flux of higher charge state increases towards the higher energy side by increasing the target density. The ion flux of 5th charge state of carbon and 6th charge state of oxygen shows the broader energy range with approximately similar flux all over the range with increase in the target density. The same trend has been seen by the convoluted ion collector signals (Figure 4.5(b-c)) that the flux and velocity is higher for higher density targets.

Presence of less energetic ions in case of lower density TACs indicates less hydrodynamic motion in case of low density TAC foams. However, in the case of over dense targets, the heating is subsonic and the hydrodynamic wave over takes the heat wave and impart energy for ion acceleration and higher ion's flux. The effect of laser intensity on the energy distribution of different charge states of ions is also studied. The results are plotted in Figure 4.8(c-d) for 4th and 5th charge states of carbon and oxygen ions respectively for 4mg/cc TAC target. With increase in the energy of laser, the flux of higher energetic ions increases. The same results are observed for other charge states.

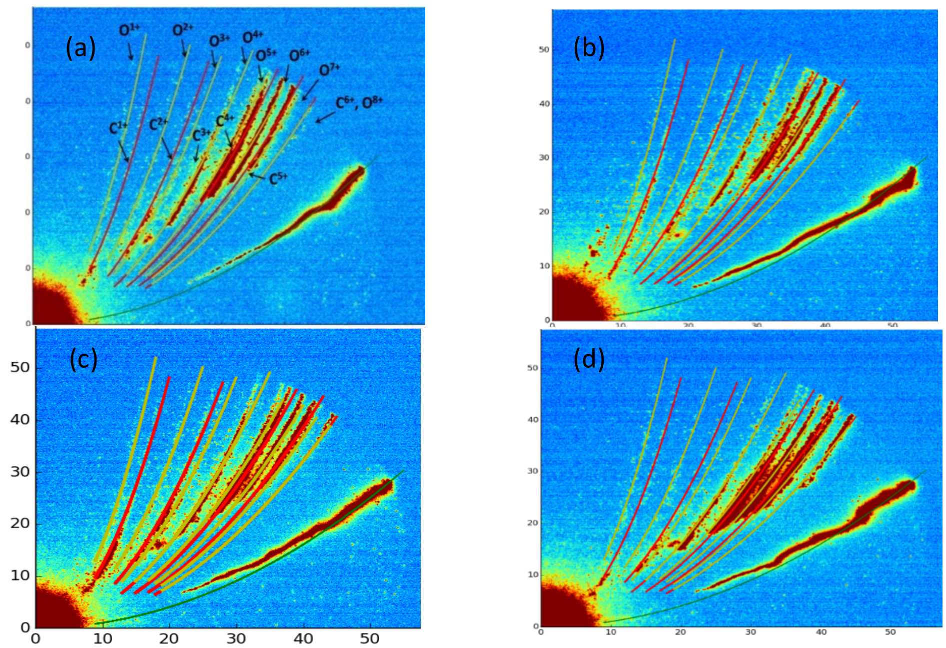

Figure 4.7 *Images obtained with the Thomson mass spectrometer for TAC targets with a density of 2 (a), 3 (b), 4 (c), and 10 mg cm^{-3} (d) for a laser energy of ~4.9 J superimposed with the calculated curves for oxygen (yellow curves) and carbon (red curves) ions.*

4.6 Studies on TAC with Constant areal density

The studies on TAC foams are further explored by keeping areal density constant. The density of TAC foams is 2 mg/cc, 4 mg/cc, 7mg/cc, and 20 mg/cc with thickness 1030 µm, 520 µm, 280 µm and 100 µm respectively. The targets were therefore mass-matched such that the areal density (ρ.r) presented along the laser axis was held constant at around 0.2 mg/cm^2 since the thickness of the targets varies in inverse proportion to the density. X-ray conversion efficiency in different spectral ranges were measured and dynamics targets irradiated with laser was measured using multi-frame optical shadowgraph. The details of the shadowgraphy system is reported somewhere else [56].

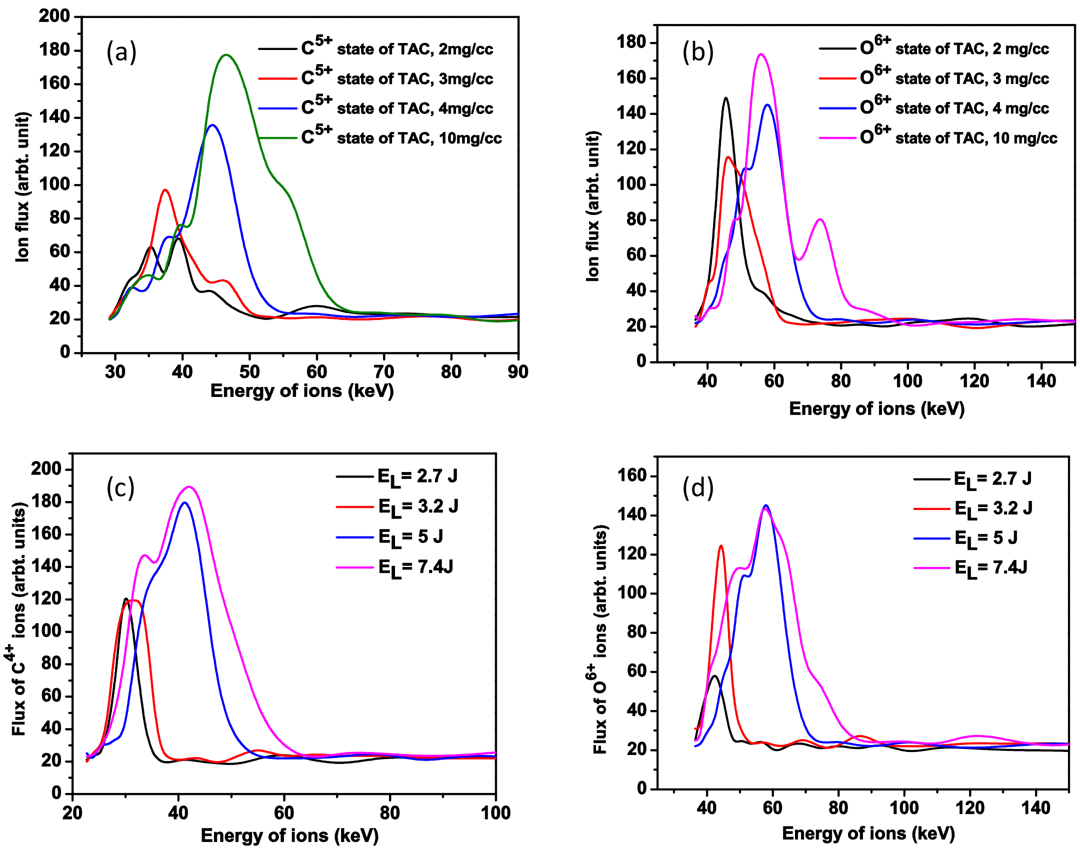

Figure 4.8 *(a) Flux of C^{5+} charge state for four different densities of TAC at laser energy 4.9 J (b) Flux of O^{6+} state for four different densities of TAC at laser energy 4.9 J (c) Flux of C^{4+} charge state for different laser energies for 4 mg/cc TAC (d) Flux of O^{6+} charge state for different laser energies for 4 mg/cc TAC.*

4.6.1 X-ray Conversion Efficiency (CE)

The quantitative measurement of X-ray emissions from the front surface of the mass-matched foam targets at the constant laser energy of 7.5 J in two spectral ranges (5-8 keV) and (4.5-16 keV) is performed. The quantitative measurement of X-ray yield from the foam plasma was carried out by measuring the amount of charge generated by the X-ray photons of different spectral ranges using formula Q (charge created by photon)=V_{out} (voltage generated on oscilloscope) × C_F (capacitance used in pre-amplifier)[137].Hence, the quantum efficiency (total number of electrons generated by X-ray photons) of the photodiodes was measured which also matches with the quantum efficiency data provided by manufacturers. The average energy required to generate 1 electron hole pair is 3.6 eV. Once we know the quantum efficiency and the number of electron-hole pairs generated, we can measure the energy of X-ray flux on the photodiodes. Finally, X-ray energy in l J/Sr is obtained by dividing the total X-ray energy recorded by photo diode with the solid angle subtended by diode on the target (on focal spot). Figures 4.9 and 4.10 show the hard X-ray yield variation with mass-matched targets in these spectral ranges. The X-ray yield (and hence the conversion efficiency) increases by a factor of 2.3 in 2mg/cc (under-dense) foam target as compared to the 20 mg/cc (over-dense) target in both spectral ranges. While there is an excellent match in the trend seen in the data between the simulation and the experiment, there is also some discrepancy between the absolute values. Given that the normalized data matches so well, it is felt that this can be probably explained by the fact that the simulations are one-dimensional and take no account of the intensity variation across the focal spot.

Simulations are performed using the Lagrangian one-dimensional radiation-hydrodynamics simulation code HYADES [95]. The simulations employ a flux-limited diffusion transport model for electron conduction and a multi-group diffusion model of radiation transport with 100 radiation groups, 99 of which are arranged logarithmically between 1 eV and 20 keV (the lower bound of the lowest energy group is set by default at 1 meV). A SESAME equation of state file is employed; however, this file describes the equation of state of a continuous solid, rather than foam. To render the modelling more representative of the foam targets employed in the experiment, a foam model is employed in the simulation that amounts to have a variation in the density of material in the initial Lagrangian mesh from one cell to the next between some non-zero minimum (in this case, 0.1mg/cc) and twice the mean foam density such that the overall mean density of the target is preserved at the value employed in the experiment. An average atom model is employed in the inline multi-group opacity calculation. While comparing with the experimental data, the effective surface area of the target of 1 cm^2 is taken into account in the simulation.

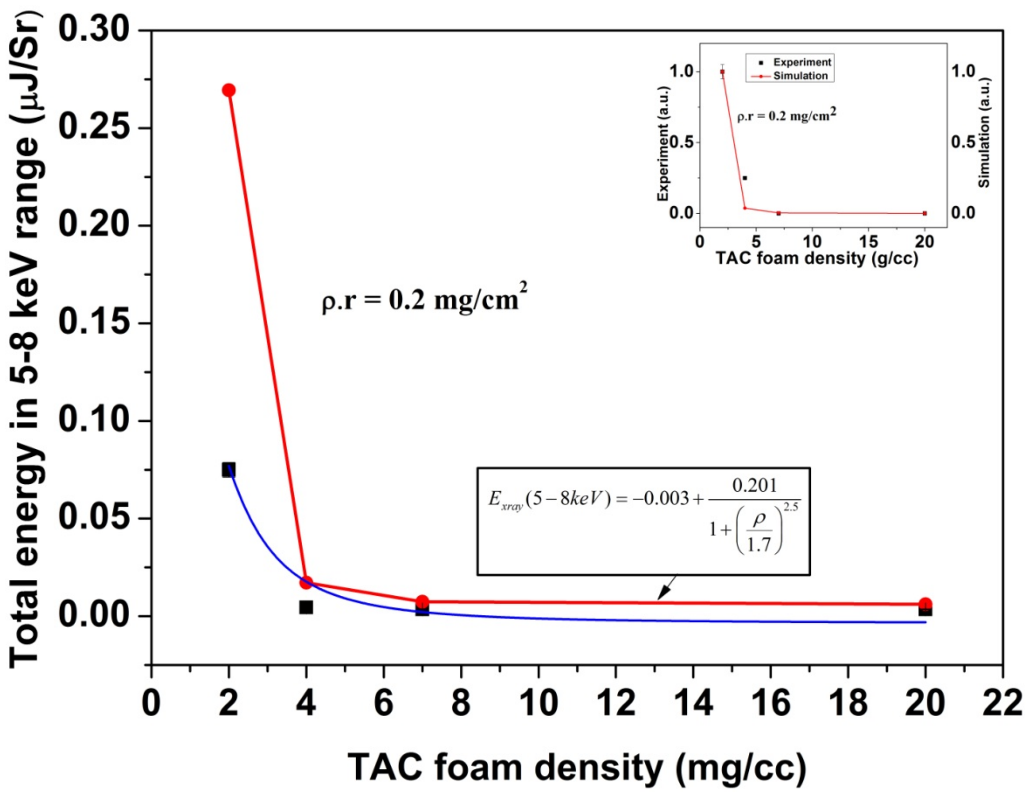

Figure 4.9 *Effect foam density on soft X-ray emission in the spectral range (5keV-8keV) for a constant areal density 0.2mg/cm^2.*

The enhancement in X-ray conversion efficiency in sub-critical targets can be explained as follow. The laser absorption in the porous materials depends on the thickness / diameter of the fibrous wire of solid density and the spacing between them (i.e., pore size) constituting the 3D network of foam targets. The absorption length along the direction of laser beam in which the laser beam cross section overlap with the expanding dense element of the porous material is called the geometrical transparency length and is given as [138]

$$L_T = \frac{9.2\times10^{-8}}{Z}\left(\frac{A}{Z}\right)^2 \frac{T^{3/2}}{\lambda^2.\rho^2} \tag{4.1}$$

Here A, Z are the atomic number and charge of the plasma ions respectively, λ is the wavelength of the laser light (μm), T is the electron temperature (keV) and ρ is the plasma density (g/cc). From the above equation, it is clear that the radiation absorption length is inversely proportional to the square of the density of the foam (plasma). To get exact relation between the experimentally measured X-ray yield and density, a numerical fit was performed as shown in Figure 4.9 and 4.10. The X-ray yield varies with foam density in the two spectral ranges being investigated as follows

$$\boxed{E_{xray}(5-8keV) = -0.003 + \frac{0.201}{1+\left(\frac{\rho}{1.7}\right)^{2.5}}} \quad \text{and} \quad \boxed{E_{xray}(4.5-16keV) = 0.216 + \frac{0.532}{1+\left(\frac{\rho}{2.74}\right)^{2}}} \tag{4.2}$$

The scaling with density is similar to that predicted from the theory as given in Eq. (4.1). The higher yield in the case of hard X-rays can also be explained by the fact that the supersonic heat-wave creates hot plasma which is denser and therefore more efficient in producing multi-keV X-rays. On the contrary, in an over-critical density targets, the formation of the ablation front results in the material in the ablation front (subsonic heating in over-dense plasma) rising to a higher pressure. This results in a higher kinetic energy per unit of mass heated and a higher exhaust velocity than in a sub-critical density target. This is the reason for the enhancement of the coronal emission in the multi-keV X-ray region.

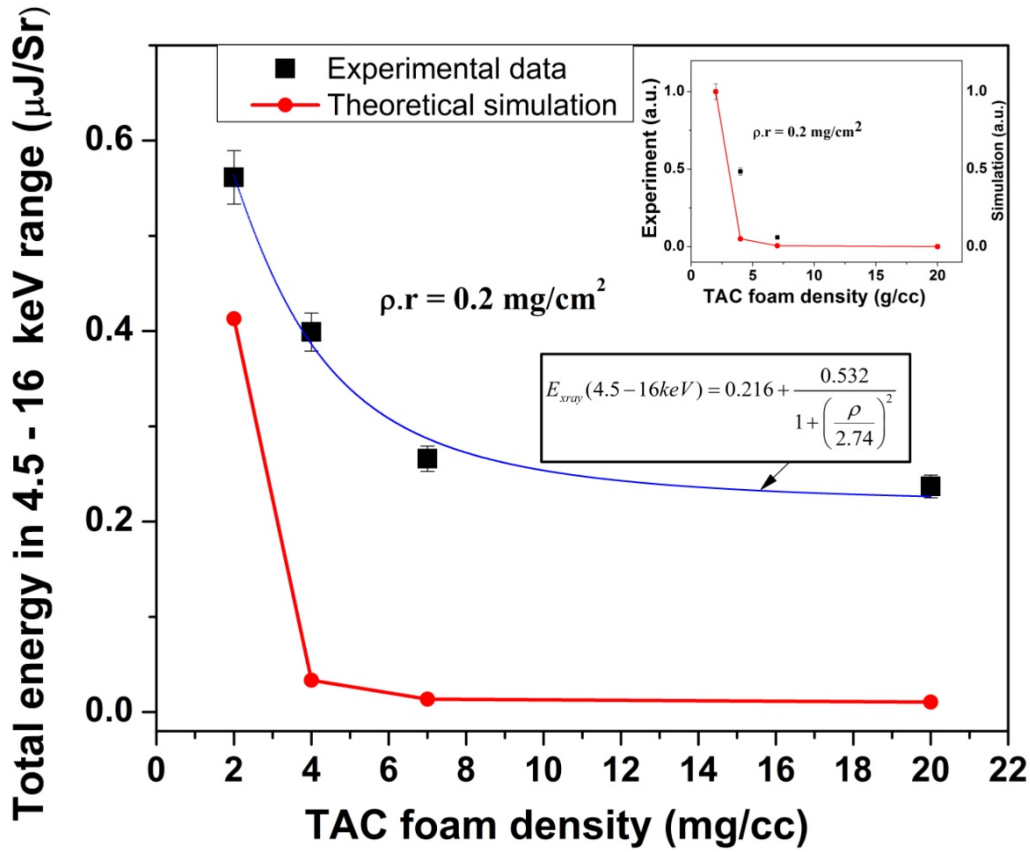

Figure 4.10 *Effect foam density on soft X-ray emission in the spectral range (4.5 - 16keV) for a constant areal density 0.2 mg/cm^2.*

To provide some information on the hydrodynamic behaviour of the targets, we have set up a two-frame optical shadowgraph with a time delay of 4.8 and 8.3 ns with respect to the arrival of the main laser pulse at the target. The shadowgraphs of 2mg/cc and 20mg/cc foam targets at three-time delays, i.e., t=0 ns, t=4.8 ns, and 8.4 ns are shown in Figure 4.11(a-f). From the Figure, it is seen that the plasma diameter and the rear surface accelerated targets exceed the laser focal spot size (100 μm) on the 2mg/cc foam target by several times. The diameter of laser produced plasma reaches approximately 1494 μm at a delay of 8.3 ns due to fast lateral heat transport in the low-density target and reduces to approximately half of this for the 20 mg/cc density target. This enhanced lateral dimension of plasma and rear surface accelerated foam target may be due to the larger volume heating in case of low density foam (2mg/cc). However, it is lower and more directional for 20 mg/cc (supercritical) foam targets which may be due to shock wave and subsonic directional heating.

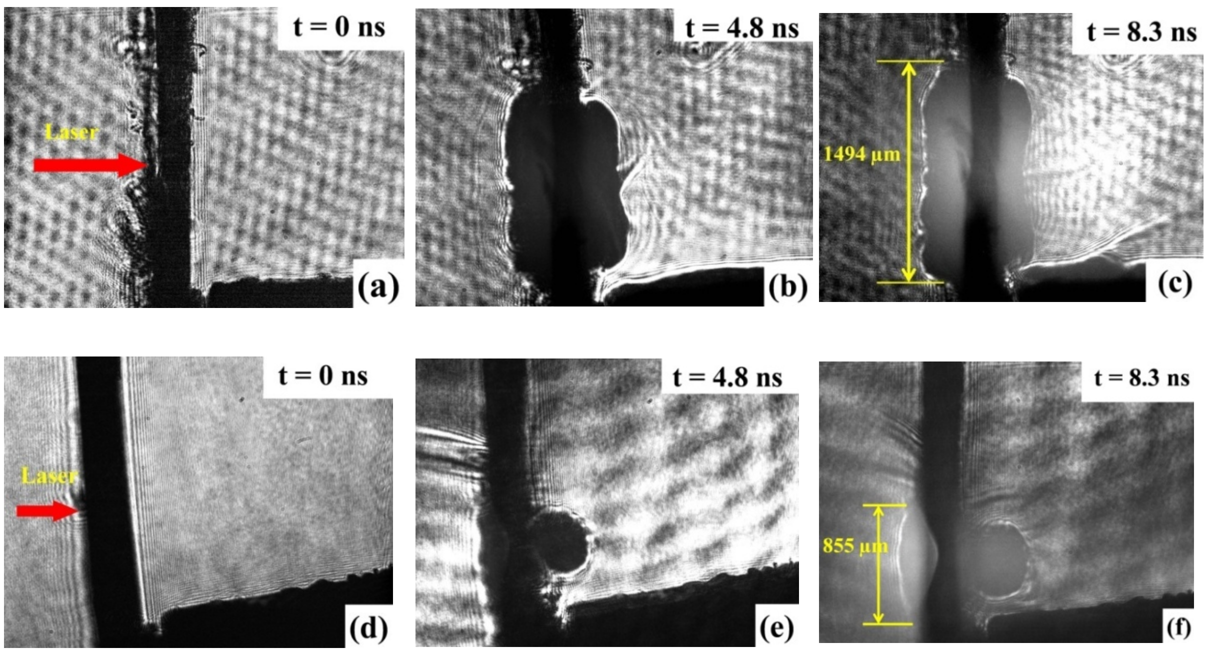

Figure 4.11 *Shadowgraph of 2 mg/cc foam target at a delay of (a) t = 0 ns, (b) t = 4.8 ns, (c) t = 8.3 ns relative to the arrival of the laser pulse, and for the 20 mg/cc foam targets at delays of (d) t = 0 ns, (e) t = 4.8 ns, and (f) t = 8 ns.*

Shadowgraphy results also indicate that in under dense material, the heating is supersonic and volumetric. The enhancement of the volume of X-ray emission is due to initial penetration of laser to a large extent due to the transparency of target. This region is then converted into plasma of under critical density. However, in the case of over-dense material, the heat wave propagation is subsonic, taking the form of an ablation wave. In the case of under-dense (<4 mg/cc) plasma, since the heating is supersonic, no hydrodynamic motion of the dense plasma takes place, and hence, no shock wave formation takes place. Therefore, there is no loss of energy in hydrodynamic motion. In the case of over-dense (>4mg/cc) plasma, shock formation takes place which reduces the conversion of the laser energy to the X-ray energy. Xu et al. [139] has done simulations using the one-dimensional multi-group Radiation hydrodynamics code RDMG and shown that sub-critical density plasma is heated supersonically, and no shock wave formation takes place, while in over-dense plasma, the situation is reversed.

Our simulations demonstrated a similar effect, but, as previously mentioned, now with a "foam-like" initial density perturbation in the simulated plasma. The dynamics of laser light absorption in the low-density porous material is explained by a long homogeneous period during which there exist stochastically distributed sub-critical density regions in the plasma. Thus, the radiation is absorbed in a volume at the so-called geometrical transparency length which is determined by classical collision mechanisms.

4.7 Studies on TAC irradiated with ultrashort laser pulse

The use of ultra-short laser pulses to generate X-rays is also important because X-ray pulse duration is a key parameter for observing rapidly expanding phenomenon such as rapidly expanding plasmas, propagation of shock waves in solids, study of microscopic living cells and so on. The interaction of ultrashort pulses with matter results in production of short intense X-rays pulses having photon energies in the range of hundreds of eV to MeV. Keeping this in view, experiments are performed at TIFR, Mumbai. The soft X-rays emission in different ranges and hard X-ray emission is compared after irradiating the targets with ultrashort pulses.

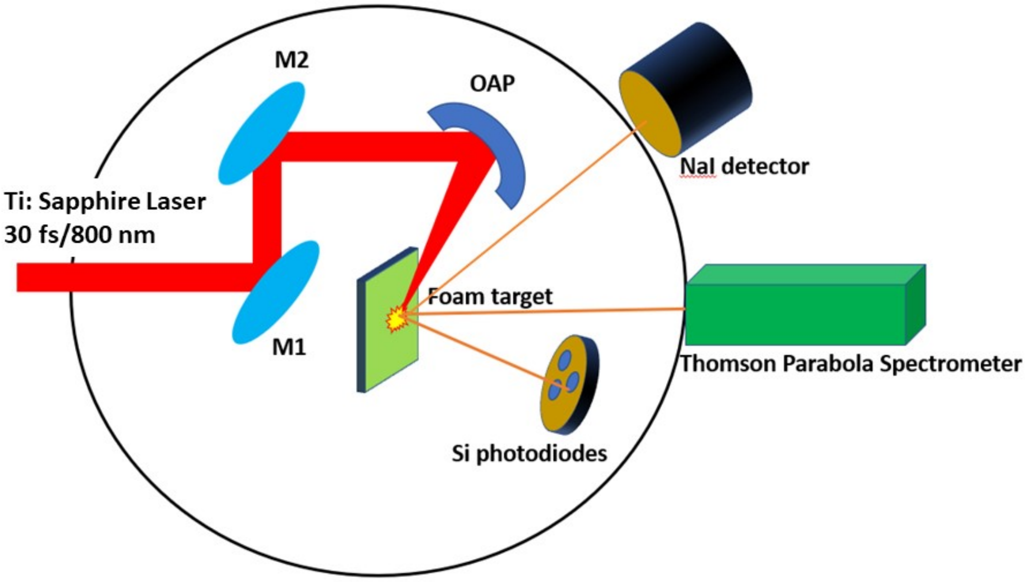

Figure 4.12 *Schematic of Experimental set up*

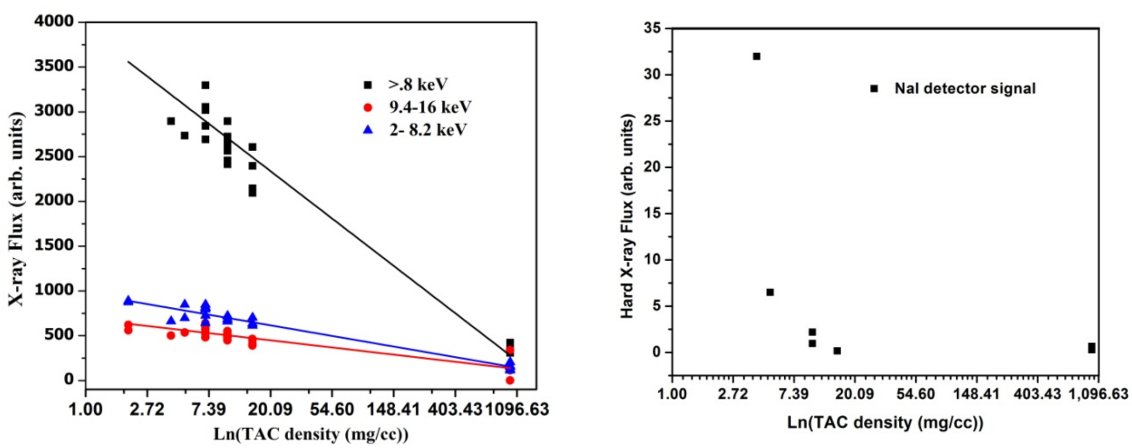

Figure 4.13 *(a) Soft X-ray flux recorded by photo-diodes in different energy ranges (b) Hard X-ray flux recorded by NaI detector.*

The 400mJ, 30fs laser pulse is focused on the target to 30 microns using dielectric parabolic mirror (f/2 = 150mm) to impinge 2×10^{19}W/cm2 intensity beam on the target. The target holder is moved on the XYZ stage to optimize the hard X-ray signal and the Proton trace in the (front side) Thomson Parabola Spectrometer, which correlates to best focus. The Z focus is moved around the focus, to check the systematic variation in the X-ray signal (NaI) and TPS trace. Laser pulse contrast was increased to 1e-9, whose signal was also observed in the TPS spectrum. 20 TW (40mJ on target) was taken out of the amplifier without second stage amplification. All the experiments were done in single shot mode. The camera and NaI detector was triggered using the master trigger from the oscillator. TPS is aligned such that the 40 mm phosphor screen could embrace most of the proton trace. 100 μm aperture was kept in between the plasma and the TPS, such that the central spot magnification is minimum. The focal spot, 100 μm aperture and the optimized spot on phosphor screen are aligned using diode laser. The schematic of experimental set up is shown in Figure 4.12. The TAC foams with density 2, 4, 5, 7, 10 and 15 mg/cc and solid polyethylene plastic with density 980 mg/cc are used for the studies. We found many fold enhancement in soft X-ray and hard X-ray for low density TAC in comparison to solid.

4.8 Summary

This work describes the results of experiments on the interaction of laser pulses of moderate intensity (30 J, 500 ps) at a wavelength of 1064 nm with TAC targets with a density ranging from a subcritical density to three times the critical density. The characteristics were studied, including the transmittance to laser radiation, the yield of X-ray radiation with photon energies of several keVs, and the dynamic of ions and X-ray conversion efficiency with respect to areal density from the plasma. The effects of target density and laser radiation intensity on these characteristics were analyzed. The duration and amplitude of transmitted laser pulses were shown to decrease with increasing column target density. Specifically, the pulse duration shortened from 680 ps (FWHM) to 360 ps after passage through the targets with a column density of about 600-900 mg/ $cm^2$and to 176 ps for a target with a column density of about

2000 mg/cm^2 (density r = 2 mg / cm^3, thickness h = 1000 mm). The pulsed laser irradiation of a subcritical density target was found to give rise to harder X-rays than the irradiation of a supercritical density target. This may be due to the supersonic and volume heating of the subcritical density targets by a thermal wave as well as to the absence of significant energy loss for hydrodynamic ion motion. An analysis of the ion emission revealed an increase in ion flux and a shift of ion energy spectrum to higher energies in going to supercritical density targets. Same trend has been seen from individual charge states of carbon and oxygen. The laser to X-ray conversion efficiency in the spectral ranges, 5-8 keV and 4.5-16 keV is found to be approximately 2.3 times greater in 2 mg/cc foam targets as compared to 20 mg/cc foam targets while the areal density is kept constant (0.2 mg/cm^2). Simulations are performed using a one-dimensional radiation-hydrodynamics simulation code to verify the experimental results. The simulations agree well with the experimental results. The shadowgraphs show the diameter of laser produced plasma approaches to 1494 μm at a delay of 8.3 ns due to fast lateral heat transport in the low-density target and reduces to approximately half of this for the 20 mg/cc density target.

Chapter 5

X-ray and Ion Emission Studies from Silica Aerogel and Deuterated Foams

5.1 Introduction

The demand of enhancement of X-ray from laser plasma interaction and role of foam targets have already been discussed in last chapters. In chapter-4, results from TAC foams are discussed which show a significance enhancement in multi KeV X-rays. This chapter will provide the studies from silica aerogel and deuterated foams. The silica aerogels targets are similar to hydro-carbon foams but the prepared by different process, i.e., sol-gel technique followed by super critical drying of highly cross linked network. The easy access, higher uniformity and homogeneity makes aerogel target an excellent material for laser plasma studies. Furthermore, the deuterated polyethylene target plays an important role in inertial confinement fusion as it is an intense neutron source. With the irradiation of a very high-power laser, a high fusion rate can be achieved from these targets because of very high energy gain by particles via ion acceleration mechanism. The increasing demand of foam targets in the coating of outer layer of DT fuel to reduce instabilities and in fast ignition scheme to increase the coupling of laser have triggered their research in the field of laser plasma interaction [140]–[142]. The light element foams with densities greater than critical one could act as an effective target ablator giving rise to high pressure under the irradiation by laser pulse. The layer of the light element as ICF ablator should be properly chosen in terms of thickness and density so that the inhomogeneity's in heating process can be smoothen out. Therefore, the studies on laser absorption including X-rays, evolution of the ions emission and distribution of their energy for low density foam target are essential. In this chapter, the X-ray and ion emission studies from low Z foams, silica aerogels and deuterated foams is discussed along with simultaneously measurement of the optical shadowgraphy of the plasma. The procedure of preparing of foam targets is also briefly described.

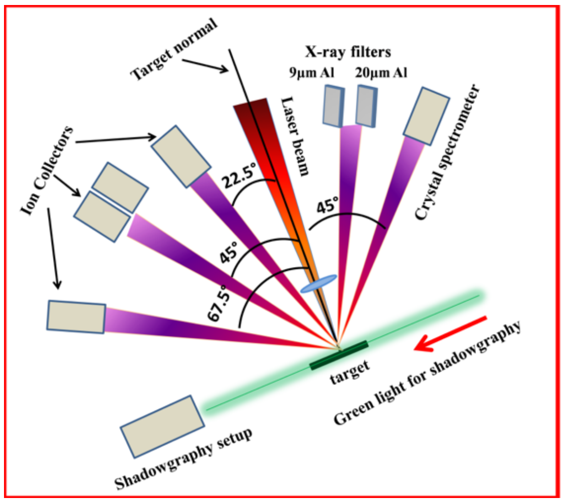

Figure 5.1 *Schematic of various X-ray and ions diagnostics used in the experiment.*

5.2 Studies from silica aerogel

5.2.1 Description of the experiment

The laser system used in these experiments is a 15 J/500 ps Nd: Glass laser with intensity 10^{13}-10^{14} W/cm^2. Targets used are solid quartz and 50 mg/cc pure SiO_2 aerogel foam along with (25% CH_3+75% SiO_2) foam of 60 and 40 mg/cc densities. The spectral ranges selected for soft and hard X-rays are chosen as (0.8-1.56 keV) and (3.4-16 keV) respectively. The ion collectors are placed at 22.5°, 30°, 45°, and 67.5° with respect to the target normal and laser axis to measure the plasma evolution and its size. To study the dynamic motion of the plasma and its volume, a transverse two-frame optical shadowgraphy system was developed. The experimental set up is shown in Figure 5.1.

5.2.2 Method of preparation of SiO_2 Foam Targets

The preparation of silica aerogel mainly includes three steps: gel preparation, aging of the gel, and drying of the gel. The aerogel (i.e., silica foam targets) is prepared by the sol-gel process followed by supercritical drying in which tetramethoxysilane (TMOS) is the source of silica. In the first step, the hydrolysis of TMOS is done by adding 0.001 M oxalic acid to initiate polymerization. As the TMOS is only partially miscible with water, alcohol (methanol) is added as a solvent to this solution to ensure the same phase for the reaction to occur. Ammonium hydroxide is used as a catalyst to increase the condensation reaction speed. To obtain the low-density silica aerogels, the molar ratio of TMOS: MeOH: H_2O was kept constant at 1:12:4. All the solutions (silicon alkoxide, solvent, water, and catalyst) were mixed in a 100 ml Pyrex beaker, and the resulting sols were immediately transferred to Pyrex test tubes and closed air tight. After gelation, the resulting alcogels were covered with methanol to prevent the shrinkage and cracking of the wet gels. All the alcogels were supercritically dried in an autoclave to obtain the low-density silica aerogels. The 25% CH_3 and 75% silica aerogels (foam targets) were produced by using the methyltrimethoxy precursor in the place of TMOS precursor and followed the same procedures in making the aerogels. The MTMS precursor was diluted with methanol and hydrolyzed using the 0.001 M oxalic acid. After 12 hours of hydrolysis, the condensation of the resulting methyl modified silica sol (25% CH_3 and 75% silica) was carried out using 13 M ammonium hydroxide. The 60 mg/cc and 40 mg/cc MTMS based aerogel were obtained by keeping the molar ratios of MTMS: Methanol: water at 1:20:4 and 1:34:4, respectively. The acidic and basic catalysts were added in the form of water. Silica aerogel of different composition grown in test tube are shown in Figure 5.2(a). More details are given on the preparation of the silica aerogels elsewhere [34], [143]–[145]. The scanning electron microscope (SEM) image of 50 mg/cc silica aerogel foam is shown in Figure 5.2(b).

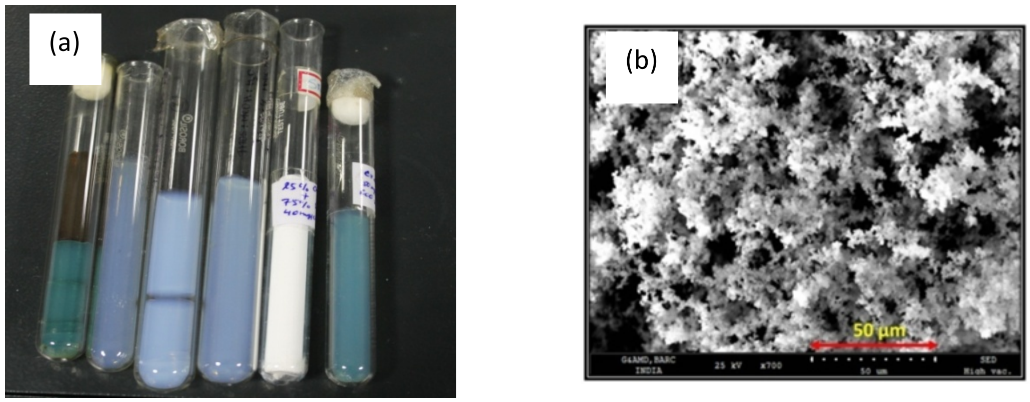

Figure 5.2 *Images of (a) Silica aerogel foams, (b) SEM images of silica aerogel*

5.2.3 Effect of target densities on soft and hard X-ray yields

We have measured the X-ray radiation due to free-free and free-bound transitions using X-ray photodiodes covered with different filters to measure the soft and hard X-rays [146]. The output of the photodiode signals for the soft and hard X-rays are plotted with respect to the laser intensity in Figure 5.3(a-b), respectively. From the figures, it can be seen that the X-ray flux (I_x) scales with the laser intensity (I_L) at a constant pulse duration and wavelength as $I_x = (I_L)^\alpha$, where α is constant. However, the value of α is calculated by slope of the graph plotted between $\ln(I_x)$ versus $\ln(I_L)$ and found to be 1 and 0.5 for quartz and SiO_2 aerogel foam targets, respectively, in case of soft X rays. However, in the case of hard X rays, these values are 0.9 and 0.6 for quartz and SiO_2 aerogel foam targets, respectively. Similar scaling factor of soft and hard x-rays intensity with laser intensity for the solid targets are reported in past. However, for low density targets it is lower than the solid targets. Though, the scaling factor is lower compare to solid target but at moderate laser intensity, it is observed that the soft X-ray emission (0.9-1.56 keV) from the low-density (50 mg/cc) SiO_2 aerogel foam is almost 2-2.5 times higher than in solid quartz for almost all the investigated laser intensities and decreases with increase of the foam density. The soft X-ray yield from 70 mg/cc pure SiO_2 is lying in between solid quartz and 50 mg/cc pure SiO_2 aerogel foam target. However, in the case of hard X-ray emission (3.4-16 keV), the flux from low-density SiO_2 aerogel foam is ~1.8 times lower than the yields from the solid quartz. The X-ray flux from the silica foam with composition (25% CH_3+75% SiO_2) of densities 60 and 40 mg/cc are also measured. It is observed that the soft X-ray yield from these targets are slightly lower than the pure SiO_2 aerogel foam target of density 50 mg/cc and at the same time higher than the X-ray yield from the quartz target. The enhancement of the soft X-ray emission in the low-density foam target is mainly due to two reasons. Firstly, it is due to lower losses to hydrodynamic phenomenon (shock formation), and secondly and more prominently it is due to volumetric heating [40].

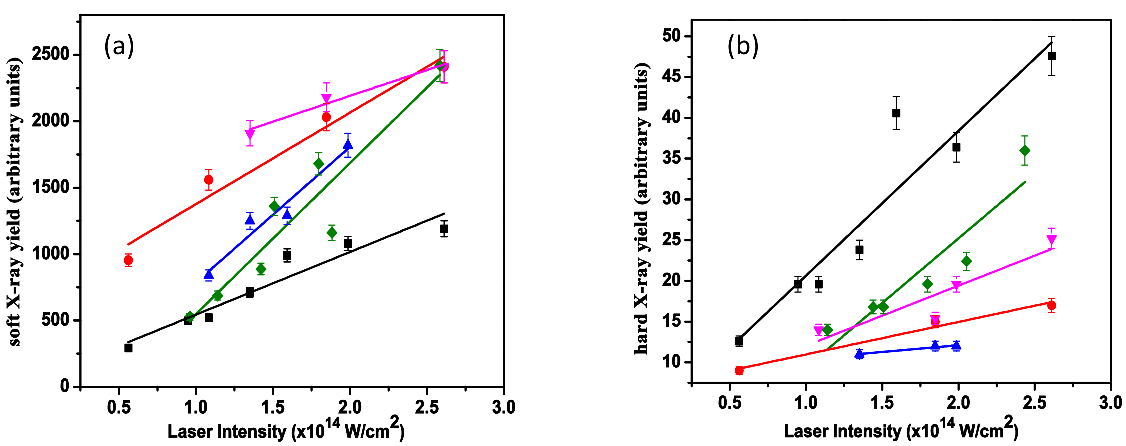

Figure 5.3 *Comparison of (a) Soft X-ray fluxand (b) hard X-ray flux from solid quartz with SiO_2foam of various densities such as 50mg/cc, 25% CH_3 + 75% SiO_2foam of 60 mg/cc and 40 mg/cc densities.*

To validate volumetric heating concept, we imaged the targets after 2 ns and 8 ns with respect to the irradiation of laser pulse on targets. The shadowgraphs for the quartz and for 50 mg/cc SiO_2 aerogel foam targets can be seen in the Figure 5.4(a-c) and Figure 5.4(d-f) respectively Figure 5.4(c) and 5.4(f) showing the plasma volume after 8 ns of the arrival of incident laser. The lateral plasma size in case of SiO_2 aerogel foam case is 1.35 times larger than the solid quartz. It can also be seen from Figure 5.4(d) (without laser), 5.4(e) (2 ns delay), and 5.4(f) (8 ns delay) that the heated volume is larger inside the targets (shown with dotted circles). However, in the case of quartz, the interaction is only at the solid surface.

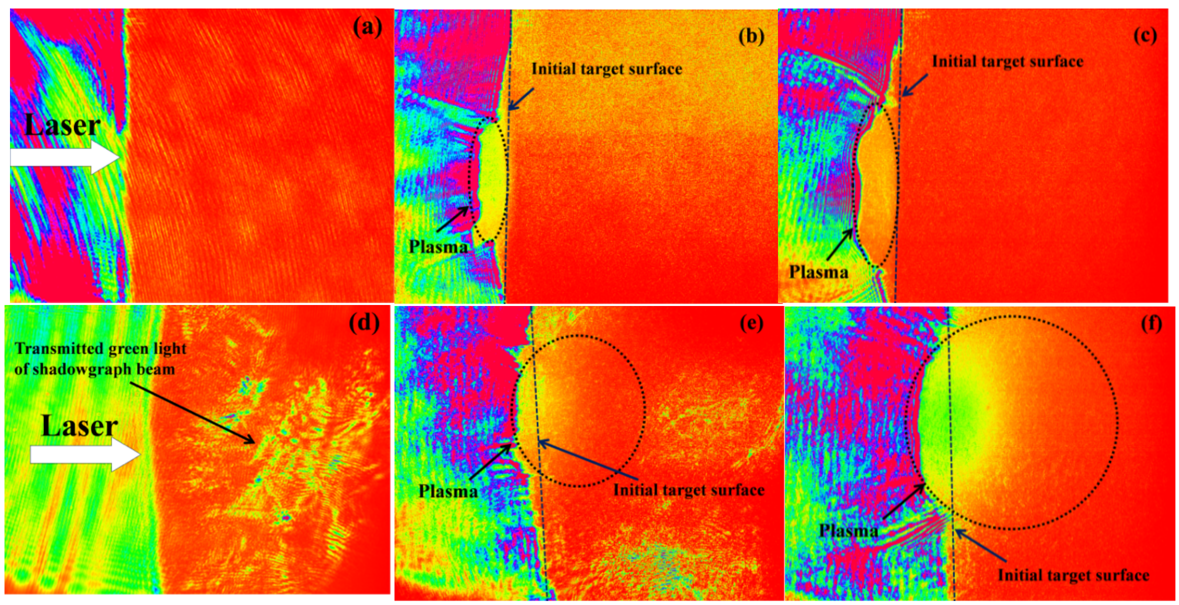

Figure 5.4 *Shadowgraph of solid quartz (a) at t = 0 ns (b) at t = 2 ns (c) at t = 8 ns after laser pulse on the targets, and for foam targets at (d) t = 0 ns (e) at t = 2 ns (f) at t = 8 ns after laser pulse on the targets. The dotted circle in each image is showing the region of plasma.*

5.2.4 Effect of target densities on distribution of ions

We also recorded the time-integrated spectrum of ions from LPP with the help of ions collectors placed at four different angles from target normal (i.e., at 22.5°, 30°, 45°, and 67.5°) to verify the volumetric heating concept. The angular distribution of the amplitude of the thermal ions (plasma) are plotted in Figure 5.5, for two different laser shots of same energies on the targets of 50 mg/cc SiO_2 aerogel foam and quartz target. The angular distribution of the thermal ions are scaled as $P(\theta) = P(0) \cos^n\theta$, where n = 3.8 and 4.8 for the foam and quartz targets, respectively. It can be seen from Figure 5.5, that the thermal ion flux from the foam target is larger and closer to isotropic (hence the larger volume) compared with the thermal ion flux from the quartz. A similar behavior has been observed via theoretical simulation done by our group using 2D Eulerian radiative-hydrodynamic code POLLUX, which is briefly described in the next section.

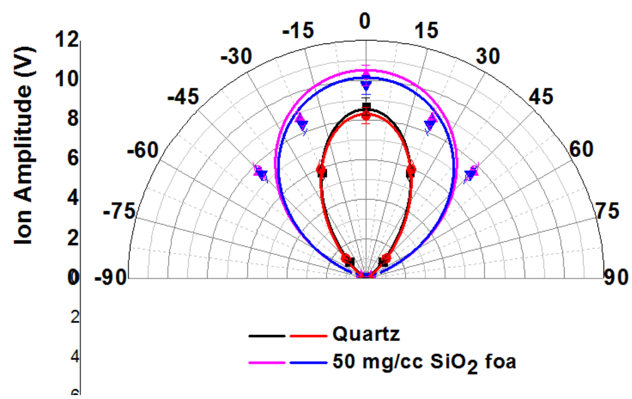

Figure 5.5 *Angular distribution of the thermal ion flux from the 50 mg/cc SiO_2 foam and quartz for two laser shots of approximately same energy.*

5.2.5 Simulation results to verify the volume effect

The 2D Eulerian radiative-hydrodynamic code POLLUX was originally developed to model moderate irradiance (10^{10} W/cm^2) optical and infrared laser irradiation of a solid target and the subsequently produced strongly ionized plasma, which further interacts with the incident laser beam. The code solves the three first-order quasi-linear partial differential equations of hydrodynamic flow using the flux-corrected transport model of Boris & Book

[147], with an upwind algorithm [148] for the first term. The energy is absorbed by the plasma electrons through inverse bremsstrahlung and distributed through electron-ion collisions, the equilibration of which is determined by the Spitzer plasma collision rate [149]. For calculation of the EOS variables, POLLUX utilizes in-line hydrodynamic EOS subroutines from the Chart-D [150]. EOS package developed at Sandia National Laboratories, Livermore, CA, USA. This code uses an explicit solver; therefore, a Courant number of ~1 has been used to increase stability where the Courant number(C) is given by

$$C = \frac{u_x \Delta t}{\Delta x} + \frac{u_y \Delta t}{\Delta y} \sim 1 \tag{5.1}$$

where u_x and u_y are magnitudes of the particle velocities in the respective directions, Δt is the time step, and Δx and Δy are the cell spatial dimensions. The ionization and level populations are calculated assuming local thermodynamic equilibrium, an assumption which is justified for hydrodynamic time scales (>1 ps). To enable the ray tracing of the incident laser pulse within the code, the Eulerian mesh is subdivided into triangular cells with the Eulerian mesh center points at the triangle corners allowing for the refractive index and associated gradient within each cell to be calculated via direct differencing. The refractive index is continuous across cell boundaries and assumes a linear electron density variation within each cell. The (x, y) trajectory of each ray in the cell is then assumed to be parabolic dependent upon the refractive index(n_0) and its derivative (n_1), given by,

$$y^2 = 4\left(\frac{n_0}{n_1}\right)x \tag{5.2}$$

The parameters used in the code were a p-polarized laser intensity of 1×10^{14} W/cm^2 incident onto solid quartz with a density of 2.65 g/cm^3 and silica foam with a density of 50 mg/cm^3. The contour plot for the electron density and electron temperature at t = 1 ns after the start of the laser pulse are shown in Figure 5.6. It can be seen from Figure 5.6 that the plasma expansion differs greatly between the two targets with the foam targets creating much larger lower density plasma. It proves that the enhancement is due to a volume effect where the foam target has a much greater volume of emitting plasma, which is in consistent with the results obtained by shadowgraphy and the ion collector.

5.2.6 Comparison of the K-shell spectra

The K-shell spectroscopy of Si plasma is discussed in chapter-3. The plasma temperature and density are estimated by taking into account the ratio of the dielectronic satellite of He_α line (i.e., $1s^2 2p$–$1s2p^2$) to its parent resonance line, that is, He_α line($1s^2$–$1s2p$) and intercombination line ($1s^{21}S_0$- $1s2p3P^1$) to He-α ($1s^2 1S_0$–$1s2p^1P_1$), respectively. A comparison has performed to know the difference in temperature and density for quartz and silica aerogel foams. The simulation is carried out using the FLYCHK software, which generates a synthetic spectrum that is matched with the experimental data after several iterations for a range of temperatures and densities. The experimental spectra matched with FLYCHK for He-like lines of the silicon in the quartz target at T_c= 180 eV, T_h= 1000 eV, f = 0.009, $n_e = 7 \times 10^{20}$ cm^{-3}, and for SiO_2 aerogel foam at T_c = 190 eV, T_h= 800 eV, f = 0.01, and $n_e = 4 \times 10^{20}$ cm^{-3} as shown in Figure 5.7(a-b), where T_c and T_h are the cold and hot electron temperatures, respectively, f is flux limiter and n_e is the electron density. The amplitude of the line emission is lower in the case of the foam target, which is due to a lower plasma density as can be seen from simulation results where the density of the foam plasma is 4×10^{20} cm^{-3}. The hot electron temperature is lower and the value of f is higher in the case of foam targets, which indicates lower hard X-ray emission than the solid quartz.

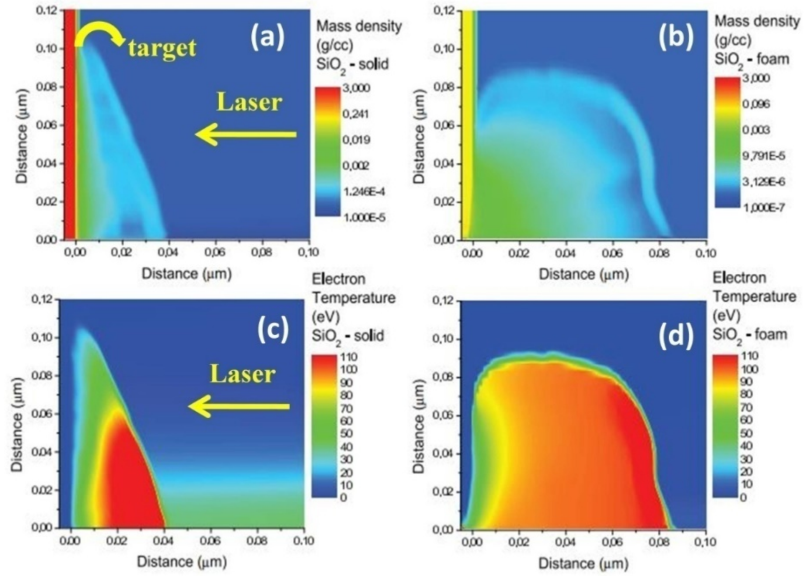

Figure 5.6 *(a-b) Contour plots for solid quartz and SiO_2 foam for electron density. (c-d) for electron temperature after a delay of t = 1 ns with respect to the start of the laser pulse on the target.*

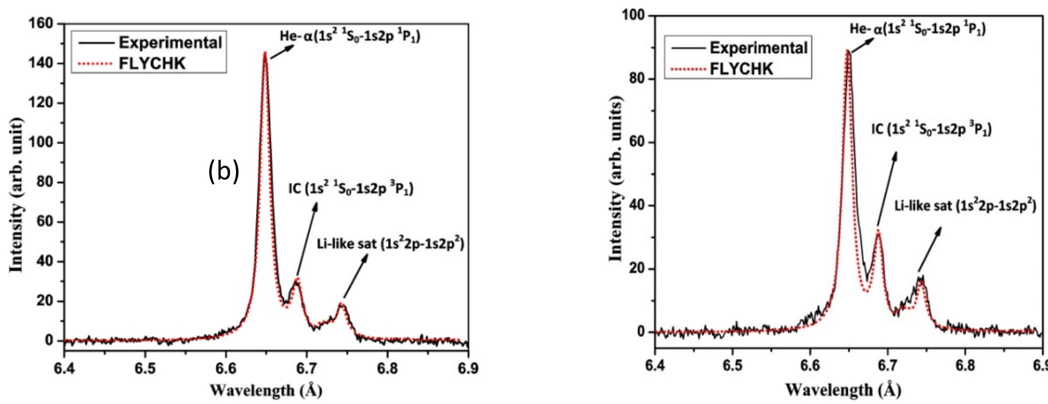

Figure 5.7 *Experimental spectrum matched with FLYCHK for He-like lines of the Silicon in the (a) quartz at T_c = 180 eV, T_h = 1000 eV, f = 0.009 and n_e = 7 ×10^{20} cm^{-3} (b) SiO_2 foam at T_c = 190 eV, T_h = 800 eV, f = 0.01 and n_e = 4 ×10^{20} cm^{-3}.*

5.3 Studies from deuterated $(CD_2)_n$ foams

This section will explain the experimental investigation of ion dynamics from deuterated foam plasma (CD_2 foam). The $(CD_2)_n$ foam with densities 275 and 440 mg/cc have been used. In the present study, up to 5 J laser pulse has been utilized which corresponds to the intensity up to 7×10^{13} W/cm^2. The ion collectors are placed at different distances and at four different angles (22.5°, 45°, 52° and 63°) with respect to target normal. The measurement of time resolved X-ray signal is done using X-ray streak camera with a resolution of 10 ps. The streak camera is placed at an angle of 22.5° with respect to target normal.

5.3.1 Distribution of flux deuterium ions

The acceleration of ions from the plasma can be described by various phenomenon (contaminants on target surface, hot electrons, charge separation) but the most dominating mechanism is the charge separation. In this phenomenon, the interacting laser pulse with plasma transfers its energy to electrons instead of ions (mass difference).

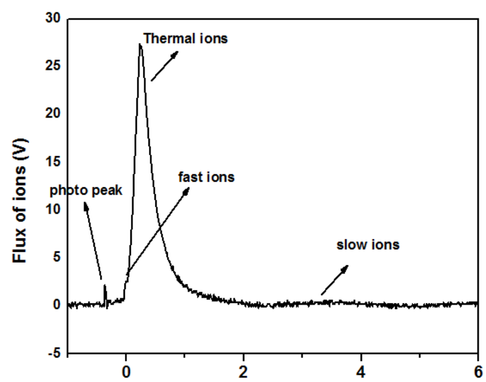

Figure 5.8 *(a) Typical signal of ion collector placed at 22.5° from target normal at 3 J laser energy (target: 0.275 gm/cc CD_2 foam).*

Then electrons transfer their energy to ions via collision. Electrons being the lightest species acquire very high thermal velocity and escape from plasma. But this charge separation between ions and electrons results in an electrostatic field which accelerates the ions to very high velocities and hence higher energies. The ion collector signal consists of three parts apart from photo peak and proton signals (due to contamination). The higher energy part is due to hot/fast electrons generated from non-linear processes occurring in plasma and hence fast ions. Thermal ions are due to thermal electrons and slowest ions which are coming from the vicinity of focal spot heated by X-ray radiations from plasma. For studying these accelerated ions to diagnose plasma parameters, Time of Flight (TOF) and TPS are very efficient tools.

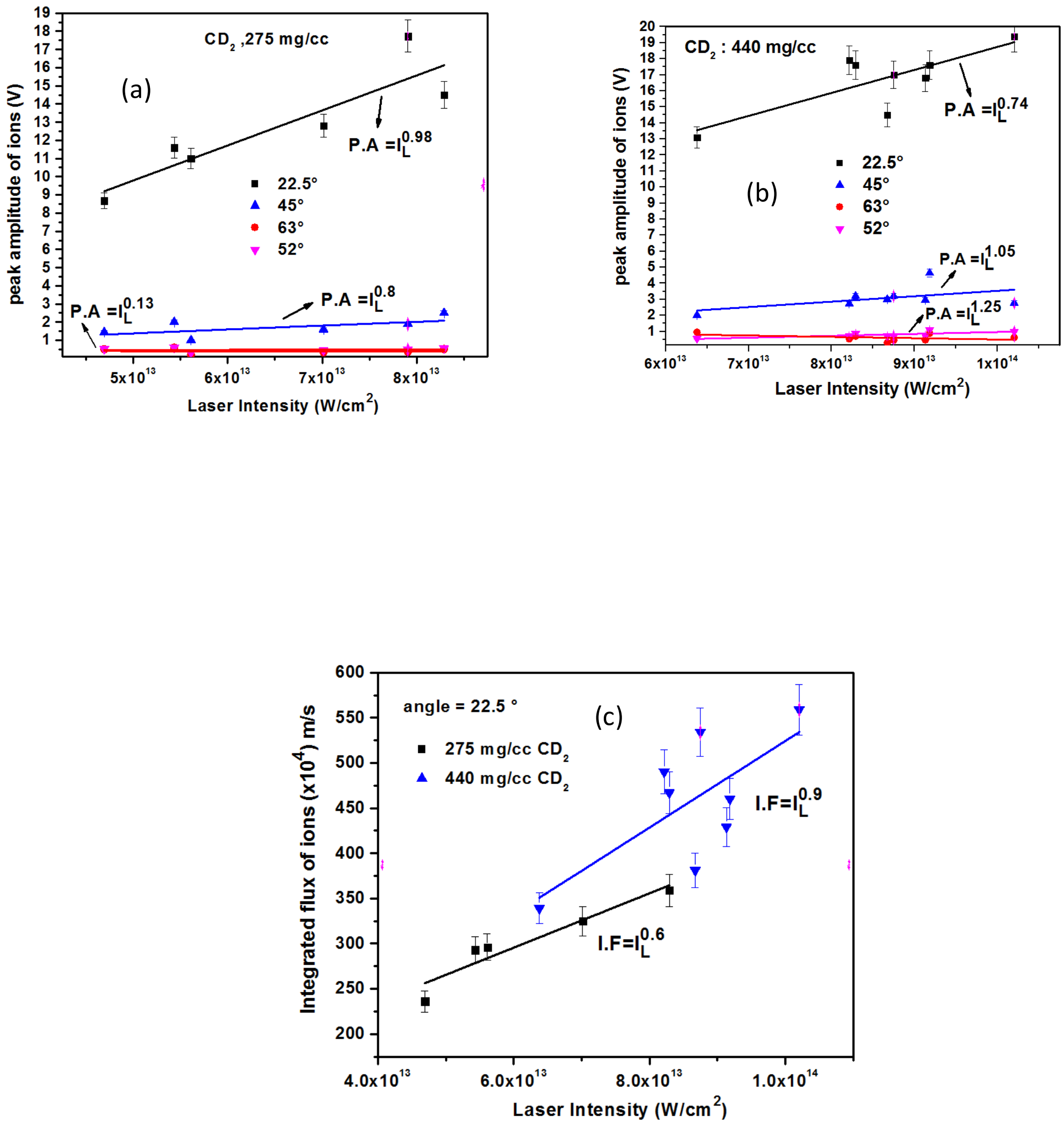

Figure 5.9 *Peak amplitude of ions with respect to laser intensity for (a) 275 mg/cc (b) 440 mg/cc CD_2 target (c) comparison of integrated flux for all both densities at 22.5°.*

The peak amplitude of ions from ion collector signal is calculated at different angles from the target normal. The peak amplitude corresponding to the four different angles (22.5°, 45°, 52° and 63°) are shown in Figure 5.9(a) and 5.9(b) for CD_2 foam with density 275 mg/cc and 440 mg/cc respectively. The flux of ions arriving at an angle 22.5° from target normal is high (almost 5 times high) in comparison to larger angles (45°, 52° and 63.5°) from target normal for the same laser intensity. With increase in laser intensity, the absorption of laser increases and hence the flux of deuterium ions increases. The scaling of ion flux follows the power law $I=I_L^{\alpha}$ with laser intensity where α=0.6, 1, 0.13 and 0.12 for the angles 22.5°, 45°, 52° and 63.5° respectively. The integrated flux of ion arriving at a particular angle for two densities of CD_2 foam is compared. The integrated ion flux at an angle of 22.5º from target normal for 275 mg/cc and 440 mg/cc dense CD_2 foam targets is shown in Figure 5.9(c). The α is 0.65, 0.9 for 275 mg/cc, 440 mg/cc CD_2 foam respectively. This indicates more flux of ions for large density i.e. 440 mg/cc in comparison to 275 mg/cc CD_2 foam targets.

5.3.2 Distribution of peak velocity of deuterium ions

The peak ion velocity is calculated for ion collectors placed at different angles from target normal. The velocity is maximum in the target normal direction which indicates a maximum acceleration towards target normal direction because of large coulomb field in this direction. In Figure 5.10(a), the peak velocity for 275 mg/cc CD_2 foam is plotted with respect to laser intensity at different angles from target normal. The ion velocity increases from 35 $\times 10^4$ m/s to 45×10^4 m/s and in terms of energy from 1 keV to 2 keV with the increase in the laser intensity from 4×10^{13} W/cm^2 to 8.5×10^{13} W/cm^2. The velocity and energy of ions detected at larger angles from target normal is less than 20×10^4 m/s and 500 eV respectively.

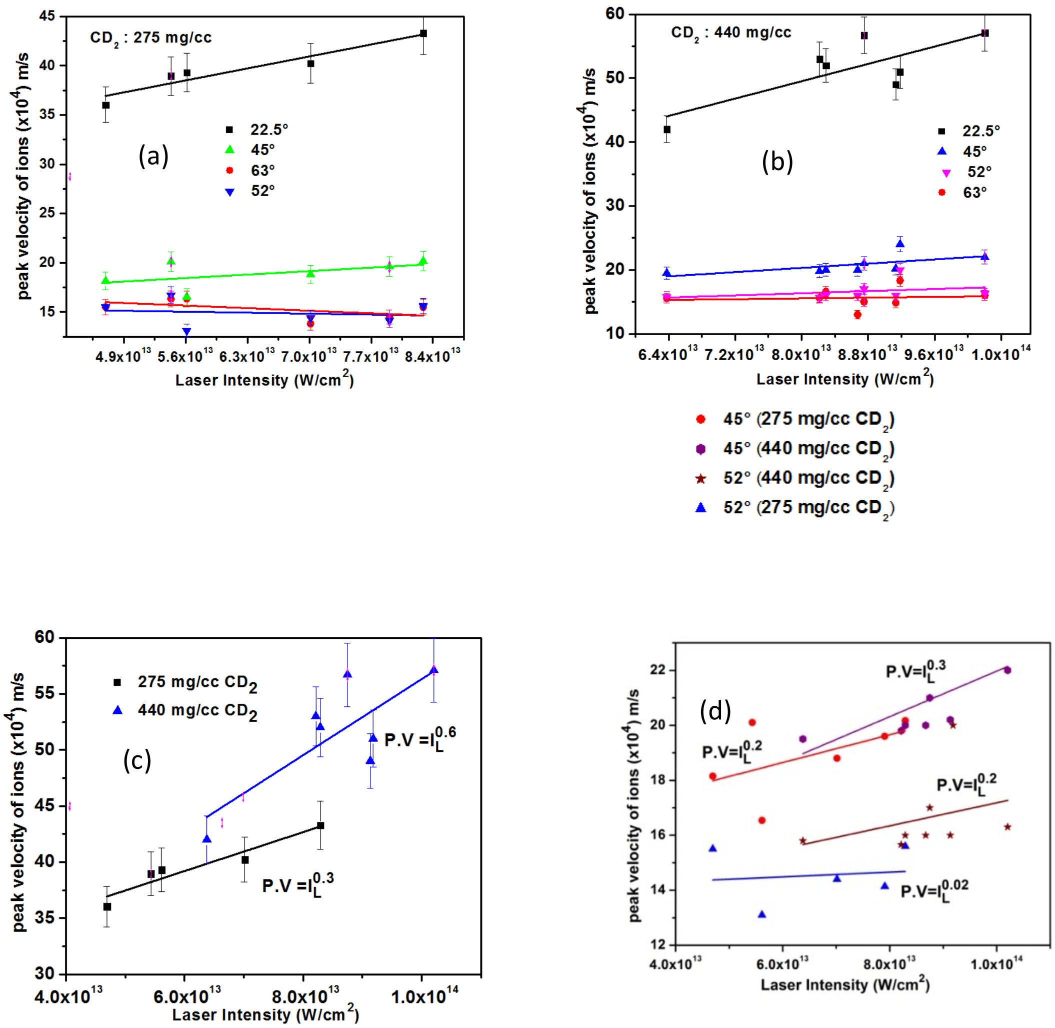

Figure 5.10 *(a) Peak velocity at all angles corresponding to 275 mg/cc CD_2, (b) peak velocity at all angles corresponding to 440 mg/cc CD_2 (c) comparison of peak velocity for 440 and 275 mg/cc CD_2 foam at 22.5° (d) comparison of peak velocity for 440 and 275 mg/cc CD_2 foam at 45° and 52°.*

At angle 22.5º from target normal, scaling of velocity with laser intensity provides large scaling factor for 440 mg/cc CD_2 foam as shown in Figure 5.10(c). However, at larger angles the difference is not so prominent. It indicates the emission of more energetic ions from higher density CD_2 foam towards target normal in comparison to low density foams.

5.3.3 Velocity mapping

A velocity map of ions utilizing Faraday collector's data is drawn at different laser intensities. The algorithm is compiled in Python. This will process the output files of ion collectors and provide the angular distribution of the ions flux corresponding to different velocities of ions at different laser intensities. From Figure 5.11(a), at laser intensity 8.28×10^{13} W/cm^2, flux of ions with velocity 42×10^4 m/s is large and maximum emission is along the target normal. For the same laser shot, ion flux corresponding to velocities 35×10^4, 50×10^4 m/s is less and minimum for velocities 25×10^4, 50×10^4, 60×10^4, 70×10^4 m/s. The forward peaking of ions is also reduced for low velocity ions. When the laser intensity decreases, the velocity of ions also decreases. At 7×10^{13} W/cm^2, flux of ions with velocity 35×10^4 m/s is large. When the laser energy reduces to 4.68×10^{13} W/cm^2, flux and velocity of ions goes down further. Similar velocity map is drawn for 440 mg/cc CD_2 foam for three different laser energies. The effect of target density on the velocity and flux of ions can be evaluated from Figure 5.11(a-d), at the same laser intensity (8.28×10^{13} W/cm^2). The comparison shows existence of more energetic ions (50×10^4 m/s) towards target normal for higher density 440 mg/cc foam. The flux of ions corresponding to this velocity is also high. These maps also indicate a higher flux of ions corresponding to the velocity 60×10^4 m/s for same target density (440 mg/cc). Similar trend is observed by comparison of Figure 5.11(b) and 5.11(e), in which the laser intensity is little bit high for 275 mg/cc CD_2 foam but still more energetic ions are present in higher density CD_2 foam (440 gm/cc).

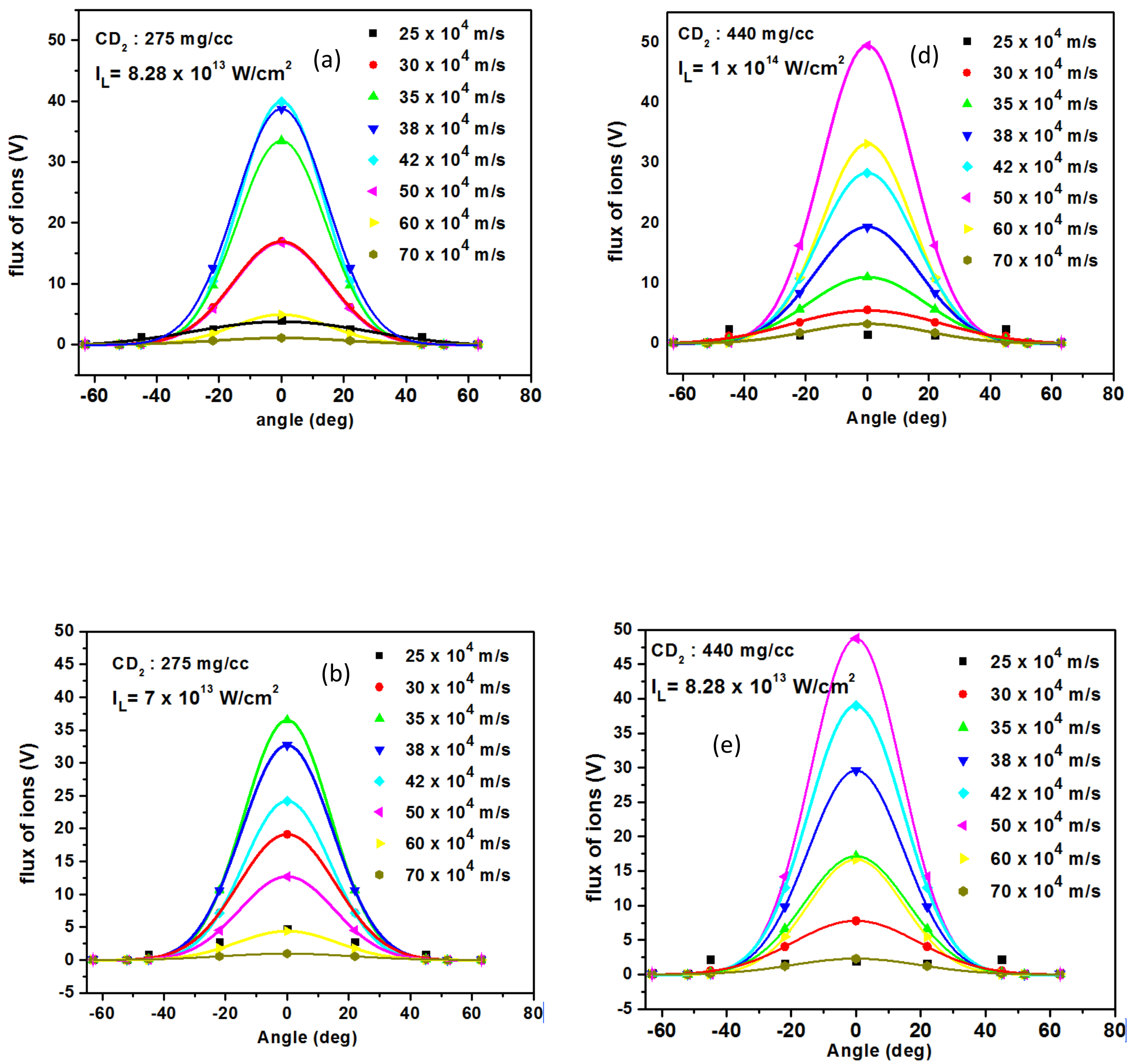

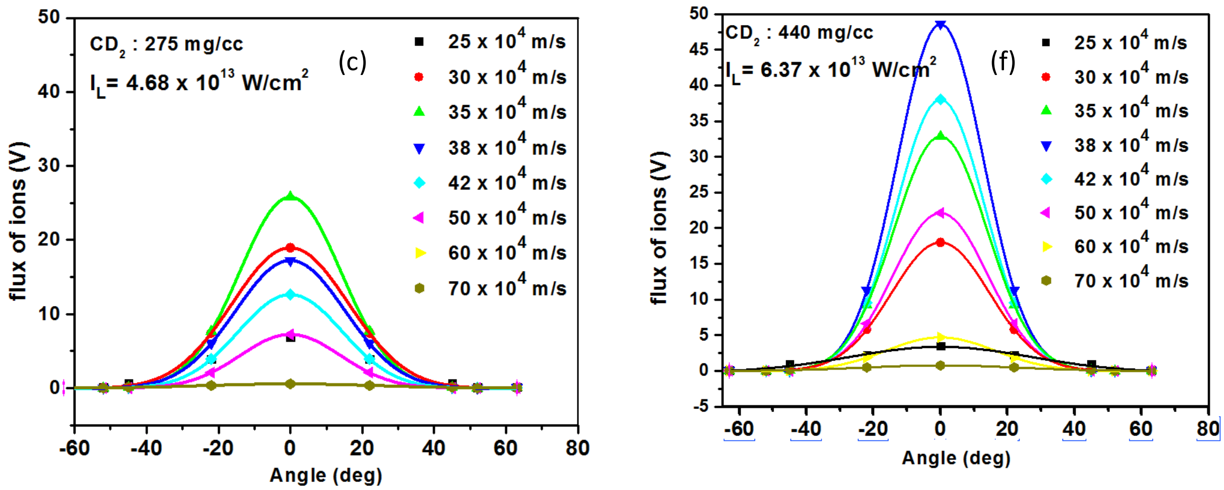

Figure 5.11 *Angular distribution of ions of various velocities for (a), (b), (c) 275 mg/cc CD_2 foam and (d), (e), (f) for 440 mg/cc CD_2 foam at different energies of incident laser.*

5.3.4 Thomson Parabola data analysis

The data recorded by TPS is shown in Figure 5.12(a). The different parabolas correspond to six charge states of carbon, deuterium and protons. Being same m/q ratio, the parabolas for C^{6+} and deuterium are overlapped. Figure 5.12(c-d) represents the laser intensity verses ion flux plot for deuterium ions for 275 mg/cc and 440 mg/cc CD_2 foam respectively. There is clear indication that with increase in laser intensity, ions in high energy side starts contributing. Figure 5.12(e) shows the deuterium ions energy spectrum from 275 mg/cc and 440 mg/cc CD_2 foam targets at laser intensity 8.28 x 10^{13} W/cm^2 and Thomson parabola fixed at 45° from target normal. The ions with high energy and flux ions reaches faster at TP for the case of 440 mg/cc CD_2 in comparison to 275 mg/cc CD_2 foam which supports our previous results obtained with the help of ion collectors. But at lower laser intensity [Figure 5.12(f)], effect of target density is not prominent. Therefore, we can conclude that the target density influences the forward peaking of ions. This means as lower the density, the ion emission is more towards isotropic nature due larger plasma volume and for high density peaking is towards target normal. Also,

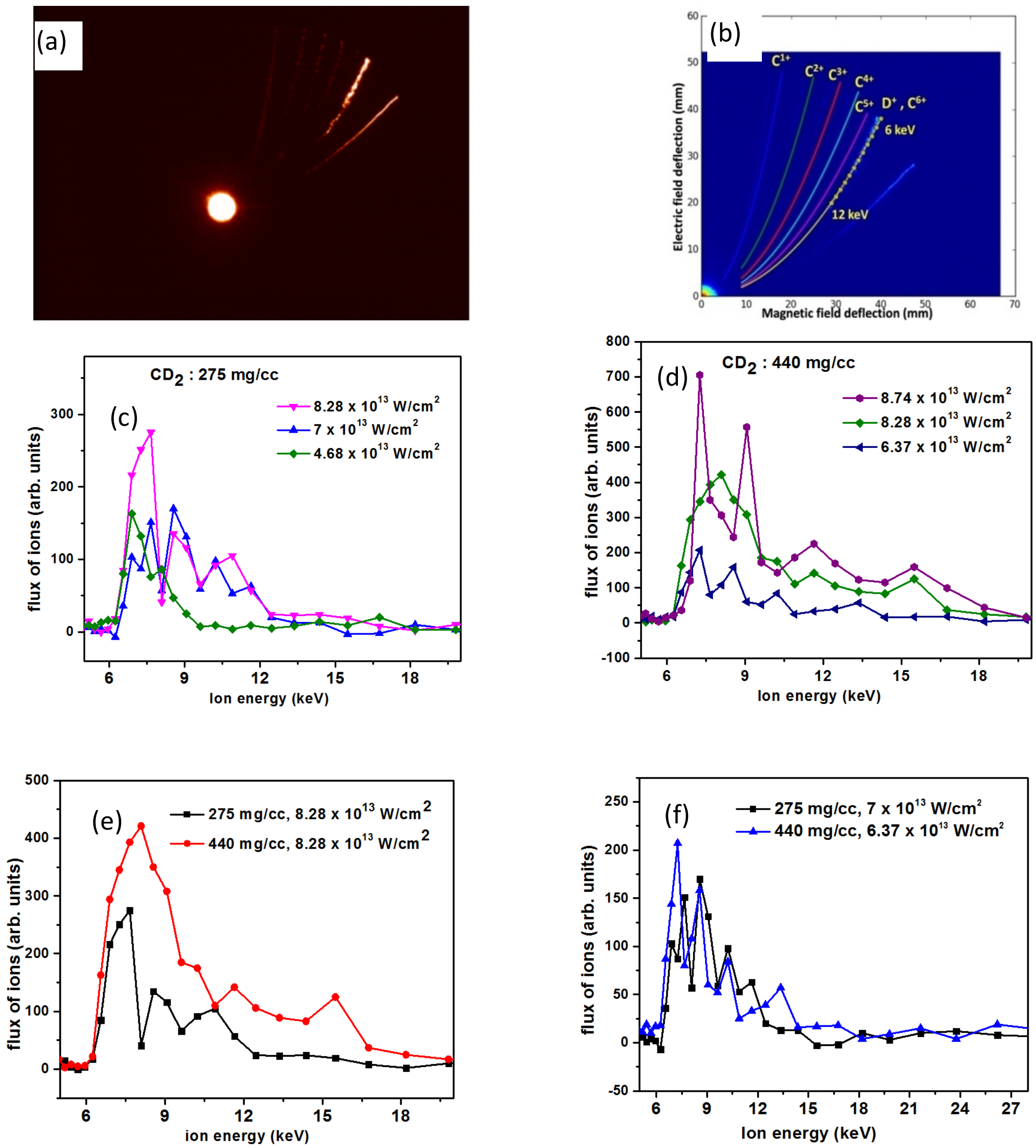

Figure 5.12 *(a) Data recorded by Thomson Parabola Spectrometer (TPS) (b) Analysis of the same data for extraction of ions energy and ion flux. Energy Vs flux for (c) 275 mg/cc and (d) 440 mg/cc CD_2 foam at different intensities of laser (e-f) effect of target density on energy and flux of ions at two laser energies.*

with decrease in density of target, volume of plasma increases indicating more flux of ions in low density CD_2 foam.

5.3.5 Comparison of X-ray flux

The X-rays are recorded with the help of X-ray streak camera. The noise is subtracted from the raw signal. The final X-ray pulse for 275 mg/cc and 440 mg/cc is plotted in Figure 5.13(a-b). The influence of laser intensity on X-ray flux and X-ray pulse width is studied and found to vary linearly with increasing laser energy

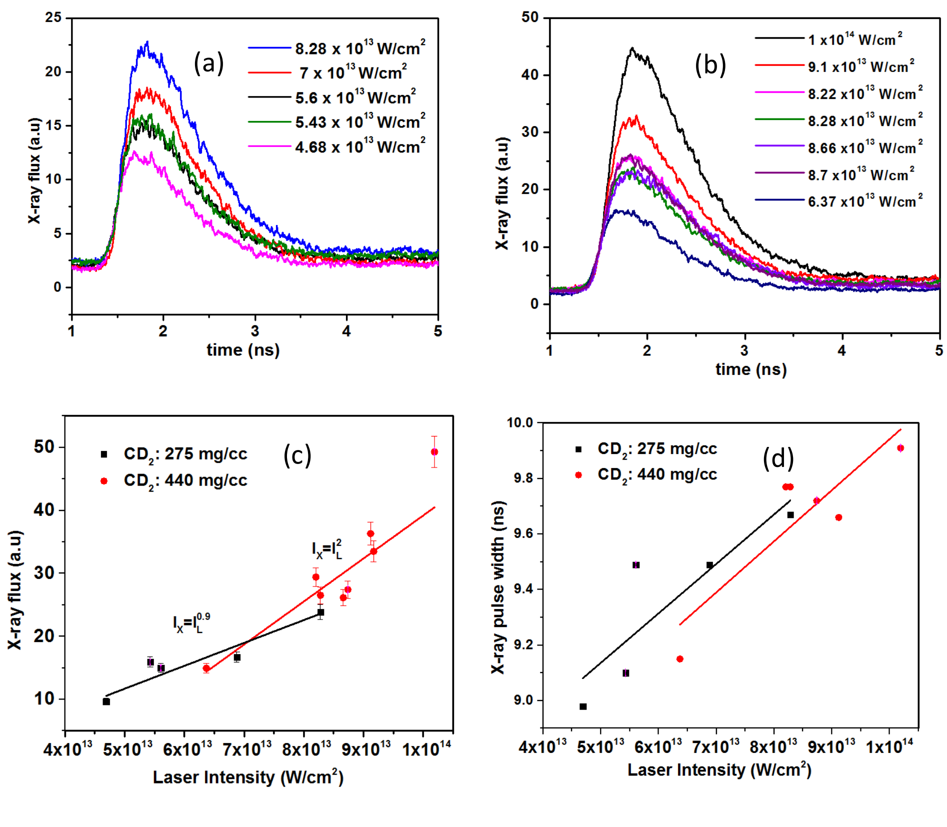

Figure 5.13 *(a) X-ray streak for 275 mg/cc CD_2 at various laser energies (b) X-ray streak for 440 mg/cc CD_2 at various laser energies (c) X-ray flux for all densities of CD_2 with varying laser energy. (d) X-ray pulse width in ns for all densities of CD_2 foam.*

5.4 Summary

A comparison of soft and hard X rays flux from quartz and low-density SiO_2 aerogel foam targets is done. Pure SiO_2 aerogel foam with density 50 and 70 mg/cc, and (25%CH_3 + 75% SiO_2) of densities 60 and 40 mg/cc are used. Two X-ray diodes with different filters are used to examine X-ray emission in soft (0.9-1.56 keV) and hard X-ray (3.4-16 keV) regions. An enhancement of 2.5 times in soft X-ray emission and a decrease of 1.8 times in hard X-ray emission for 50 mg/cc SiO_2 aerogel foam is observed compared with the solid quartz. The ion collector's data show that, the ion flux from the solid quartz is found to be more directional, whereas from SiO_2 aerogel foam, it is nearly isotropic. This behavior was attributed to the volume effect, which has been further verified by shadowgraph profiles of the plasma plume at two different time scales during the plasma evolution (2 and 8 ns) and simulation. Simulations with a 2D hydrodynamic code POLLUX supported the indication of volume heating of plasma being the cause for the change in X-ray emission. For determination of the plasma temperature and density, the spectra including He-like resonance line along with satellites and intercombination of Si plasma were matched with synthetic spectrum generated by using FLYCHK for both quartz and 50 mg/cc SiO_2 aerogel foam targets. The calculated plasma parameters are T_c = 180 eV, T_h= 1000 eV, f = 0.009, and $n_e = 7 \times 10^{20}$ cm^{-3} and T_c = 190, T_h= 800 eV, f = 0.01, and $n_e = 4 \times 10^{20}$ cm^{-3} for quartz and SiO_2 aerogel foam, respectively. Furthermore, the $(CD_2)_n$ foam with densities 275 and 440 mg/cc have been used. The angular distribution of ion flux and velocities is measured by ion collectors signal employing Time-of-Flight (TOF) technique. The peak ion velocity and ion flux are presented as a function of the laser intensity and target densities. Both the parameters are found to be maximum in the direction of target normal for both densities and are related by power law (I_L), with laser intensity (I_L). However, the scaling factor is more in case of 440 mg/cc in comparison to 275 mg/cc indicating a high velocity and more flux of ions in high dense CD_2. For the detailed studies of ions dynamics, a velocity mapping of ion collector's signal is done in Python which indicate the presence of more energetic ions in case of 440 mg/cc in comparison to 275 mg/cc CD_2 at the same laser energy. The ion spectrometry of $(CD_2)_n$ foam plasma was also done using high resolution Thomson parabola spectrometer aligned at 45° from target normal. It reveals that the effect of density of target on ion energy is more pronounced towards target normal instead of 45°.

Chapter 6

Studies from Gold Foam Targets

6.1 Introduction

The conversion efficiency of laser to X-rays can be increased by optimizing laser parameters such as laser wavelength, pulse width, intensity, focal spot size on targets. Change in the target parameters (atomic number, density, and structure etc.,) results in an efficient X-ray source. The X-ray yield emitted from laser-plasma is proportional to the atomic number of targets (Z) [21]. Therefore, using high Z (Z>20) materials in LPP, laser to X-ray conversion efficiency (CE) can be increased by many folds. This happens because ions with several bound electrons dominate in the resulting plasma which gives rise to complex (many electrons) line emission processes. Due to these characteristics, L- and M- band of high Z materials are used for X-ray back-lighter in absorption spectroscopy experiments [151]–[153]. Further, the use of foam targets for increasing X-ray flux is already described in previous chapters. Making the low-density foam targets of high Z materials is a perfect combination for enhancement of X-rays from LPP. The study of gold foam is essential because it is used for homogenous heating of the sample plasmas in point projection radiography [152], [154]. The soft X-ray source obtained from gold foam targets has applications in indirect drive scheme of ICF research and in high energy density physics [155]–[157]. In the indirect drive scheme, wall of the hohlraum is made of gold materials due to it high conversion efficiency. For the further enhancement of conversion efficiency from gold plasmas, alloy of gold targets (Cu-Au, Au-Sm etc.) were used [102]. The hohlraum cavity made up of solid gold and it's alloy was having problem of inhomogeneous heating, hot spots and high kinetic energy of ions. Also, with the plasma blow off (X-ray emission) away from the wall and reduction of laser coupling due to various scattering processes results in non-uniform compression, which leads to inefficient compression. Earlier for homogenization filling, helium gas was proposed for laser propagation which limit the motion of emission region, but it was having problem of reducing the fraction of transmitted laser energy, increasing the total reflected light and causing the growth of Rayleigh-Taylor instability at gold-helium interface [158]. In 2003 and subsequently in 2005, Hammer and Rosen proposed to use low density gold foam material for the Hohlraum cavity to the reduction of wall loss and consequently enhancement of X-ray emission yield [159], [160] and thereafter, a few experiments on enhancement of X-rays by gold foam targets are reported. The conversion efficiency of laser to X-ray is investigated for low density gold foam target using 1D hydrodynamic theoretical simulation and several experiments are performed [132], [161]–[163]. Considerable enhancement in multi-eV to multi-keV has been noticed for 0.1 g/cc Au in comparison to solid gold. This is attributed to the increment of X-ray emission zone length and decrease of conduction zone in low density gold foam. A decrease in kinetic energy of ions has been observed for the same reason, however there are no reports on ion dynamics measurement. Also, there are a very few experimental measurements of X-ray and ion emission from low density gold foam and its comparison with solid gold reported. Regarding this demand, we move a step forward to study the temporal evolution of X-ray flux using X-ray streak camera along with the ion emission spectroscopy from low density gold foam.

This chapter presents the influence of gold density on X-ray flux, X-ray plume size, pulse width and ion peak velocity. A 2D simulation is performed using Pollux hydrodynamic code to calculate the conversion efficiency of laser energy to X-ray as a function of laser intensity as well as gold density. A comparison of fast ions, thermal ions and protons is also performed based on target density.

6.2 Experimental procedure

The X-ray and ion emission studies are performed using laser facility at BARC. The experimental set up is shown in Figure 6.1. The gold foams or solid gold were kept at the center of vacuum chamber. The gold foam is irradiated with 500 ps Nd: Glass laser system working in the IR region providing energy up to energy 4 J energy in each single shot. The laser intensity in present experiment varies in the range of 10^{13} to 1 x 10^{14} W/cm^2. The densities of the gold foam used are 0.2 gm/cc, 0.13 gm/cc, 0.1 gm/cc and that of solid gold is 19.32 gm/cc. The ion diagnostics involves ion collectors at different angle (22.5°, 45°, 52° and 63°), Thomson Parabola Spectrometer (TPS). For observation of X-rays, an X-ray streak camera (BIFO make -K010X) is used. This enabled us to record the time dependent flux of X-rays with resolution of 10 ps placed at 22.5° with respect to the target normal. The streak camera cathode is covered with the B-10 filter allowing the transmission of X-rays with energies greater than 0.8 keV and block charge particles entrance to the streak camera slit. A two-frame optical shadowgraphy system with spatial and temporal resolution of 12 μm and 300 ps was aligned to measure the plasma evolution. The shadowgraphy light used was second harmonics of main laser beam (532 nm @ 300 ps pulse width).

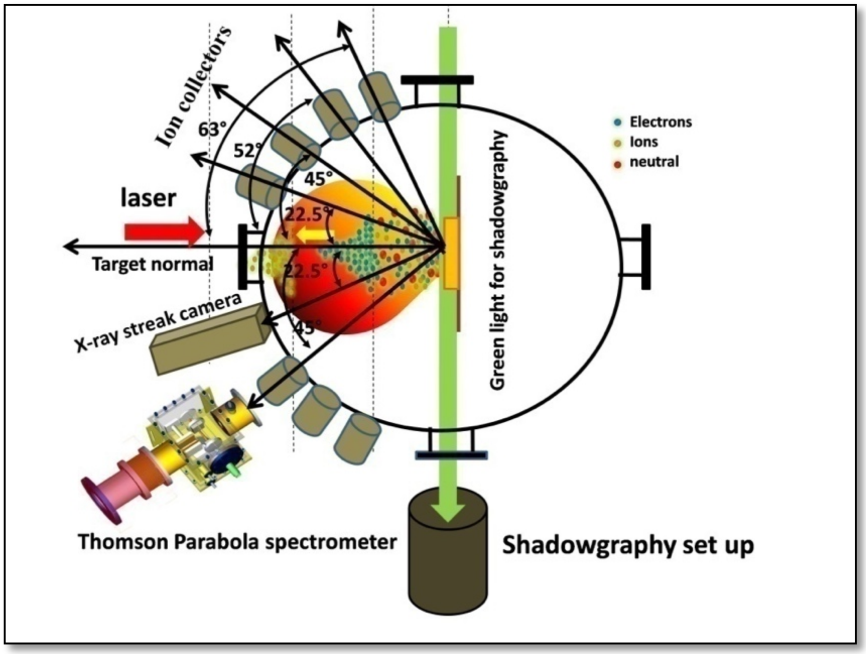

Figure 6.1 *Schematic of Experimental setup*

6.3 Target Preparation

Gold foams are prepared by sedimentation of nanoparticles from their vapours in the rare gas flow [164], [165]. The dimensions of pores ≈ 1 μm, nanoparticle ≈ 15-40 nm. Metal nanoparticle production as well as the layer formation is performed inside the set-up presented on. According to widely used method the layers are formed from the ‘‘fog’’ in low-pressure inertial gas atmosphere. Normally Ar or He depressed down to 150–700 Pa are used. The heater allows obtaining a thick metal flux of atomic structure. Nanoparticles and fiber-like clusters (nano-snow) sometimes of fractal structure are formed inside this flux in the low-pressure inertial gas atmosphere. Metal nanoparticle diameter and expected layer thickness depend on the gas pressure in the chamber and on gas composition itself. He atmosphere results in smaller nanoparticles and lower layer densities in comparison to Ar at the same pressure. The optimum pressure for layers of less than 10 % of solid metal density production is found to be 150–700 Pa. Hot metal flux is emitted within several minutes while metal nano-snow precipitation takes 16-48 hours.

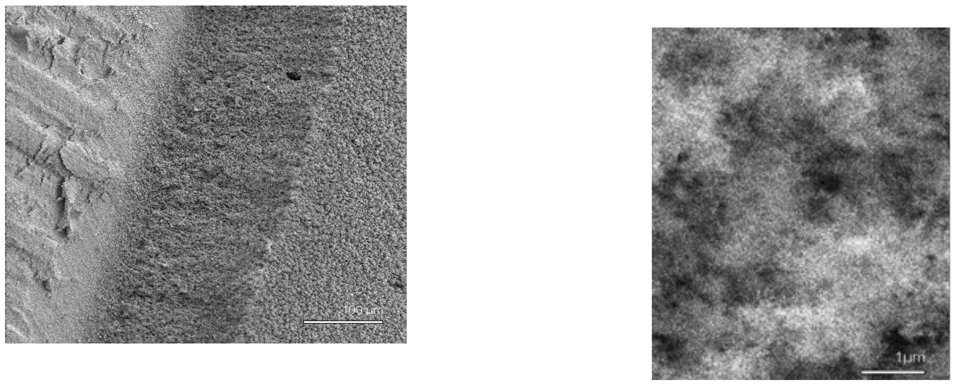

Figure 6.2 (a) *Metal nanoparticle layer cut, scale 100 micrometers (b) SEM picture of an Au ultra-dispersive layer obtained by an improved technique aimed at the production of more fine powder. The size of particles ~ 30nm. Scale 1 µm.*

6.4 X-rays emission studies from gold foam

In our experiment, we measured the time resolved X-ray signal from solid and low-density gold foam irradiated by sub-nanosecond laser using X-ray streak camera. The streak recorded by X-ray streak camera for solid gold and 0.2 g/cc gold foam is plotted in Figure 6.3 (a-b). It is clear from the Figure 6.3(a-b), that the X-ray pulse duration and amplitude from gold foam targets are greater than the solid gold. The effect of laser energy/intensity on the production of X-rays from 0.2 g/cc gold foam targets are studied and shown in Figure 6.3(c - d). X-ray flux is found to increase with increasing laser intensity. X-ray pulse width also slightly increases with laser intensity. As the laser intensity increases, the absorption of laser increases in the larger volume due to greater supersonic heat wave velocity. This gives rise to large plasma volume which enhances X-ray flux due to bulk absorption and density homogenizations of laser energy in all directions through supersonic heating. The X-ray flux also emitted from the bulk region which makes elongation of X-ray pulse duration than the solid gold target. In Figure 6.3(c), double peaks at lower intensities are also there but are not visible due to small signal. Figure 6.3(d) shows the plot of X-ray yield and X-ray pulse duration with respect to the laser intensities, which are following a scaling law of $I_L^{0.8}$ and $I_L^{0.3}$ respectively. Here, scaling of yield are following similar scaling law as we have measured using XRD in previous chapter and in past. In case of X-ray pulse duration, it is mainly function of laser pulse duration and slightly depends on the laser intensity as the recombination time increases and hence the lower scaling. Comparison of X-ray pulse emitted from solid gold targets and from gold foam targets of various densities are shown in Figure 6.4(a). From the figure, the X-ray emission pulse profile and intensity from gold foam targets are higher than solid gold. For the better visibility zoomed part of the peak area of the pulse profile are shown in Figure 6.4(b). From the figure, it can be seen that with decrease in the foam density X-ray pulse amplitude is increasing. The foam targets have this peculiar nature due to contrast of density in them- solid fibers having density greater than critical and pores have density lower than critical. When this stochastically distributed density is faced by the laser, it gets reflected in random directions and reaches deeply inside the foam which are not otherwise possible with the use of solid targets (where laser can go up to critical surface only). This results in an enhanced volume of plasma. Then the plasma fluxes coming from different directions collide and results in dissipation of shock wave.

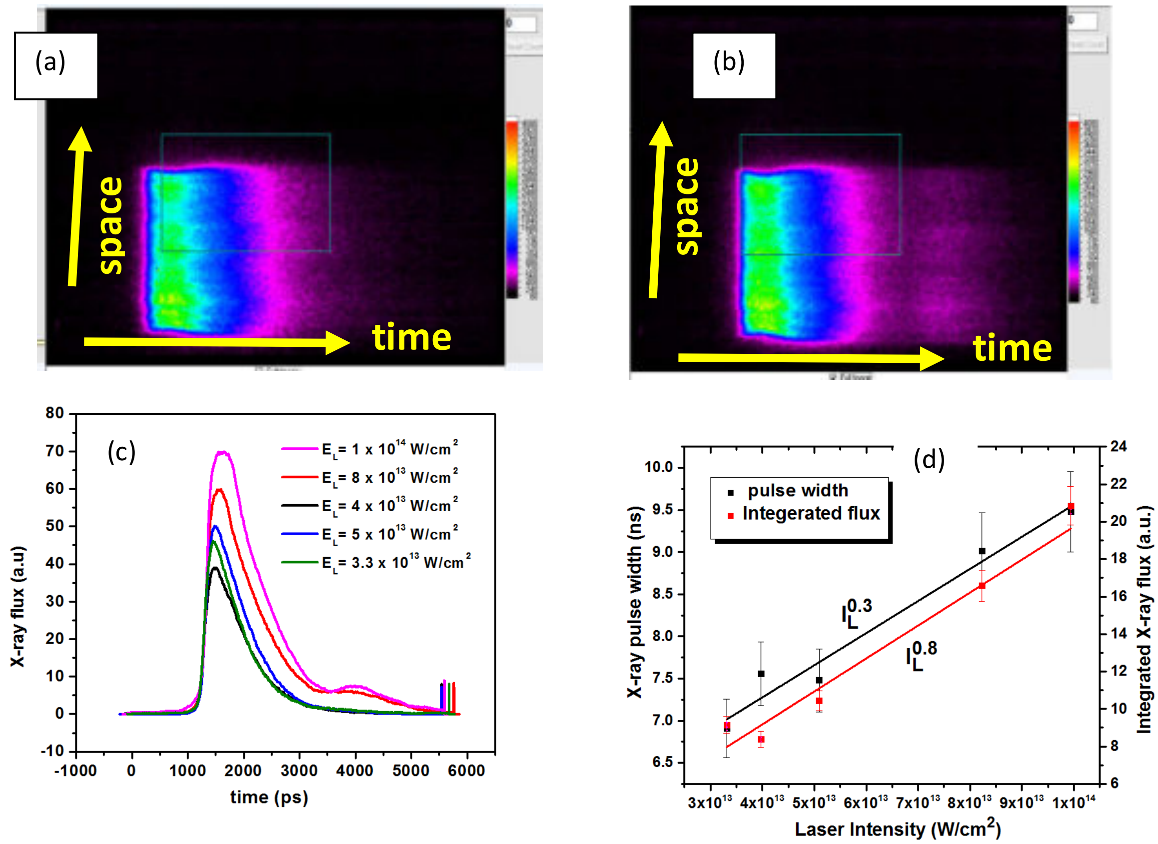

Figure 6.3 *Time resolved X-ray signal recorded by X-ray streak camera at laser intensity ≈1 × 10^{14} W/cm^2 for (a) solid gold, 19.3 g/cc (b) 0.2 g/cc gold foam target (c) plot of X-ray signal at different intensities of laser (d) scaling of X-ray pulse width and integrated flux of X-rays with different laser intensities.*

The measurement of the relative conversion efficiency (laser to X-ray) for X-rays in the spectral range > 0.8 keV as a function of laser intensity and target density is shown in Figure 6.5(a-b). The relative X-ray conversion efficiency is found to decrease (Figure 6.5(a), gold foam density- 0.2 g/cc) with increase in laser intensities. The X-ray flux is calculated by measuring the solid angle subtended on the streak camera slit by the plasma plume. The flux is multiplied by the 4π for the total X-ray yield emitted. In Figure 6.5(b), decrease in conversion efficiency with increase in target density of gold at fixed laser intensity of 9.9 × 10^{13} W/cm^2 can be seen. A 13 % higher X-ray conversion efficiency is found in 0.1 g/cc gold foam target in comparison to solid gold for X-ray spectral range > 0.8 keV. It means that the low-density foams are better convertors of X-rays at moderate laser intensities. The experimental data for conversion efficiency with density of foam targets were numerically fitted and observed to follow the relation $-0.026 + \frac{1.74}{1+\left(\frac{\rho}{0.107}\right)^{0.87}}$.

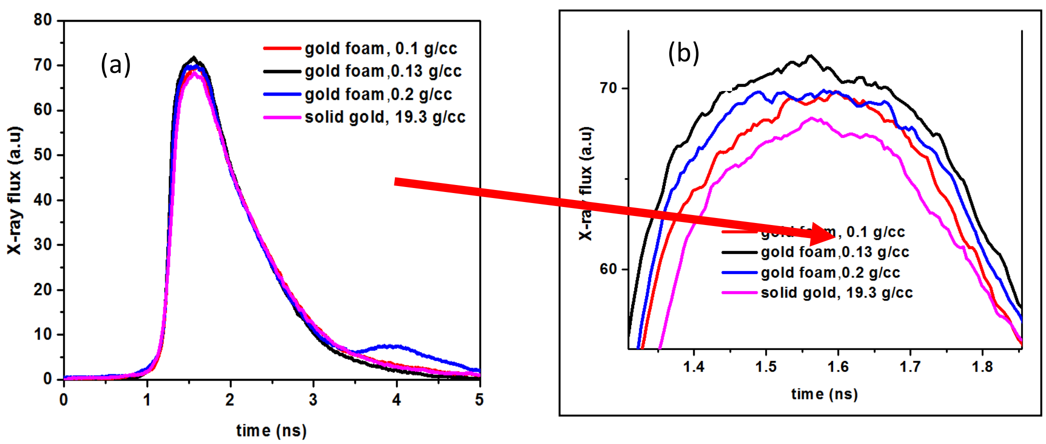

Figure 6.4 *(a) Comparison of X-ray streak signal for solid gold with three densities of gold foam (0.1, 0.13, and 0.2 g/cc) (b) zoom part of figure (a) showing reduction in X-ray flux from solid gold.*

The interaction of laser radiation with targets was simulated by the RADIAN one-dimensional numerical code [166]. The physical-mathematical model used in the RADIAN code contains the equation of two-temperature radiation hydrodynamics, the equations of state for ions and electrons. The classical or reduced Spitzer thermal conductivity is taken into account. The equations of gas dynamics are solved together with the radiation transfer equation in the multi-group approximation. The energy of the laser radiation is absorbed by the Bremsstrahlung mechanism. Laser radiation reaching the critical density is completely absorbed at the critical density point. In this series of calculations, the optical absorption coefficients were found by the THERMOS code [167].

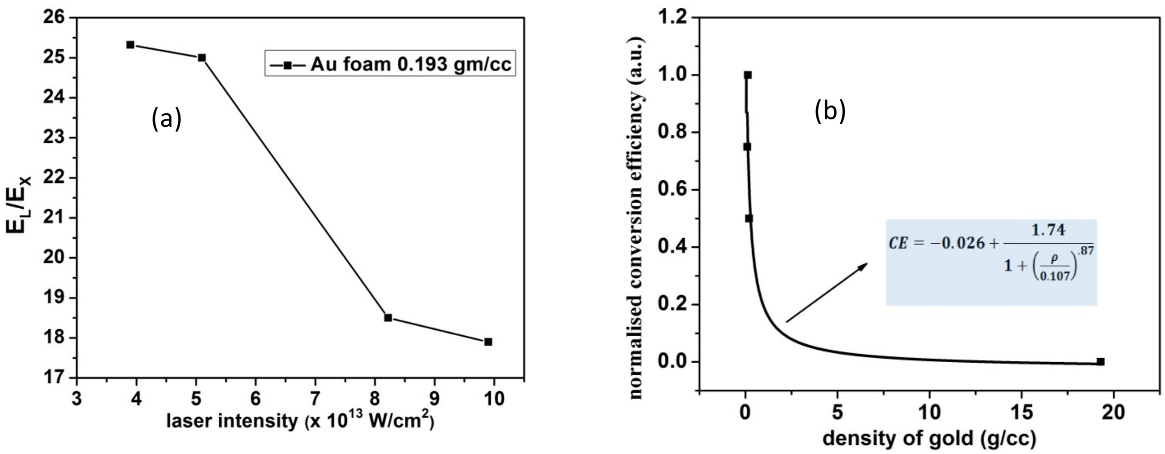

Figure 6.5 *Variation of (a) conversion efficiency for the 0.2 g/cc gold foam with different intensities of laser (b) conversion efficiency for different densities of gold target.*

The simulation was carried out in a plane one-dimensional geometry in a wide range of parameters. The first harmonic Nd- laser pulse of 0.5 ns half-width, the temporal shape of which corresponds to the experimental one, had a maximum radiation flux density in the range of 3.3×10^{13} -10^{14} W / cm^2. The impulse is heating a plane gold layer of 19.32, 0.2 and 0.1 g / cc density. In the calculations, the linear mass for the targets of different density was chosen to be the same. Figure 6.6 shows the density (curves 1,3) and temperature (curves 2,4) profiles formed in gold plasma with an initial density of 19.32 and 0.2 g / cm^3 under the action of laser radiation q = 10^{14} W / cm^2,1 ns after the laser pulse onset. The density and temperature profiles of the target with ρ_0 = 19.32 g / cc are characteristic of the plasma formed under the action of laser radiation on a solid matter. The density and temperature profiles of the target with ρ_0 = 0.2 g / cc are noticeably different. Absorption of laser radiation occurs in the region of densities less than the critical one, which is $n_e = 10^{21}$/cc for the first harmonic of the Nd laser. When the degree of ionization is z = 40 in the region of absorption of laser radiation, the critical density of gold under these conditions is 8×10^{-3} g / cc. With such a critical density, all targets turn out to be supercritical, laser radiation is absorbed in the outer layers of the targets. The 0.2 g / cc density target is expanded faster than the target of 19.32 g / cc density, so by the time t = 1 ns the linear size of the low-density target is 35 μm larger. From the laser radiation absorption region, the energy is transferred to the medium by means of a radiation wave and hydrodynamically, and makes the medium heated. The velocity of the radiation wave is inversely proportional to the degree of density $x \sim \rho^{-\alpha}$ [168], it decreases with increasing density, and the role of hydrodynamic processes increases, which we observe on curves 1 and 2 (ρ_0 = 19.32 g / cc).

The formation of the compression and unloading waves occurs. Curve 1 (ρ_0 = 19.32g / cm^3) demonstrates a shock wave. On the profile of density curve 3 (ρ_0 = 0.2g / cm^3), an increase in density is much less pronounced. The substance in front of the shock wave proves to be essentially heated by the radiation. As a result, the shock wave is not strong. For gold foam with density 0.2 g / cc, the heating by the radiative wave is the leading process. The radiative wave heats the matter at a greater depth than it occurs in targets with a density of 19.32 g /cc. By the time of 1ns the radiation wave is heating the target by the depth ~ 100 μm. Thus, in the lower-density plasma, the heated region is much more extended than in plasma formed in a substance, which originally had been a solid state matter. This is the cause of the experimentally observed widening of a plasma glowing spot in the eigen-radiation. The emissivity of the plasma is also shown in same figure. At ρ_0 = 0.2g / cc, the emissivity region is wider and lies closer to the surface of the substance than in the target, originally being in solid state (see curves 5 and 6), which corresponds to the plasma emission recorded in the experiments (Figure 6.6). Figure 6.6(b) shows schematically the correspondence of the position of the glow regions J1 (R1) and J2 (R2) and their locations X1 and X2 on the pinhole image.

Figure 6.7 shows the results of numerical simulation of the X-ray emission (in the range > 0.8 keV) as a function of time for different laser intensities for a low-density gold target of 0.2g /cc. The shape of the X-ray pulse depicts the laser pulse shape. The half width of the X-ray pulse increases with increasing of laser radiation flux. As the laser flux increases, the absolute X-ray yield increases as well. These conclusions are consistent with the experimental results.

With a decrease in the gold foam initial density (low density gold foam), the conversion to X-rays increases, and that was shown, in particular, in [168]. In this series of calculations, the effect of laser radiation with a fixed intensity (10^{14} W / cm^2) on the target was considered at different initial values of the gold foam density, including the density of a solid body. Figure 8 shows the temporal form of X-rays in the spectral energy range> 0.8 keV. The results of simulation are given for the targets with 0.2 g / cc and 19.32 g / cc initial values of the density of gold foam. The output of X-rays at low densities is higher than at the density of a solid, which is consistent with the experimental data of this work (Figure 6.8). In calculations of the targets with the same linear mass, the X-ray emission in the region (>0.8keV) with a decrease in density from 19.32 to 0.1 g / cc increases by 14%.

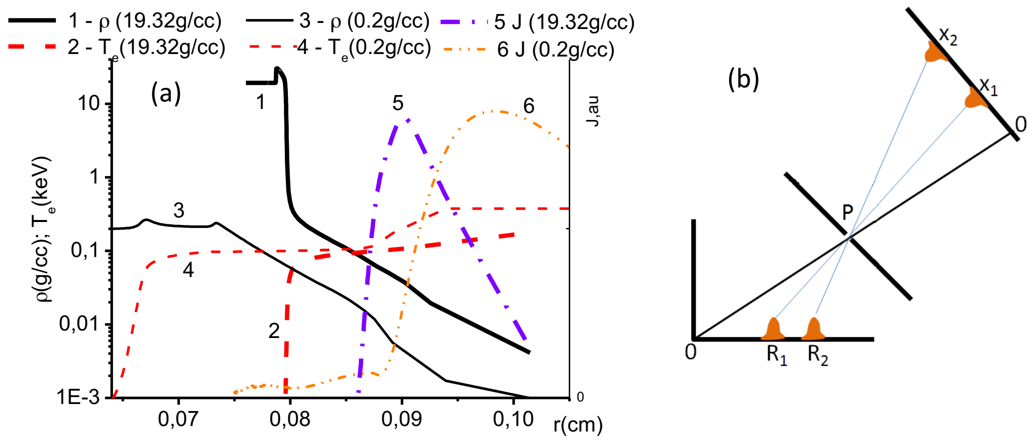

Figure 6.6 *(a) Hydrodynamic profiles obtained in the calculation of the interaction of laser radiation $q = 10^{14}$ W / cm^2 with plane targets made of gold at the moment t = 1 ns. Thick lines refer to the targets with initial density of $\rho_0 = 19.32$ g / cm^3, thin ones - with $\rho_0 = 0.2$ g / cm^3; density - solid lines (1), (3); temperature - dashed lines (2), (4); plasma emissivity - dotted lines (5), (6) (b) The maximum plasma emissivity is located at a distance R1 and R2 from the plasma surface (0). Through the pinhole (P) these areas are projected at a distance of X1 and X2 from the axis 00 on the image.*

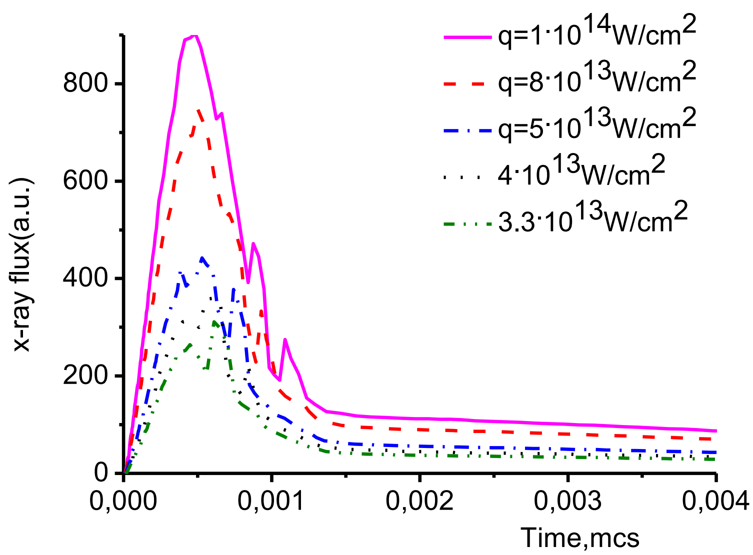

Figure 6.7 *The X-ray yield as a function of time for a low-density target ($\rho_0 = 0.2$ g / cm^3) at different intensities of laser.*

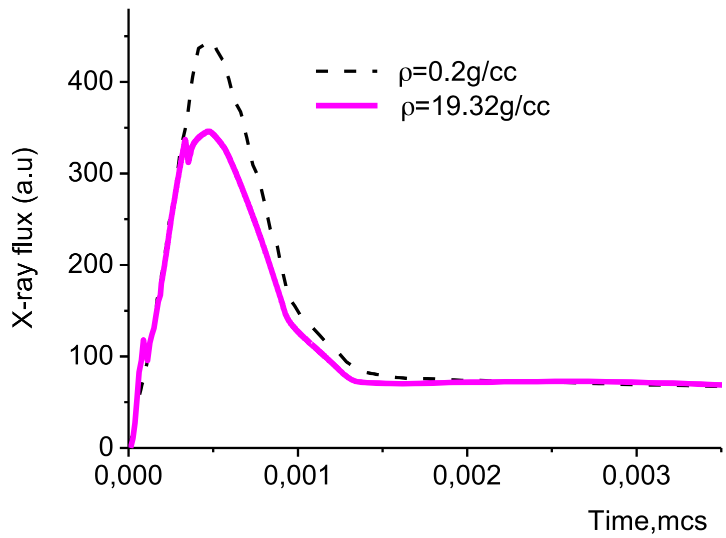

Figure 6.8 *The X-ray yield as a function of time for a target heated by a laser intensity 10^{14} W / cm^2: solid line – target has initial density 19.32 g/cm^3; dotted line - initial density 0. 2 g/cm^3.*

In order to understand the underlying Physics of X-ray enhancement of X-ray emission from gold foam target compared to the solid gold targets an analytical model proposed by Hammer and Rosen [160] will be briefly discuss. To derived an analytical expression, two criteria of the absorption of laser in the case of foam target is to be taken (1) volumetric heating by supersonic heat wave and (2) reduction of energy due to loss in the kinetic energy/ hydrodynamic motion. The above parameters can be discussed by taking the radiation wave (Marsek wave) which is important for the calculation of the energy transport for the energy balance in the laser matter interaction studies. To get the condition of the heat flows in high Z foam and solid targets, a steepness parameter of heat front, the internal energy (e) and opacity (K) varies as $\varepsilon = \beta/(4+\alpha)$ (0.3 for gold), T^{β} and $T^{-\alpha}$ respectively and hence the diffusion equation for the heat flow can be written as

$$\rho \frac{\partial \rho}{\partial t} = \frac{4}{3}\frac{\partial}{\partial x}\frac{1}{k\rho}\frac{\partial(\sigma T^4)}{\partial x} \tag{6.1}$$

where

$$1/\mathrm{K} = g^{-1}T^{-\alpha}\rho^{\lambda} \text{ and } e = fT^{\beta}\rho^{-\mu} \tag{6.2}$$

Here, f and g are constant and α, β, μ, and λ are the tabulated value for the given material. For gold its values are 1.5, 1.6, 0.14 and 0.2 respectively [159].

In case of supersonic heating, the heat wave travels much faster than the hydrodynamic motion and hence the change in the density can be assumed negligible and treated as ρ = constant, then the heat front position for a time t can be obtained by solving above equation (6.1) and is given as

$$X_F = \sqrt{\frac{2}{3}\frac{1}{K\rho^2}\frac{\sigma T_S^4}{\rho_s}t} \tag{6.3}$$

where T_s is the surface temperature and $T = T_s\,(1+ X/X_F)$ is the temperature at distance X_F at time t. Using Eq. 6.2 and 6.3, we can rewrite the equation 6.1 as

$$\frac{\partial}{\partial t}T^{\beta} = C\frac{\partial^2}{\partial x^2}T^{4+\alpha} \tag{6.4}$$

$$C = \frac{16}{4+\alpha}\frac{g\sigma}{3f\rho^{2-\mu+}} \tag{6.5}$$

The value of f and g for gold target are 3.4×10^6 J/g and 1/7200 g/cm^2, So value of $C = 4.08 \times 10^{-7}/\rho^{2.06}$.

The Eq. (6.5) can be simplified as

$$X_F = 0.0029\, T_{100}^{1.95} t^{0.5}/\rho^{0.17} \tag{6.6}$$

Here, t is laser pulse duration, T_{100} is temperature in 100 eV. The change in the wall energy per unit area is written as

$$E/A = \rho.e.X_M = \frac{0.0029\, T_{100}^{3.55} t^{0.5}}{\varrho^{0.17}}\, (\mathrm{MJ/cm^2}) \tag{6.7}$$

Thus, distance travelled by heat wave and energy absorbed per unit area are inversely dependent on the density of the gold foam. From above equation if density increases, the heat wave velocity ($\dot{X}_F$) decreases this means heat wave may still travel with supersonic wave but the tail of the wave profile develops a rarefaction wave and hence loses energy. So, in case of low density foam targets with density greater than the under dense density, a considerable amount of energy will be converted in to rarefaction wave and hence a correction factor is added to the wall energy loss per unit area and can be written as

$$\frac{E}{A} = \frac{0.0029\, T_{100}^{3.35}\ \tau^{0.5}}{\rho_0^{0.17}} + .0035 \rho_0^{0.74} T^{2.4} \tau \tag{6.8}$$

On the other hand, to solve the radiation diffusion equation in solid gold heated with laser radiation, it is necessary to solve three hydrodynamic equation of conservation laws (Rankin-Hugoniot relation)

$$\frac{\partial V}{\partial t} = \frac{\partial u}{\partial m}$$

$$\frac{\partial u}{\partial t} = -\frac{\partial \rho}{\partial m}$$

$$\frac{\partial \rho}{\partial t} + P\frac{\partial V}{\partial t} = \frac{4}{3}\frac{\partial}{\partial m}\frac{1}{K}\frac{\partial \sigma T^4}{\partial m} \tag{6.9}$$

V=1/ρ is specific mass, the mass variable $= \int \rho dx$, P is Pressure, and u is fluid velocity. By putting the boundry condition for the effectively infinite density at the ablation front, i.e., u, V, T →0 and T(0,t) = T_s(t) and using power law for opacity and equation of state (EOS) variables

$$e = fT_{100}^{\beta}V^{\mu}$$

$$\frac{1}{K} = gT_{100}^{\alpha}V^{\lambda}$$

$$P = r\frac{\varrho}{V} = rfT_{100}^{\beta}V^{\mu-1} \tag{6.10}$$

where value of parameters μ and r for gold at temperature 100-300 eV are 0.14 and 0.25 respectively. By solving above equations, self-similar time dependent solutions for

$$\text{ablated mass } m(t) = m_0 T(t)_s^{1.914}$$

$$\text{absorbed flux } F(t) = F_o T_s(t)^{3.35}\tau^{-0.41} \tag{6.11}$$

$$\text{ablations pressure } P(t) = P_o T_s(t)^{2.630}\tau^{0.4479}$$

for k=0 lowest order and T=100-300 eV, m_o=9.90x10^{-4} g/cm^2, F_o=3.40 x 10^{-3} MJ/ns.cm^2, P_o=2.89 Mbar

By simplifying $F = \int F.dt$ we get

$$E/_A = 0.0058\, T_{100}^{3.35}t^{0.59} \qquad \text{with } T_s = T_{100}\, t^{q}_{0/5.5} \tag{6.12}$$

here if we take lowest order i.e. k= 0 then the values of heat loss (using equation (6.8)) are 0.1188, 0.01138 and 0.011807 MJ/cm^2 for 0.1, 0.13 and 0.2 g/cc respectively. The heat loss for solid gold is 0.1498 MJ/cm^2. The change in the wall loss with increase of density using this analytical model is not comparable to our experimental and simulation data shown in Figure 6.5(b). However, it is showing similar trend i.e. by increasing density, the wall loss is increasing and hence X-ray yield is decreasing. This indicates that, the enhancement of X-ray yield with lower density is not just due to reduction in wall loss mechanism rather it is one of the reason.

6.5 Comparison of photo peak

The photo peaks recorded by the ion collectors are compared which consists of integrated radiation flux emitted from plasma. In a typical condition, relevant to LPP, peak of the spectral self-emissivity of the plasma is located in X-ray region.

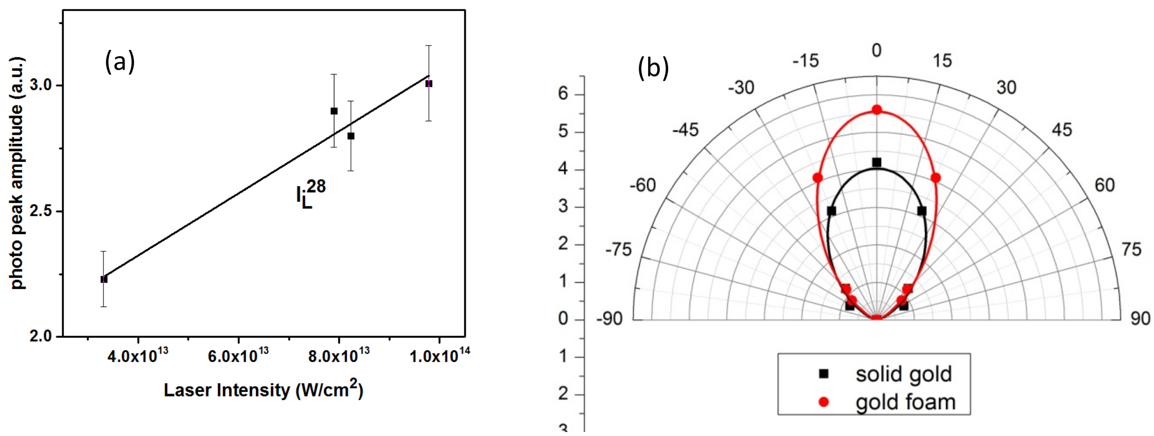

Figure 6.9 *(a) Scaling of photo peak amplitude from signal of ion collector with laser intensity (b) angular distribution of photo peak for solid gold and gold foam (0.1 g/cc).*

Therefore, the features of photo peak can be considered as finger prints of X-rays from LPP. Only difference in ion collector photo peak and XRD signal is that ion collectors are not covered with any x-ray filters, so it detects photon emission of all wavelength. The photo peak amplitude increases with increasing laser intensity according to power law $I_L^{0.28}$, I_L is intensity of laser. This scaling is at an angle of 22.5° from target normal. Since ions collectors are placed at different angles from target normal so the angular distribution of radiation flux is also calculated by taking the photo peaks of ion collectors placed at various angle with target normal and is drawn in Figure 6.9(b). The emission of radiation is found to follow a distribution $\cos^{n}\theta$, where n = 2, and 5 for solid gold and gold foam (0.1 g/cc) respectively and θ is angle with respect to target normal. The maximum flux peaks towards target normal and is high for low density gold foam in comparison to solid gold at same laser intensity.

6.6 Comparison of radiation from pinhole camera used in Thomson Parabola Spectrometer

To increase the Thomson Parabola resolution, we have introduced an 80 μm diameter aperture just before the magnetic shoes. This pinhole acts as a pinhole camera with relatively lower resolution than the standard pinhole camera which are nearly 25-30 μm. The distances between plasma source and pinhole and from pinhole to detector are 41 cm and 52.7 cm respectively. The magnification of the pinhole camera is 1.28 with this magnification factor the resolution of the camera is calculated using $\left(1+\frac{1}{m}\right)d$ and is 142μm. The comparison of size of plasma from 0.1 g/cc and solid gold can be seen from pinhole images shown in Figure 6.7(a-b) and corresponding profile is plotted in Figure 6.9(c). The size of X-ray plume and the X-ray flux in case of gold foam targets are 13% larger and about 10% higher respectively in comparison to solid gold. Our X-ray streak camera records are also showing similar results.

6.7 Optical shadowgraphy of solid gold and 0.1 g/cc gold foam targets

Shadowgrams presented show differences in the plasma plume movement towards the laser. The integral profile shapes of the moving corona is more symmetrical in the foam for the 8 ns than that in the solid target. The volume of the heated low-density hot corona is a factor of 1.78 larger for the foam target than for solid one as could be judged from the shadowgrams.

However, corona movement towards the laser direction is similar than the transverse spread of the energy (26% more than solid) which seems good for foam to be used as converter of laser energy to the X-rays. There is evidence of crater at the centre of plume in both solid and foam target at 2 ns delay, however, after the delay of 8.2 ns, the surface underlying the corona in the foam seems more uniformly distributed and in solid the crater depth increases together with their coronas.

This means, temporal evolution of the corona profile on the full scale more regular in the foam than in the solids. This means solid gold corona expansion remember earlier profile surface irregularities and laser imprint, whereas the shape of foam profileis more regular (circular segment) and has no essential assymmetry as solids show. The shape of foam corona withnesses that the foam movement is better organized with only small self-similar riples on the boundary with no deforming as symmentry of the matter fluxes from plasma. The nanoparticles induced small scale turbulence could be responsible for that.

6.2 Comparison of ions signal of gold foam with solid one

The accelerated ions are measured by Faradays ion collector in TOF geometry at four angles such as 22.5°, 45°, 52° and 63°. The typical ion collector signals for gold foam targets are shown in Figure 6.12(a). The signals recorded by ions collectors can be divided into five parts- the first part is photo peak due to X-ray photons, second part is fast ions contributed by contamination on targets (protons H^+), third is fast ion components of targets material, fourth is thermal ions coming from thermal conduction region of plasma, then fifth is slow ions coming from inside part and from surrounding area heated by the X-rays. The influence of laser intensity on the ion flux and peak velocity is observed for 0.1 g/cc gold foam. From Figure

6.12(a), it is clear that the amplitude of the ion flux of higher velocity increases with the laser intensity.

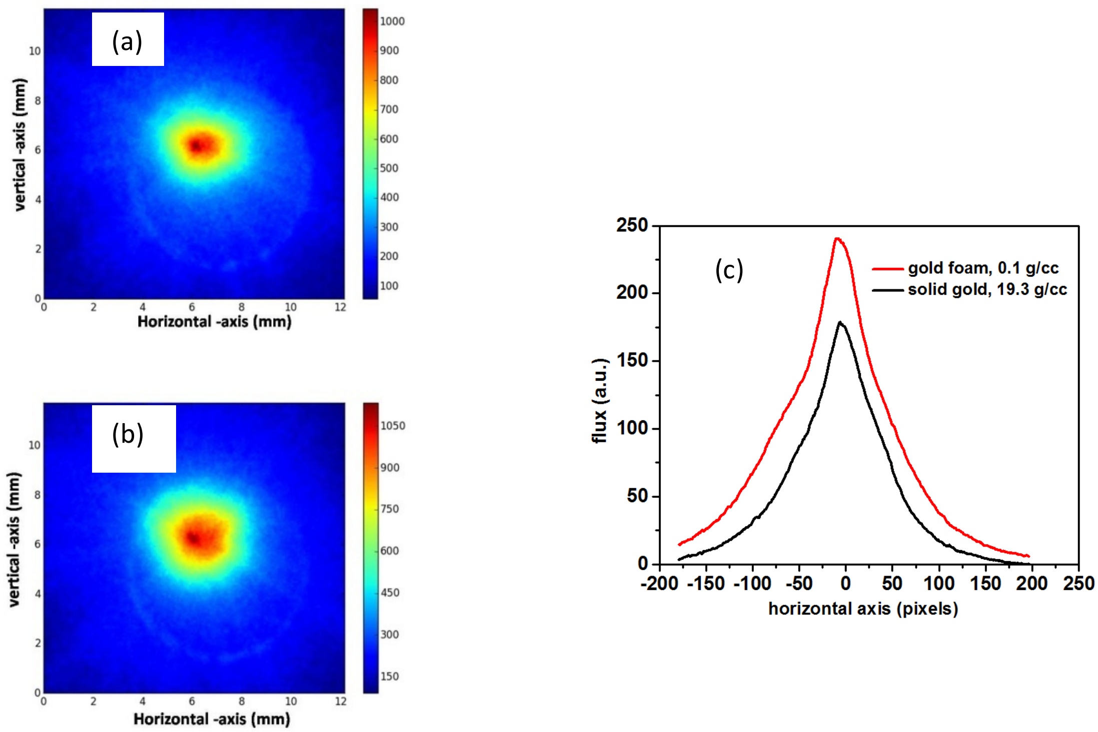

Figure 6.10 *Comparison of plasma size for (a) solid gold (b) 0.1 g/cc gold foam (c) plot for comparison of 0.1 g/cc foam and solid gold target.*

It can be understood by the relation $T_h = A\,(I_L^{\alpha})$, where α is constant. So, by increasing the laser intensity, the hot electron and hence faster ions temperature increases which leads to generation of larger flux of higher energy ions. It is also clear from the Figure 6.12(b), that the maximum velocity of ions is towards target normal and scale with higher scaling factor with laser intensity than the ions at larger angle from the target normal. The scaling factor for the ion velocity with laser intensity at 22.5°, 45° and 52° angles are 1.3, 0.8 and 0.13 respectively. When the ions signal of foam is compared with solid gold at same laser energy, a large difference in ions kinetic energy and ion flux are seen as shown in Figure 6.13(a).

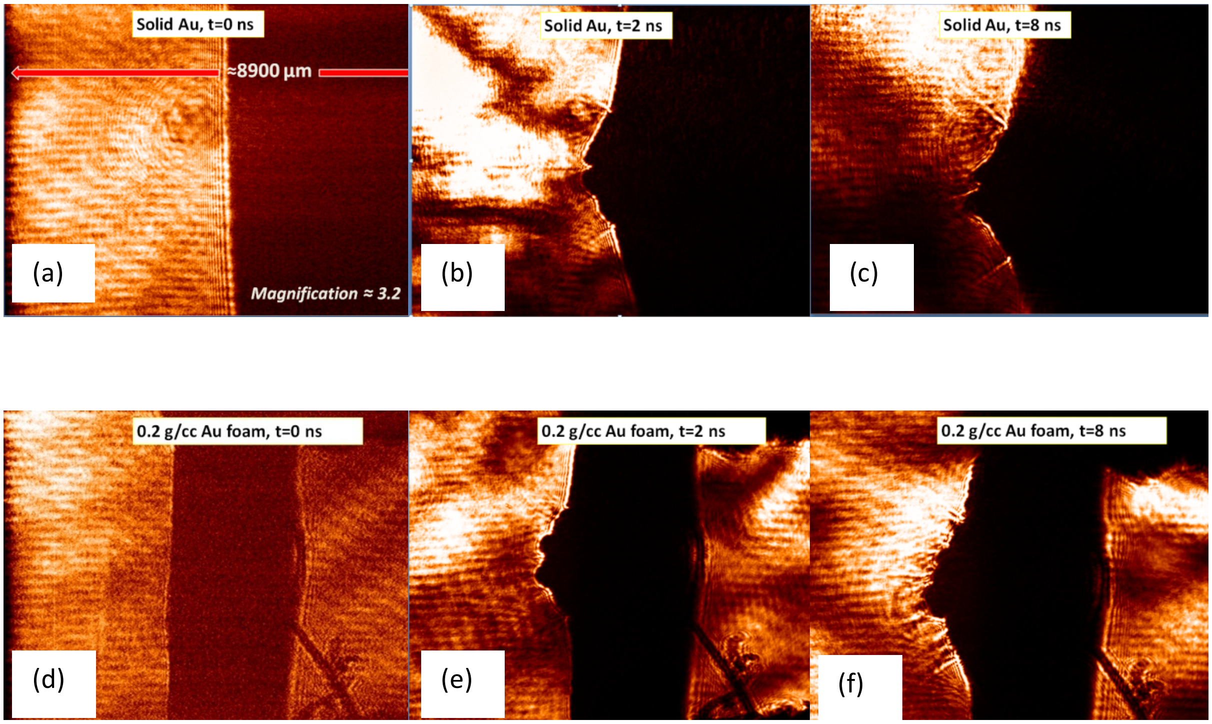

Figure 6.8 *Shadowgraphy results showing expansion of gold plasma (a) before arrival of laser pulse (b) after 2 ns of laser pulse arrival (c) after 8.2 ns of laser pulse arrival and (d-f) are showing expansion plasma for 0.1 g/cc gold foam targets just before arrival of laser pulse, at 2 ns and at 8.2 ns after arrival of laser pulse respectively.*

The ion signal from solid gold target is reduced by one third to bring it to scale length of the figure with signals from foam. It can be seen from the Figure that for solid gold, the flux of thermal ion is large but emits in a narrower energy range and is faster than the thermal ion emitted from foam targets. In case of gold foam, the thermal ions are distributed in a broad energy range. This implies that in case of gold foam targets, ions are thermalizing at lower energy which is also important criteria for the fusion research where lower energy ions are preferable. This indicates lower ion temperature in case of gold foam targets in comparison to solid gold plasma implying less movement of plasma from wall when a laser interacts with foam wall hence more absorption of laser energy resulting more X-ray emission in comparison with solid gold. Figure 6.13(b) shows the zoomed part of the ion collector signal for better visualization of fast ion components. Here, fast ion from solid gold also having narrower energy width with higher energy than gold foam targets. This indicates that the gold foam targets are better X-ray converter but slower ion emitters.

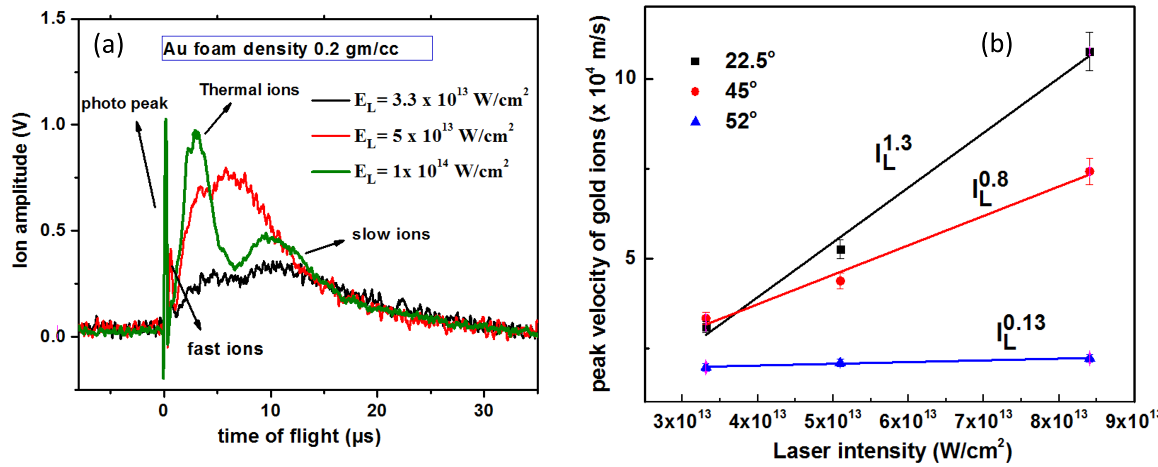

Figure 6.12 *(a) Ion collector signal (placed at 22.5 ^{O} from target normal) comprises of time of flight and ion amplitude at different laser intensities for 0.2 g/cc gold foam. (b) Scaling of ion peak velocity for ion collectors placed at three angles (22.5º, 45º and 52º from target normal) for 0.2 g/cc gold foam target.*

Angular mapping of ion acceleration and flux is shown in Figure 6.14. The peak velocity of ions is plotted with respect to different angles from target normal. In case of solid gold, the peak velocity is high towards target normal indicating the emission of high energetic ions towards target normal. On the other hand, there is no forward peaking of high velocity ions in low density foam. Thus, the ions coming out from low density targets have very less kinetic energy in comparison to ions from solid gold which are supporting the reason of higher X-ray flux. Though, velocity of the ions from foam targets are much lower than ions from solid gold, but the integrated flux of ions integrated over full ion collector signal is comparable to the flux of ions from solid gold in spite of density of the foam targets are 1/100th to 1/200th of solid gold. This means these ions are coming from a large volume of plasma supporting the volumetric absorption of laser light in case of low density gold foam as can be seen from shadowgraphs and simulation. Shang et al. has shown in their simulation using 1 D hydrodynamics code that radiation energy for 0.1 g/cc gold foam is higher than the solid gold however for the kinetic energy of thermal ions with time shows reduction in case of 0.1 g/cc compared to solid gold [127], however, they have not supported it by experiments. Our results are first to validate his simulation. Our experimental results also show that in case of solid gold, thermal ions peak velocity is 31×10^4 m/s and spread in narrow energy width, however, in case of 0.1 g/cc, peak velocity reduces to 6 $\times 10^4$ m/s towards target normal and emitted in broad energy range. This measurement is very much important in the designing of the hohlraum cavity for the fusion research. The importance of lower plasma blows off velocity can be understood that when a high-power laser interact with inner wall of the hohlraum, hot and low density plasma expanded towards the center of the hohlraum. As the plasma blow off the wall, the X-ray emitting region and laser absorption layer also move and laser scattering increases by laser plasma instabilities, e.g., stimulated Brillouin scattering, (2) altering where lasers couple by moving the critical surface away from the walls and changing the refractive index, and (3), in the case of vacuum hohlraums, ablating directly into contact with the ablation layer of the fuel capsule, which means the coupling efficiency of laser decreases. As we have demonstrated from the ions measurement that the plasma blows off velocity is lower in case of foam gold targets and hence lower losses than solid which improves the X-ray conversion efficiency from foam targets than solid. This is another way of explanation of our measurement of enhanced X-ray conversion efficiency.

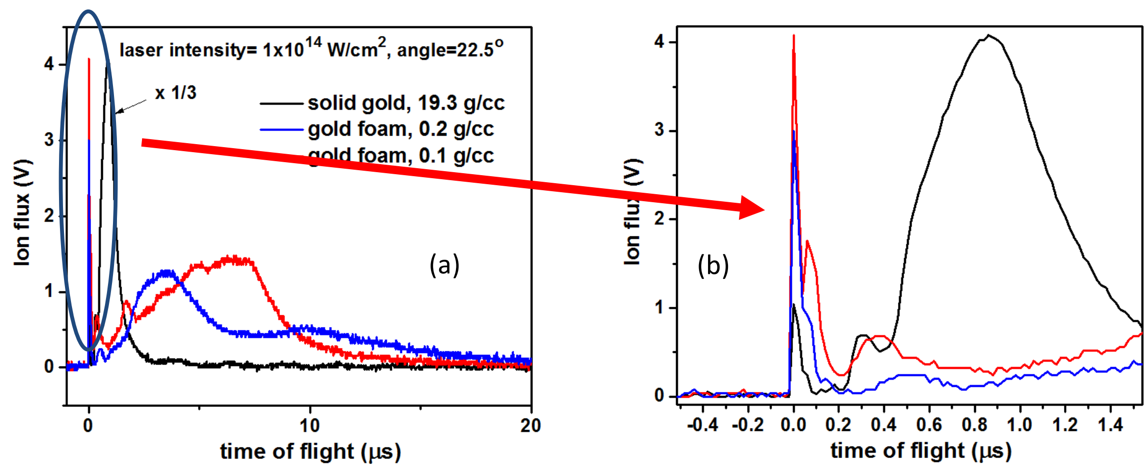

Figure 6.13 *(a) comparison of ion flux for different target densities at angle 22.5° from target normal. (b) zoomed portion of the circled area near to photo peak.*

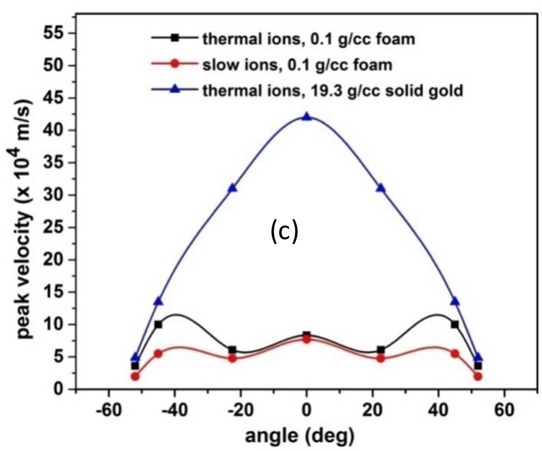

Figure 6.14 *Angular distribution of peak velocities of thermal ions for 0.1 g/cc gold foam with that of solid gold. Angular distribution of slow ions for 0.1 g/cc gold foam is also drawn.*

We have also done ion energy spectrum analysis from our high-resolution Thomson Parabola records for solid gold, 0.2 g/cc and 0.1 g/cc density foam gold targets as shown in Figure 6.15(a-c) at laser fixed energy of 3.8 J. The Thomson Parabola recorded spectrum of a few charge states of solid gold plasmas, however, trace of the ion spectrum from the similar charge states or other charge states are very faint or below the recordable limit. This implies that the fluxes of particular charge states in gold foam targets are lower than the solid gold targets. The energy spectrum of protons flux from the low-density foam targets and solid targets are plotted and shown in Figure 6.12(d). The protons flux is also lower and in narrow energy range at 45° from target normal than the solid gold targets.

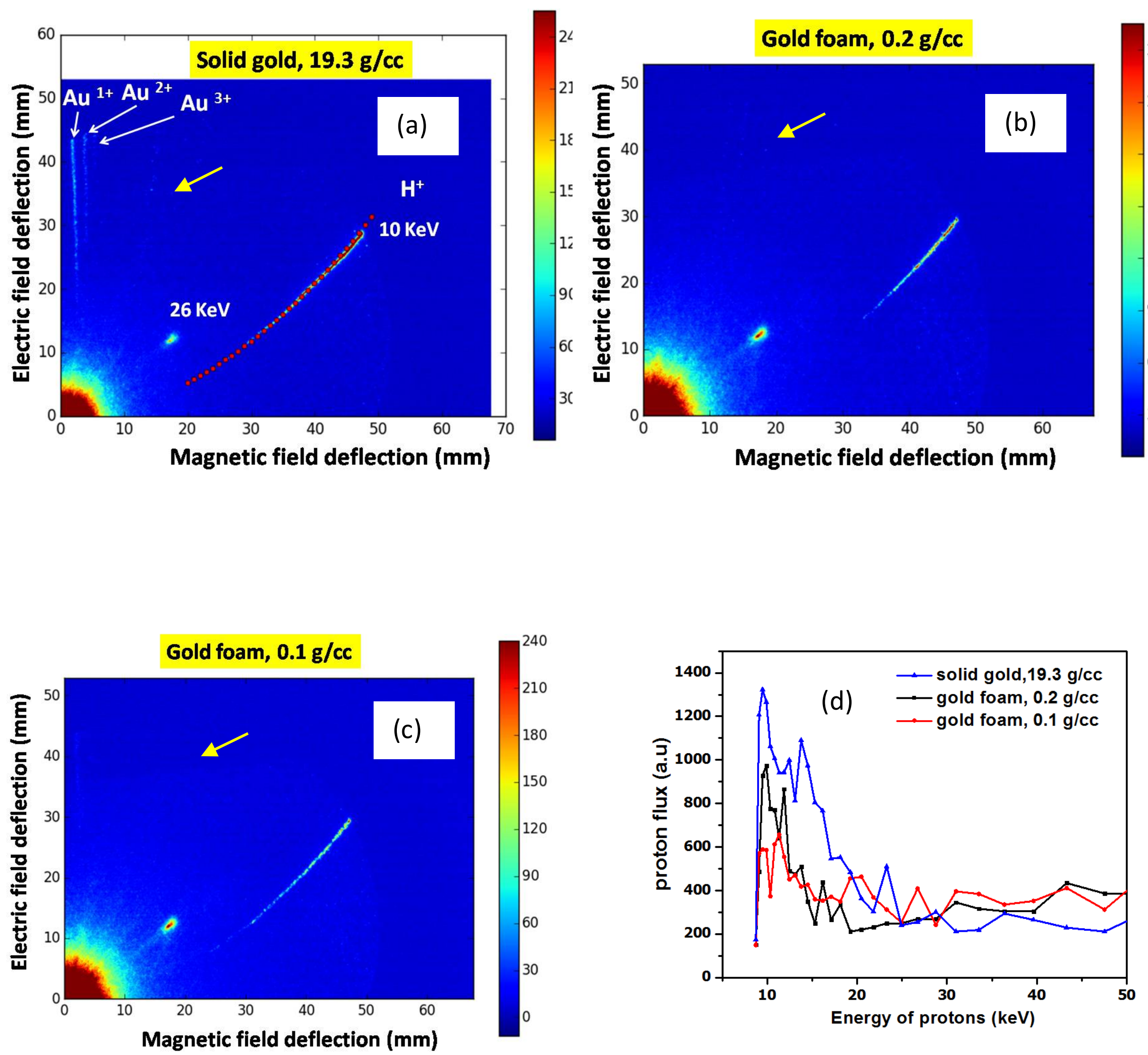

Figure 6.15 *Results of Thomson parabola spectrometer for (a) solid gold (b) 0.2 g/cc gold foam (c) 0.1 g/cc gold foam (d) plot of proton flux with respect to proton energies for solid gold and gold foam targets with densities 0.2 and 0.1 g/cc.*

6.3 Summary

A comparative study on the emission of X-ray and ions from low density gold foam targets of densities 0.1 g/cc, 0.2 g/cc targets and solid gold targets is performed using a Nd: Glass laser with focusable intensities in the range of 10^{13} -1 x 10^{14} W/cm^2. It is observed that the laser absorption in the foam targets are volumetric and hence enhanced the X-ray emission by 13% than the solid targets. It is also observed that the X-ray pulse duration in case of foam targets are slightly larger. X-ray pinhole camera and optical shadowgraphs are showing that the X-ray emitting region on foam targets are larger in transverse direction indicating the volumetric heating by supersonic heat wave which is in all direction. Ions Time-of-Flight spectroscopy measurements shows that the thermal ions peak velocity is 31x10^4 m/s and spread in narrow energy width in case of solid target, whereas, in case of 0.1 g/cc gold foam target, the peak velocity reduces to 6 x10^4 m/s towards target normal and emitted in broad energy range. However, total ion flux from foam and solid targets are comparable indicates that the ion emissions are from larger volume. The 1D hydrodynamic simulation also indicates the higher conversion of laser to X-rays for low density gold foams. The simulation results well match with the experimental studies.

Chapter-7

Summary and Future research plans

7.1 Summary

The thesis involves experimental investigation of X-ray and ion emission with the help of various plasma diagnostics. The experiments are carried out at 30J /500 ps Nd: Glass laser, 2J/8 ns Nd: Glass laser available at Laser Shock Laboratory, BARC and 1J /30 fs Ti: Sapphire laser, TIFR. The diagnostics involves X-ray photo-diodes, X-ray streak camera, flat crystal spectrometer with X-ray CCD camera, NaI detector, Faraday's ion collector and Thomson Parabola Spectrometer (TPS). The research work primarily focused on the study the conversion efficiency of laser to X-rays as a function of target density, spectroscopic studies for determination of plasma parameters, evolution of ions and the energy distribution of ions for metallic solids and foam targets (low to high Z). The primarily aim is the characterization and optimization of laser plasma driven X-ray sources for various applications. The bright X-ray source is the central demand of various applications. Foam targets are apposite choice to fulfill this demand. Keeping this in view, a series of experiments are performed on plastic, silica aerogel, deuterated and gold foams to see the effect of foam density on X-ray yield. The X-ray emission take place through free-free, free-bound and bound-bound transitions. The multi-keV continuum X-rays are observed in different energy ranges. The K- and L- shell spectroscopy is performed using solid targets, i.e., Al, Quartz, Cu and silica aerogel. Atomic codes are used to find the transition wavelengths, transition probabilities and oscillator strengths of the spectral lines and charge state distribution of ions. Along with X-rays, ion emission is investigated to reveal the complete picture of interaction of intense laser beams with foam targets. The ion emission is detected at different angles from target normal to see the angular distribution of ion flux and energies. It provides the finger prints of plasma evolution and hydrodynamic motion in vacuum. The thesis also describes the development of high resolution Thomson Parabola Spectrometer (TPS) which is successfully used in probing ion emission from laser irradiated solid as well as foam targets. The simulations are performed using SIMION software to design the spectrometer. Besides X-rays and ion studies, shadowgraphy is used to capture plasma expansion dynamics at different time delays with respect to the incident laser. In this way, present thesis provides the complete information about laser-plasma X-ray and ion emission from the low density foams along with the spectroscopic studies which are helpful in diagnostic of the plasma. The main results of the thesis are discussed below

1. A high resolution/high dispersion ion spectrometer comprising of a ring type ion collector and Thomson parabola with varying magnetic field (100 Gauss to 2 kGauss, using permanent magnetic) and varying electric fields (few Volts to several kV) has been developed. The optimization of the spectrometer is performed using carbon target irradiated with intensity up to 7×10^{14} W/cm^2 producing six charge states of carbon (C^{1+} to C^{6+}) with energy range (3 keV to 300 keV) along with protons with energy range (15 keV to 45 keV). For in-situ measurements of ion parameters such as ion energy, momentum, energy and mass resolution of ions, a python based software is developed. The energy resolution of the TPS is found to $\Delta E/E \sim 0.026$@ 31 keV and mass resolution is $\Delta m/m \sim 0.026$ @ 35 keV for charge state C^{4+} of carbon plasma. The angular distribution of the integrated and individual charge states of carbon ions is calculated. The higher

charge states of carbon (C^{5+}, C^{6+}) are found to be more directional towards target normal than corresponding lower charge states.

2. Spectroscopic studies are performed from laser produced X-ray using a 30 J/500 ps Nd: glass laser in the intensity range of 10^{13}- 4×10^{14} W/cm^2. The observed spectrum consists of He-β, γ, δ, ε and H-like lines from Al plasma. The intensity of resonance lines is found to vary with laser intensity per a power law $E \propto I^{\alpha}$ with α=2.2, 2.3,2.4 for He_β, He_γ, He_δ, respectively. The temperature and densities calculated by analytical models based on line ratio methods are 260 - 420 eV and 1.6 - 2.8×10^{20} cm^{-3}, respectively, which is in good agreement with the results obtained by FLYCHK (T_e=160eV, T_h=1 keV, f=0.008 and $n_e=5\times10^{20}$ cm^{-3}). The opacity effects are found to be more pronounced for lines with transition from low n lines e.g. He_β ($1s^2$-1s3p) whereas opacity effects reduce for higher values of transition states, n, i.e., He_γ, He_δ and He_ε. The high temperature corresponding to H-like line in comparison to He-like shows the emission of these lines from different regions of plasma. The L-spectrum of Copper consists of Ne, F and O- like Rydberg resonance lines along with some of the inner shell satellite lines in the wavelength range of 7.9-9.5Å. The average temperature and density of the most strongly radiating portion of the plasma is 150-350 eV and 4.5×10^{20} /cm^3 for laser intensities in the range 1.3×10^{14} - 4×10^{14} W/cm^2. The effect of change in laser intensity on the L-shell spectrum of Cu is studied which indicates the switching between lower (Cu XX) and higher charge states (Cu XXI, Cu XXII) at higher laser intensities.

3. In the experiment based on irradiation of Cellulose Triacetate foams (TAC), the laser pulse duration shortened from 680 ps (FWHM) to 360 ps after passage through the TAC with a column density of about 600-900 mg/cm^2 and to 176 ps for a target with a column

density of about 2000 mg/cm^2 (density r = 2 mg/cm^3, thickness h = 1000 mm). In case of subnanosecond laser pulse irradiation, the TACs with subcritical densities provide more hard X-ray yields than that of supercritical density target. The quantitative measurement of X-ray conversion efficiency shows 2.3 times higher yield in 2 mg/cc foam targets as compared to 20 mg/cc foam targets in the spectral ranges, 5-8.3 keV and 4.5-16 keV. Large ion flux and shift of ion energy spectrum towards higher energies is observed in supercritical density targets. Same trend has been seen from individual charge states of carbon and oxygen. The simulations performed using one-dimensional radiation-hydrodynamics agree well with the experimental results. When TAC foams are irradiated with 25fs/1J laser, many fold enhancement is noticed in case of soft X-rays as well as hard X-ray in comparison to solid plastic.

4. The experiment based on silica aerogel foams shows an enhancement of 2.5 times in soft X-ray emission (0.9-1.56 keV) and a decrease of 1.8 times in hard X-ray emission (3.4-16 keV) for 50 mg/cc SiO_2 aerogel foam in comparison with the solid quartz. The ion flux from the solid quartz is found to be more directional, whereas from SiO_2 aerogel foam, it is nearly isotropic. The shadowgraph profiles of the plasma show more volume of the plasma at 2 ns and 8 ns time delays with respect to laser irradiation. Simulations with a 2D hydrodynamic code POLLUX supported the indication of volume heating of plasma being the cause for the change in X-ray emission. The calculated plasma parameters are T_c = 180 eV, T_h= 1000 eV, f = 0.009, and $n_e = 7 \times 10^{20}$ cm^{-3} and T_c = 190, T_h= 800 eV, f = 0.01, and $n_e = 4 \times 10^{20}$ cm^{-3} for quartz and SiO_2 aerogel foam, respectively.
5. In case of $(CD_2)_n$ foams, the peak ion velocity and ion flux are found to be maximum in the direction of target normal for 275 and 440 mg/cc $(CD_2)_n$ foam. With respect to laser

intensity, the scaling factor is more in case of 440 mg/cc in comparison to 275 mg/cc indicating a high velocity and more flux of ions in high dense CD_2. The velocity mapping indicates the presence of more energetic ions in case of 440 mg/cc in comparison to 275 mg/cc CD_2 at the same laser energy. The TPS results reveal that the effect of density of target on ion energy is more pronounced towards target normal instead of 45°.

6. In case of gold foam, the laser absorption in the foam targets are found to be volumetric and enhanced the X-ray emission by 13 % than the solid targets. It is also observed that the X-ray pulse duration in case of foam targets are slightly larger. X-ray pinhole camera and optical shadowgraphs are showing that the X-ray emitting region on foam targets are larger in transverse direction indicating the volumetric heating by supersonic heat wave which is in all direction. Ions Time-of-Flight spectroscopy measurements show that the thermal ions peak velocity is 31×10^4 m/s and spread in narrow energy width in case of solid target, whereas, in case of 0.1 g/cc gold foam target, the peak velocity reduces to 6 $\times10^4$ m/s towards target normal and emitted in broad energy range. However, total ion flux from foam and solid targets are comparable indicating that the ion emissions are from larger volume. This implies that the fluxes of particular charge states in gold foam targets are lower than the solid gold targets.

In short, the present thesis unravels many features of interaction of subnanosecond and ultrashort pulses with low density foam targets. In all the studies, the more isotropic nature of ions from the low-density targets is sign of volumetric absorption of laser light and less density gradients towards target normal. The presence of lower energy ions in low-density foam targets shows the less energy loss in hydrodynamic motion. The presence of less energetic ions in case of low density foams are also verified by results of Thomson Parabola Spectrometer. The shadows of the produced plasma clearly show the large volume of plasma inside the foam target and large size of expanding plasma plume. The calculations performed by hydrodynamic simulations indicate the effect of target density on temperature and density profile of plasma. This demonstration of low density foam targets as bright X-ray sources is important for using these targets in applications such as indirect drive ICF, X-ray backlighters and radiography experiments.

7.2 Future Research Plans

The work presented in this thesis can be followed by a number of directions to gain better understanding.

- The data analysis software for TPS can be improved further to include the non-linearity arising due to fringe effect of magnetic field. It helps in better match of lower charge states which are most affected due to these fields.
- The K and L- spectrum can be utilized as a probe in point projection absorption experiment. This help in finding opacity of technically important materials.
- The present foam targets can be irradiated by more powerful lasers, i.e., 100 TW to PW to reveal the features of X-ray and ion emission at high intensities of laser.
- In case of ultra-short laser experiments, along with measurement of hard X-rays, hot electrons can be observed to see the effect of foam density on non-linear processes.
- The deuterated foams can be utilized as an efficient neutron source.

References

[1] L. Tonks and I. Langmuir, “Oscillations in ionized gases,” *Phys. Rev.*, vol. 33, no. 2, pp. 195–210, 1929.

[2] J. J. Boyd, T.J.M., Sanderson, *Chen, F. F. Introduction to plasma physics and controlled fusion. Plenum Press, New York, (1974).Plasmas*. 2012.

[3] B. J., A., “Fundamentals of Plasma Physics Third Edition,” *Springer*, 2004.

[4] M. Göppert-Mayer, “Uber Elementarakte mit zwei Quantensprüngen,” *Ann. Phys.*, vol. 401, no. 3, pp. 273–294, 1931.

[5] P. Agostini, G. Barjot, J. Bonnal, G. Mainfray, C. Manus, and J. Morellec, “Multiphoton ionization of hydrogen and rare gases,” *IEEE J. Quantum Electron.*, vol. 4, no. 10, pp. 667–669, 1968.

[6] G. S. Voronov, G. A. Delone, and N. B. Delone, “Multiphoton ionization of atoms. ii. ionization of krypton by ruby-laser radiation,” *Jetp*, vol. 24, no. 6, pp. 1122–1125, 1967.

[7] “No Title.” [Online]. Available: http://wof-cluster.desy.de/sites/site_photonscience/content/e58/e186104/e186825/e186879.

[8] P. P. Rajeev, “Intense , Femtosecond Laser-Solid Interactions,” *PhD Thesis*, 2003.

[9] L. V. Keldysh, “Ionization in the field of a strong electromagnetic wave,” *Sov. Phys. JETP*, vol. 20, no. 5, pp. 1307–1314, 1965.

[10] A. V. Gaponov and M. A. Miller, “Potential wells for charged particles in a high-frequency electromagnetic field,” *J. Exp. Theor. Phys.*, no. 1, pp. 242–243, 1958.

[11] B. N. Chichkov, C. Momma, S. Nolte, F. Von Alvensleben, and A. Tünnermann, “Femtosecond, picosecond and nanosecond laser ablation of solids,” *Appl. Phys. A*

Mater. Sci. Process., vol. 63, no. 2, pp. 109–115, 1996.

[12] S. Eliezer, "The Interaction of High-Power Lasers With Plasmas," *Plasma Phys. Control. Fusion*, 2003.

[13] P. Gibbon, "Short Pulse Laser Interactions with Matter: An Introduction," *Short Pulse Laser Interact. with Matter An Introd.*, 2005.

[14] W. Shang, W. Zhang, R. Yu, and J. Yang, "Decay of electron conduction zone length by preheating in laser-produced plasma," *Mater. Express*, vol. 6, no. 4, pp. 377–381, 2016.

[15] R. S. Craxton *et al.*, "Direct-drive inertial confinement fusion: A review," *Phys. Plasmas*, vol. 22, no. 11, 2015.

[16] W. Kruer, *The physics of laser plasma interactions*. CRC Press, 2018.

[17] R. Fedosejevs, R. Ottmann, R. Sigel, G. Kühnle, S. Szatmári, and F. P. Schäfer, "Absorption of subpicosecond ultraviolet laser pulses in high-density plasma," *Appl. Phys. B Photophysics Laser Chem.*, vol. 50, no. 2, pp. 79–99, 1990.

[18] D. Colombant and G. F. Tonon, "X-ray emission in laser-produced plasmas," *J. Appl. Phys.*, vol. 44, no. 8, pp. 3524–3537, 1973.

[19] J. V Waszczak, A. T. Bel, M. Hill, and C. Vettier, "Letters 23," vol. 56, no. 25, pp. 2700–2703, 1986.

[20] M. J. Bernstein and G. G. Comisar, "X-ray production in laser-heated plasmas," *J. Appl. Phys.*, vol. 41, no. 2, pp. 729–733, 1970.

[21] D. Giulietti and L. A. Gizzi, "X-Ray Emission from Laser Produced Plasmas," *Riv. Del Nuovo Cim.*, 21, no. 10, pp. 1-93, *1998.*

[22] H. R. Griem, *Principles of plasma spectroscopy*, vol. 2. Cambridge University Press, 2005.

[23] R. L. Kauffman and A. RUBENCHIK, “Handbook of plasma physics,” *AM Rubenchik S. Witkowski, eds*, vol. 3, p. 111, 1991.

[24] V. Arora, Phd Thesis “X-RAY SPECTROSCOPIC STUDIES OF PLASMA PRODUCED BY INTENSE LASER BEAMS,” 2013.

[25] J. Cooper, “Plasma spectroscopy,” *Reports Prog. Phys.*, vol. 29, no. 1, pp. 35–130, 1966.

[26] T. Fujimoto and R. W. P. McWhirter, “Validity criteria for local thermodynamic equilibrium in plasma spectroscopy,” *Phys. Rev. A*, vol. 42, no. 11, p. 6588, 1990.

[27] H. K. Chung, M. H. Chen, W. L. Morgan, Y. Ralchenko, and R. W. Lee, “FLYCHK: Generalized population kinetics and spectral model for rapid spectroscopic analysis for all elements,” *High Energy Density Phys.*, 2005.

[28] J. Krása *et al.*, “The effect of laser-produced plasma expansion on the ion population,” *Appl. Phys. Lett.*, vol. 75, no. 17, pp. 2539–2541, 1999.

[29] I. V Roudskoy, “General features of highly charged ion generation in laser-produced plasmas,” *Laser Part. Beams*, vol. 14, no. 3, pp. 369–384, 1996.

[30] L. Torrisi, S. Gammino, L. Andò, and L. Làska, “Tantalum ions produced by 1064 nm pulsed laser irradiation,” *J. Appl. Phys.*, vol. 91, no. 7, pp. 4685–4692, 2002.

[31] N. G. Borisenko, A. I. Gromov, Y. A. Merkul’ev, A. V Mitrofanov, and W. Nazarov, “Regular foams, loaded foams and capsule suspension in the foam for hohlraums in ICF,” *Fusion Technol.*, 2000.

[32] N. G. Borisenko *et al.*, “Regular 3-D networks with clusters for controlled energy transport studies in laser plasma near critical density,” *Fusion Sci. Technol.*, vol. 49, no.

4, pp. 676–685, 2006.

[33] A. Venkateswara Rao, S. D. Bhagat, H. Hirashima, and G. M. Pajonk, "Corrigendum to 'Synthesis of flexible silica aerogels using methyltrimethoxysilane (MTMS) precursor' [J. Colloid Interface Sci. 300 (2006) 279-285] (DOI:10.1016/j.jcis.2006.03.044)," *Journal of Colloid and Interface Science*. 2006.

[34] A. V. Rao, M. M. Kulkarni, D. P. Amalnerkar, and T. Seth, "Superhydrophobic silica aerogels based on methyltrimethoxysilane precursor," *J. Non. Cryst. Solids*, 2003.

[35] A. Venkateswara Rao and S. D. Bhagat, "Synthesis and physical properties of TEOS-based silica aerogels prepared by two step (acid-base) sol-gel process," *Solid State Sci.*, 2004.

[36] S. Y. Gus'Kov *et al.*, "Absorption coefficient for nanosecond laser pulse in porous material," *Plasma Phys. Control. Fusion*, vol. 57, no. 12, 2015.

[37] S. Y. Gus'kov and V. B. Rozanov, "Interaction of laser radiation with a porous medium and formation of a nonequilibrium plasma," *Quantum Electron.*, vol. 27, no. 8, pp. 696–701, 1997.

[38] S. Y. Gus'kov, J. Limpouch, P. Nicolaï, and V. T. Tikhonchuk, "Laser-supported ionization wave in under-dense gases and foams," *Phys. Plasmas*, vol. 18, no. 10, 2011.

[39] W. Shang, J. Yang, and Y. Dong, "Enhancement of laser to x-ray conversion with a low density gold target," *Appl. Phys. Lett.*, vol. 102, no. 9, p. 720, 2013.

[40] Y. Xu, T. Zhu, S. Li, and J. Yang, "Beneficial effect of CH foam coating on x-ray emission from laser-irradiated high-Z material," *Phys. Plasmas*, vol. 18, no. 5, 2011.

[41] J. Lindl, "Development of the indirect-drive approach to inertial confinement fusion and the target physics basis for ignition and gain," *Phys. Plasmas*, vol. 2, no. 11, pp. 3933–

4024, 1995.

[42] 王瑞荣 Ruirong Wang, 陈伟民 Weimin Chen, 毛楚生 Chusheng Mao, 董佳钦 Jiaqin Dong, and 傅思祖 Sizu Fu, “Laser-produced plasma He-alpha source for pulse radiography,” *Chinese Opt. Lett.*, vol. 7, no. 2, pp. 156–158, 2009.

[43] L. Rymell, M. Berglund, and H. M. Hertz, “Debris- free single- line laser- plasma x-ray source for microscopy,” *Appl. Phys. Lett.*, vol. 66, no. 20, pp. 2625–2627, 1995.

[44] L. J. Dhareshwar *et al.*, “X-ray back-lighter characterization for iron opacity measurements using laser-produced aluminium K-alpha emission To cite this version : HAL Id : hal-00569820 X-ray back lighter characterisation for iron opacity measurements using laser produced aluminium,” 2011.

[45] J. C. Wood *et al.*, “Ultrafast Imaging of Laser Driven Shock Waves using Betatron X-rays from a Laser Wakefield Accelerator,” *Sci. Rep.*, vol. 8, no. 1, pp. 1–10, 2018.

[46] T. Tajima, D. Habs, and X. Yan, “Laser Acceleration of Ions for Radiation Therapy,” *Rev. Accel. Sci. Technol.*, vol. 02, no. 01, pp. 201–228, 2009.

[47] R. Jafer *et al.*, “Proton radiography of a laser-driven cylindrical implosion,” *AIP Conf. Proc.*, vol. 1209, no. July, pp. 47–50, 2010.

[48] M. Roth *et al.*, “Fast ignition by intense laser-accelerated proton beams,” *Phys. Rev. Lett.*, vol. 86, no. 3, pp. 436–439, 2001.

[49] S. Chaurasia, D. S. Munda, and L. J. Dhareshwar and 2008. BARC/2008/E/19, “BARC newsletter.

[50] “TIFR website.” [Online]. Available: http://www.tifr.res.in/~uphill/laser-plasma-dynamics.html.

[51] J. J. Thomson, "XLVII. On rays of positive electricity," *London, Edinburgh, Dublin Philos. Mag. J. Sci.*, vol. 13, no. 77, pp. 561–575, 1907.

[52] S. Chaurasia *et al.*, "In situ measurement of ions parameters of laser produced ion source using high resolution Thomson Parabola Spectrometer," *J. Instrum.*, vol. 11, no. 8, 2016.

[53] S. Chaurasia, V. Rastogi, D. S. Munda, R. K. Bhatia, and V. Nataraju, "Thomson parabola: a high resolution ion spectrometer," *BARC Newsl.*, no. 345, pp. 18–21, 2015.

[54] T. N. Hansen, J. Schou, and J. G. Lunney, "Angular distributions of silver ions and neutrals emitted in vacuum by laser ablation," *EPL (Europhysics Lett.*, vol. 40, no. 4, p. 441, 1997.

[55] A. Thum-Jager and K. Rohr, "Angular emission distributions of neutrals and ions in laser ablated particle beams," *J. Phys. D. Appl. Phys.*, vol. 32, no. 21, p. 2827, 1999.

[56] S. Chaurasia *et al.*, "Simultaneous measurement of particle velocity and shock velocity for megabar laser driven shock studies," *BARC Newslett*, vol. 317, pp. 13–21, 2010.

[57] H.-J. Kunze, *Introduction to plasma spectroscopy*, vol. 56. Springer Science & Business Media, 2009.

[58] V. A. Boiko, A. Y. Faenov, and S. A. Pikuz, "X-ray spectroscopy of multiply-charged ions from laser plasmas," *J. Quant. Spectrosc. Radiat. Transf.*, vol. 19, no. 1, pp. 11–50, 1978.

[59] U. I. Safronova, M. S. Safronova, R. Bruch, and L. A. Vainshtein, "Dielectronic satellite spectra of the 1s3p-1s2 lines for highly-charged ions with Z= 6-54 (1s2l3l'-1s2 2l transitions)," *Phys. Scr.*, vol. 51, no. 4, p. 471, 1995.

[60] O. Ciricosta *et al.*, "Direct measurements of the ionization potential depression in a dense plasma," *Phys. Rev. Lett.*, vol. 109, no. 6, pp. 1–4, 2012.

[61] L. P. Presnyakov, "X-ray spectroscopy of high-temperature plasma," *Sov. Phys. Uspekhi*, vol. 19, no. 5, p. 387, 1976.

[62] C. Biedermann, R. Radtke, and K. B. Fournier, "Spectroscopy of heliumlike argon resonance and satellite lines for plasma temperature diagnostics," *Phys. Rev. E*, vol. 66, no. 6, p. 66404, 2002.

[63] S. H. Glenzer *et al.*, "Accuracy of K-shell spectra modeling in high-density plasmas," *Phys. Rev. E*, vol. 62, no. 2, p. 2728, 2000.

[64] H. S. Vora, "PROMISE-a software package for profile measurement," CAT Report No. CAT/1996/10, 1996.

[65] P. D. Gupta, R. Popil, R. Fedosejevs, A. A. Offenberger, D. Salzmann, and C. E. Capjack, "Temperature and x- ray intensity scaling in KrF laser plasma interaction," *Appl. Phys. Lett.*, vol. 48, no. 2, pp. 103–105, 1986.

[66] F. Bely-Dubau, A. H. Gabriel, and S. Volonté, "Dielectronic satellite spectra for highly charged helium-like ions–III. Calculations of n= 3 solar flare iron lines," *Mon. Not. R. Astron. Soc.*, vol. 186, no. 3, pp. 405–419, 1979.

[67] A. H. Gabriel and T. M. Paget, "Measurement and interpretation of dielectronic recombination satellite line intensities," *J. Phys. B At. Mol. Phys.*, vol. 5, no. 3, p. 673, 1972.

[68] N. Konjević, M. Ivković, and N. Sakan, "Hydrogen Balmer lines for low electron number density plasma diagnostics," *Spectrochim. Acta Part B At. Spectrosc.*, vol. 76, pp. 16–26, 2012.

[69] N. Konjevic and J. R. Roberts, "A critical review of the Stark widths and shifts of spectral lines from non- hydrogenic atoms," *J. Phys. Chem. Ref. Data*, vol. 5, no. 2, pp.

209–257, 1976.

[70] J. J. Olivero and R. L. Longbothum, "Empirical fits to the Voigt line width: A brief review," *J. Quant. Spectrosc. Radiat. Transf.*, vol. 17, no. 2, pp. 233–236, 1977.

[71] A. V. Vinogradov, I. I. Sobel'man, and E. A. Yukov, "Spectroscopic methods for diagnostics of superdense hot plasma," *Quantum Electron.*, vol. 4, no. 2, pp. 149–154, 1974.

[72] H. Kondo and T. Tomie, "Optimization of a laser- plasma x- ray source for contact x-ray microscopy," *J. Appl. Phys.*, vol. 75, no. 8, pp. 3798–3805, 1994.

[73] C. J. Keane, B. A. Hammel, A. L. Osterheld, and D. R. Kania, "Density and temperature sensitive features in high temperature plasma L-shell xenon emission spectra," *Phys. Rev. Lett.*, vol. 72, no. 19, p. 3029, 1994.

[74] C. A. Back *et al.*, "Efficient multi-keV underdense laser-produced plasma radiators," *Phys. Rev. Lett.*, vol. 87, no. 27, p. 275003, 2001.

[75] J. E. Rice *et al.*, "X-ray observations of 2l-nl'transitions in Mo 3 0+–Mo 3 3+ from tokamak plasmas," *Phys. Rev. A*, vol. 51, no. 5, p. 3551, 1995.

[76] G. V Brown, P. Beiersdorfer, D. A. Liedahl, K. Widmann, and S. M. Kahn, "Laboratory measurements and modeling of the Fe XVII X-ray spectrum," *Astrophys. J.*, vol. 502, no. 2, p. 1015, 1998.

[77] N. S. Brickhouse *et al.*, "Coronal structure and abundances of Capella from simultaneous EUVE and ASCA spectroscopy," *Astrophys. J.*, vol. 530, no. 1, p. 387, 2000.

[78] E. Träbert, S. B. Hansen, P. Beiersdorfer, G. V Brown, K. Widmann, and H.-K. Chung, "L-shell spectroscopy of Au as a temperature diagnostic tool," *Rev. Sci. Instrum.*, vol.

79, no. 10, p. 10E313, 2008.

[79] K. B. Fournier *et al.*, "Electron-density scaling of conversion efficiency of laser energy into L-shell X-rays," *J. Quant. Spectrosc. Radiat. Transf.*, vol. 99, no. 1–3, pp. 186–198, 2006.

[80] M. Shahzad, G. J. Tallents, A. B. Steel, L. Hobbs, D. J. Hoarty, and J. Dunn, "Electron temperature and density characterization using L-shell spectroscopy of laser irradiated buried iron layer targets," *Phys. Plasmas*, vol. 21, no. 8, p. 82702, 2014.

[81] A. Ecuvillon, G. Israelian, N. C. Santos, M. Mayor, V. Villar, and G. Bihain, "C, S, Zn and Cu abundances in planet-harbouring stars," *Astron. Astrophys.*, vol. 426, no. 2, pp. 619–630, 2004.

[82] J. Cooper, "Plasma spectroscopy," *Reports Prog. Phys.*, vol. 29, no. 1, p. 35, 1966.

[83] I. P. Grant, B. J. McKenzie, P. H. Norrington, D. F. Mayers, and N. C. Pyper, "An atomic multiconfigurational Dirac-Fock package," *Comput. Phys. Commun.*, vol. 21, pp. 207–231, 1980.

[84] J. H. Parkinson, "New observations of Fe XVII in the solar X-ray spectrum," *Astron. Astrophys.*, vol. 24, p. 215, 1973.

[85] R. J. Hutcheon, L. Cooke, M. H. Key, C. L. S. Lewis, and G. E. Bromage, "Neon-like and fluorine-like x-ray emission spectra for elements from Cu to Sr," *Phys. Scr.*, vol. 21, no. 1, p. 89, 1980.

[86] K. B. Fournier *et al.*, "Observations of high-n transitions in the spectra of near-neon-like copper ions from laser-produced plasmas," *J. Phys. B At. Mol. Opt. Phys.*, vol. 35, no. 15, p. 3347, 2002.

[87] H. Gordon, M. G. Hobby, and N. J. Peacock, "Classification of the X-ray spectra of

transitions in the Ne, F and OI isoelectronic sequences of the elements from iron to bromine and in the Na I isoelectronic sequence of gallium to bromine," *J. Phys. B At. Mol. Phys.*, vol. 13, no. 10, p. 1985, 1980.

[88] K. B. Fournier *et al.*, "Influence of optical thickness and hot electrons on Rydberg spectra of Ne-like and F-like copper ions," *Phys. Rev. E*, vol. 67, no. 1, p. 16402, 2003.

[89] M. Swartz, S. Kastner, E. Rothe, and W. Neupert, "Soft X-ray spectra of Cr, Mn, Fe, Co, Ni, Cu; classifications in Ne I, FI, OI, NI, and CI isoelectronic sequences," *J. Phys. B At. Mol. Phys.*, vol. 4, no. 12, p. 1747, 1971.

[90] V. K. Unnikrishnan, K. Alti, V. B. Kartha, C. Santhosh, G. P. Gupta, and B. M. Suri, "Measurements of plasma temperature and electron density in laser-induced copper plasma by time-resolved spectroscopy of neutral atom and ion emissions," *Pramana*, vol. 74, no. 6, pp. 983–993, 2010.

[91] G. V Brown, P. Beiersdorfer, H. Chen, M. H. Chen, and K. J. Reed, "Diagnostic utility of the relative intensity of 3C to 3D in Fe XVII," *Astrophys. J. Lett.*, vol. 557, no. 1, p. L75, 2001.

[92] R. Bruch, U. I. Safronova, A. S. Shlyaptseva, J. Nilsen, and D. Schneider, "Theoretical analysis of the doubly excited 3lnl'states of sodiumlike copper," *Phys. Scr.*, vol. 57, no. 3, p. 334, 1998.

[93] S. Bollanti *et al.*, "Na-like autoionization states of copper ions in plasma, heated by excimer laser," *Phys. Scr.*, vol. 51, no. 3, p. 326, 1995.

[94] A. L. Osterheld, J. Nilsen, S. Y. Khakhalin, A. Y. Faenov, and S. A. Pikuz, "Dielectronic satellites to the Ne-like yttrium resonance lines," *Phys. Scr.*, vol. 54, no. 3, p. 240, 1996.

[95] H. is a commercial product of C. A. Sciences., *No Title*. .

[96] D. M. O'Neill, C. L. S. Lewis, D. Neely, S. J. Davidson, S. J. Rose, and R. W. Lee, "Characterization of a laser-produced plasma using the technique of point-projection absorption spectroscopy," *Phys. Rev. A*, vol. 44, no. 4, p. 2641, 1991.

[97] C. L. S. Lewis and J. McGlinchey, "Quasi-monochromatic, projection radiography of dense laser driven spherical targets," *Opt. Commun.*, vol. 53, no. 3, pp. 179–186, 1985.

[98] L. Miaja-Avila *et al.*, "Laser plasma x-ray source for ultrafast time-resolved x-ray absorption spectroscopy," *Struct. Dyn.*, vol. 2, no. 2, p. 24301, 2015.

[99] E. Förster, K. Gäbel, and I. Uschmann, "X-ray microscopy of laser-produced plasmas with the use of bent crystals," *Laser Part. Beams*, vol. 9, no. 1, pp. 135–148, 1991.

[100] A. K. Rossall *et al.*, "X-ray back-lighter characterization for iron opacity measurements using laser-produced aluminium K-alpha emission," *J. Phys. B At. Mol. Opt. Phys.*, vol. 43, no. 15, p. 155403, 2010.

[101] A. A. Andreev, J. Limpouch, A. B. Iskakov, and H. Nakano, "Enhancement of x-ray line emission from plasmas produced by short high-intensity laser double pulses," *Phys. Rev. E*, vol. 65, no. 2, p. 26403, 2002.

[102] S. Chaurasia, D. S. Munda, C. G. Murali, N. K. Gupta, and L. J. Dhareshwar, "X-ray and ion measurements in laser produced plasma from gold-copper alloy targets," *J. Appl. Phys.*, vol. 103, no. 1, p. 13307, 2008.

[103] S. Chaurasia, S. Tripathi, P. Leshma, C. G. Murali, and J. Pasley, "Optimization of bremsstrahlung and characteristic line emission from aluminum plasma," *Opt. Commun.*, vol. 308, pp. 169–174, 2013.

[104] H. Fiedorowicz, A. Bartnik, R. Jarocki, R. Rakowski, and M. Szczurek, "Enhanced X-ray emission in the 1-keV range from a laser-irradiated gas puff target produced using

the double-nozzle setup," *Appl. Phys. B*, vol. 70, no. 2, pp. 305–308, 2000.

[105] M. H. Mahdieh, R. Fazeli, and G. J. Tallents, "Soft x-ray enhancement from a porous nano-layer on metal targets irradiated by long laser pulses," *J. Phys. B At. Mol. Opt. Phys.*, vol. 42, no. 12, p. 125602, 2009.

[106] P. P. Rajeev, P. Taneja, P. Ayyub, A. S. Sandhu, and G. R. Kumar, "Metal nanoplasmas as bright sources of hard x-ray pulses," *Phys. Rev. Lett.*, vol. 90, no. 11, p. 115002, 2003.

[107] N. G. Borisenko *et al.*, "Regular 3-D networks with clusters for controlled energy transport studies in laser plasma near critical density," *Fusion Sci. Technol.*, vol. 49, no. 4, pp. 676–685, 2006.

[108] R. Benocci *et al.*, "Direct evidence of gas-induced laser beam smoothing in the interaction with thin foils," *Phys. Plasmas*, vol. 16, no. 1, p. 12703, 2009.

[109] T. Hall, D. Batani, W. Nazarov, M. Koenig, and A. Benuzzi, "Recent advances in laser–plasma experiments using foams," *Laser Part. Beams*, vol. 20, no. 2, pp. 303–316, 2002.

[110] A. Benuzzi *et al.*, "Dynamics of laser produced shocks in foam–solid targets," *Phys. Plasmas*, vol. 5, no. 8, pp. 2827–2829, 1998.

[111] B. Canaud *et al.*, "High-gain direct-drive target design for the laser megajoule," *Nucl. fusion*, vol. 44, no. 10, p. 1118, 2004.

[112] K. B. Fournier *et al.*, "Absolute X-ray yields from laser-irradiated germanium-doped low-density aerogels," *Phys. Plasmas*, vol. 16, no. 5, p. 52703, 2009.

[113] S. Chaurasia *et al.*, "Studies on subcritical and overcritical density laser ablated TAC foam targets," *Opt. Commun.*, vol. 343, pp. 1–5, 2015.

[114] J. Limpouch *et al.*, "Laser absorption and energy transfer in foams of various pore structures and chemical compositions," in *Journal de Physique IV (Proceedings)*, 2006,

vol. 133, pp. 457–459.

[115] S. N. Chen *et al.*, "Density and temperature characterization of long-scale length, near-critical density controlled plasma produced from ultra-low density plastic foam," *Sci. Rep.*, vol. 6, p. 21495, 2016.

[116] S. Chaurasia *et al.*, "Laser interaction with low-density carbon foam," *Pramana*, vol. 75, no. 6, pp. 1191–1196, 2010.

[117] F. Girard, "Review of laser produced multi-keV X-ray sources from metallic foils, cylinders with liner, and low density aerogels," *Phys. Plasmas*, vol. 23, no. 4, p. 40501, 2016.

[118] R. Liska, J. Limpouch, M. Kuchařík, and O. Renner, "Selected laser plasma simulations by ALE method," *J. Phys. Conf. Ser.*, vol. 112, no. Part 2, 2008.

[119] J. Limpouch *et al.*, "Laser interactions with plastic foam - Metallic foil layered targets," *Plasma Phys. Control. Fusion*, vol. 46, no. 12 A, pp. 1831–1841, 2004.

[120] C. Labaune *et al.*, "Laser-plasma interaction physics in multi kilojoule experiments," *J. Phys. Conf. Ser.*, vol. 244, no. PART 2, 2010.

[121] G. A. Vergunova, S. Yu, V. B. Rozanov, and O. N. Rozmej, "FORMATION OF A PLANE LAYER OF PLASMA UNDER IRRADIATION BY A SOFT X-RAY SOURCE," vol. 31, no. 5, pp. 509–518, 2010.

[122] F. NAJMABADI *et al.*, "Fusion Energy Research with Lasers, Direct Drive Targets, and Dry Wall Chambers," 2001.

[123] N. G. Borisenko, A. M. Khalenkov, V. Kmetik, J. Limpouch, Y. A. Merkuliev, and V. G. Pimenov, "Plastic aerogel targets and optical transparency of undercritical microheterogeneous plasma," *Fusion Sci. Technol.*, vol. 51, no. 4, pp. 655–664, 2007.

[124] A. M. Khalenkov, N. G. Borisenko, V. N. Kondrashov, Y. A. Merkuliev, J. Limpouch, and V. G. Pimenov, “Experience of micro-heterogeneous target fabrication to study energy transport in plasma near critical density,” *Laser Part. Beams*, vol. 24, no. 2, pp. 283–290, 2006.

[125] Y. Dong *et al.*, “The impact of low-Z impurities on x-ray conversion efficiency from laser-produced plasmas of low-density gold foam targets,” *Phys. Plasmas*, vol. 20, no. 12, p. 123305, 2013.

[126] W. Shang *et al.*, “Experimental demonstration of laser to x-ray conversion enhancements with low density gold targets,” *Appl. Phys. Lett.*, vol. 108, no. 6, p. 64102, 2016.

[127] W. Shang *et al.*, “Experimental study of X-ray emission properties of laser produced plasmas with Au and Au foam layer targets,” *J. Alloys Compd.*, vol. 578, pp. 1–4, 2013.

[128] W. Shang, J. Yang, and Y. Dong, “Enhancement of laser to x-ray conversion with a low density gold target,” *Appl. Phys. Lett.*, vol. 102, no. 9, p. 94105, 2013.

[129] B. A. Remington *et al.*, “Supernova hydrodynamics experiments on the Nova laser,” *Phys. Plasmas*, vol. 4, no. 5, pp. 1994–2003, 1997.

[130] R. I. Klein, K. S. Budil, T. S. Perry, and D. R. Bach, “Interaction of supernova remnants with interstellar clouds: from the NOVA laser to the galaxy,” *Astrophys. J. Suppl. Ser.*, vol. 127, no. 2, p. 379, 2000.

[131] B. A. Remington, R. P. Drake, H. Takabe, and D. Arnett, “A review of astrophysics experiments on intense lasers,” *Phys. Plasmas*, vol. 7, no. 5, pp. 1641–1652, 2000.

[132] Y. Dong, L. Zhang, J. Yang, and W. Shang, “Detailed energy distributions in laser-produced plasmas of solid gold and foam gold planar targets,” *Phys. Plasmas*, vol. 20,

no. 12, p. 123102, 2013.

[133] S. Chaurasia, C. Kaur, N. G. Borisenko, J. Pasley, A. Orekhov, and M. N. Deo, "Enhancement of keV X-rays from low-density cellulose triacetate (TAC) foam targets," *Phys. Plasmas*, vol. 24, no. 7, p. 73110, 2017.

[134] C. Kaur *et al.*, "Interaction of high-power laser radiation with low-density polymer aerogels," *Quantum Electron.*, vol. 47, no. 6, pp. 495–502, 2017.

[135] N. G. Borisenko, A. M. Khalenkov, V. Kmetik, J. Limpouch, Y. A. Merkuliev, and V. G. Pimenov, "Plastic aerogel targets and optical transparency of undercritical microheterogeneous plasma," *Fusion Sci. Technol.*, vol. 51, no. 4, pp. 655–664, 2007.

[136] E. E. Sheveleva, V. G. Pimenov, I. V Pikulin, and A. M. Sakharov, "The formation of ultralow-density microcellular diane-formaldehyde gels and aerogels," *Polym. Sci. Ser. B*, vol. 58, no. 2, pp. 173–182, 2016.

[137] B. R. N. S. Chaurasia, D. S. Munda, and L. J. Dhareshwar and 2008. BARC/2008/E/19, "BARC newsletter."

[138] A. E. Bugrov *et al.*, "Interaction of a high-power laser beam with low-density porous media," *J. Exp. Theor. Phys.*, vol. 84, no. 3, pp. 497–505, 1997.

[139] Y. Xu, T. Zhu, S. Li, and J. Yang, "Beneficial effect of CH foam coating on x-ray emission from laser-irradiated high-Z material," *Phys. Plasmas*, vol. 18, no. 5, p. 53301, 2011.

[140] L. Torrisi, "Ion acceleration and DD nuclear fusion in laser-generated plasma from advanced deuterated polyethylene," *Molecules*, vol. 19, no. 10, pp. 17052–17065, 2014.

[141] P. A. Norreys *et al.*, "Neutron production from picosecond laser irradiation of deuterated targets at intensities of," *Plasma Phys. Control. fusion*, vol. 40, no. 2, p. 175, 1998.

[142] J. Krása and D. Klír, “Fast neutrons available through beam-target reactions driven by TW lasers,” in *4th Workshop-Plasmi, Sorgenti, Biofisica ed Applicazioni*, 2015, vol. 2014, pp. 44–47.

[143] G. M. Pajonk, A. V. Rao, B. M. Sawant, and N. N. Parvathy, “Dependence of monolithicity and physical properties of TMOS silica aerogels on gel aging and drying conditions1,” *J. Non. Cryst. Solids*, vol. 209, no. 1–2, pp. 40–50, 1997.

[144] A. V. Rao, S. D. Bhagat, H. Hirashima, and G. M. Pajonk, “Synthesis of flexible silica aerogels using methyltrimethoxysilane (MTMS) precursor,” *J. Colloid Interface Sci.*, vol. 300, no. 1, pp. 279–285, 2006.

[145] A. V. Rao, G. M. Pajonk, D. Haranath, and P. B. Wagh, “Effect of sol-gel processing parameters on optical properties of TMOS silica aerogels,” *J. Mater. Synth. Process.*, vol. 6, no. 1, pp. 37–48, 1998.

[146] C. Kaur *et al.*, “X-ray and ion emission studies from subnanosecond laser-irradiated SiO 2 aerogel foam targets,” *Laser Part. Beams*, vol. 35, no. 3, pp. 505–512, 2017.

[147] J. P. Boris and D. L. Book, “Flux-corrected transport. III. Minimal-error FCT algorithms,” *J. Comput. Phys.*, vol. 20, no. 4, pp. 397–431, 1976.

[148] R. Courant, E. Isaacson, and M. Rees, “On the solution of nonlinear hyperbolic differential equations by finite differences,” *Commun. Pure Appl. Math.*, vol. 5, no. 3, pp. 243–255, 1952.

[149] L. Spitzer Jr and R. Härm, “Transport phenomena in a completely ionized gas,” *Phys. Rev.*, vol. 89, no. 5, p. 977, 1953.

[150] S. L. Thompson, “IMPROVEMENTS IN THE CHART D RADIATION-HYDRODYNAMIC CODE I: ANALYTIC EQUATIONS OF STATE.,” Sandia Labs.,

Albuquerque, N. Mex., 1970.

[151] J. Balmer *et al.*, “X-ray absorption spectroscopy of laser-produced plasmas: A study of the experiment and data analysis,” *Phys. Rev. A*, vol. 40, no. 1, p. 330, 1989.

[152] H. Merdji *et al.*, “Absorption spectroscopy of a radiatively heated samarium plasma,” *Phys. Rev. E*, vol. 57, no. 1, p. 1042, 1998.

[153] P. Audebert *et al.*, “Picosecond time-resolved x-ray absorption spectroscopy of ultrafast aluminum plasmas,” *Phys. Rev. Lett.*, vol. 94, no. 2, p. 25004, 2005.

[154] P. E. Young *et al.*, “Demonstration of the density dependence of X-ray flux in a laser-driven hohlraum,” *Phys. Rev. Lett.*, vol. 101, no. 3, p. 35001, 2008.

[155] R. E. Olson *et al.*, “X-ray conversion efficiency in vacuum hohlraum experiments at the National Ignition Facility,” *Phys. Plasmas*, vol. 19, no. 5, p. 53301, 2012.

[156] J. D. Lindl *et al.*, “The physics basis for ignition using indirect-drive targets on the National Ignition Facility,” *Phys. Plasmas*, vol. 11, no. 2, pp. 339–491, 2004.

[157] E. L. Dewald *et al.*, “X-ray conversion efficiency of high-Z hohlraum wall materials for indirect drive ignition,” *Phys. Plasmas*, vol. 15, no. 7, p. 72706, 2008.

[158] P. Amendt *et al.*, “Low-adiabat rugby hohlraum experiments on the National Ignition Facility: Comparison with high-flux modeling and the potential for gas-wall interpenetration,” *Phys. Plasmas*, vol. 21, no. 11, p. 112703, 2014.

[159] M. D. Rosen and J. H. Hammer, “Analytic expressions for optimal inertial-confinement-fusion hohlraum wall density and wall loss,” *Phys. Rev. E*, vol. 72, no. 5, p. 56403, 2005.

[160] J. H. Hammer and M. D. Rosen, “A consistent approach to solving the radiation diffusion equation,” *Phys. Plasmas*, vol. 10, no. 5, pp. 1829–1845, 2003.

[161] W. Shang *et al.*, “Experimental demonstration of laser to x-ray conversion

enhancements with low density gold targets," *Appl. Phys. Lett.*, vol. 108, no. 6, pp. 1–5, 2016.

[162] K. Lan and P. Song, "Foam Au driven by 4 ω–2 ω ignition laser pulse for inertial confinement fusion," *Phys. Plasmas*, vol. 24, no. 5, p. 52707, 2017.

[163] L. Zhang *et al.*, "Reducing wall plasma expansion with gold foam irradiated by laser," *Phys. Plasmas*, vol. 22, no. 11, p. 110703, 2015.

[164] A. I. Gromov, N. G. Borisenko, S. Y. GUS'KOV, Y. A. Merkul'Ev, and A. V Mitrofanov, "Fabrication and monitoring of advanced low-density media for ICF targets," *Laser Part. Beams*, vol. 17, no. 4, pp. 661–670, 1999.

[165] I. V Akimova, A. A. Akunets, L. A. Borisenko, A. I. Gromov, Y. A. Merkuliev, and A. S. Orekhov, "Metals produced as nano-snow layers for converters of laser light into X-ray for indirect targets and as intensive EUV sources," *J. Radioanal. Nucl. Chem.*, vol. 299, no. 2, pp. 955–960, 2014.

[166] G. A. Vergunova and V. B. Rozanov, "Influence of intrinsic X-ray emission on the processes in low-density laser targets," *Laser Part. Beams*, vol. 17, no. 3, pp. 579–583, 1999.

[167] A.F. Nikiforov, V. G. Novikov, *Quantum–Statistical Model. High-Temperature Plasma*. (Fizmatlit, Moscow, 2000) [in Russian].

[168] G. A. Vergunova, V. B. Rozanov, A. S. Grushin, V. G. Novikov, N. Y. Orlov, and O. N. Rozmej, "Heating of Low-Density Matter by Soft X-Ray Radiation and Radiation Waves," *J. Russ. Laser Res.*, vol. 34, no. 5, pp. 441–452, 2013.